

Torsional Performance of Large Wind Turbine Blades – Experimental and Numerical Analysis

Technical University of Denmark
Department of Mechanical Engineering
Coastal, Maritime and Structural Engineering

Risø National Laboratory
Wind Energy Department (VEA)
Structural Design Group

Peter Berring & Henrik Knudsen

Peter Berring

Henrik Knudsen

Table of contents

1. ACKNOWLEDGEMENTS.....	4
2. INTRODUCTION.....	5
2.1. AIM OF PRE-PROJECT.....	6
2.2. AIM OF MASTER THESIS	7
2.3. THE AEROELASTIC CODE HAWC2	8
3. FUNDAMENTAL THEORY.....	9
3.1. CLASSICAL AND FIRST-ORDER THEORIES OF LAMINATED COMPOSITE PLATES	9
3.1.1. <i>The classical laminated plate theory</i>	9
3.1.2. <i>The first-order shear deformation laminated plate theory</i>	15
3.2. SIMPLE COMPOSITE BEAM MODEL WITH BEND-TWIST COUPLING	19
3.2.1. <i>Theoretical estimation of the stiffness parameters, and coupling coefficient</i>	20
3.3. BEAM THEORIES	22
3.3.1. <i>Bernoulli-Euler beam theory</i>	22
3.3.2. <i>Timoshenko beam theory</i>	24
3.4. TORSION.....	26
3.4.1. <i>Circular cross section</i>	26
3.4.2. <i>Non-circular cross section</i>	28
3.4.3. <i>Closed thin-walled cross-section</i>	32
4. THE BEAM PROPERTY EXTRACTION (BPE) METHOD BY MALCOLM AND LAIRD.....	38
4.1. EXTRACTION OF THE EQUIVALENT BEAM PROPERTIES	38
4.1.1. <i>Stiffness matrix K</i>	38
4.1.2. <i>Constitutive matrix k</i>	40
4.1.3. <i>Elastic center</i>	42
4.1.4. <i>Principal axes rotation</i>	43
4.1.5. <i>Shear center</i>	44
4.1.6. <i>Translation and rotation of coordinates</i>	45
4.2. INSIGHT INTO THE 3D TIMOSHENKO MODEL.....	47
4.3. EXTRACTION OF THE EQUIVALENT BEAM PROPERTIES FOR A 4x4 MATRIX	50
4.4. ANALYTICAL VALIDATION OF THE BEAM PROPERTY EXTRACTION (BPE) METHOD	52
4.4.1. <i>Cross sectional properties for the analytical model</i>	53
4.4.2. <i>The six load cases for the analytical model</i>	54
4.4.3. <i>Analytical validation of the method for determining the elastic center</i>	60
4.4.4. <i>Analytical validation of the method for determining the shear center</i>	60
4.4.5. <i>Analytical validation of the method for determining the orientation of the principle axes</i>	63
4.4.6. <i>Translation and rotation transformation of the constitutive matrix (k)</i>	63
4.4.7. <i>Summary and conclusion of the analytical model</i>	64
4.5. NUMERICAL VALIDATION OF THE BEAM PROPERTY EXTRACTION (BPE) METHOD.....	64
4.5.1. <i>Least squares algorithm (displacements and rotations)</i>	65
4.5.2. <i>MPC-element (displacements and rotations)</i>	72
4.5.3. <i>Comparison between least squares algorithm and MPC element</i>	73
4.5.4. <i>The numerical results of the BPE-method</i>	74
5. EXPERIMENTAL TESTING OF THE BLADE SECTION	88
5.1. THE TEST RIG.....	88
5.1.1. <i>The principle construction of the test rig</i>	89
5.1.2. <i>The five test methods</i>	92
5.2. MEASURING METHOD FOR THE ORIGINAL BLADE SECTION	97
5.3. EXPERIMENTAL DETERMINATION OF THE DEFLECTIONS AND ROTATIONS	100
5.3.1. <i>Boundary conditions</i>	103
5.4. EXPERIMENTAL RESULTS FOR THE FIVE TEST METHODS	105
5.5. BEND-TWIST COUPLING FOR THE ORIGINAL BLADE SECTION	110

5.5.1.	<i>Linear response test</i>	111
5.5.2.	<i>Superposition</i>	112
5.6.	THE BEND-TWIST COUPLED BLADE SECTION (MODIFIED BLADE SECTION).....	114
5.6.1.	<i>Experimental results for the modified blade section</i>	116
5.6.2.	<i>Bend-twist coupling for the modified blade section</i>	118
	118
6.	FINITE ELEMENT MODELING	120
6.1.	BLADE SECTION DESCRIPTION.....	120
6.1.1.	<i>Blade section layup</i>	121
6.2.	FEM DESCRIPTION.....	125
6.2.1.	<i>FEM models</i>	127
7.	VALIDATION OF FEM	153
7.1.	GLOBAL COMPARISON OF EXP. AND NUM. RESULTS FOR THE ORIGINAL BLADE SECTION.....	153
7.1.1.	<i>Flapwise bending of the original blade section (experimental vs. FEM)</i>	154
7.1.2.	<i>Edgewise bending of original blade section (experimental vs. FEM)</i>	156
7.1.3.	<i>Locked Torsion of original blade section (experimental vs. FEM)</i>	158
7.2.	COMPARISON OF STIFFNESSES FOR THE ORIGINAL BLADE SECTION	159
7.2.1.	<i>Sensitivity study for the original blade section</i>	162
7.2.2.	<i>Conclusion on the comparison of the original blade section</i>	163
7.3.	GLOBAL COMPARISON OF EXP. AND NUM. RESULTS FOR THE MODIFIED BLADE SECTION	164
7.3.1.	<i>Flapwise bending of the modified blade section (exp. vs. FEM)</i>	164
7.3.2.	<i>Sensitivity study for the modified blade section</i>	165
7.3.3.	<i>Flapwise bending and torsion of the modified blade section (experimental vs. FEM)</i>	169
7.3.4.	<i>Conclusion on the comparison of the modified blade section</i>	170
8.	CONCLUSION AND FUTURE WORK	171
9.	BIBLIOGRAPHY	173
10.	APPENDIX	174

1. Acknowledgements

We would like to thank our supervisors, Christian Berggreen from the Technical University of Denmark, Kim Branner and Anders Hansen from Risø National Laboratories for their guidance.

To Lennart Kühlmeier from Vestas Wind Systems A/S, thanks for your help and guidance regarding the material properties.

A special thanks to Christian Jensen from Risø National Laboratories for his patience and many good advises on FEM.

2. Introduction

The primary motivation for initiating this work is the concern that flutter instability may occur as a result of the development of larger wind turbine blades.

This continuous development of larger wind turbine blades will result in lower torsional eigenfrequency, which may couple with the lower bending modes. Furthermore, coupling between bending and torsion will probably become a more dominating factor in the design of future wind turbine blades, as the bending and torsion eigenfrequency are getting closer. Thus, this development has resulted in the fact that torsion related aeroelastic instabilities have been brought into focus, and stability analyses have shown that new blades are getting close to the limit of flutter, where flapwise bending vibrations and torsion vibrations couple together in a dramatic instability. It is expected that in the case of flutter instability, the amplitude of the flutter vibration will increase rapidly and may result in ultimate failure of the wind turbine. To insure sufficient safety against these instabilities it is important in the design phase to model torsional stiffness and bend-twist couplings with high precision.

However, correct modelling of bend-twist couplings and torsional stiffness based on FEM is subjected to some uncertainties, when numerical results are compared with experimental modal analyses of blades. This disagreement can be due to lack of knowledge in determining the parameters used in the structural models or direct limitations in the current FE-models.

The continuous development in the use of composite materials (e.g. use of sandwich cores and optimization of fibre lay-up) and more slender and unstiffened structures in modern blades, will result in strong anisotropic material properties and torsion flexible blades, which introduce couplings that are not accounted for in the current beam models used for aeroelastic calculations.

One of the aims with this work is to verify numerical models with special attention to the torsional behaviour and the coupling between torsion and bending. The numerical models that are dealt with are detailed FEM models based on a combination of shell and solid elements. These FE-models are used to extract an anisotropic beam element, which includes all the structural couplings introduced in the blade sections, by the layers of composite materials and its geometry. This extraction is performed by a Beam Property Extraction method which gives a quarter of the full Timoshenko stiffness matrix. From this matrix it is possible to compute the 6x6 constitutive Timoshenko matrix, which can be used as input to the modified aeroelastic code HAWC2 (this modification of HAWC2 will be described later).

Validation of the numerical models is done by comparing the response from static experiments performed on a section of a full-scale blade provided by Vestas Wind Systems A/S.

The blade section is furthermore modified by adding some additional angled UD layers on the suction and pressure side of the blade. The idea is that these UD layers shall introduce measurable bend-twist couplings, which the original blade did not have.

The comparison of the numerical and experimental response of the original and the modified blade section will give an indication of the precision of the different stiffness parameters computed by FEM.

The experimental testing is performed at the DTU test facilities on a test rig, which was designed during the pre-project *Torsional Performance of Large Wind Turbine Blades – Experimental Test Design [1]*. The aims of the pre-project are described below.

2.1. Aim of Pre-project

The aims of the pre-project were to design an experimental setup and furthermore provide an understanding of the parameters influencing on the bend-twist couplings.

Pre-project contents:

- Literature study.
- Exercise concerning the lay-up's effect on the bend-twist couplings (“Design of a boat keel blade”).
- Selection of a blade section for experimental testing.
- Creation of a relatively simple FE-model of the selected blade section.
- Design of the testrig for experimental investigation.

The test rig was designed during the pre-project but was manufactured and assembled during the beginning of this master thesis.

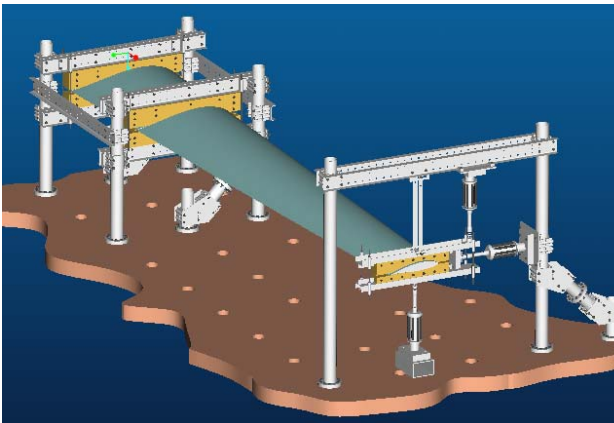


Figure 2.1.1 – CAD drawing of the test rig



Figure 2.1.2 – Picture of the test rig

2.2. Aim of Master Thesis

Below is the original description of the master thesis plan, which was the starting point for this work.

By the use of FEM and experimental analyses, the aim of the master thesis is to map the limitations in the current FE-models. The project is based on an actual blade section provided by Vestas Wind Systems A/S. The blade section is going to be tested on the testrig designed during the pre-project.

From these tests will the bending stiffness parameter (EI), the torsional stiffness parameter (GJ) and the bend-twist coupling parameter (K) be determined.

The primary focus will be on the determination of GJ and K, since these parameters are primarily subjected to uncertainties.

A detailed FE-model (shell element) of the blade section is going to be generated, so that numerical and experimental results can be compared.

The contents of the project are outlined below:

- Detailed FE-model (shell elements) of the blade section.
- Numerical determination of the stiffness matrices for the blade section, which can be used as input to the HAWC2 code. This is done by analyzing static load cases.
- Numerical analysis of the blade section's dynamic properties (modal analysis) including torsion mode shapes and their couplings to bending.
- Experimental determination of the bending stiffness parameter (EI), the torsional stiffness parameter (GJ) and the bend-twist coupling parameter (K).
- Comparison of experimental and numerical results.
- Set up guidelines for reliable determination of torsion stiffness and bend-twist couplings using FEM.

The focus was changed a bit during the project progress because of the complexity with determining the mentioned stiffness parameters. The orientation of the principle axes is varying along the blade section, the location of the shear center and the elastic axis is not the same. The blade section is build of materials with anisotropic properties which result in couplings. This means that one is not able to extract a single stiffness parameter from experiments or FEM results, because the response of the blade is not influenced by only one stiffness parameter but several (the stiffness parameters are coupled).

To analyse the blade response with high precision, one must more or less determine the full stiffness matrix. This meant that the full stiffness matrix must be determined, but still the primary focus was on torsional response and the coupling to bending.

2.3. The aeroelastic code HAWC2

HAWC2 is the aeroelastic code developed and used at Risø National Laboratories.

A prismatic Timoshenko 3D beam element is presently used in the HAWC2 code, which can be defined by the following constitutive relation:

$$\begin{pmatrix} F_x \\ F_y \\ F_z \\ M_x \\ M_y \\ M_z \end{pmatrix} = \begin{pmatrix} GA \cdot k_x & 0 & 0 & 0 & 0 & 0 \\ 0 & GA \cdot k_y & 0 & 0 & 0 & 0 \\ 0 & 0 & AE & 0 & 0 & 0 \\ 0 & 0 & 0 & EI_x & 0 & 0 \\ 0 & 0 & 0 & 0 & EI_y & 0 \\ 0 & 0 & 0 & 0 & 0 & GJ \end{pmatrix} \begin{pmatrix} \gamma_x \\ \gamma_y \\ \varepsilon_z \\ \kappa_x \\ \kappa_y \\ \kappa_z \end{pmatrix}$$

As illustrated, the constitutive matrix has only diagonal terms. GAk_x and GAk_y are the two shear stiffnesses in the x- and y-directions. AE is the axial stiffness, EI_x and EI_y are the two bending stiffnesses about the x- and y-axis, GJ is the torsional stiffness of the beam element.

The beam element is described according to the elastic axis and orientated as the principle axes, which decouples bend-bend couplings (EI_{xy}). This element can be modified to account for the location of the shear center, which results in a few off-diagonal terms in the constitutive matrix.

In order to improve the results from HAWC2 is a new 3D anisotropic beam model implemented into the code (a modification of HAWC2). This element can be fully populated, which means that it account for all couplings. These couplings can come from the material lay-up and the geometry of the blade section. The constitutive relation of the new element is illustrated below:

$$\begin{pmatrix} F_x \\ F_y \\ F_z \\ M_x \\ M_y \\ M_z \end{pmatrix} = \begin{pmatrix} k_{11} & k_{12} & k_{13} & k_{14} & k_{15} & k_{16} \\ k_{21} & k_{22} & k_{23} & k_{24} & k_{25} & k_{26} \\ k_{31} & k_{32} & k_{33} & k_{34} & k_{35} & k_{36} \\ k_{41} & k_{42} & k_{43} & k_{44} & k_{45} & k_{46} \\ k_{51} & k_{52} & k_{53} & k_{54} & k_{55} & k_{56} \\ k_{61} & k_{62} & k_{63} & k_{64} & k_{65} & k_{66} \end{pmatrix} \begin{pmatrix} \gamma_x \\ \gamma_y \\ \varepsilon_z \\ \kappa_x \\ \kappa_y \\ \kappa_z \end{pmatrix}$$

The question is how to obtain this constitutive matrix. A Beam Property Extraction (BPE) – method is used in this work. This method is based on the paper *Identification and Use of Blade Physical Properties* by David J. Malcolm and Daniel L. Laird [2]. This method works by performing six different load cases on a full FE-model and then determines a single set of displacements and rotations (three displacements and three rotations) of each beam element. The fully populated Timoshenko stiffness matrix for the beam element can be obtained from these displacements and rotations.

The beam element can be described in an arbitrary point on the cross section by using a transformation procedure.

3. Fundamental theory

The following theories are presented in this chapter:

- Classical and first-order theories of laminated composite plates
- Apparent properties
- A simple composite beam model with bend-twist coupling
- Beam theories
- Torsion theory

Not all theories are used directly in this work, because the problems that are studied are too complex and therefore not possible to solve analytically, but the fundamental theories are presented to gain some physical insight into the different topics of this work.

3.1. *Classical and first-order theories of laminated composite plates*

Classical and first-order lamination theory will be presented in the following.

3.1.1. The classical laminated plate theory

The theory of Classical Lamination Theory is presented in *Jones, R.M., Mechanics of composite materials, 2nd edition, 1998 [3]*.

A laminate is a stack of arbitrary oriented laminae/pplies assembled to form a plate. A lamina is considered thin which means it only has rigidities in its plane i.e. no bending stiffness. The laminate on the other hand, has a finite thickness and therefore a flexural rigidity.

The basic assumptions for linear laminate theory are:

- The laminate is made of an arbitrary number of linear elastic lamina/pplies that are rigidly connected to each other. The bonds are presumed to be infinitesimally thin and non-shear-deformable.
- The total thickness of the laminate is small compared with other dimensions.
- Displacements u , v and w are small (less than the plate thickness).
- Kirchhoff hypothesis is satisfied.
- The transverse stress σ_z is negligible compared to the in-plane stress components.
- The out-of-plane shear stresses τ_{xz} and τ_{yz} are also negligible.
- Strains are small compared to unity (small strain theory).
- Rotary inertia terms are negligible.

Kirchhoff hypothesis

The laminate acts as a single layer. If a laminate is thin, an originally straight line normal to the middle surface is assumed to remain straight and perpendicular to the middle surface when the laminate is deformed.

Requiring the line to remain straight and normal to the middle surface under deformation is equivalent to ignoring the shearing strains in planes perpendicular to the middle surface ($\gamma_{xz} = \gamma_{yz} = 0$) where z is the direction of the normal to the middle surface in figure 1.

In addition, the normals are presumed to have constant length which means that the strain perpendicular to the middle surface is ignored as well ($\varepsilon_z = 0$).

Lamina Stress-Strain Behavior

A lamina of an orthotropic material under plane stress, have following stress-strain relations (Hooke's law) in principal material coordinates

$$\begin{pmatrix} \sigma_1 \\ \sigma_2 \\ \tau_{12} \end{pmatrix} = \begin{pmatrix} Q_{11} & Q_{12} & 0 \\ Q_{12} & Q_{22} & 0 \\ 0 & 0 & Q_{66} \end{pmatrix} \begin{pmatrix} \varepsilon_1 \\ \varepsilon_2 \\ \gamma_{12} \end{pmatrix}$$

Equation 3.1

Where

$$Q_{11} = \frac{E_1}{1 - \nu_{12}\nu_{21}} \quad Q_{22} = \frac{E_2}{1 - \nu_{12}\nu_{21}} \quad Q_{12} = \frac{\nu_{12}E_2}{1 - \nu_{12}\nu_{21}} = \frac{\nu_{21}E_1}{1 - \nu_{12}\nu_{21}} \quad Q_{66} = G_{12}$$

Equation 3.2

Q_{ij} is the reduced stiffness matrix.

In any other coordinate system in the plane of the lamina, the stresses are:

$$\begin{pmatrix} \sigma_x \\ \sigma_y \\ \tau_{xy} \end{pmatrix} = \begin{pmatrix} \overline{Q}_{11} & \overline{Q}_{12} & \overline{Q}_{16} \\ \overline{Q}_{12} & \overline{Q}_{22} & \overline{Q}_{26} \\ \overline{Q}_{16} & \overline{Q}_{26} & \overline{Q}_{66} \end{pmatrix} \begin{pmatrix} \varepsilon_x \\ \varepsilon_y \\ \gamma_{xy} \end{pmatrix}$$

Equation 3.3

Where

$$\overline{Q}_{ij} = T^{-1} \cdot Q_{ij} \cdot T^{-T} \quad T^{-T} = R \cdot T \cdot R^{-1}$$

Equation 3.4

$$T = \begin{pmatrix} \cos(\theta)^2 & \sin(\theta)^2 & 2 \cdot \sin(\theta) \cdot \cos(\theta) \\ \sin(\theta)^2 & \cos(\theta)^2 & -2 \cdot \sin(\theta) \cdot \cos(\theta) \\ -\sin(\theta) \cdot \cos(\theta) & \sin(\theta) \cdot \cos(\theta) & \cos(\theta)^2 - \sin(\theta)^2 \end{pmatrix} \quad R = \begin{pmatrix} 1 & 0 & 0 \\ 0 & 1 & 0 \\ 0 & 0 & 2 \end{pmatrix}$$

Equation 3.5

T is the transformation matrix, R is the Reuter matrix.

Equation 3.2 is useful in the definition of the laminate stiffnesses because of the arbitrary orientation of the constituent laminae. Both equations can be thought of as stress-strain relations for the k^{th} layer of a multilayered laminate and therefore Equation 3.3 can be written as

$$\sigma_k = \begin{pmatrix} \bar{Q} \end{pmatrix}_k \cdot \varepsilon_k$$

Equation 3.6

Stress and Strain Variation in a Laminate

In order to determine the extensional and bending stiffnesses of a laminate, the variation of stress and strain through the laminate must be known.

The implication of Kirchhoff hypothesis on the laminate displacements u , v and w are derived by using the cross section in Figure 3.1.1.

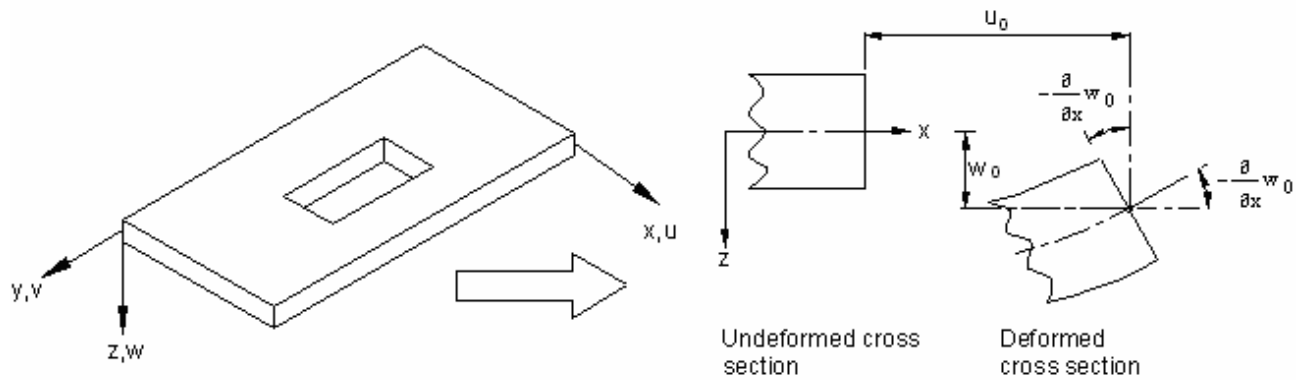


Figure 3.1.1 – Geometry of deformation in the x - z plane

The displacements field according to Kirchhoff hypothesis can be written as

$$u(x, y, z, t) = u_0(x, y, t) - z \frac{\partial}{\partial x} w_0 \quad v(x, y, z, t) = v_0(x, y, t) - z \frac{\partial}{\partial y} w_0 \quad w(x, y, z, t) = w_0(x, y, t)$$

Equation 3.7

Where (u_0, v_0, w_0) are the displacements along the coordinate lines of a material point on the xy -plane. Once the midplane displacements (u_0, v_0, w_0) are known can any arbitrary point in the 3D continuum be determined.

By Kirchhoff hypothesis, the laminate strains have been reduced to ε_x , ε_y and γ_{xy} ($\varepsilon_z = \gamma_{xz} = \gamma_{yz} = 0$). For small strains (linear strains) the remaining strains are defined in terms of displacements as:

$$\varepsilon_x = \frac{\partial}{\partial x} u \quad \varepsilon_y = \frac{\partial}{\partial y} v \quad \gamma_{xy} = \frac{\partial}{\partial y} u + \frac{\partial}{\partial x} v$$

Equation 3.8

And when inserting the derived displacements u and v , the strains are:

$$\varepsilon_x = \frac{\partial}{\partial x} u_0 - z \frac{\partial^2}{\partial x^2} w_0 \quad \varepsilon_y = \frac{\partial}{\partial y} v_0 - z \frac{\partial^2}{\partial y^2} w_0 \quad \gamma_{xy} = \frac{\partial}{\partial y} u_0 + \frac{\partial}{\partial x} v_0 - 2z \frac{\partial}{\partial x} \left(\frac{\partial}{\partial y} w_0 \right)$$

Equation 3.9

Or

$$\begin{pmatrix} \varepsilon_x \\ \varepsilon_y \\ \gamma_{xy} \end{pmatrix} = \begin{pmatrix} \varepsilon_{x0} \\ \varepsilon_{y0} \\ \gamma_{xy0} \end{pmatrix} + z \begin{pmatrix} \kappa_x \\ \kappa_y \\ \kappa_{xy} \end{pmatrix}$$

Equation 3.10

Where the middle-surface strains and middle-surface curvatures are (small strain theory):

$$\begin{pmatrix} \varepsilon_{x0} \\ \varepsilon_{y0} \\ \gamma_{xy0} \end{pmatrix} = \begin{pmatrix} \frac{\partial}{\partial x} u_0 \\ \frac{\partial}{\partial y} v_0 \\ \frac{\partial}{\partial y} u_0 + \frac{\partial}{\partial x} v_0 \end{pmatrix} \quad \begin{pmatrix} \kappa_x \\ \kappa_y \\ \kappa_{xy} \end{pmatrix} = - \begin{pmatrix} \frac{\partial^2}{\partial x^2} w_0 \\ \frac{\partial^2}{\partial y^2} w_0 \\ 2 \frac{\partial}{\partial x} \left(\frac{\partial}{\partial y} w_0 \right) \end{pmatrix}$$

Equation 3.11

The last term in the curvature vector is the twist curvature of the middle surface.

The stresses in the k^{th} layer can be expressed in terms of the laminate middle-surface strains and curvatures, by inserting *Equation 3.10* in *Equation 3.3*.

$$\begin{pmatrix} \sigma_x \\ \sigma_y \\ \tau_{xy} \end{pmatrix}_k = \begin{pmatrix} \overline{Q}_{11} & \overline{Q}_{12} & \overline{Q}_{16} \\ \overline{Q}_{12} & \overline{Q}_{22} & \overline{Q}_{26} \\ \overline{Q}_{16} & \overline{Q}_{26} & \overline{Q}_{66} \end{pmatrix}_k \cdot \left[\begin{pmatrix} \varepsilon_{x0} \\ \varepsilon_{y0} \\ \gamma_{xy0} \end{pmatrix} + z \begin{pmatrix} \kappa_x \\ \kappa_y \\ \kappa_{xy} \end{pmatrix} \right]$$

Equation 3.12

The transformed reduced stiffnesses \overline{Q}_{ij} can be different for each layer in the laminate which means that the stress variation through the laminate thickness is not necessarily linear like the strain variation. The stresses are instead piecewise linear in each layer, but discontinuous at the lamina boundaries.

Resultant Laminate Forces and Moments

By integrating the stresses in each lamina through the laminate thickness, the resultant forces and moments acting on a laminate can be obtained. But the stresses vary within each lamina as well as from lamina to lamina, so the integration is not trivial. The entire summation of force and moment resultants for an N -layered laminate is defined as:

$$\begin{pmatrix} N_x \\ N_y \\ N_{xy} \end{pmatrix} = \int_{-\frac{t}{2}}^{\frac{t}{2}} \begin{pmatrix} \sigma_x \\ \sigma_y \\ \tau_{xy} \end{pmatrix} dz = \sum_{k=1}^N \int_{z_{k-1}}^{z_k} \begin{pmatrix} \sigma_x \\ \sigma_y \\ \tau_{xy} \end{pmatrix}_k dz \quad \begin{pmatrix} M_x \\ M_y \\ M_{xy} \end{pmatrix} = \int_{-\frac{t}{2}}^{\frac{t}{2}} \begin{pmatrix} \sigma_x \\ \sigma_y \\ \tau_{xy} \end{pmatrix} \cdot z dz = \sum_{k=1}^N \int_{z_{k-1}}^{z_k} \begin{pmatrix} \sigma_x \\ \sigma_y \\ \tau_{xy} \end{pmatrix}_k \cdot z dz$$

Equation 3.13

Where z_k and z_{k-1} are directed distances and defined in the laminate geometry in *Figure 3.1.2*.

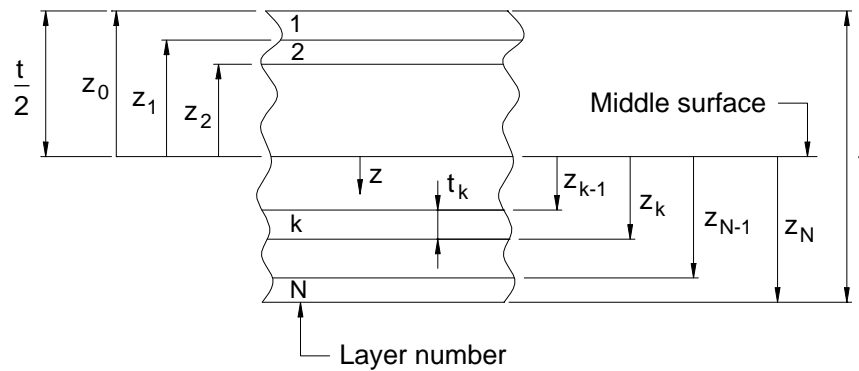


Figure 3.1.2 – Geometry of an N-layered laminate

The two *Equations* of *Equation 3.13*) can be rearranged so that the stiffness matrix goes outside the integration over each layer because the stiffness matrix for a lamina is often constant.

When combining *Equation 3.12* and *Equation 3.13* the forces and moments become:

$$\begin{pmatrix} N_x \\ N_y \\ N_{xy} \end{pmatrix} = \sum_{k=1}^N \begin{pmatrix} \overline{Q}_{11} & \overline{Q}_{12} & \overline{Q}_{16} \\ \overline{Q}_{12} & \overline{Q}_{22} & \overline{Q}_{26} \\ \overline{Q}_{16} & \overline{Q}_{26} & \overline{Q}_{66} \end{pmatrix}_k \left[\int_{z_{k-1}}^{z_k} \begin{pmatrix} \varepsilon_{x0} \\ \varepsilon_{y0} \\ \gamma_{xy0} \end{pmatrix} dz + \int_{z_{k-1}}^{z_k} \begin{pmatrix} \kappa_x \\ \kappa_y \\ \kappa_{xy} \end{pmatrix} \cdot z dz \right]$$

Equation 3.14

$$\begin{pmatrix} M_x \\ M_y \\ M_{xy} \end{pmatrix} = \sum_{k=1}^N \begin{pmatrix} \overline{Q}_{11} & \overline{Q}_{12} & \overline{Q}_{16} \\ \overline{Q}_{12} & \overline{Q}_{22} & \overline{Q}_{26} \\ \overline{Q}_{16} & \overline{Q}_{26} & \overline{Q}_{66} \end{pmatrix}_k \left[\int_{z_{k-1}}^{z_k} \begin{pmatrix} \varepsilon_{x0} \\ \varepsilon_{y0} \\ \gamma_{xy0} \end{pmatrix} \cdot z dz + \int_{z_{k-1}}^{z_k} \begin{pmatrix} \kappa_x \\ \kappa_y \\ \kappa_{xy} \end{pmatrix} \cdot z^2 dz \right]$$

Equation 3.15

Sometimes the lamina stiffness matrix is not constant through the thickness of the lamina, e.g. if a temperature gradient or moisture gradient exist in the lamina and the lamina material properties are temperature/moisture dependent, then the stiffness matrix is a function of z and must be left inside the integral. Then a more complicated solution is required.

Equation 3.14 and *Equation 3.15* can be written as:

$$\begin{pmatrix} N_x \\ N_y \\ N_{xy} \end{pmatrix} = \begin{pmatrix} A_{11} & A_{12} & A_{16} \\ A_{12} & A_{22} & A_{26} \\ A_{16} & A_{26} & A_{66} \end{pmatrix} \begin{pmatrix} \varepsilon_{x0} \\ \varepsilon_{y0} \\ \gamma_{xy0} \end{pmatrix} + \begin{pmatrix} B_{11} & B_{12} & B_{16} \\ B_{12} & B_{22} & B_{26} \\ B_{16} & B_{26} & B_{66} \end{pmatrix} \begin{pmatrix} \kappa_x \\ \kappa_y \\ \kappa_{xy} \end{pmatrix}$$

Equation 3.16

$$\begin{pmatrix} M_x \\ M_y \\ M_{xy} \end{pmatrix} = \begin{pmatrix} B_{11} & B_{12} & B_{16} \\ B_{12} & B_{22} & B_{26} \\ B_{16} & B_{26} & B_{66} \end{pmatrix} \begin{pmatrix} \varepsilon_{x0} \\ \varepsilon_{y0} \\ \gamma_{xy0} \end{pmatrix} + \begin{pmatrix} D_{11} & D_{12} & D_{16} \\ D_{12} & D_{22} & D_{26} \\ D_{16} & D_{26} & D_{66} \end{pmatrix} \begin{pmatrix} \kappa_x \\ \kappa_y \\ \kappa_{xy} \end{pmatrix}$$

Equation 3.17

Where

$$A_{ij} = \sum_{k=1}^N \left(\overline{Q_{ij}} \right)_k \cdot (z_k - z_{k-1})$$

$$B_{ij} = \frac{1}{2} \cdot \sum_{k=1}^N \left(\overline{Q_{ij}} \right)_k \cdot [z_k^2 - z_{k-1}^2]$$

$$D_{ij} = \frac{1}{3} \cdot \sum_{k=1}^N \left(\overline{Q_{ij}} \right)_k \cdot [z_k^3 - z_{k-1}^3]$$

Equation 3.18

The A_{ij} are extensional stiffnesses (membrane stiffness), the B_{ij} are bending-extension coupling stiffnesses and the D_{ij} are bending stiffnesses.

A_{16} and A_{26} represent shear-extension coupling at the laminate level. The B_{ij} represent coupling between bending and extension which is a phenomenon that is not found at lamina level.

And finally, D_{16} and D_{26} represent bend-twist coupling.

3.1.2. The first-order shear deformation laminated plate theory

The first-order shear deformation laminated plate theory is based on the Reissner-Mindlin hypothesis, which is identical to the Kirchhoff hypothesis except that the line normal to the middle surface is not restricted to remain perpendicular to the middle surface after deformation.

In the first-order shear deformation laminated plate theory is the deformation of an element the sum of the deformation due to bending and the deformation due to shear. For isotropic plates with a large slenderness ratio can the shear deformation be neglected, but for composite laminates and sandwich structures is the shear deformation more important. As an indicator of when first-order laminated plate theory should be used, are the slenderness ratio shown in *Table 3.1.1*.

CLPT is Classical Laminate Plate Theory and FSDLPT is First-order Shear Deformation Laminated Plate Theory in table *Table 3.1.1*.

	Homogeneous	Composite laminate	Sandwich
CLPT	$\lambda > 10$	$\lambda > 20$	FSDLPT

Table 3.1.1- Slenderness ratio of plates

The slenderness ratio of a plate is give as

$$\lambda = \frac{b}{t}$$

Equation 3.19

Where t is the thickness of the plate and b is the shortest in-plane dimension.

The displacement field according to Reissner-Mindlin hypothesis can be written as

$$u(x, y, z, t) = u_0(x, y, t) + z\phi_x(x, y, z) \quad v(x, y, z, t) = v_0(x, y, t) + z\phi_y(x, y, z) \quad w(x, y, z, t) = w_0(x, y, t)$$

Equation 3.20

Note that the rotations are written as:

$$\frac{\partial}{\partial z} u = \phi_x \quad \frac{\partial}{\partial z} v = \phi_y$$

Equation 3.21

Which indicates that ϕ_x and ϕ_y are the rotations of a transverse normal about the y - and x -axis, respectively (see *Figure 3.1.3*).

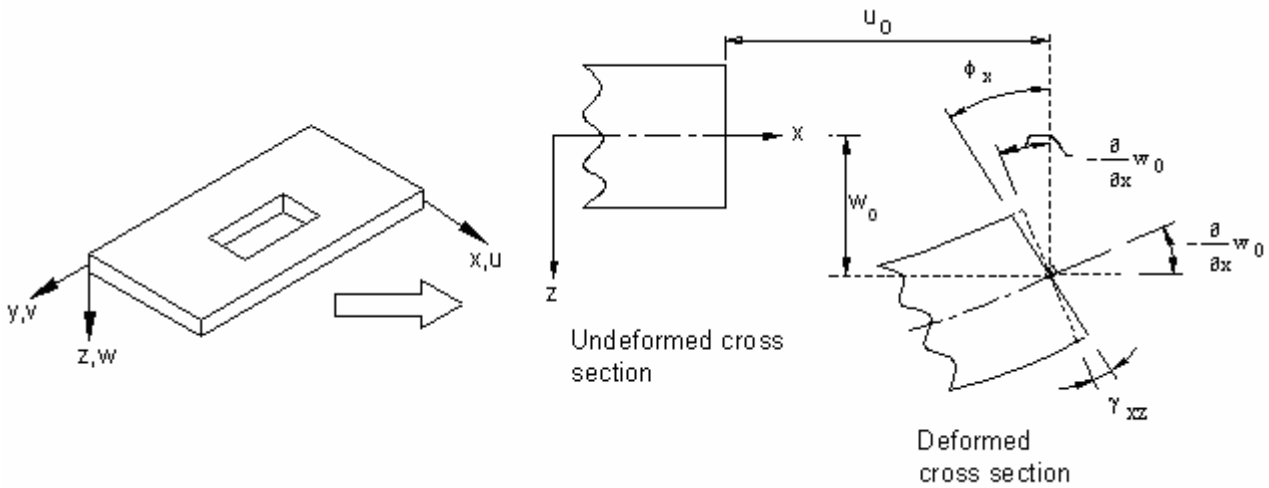


Figure 3.1.3 - Undeformed and deformed geometries of an element of a plate under the assumption of the first-order plate theory (Reissner-Mindlin hypothesis).

By using Reissner-Mindlin hypothesis and the nonlinear strain-displacement relation the nonlinear strains are given as:

$$\begin{pmatrix} \varepsilon_x \\ \varepsilon_y \\ \gamma_{yz} \\ \gamma_{xz} \\ \gamma_{xy} \end{pmatrix} = \begin{pmatrix} \varepsilon_{x0} \\ \varepsilon_{y0} \\ \gamma_{yz0} \\ \gamma_{xz0} \\ \gamma_{xy0} \end{pmatrix} + z \cdot \begin{pmatrix} \kappa_x \\ \kappa_y \\ \kappa_{yz} \\ \kappa_{xz} \\ \kappa_{xy} \end{pmatrix} = \begin{pmatrix} \frac{\partial}{\partial x} u_0 + \frac{1}{2} \left(\frac{\partial^2}{\partial x^2} w_0 \right)^2 \\ \frac{\partial}{\partial y} u_0 + \frac{1}{2} \left(\frac{\partial^2}{\partial y^2} w_0 \right)^2 \\ \frac{\partial}{\partial y} w_0 + \phi_y \\ \frac{\partial}{\partial x} w_0 + \phi_x \\ \frac{\partial}{\partial y} u_0 + \frac{\partial}{\partial x} v_0 + \frac{\partial}{\partial x} w_0 \cdot \frac{\partial}{\partial x} w_0 \end{pmatrix} + z \cdot \begin{pmatrix} \frac{\partial}{\partial x} \phi_x \\ \frac{\partial}{\partial y} \phi_y \\ 0 \\ 0 \\ \frac{\partial}{\partial x} \phi_x + \frac{\partial}{\partial y} \phi_y \end{pmatrix}$$

Equation 3.22

Note, that for the classical laminated plate theory in this work, it was assumed that the rotations of the transverse normals were so small that the following terms could be neglected (assumption of linear strain-displacement relation):

$$\left(\frac{\partial^2}{\partial x^2} w \right)^2 \quad \left(\frac{\partial^2}{\partial y^2} w \right)^2 \quad \frac{\partial}{\partial x} w \cdot \frac{\partial}{\partial x} w$$

These terms could of course be included in the classical laminated plate theory to account for rotations of a moderate size (nonlinear strain-displacement relation).

The general equations for the forces and moments resultants for the first-order shear deformation laminated plate theory can be written as:

$$\begin{pmatrix} N_x \\ N_y \\ N_{xy} \end{pmatrix} = \begin{pmatrix} A_{11} & A_{12} & A_{16} \\ A_{12} & A_{22} & A_{26} \\ A_{16} & A_{26} & A_{66} \end{pmatrix} \begin{pmatrix} \varepsilon_{x0} \\ \varepsilon_{y0} \\ \gamma_{xy0} \end{pmatrix} + \begin{pmatrix} B_{11} & B_{12} & B_{16} \\ B_{12} & B_{22} & B_{26} \\ B_{16} & B_{26} & B_{66} \end{pmatrix} \begin{pmatrix} \kappa_x \\ \kappa_y \\ \kappa_{xy} \end{pmatrix}$$

$$\begin{pmatrix} M_x \\ M_y \\ M_{xy} \end{pmatrix} = \begin{pmatrix} B_{11} & B_{12} & B_{16} \\ B_{12} & B_{22} & B_{26} \\ B_{16} & B_{26} & B_{66} \end{pmatrix} \begin{pmatrix} \varepsilon_{x0} \\ \varepsilon_{y0} \\ \gamma_{xy0} \end{pmatrix} + \begin{pmatrix} D_{11} & D_{12} & D_{16} \\ D_{12} & D_{22} & D_{26} \\ D_{16} & D_{26} & D_{66} \end{pmatrix} \begin{pmatrix} \kappa_x \\ \kappa_y \\ \kappa_{xy} \end{pmatrix}$$

$$\begin{pmatrix} Q_x \\ Q_y \end{pmatrix} = k_{scc} \begin{pmatrix} A_{44} & A_{45} \\ A_{45} & A_{55} \end{pmatrix} \begin{pmatrix} \gamma_{yz0} \\ \gamma_{xz0} \end{pmatrix}$$

Equation 3.23

Where the extensional stiffnesses A_{44} , A_{45} and A_{55} are defined by:

$$\{A_{44}, A_{45}, A_{55}\} = \sum_{k=1}^N \left(\overline{Q}_{44}, \overline{Q}_{45}, \overline{Q}_{55} \right)_k \cdot (z_k - z_{k-1})$$

Equation 3.24

The transverse forces resultants (Q_x , Q_y) are corrected by a shear correction coefficient (k_{scc}). This is done to minimize the error by assuming a constant shear strain through the laminate. The shear correction coefficient is computed so that the strain energy due to constant transverse shear stresses equals the strain energy due to the true transverse stresses.

Apparent properties

The method for determining the apparent properties is taken from [2].

An approximate laminate modulus can be computed by the extensional stiffness matrix.

Assuming that the laminate is orthotropic one can then get the Poisson's ratios as:

$$\nu_{21} = \frac{A_{12}}{A_{11}} \quad \nu_{12} = \frac{A_{12}}{A_{22}}$$

Equation 3.25

The average/apparent moduli for the laminate are then:

$$E_x = \frac{A_{11}(1 - \nu_{12}\nu_{21})}{t} \quad E_y = \frac{A_{22}(1 - \nu_{12}\nu_{21})}{t} \quad G_{xy} = \frac{A_{66}}{t}$$

Equation 3.26

Where t is the laminate thickness.

3.2. Simple composite beam model with bend-twist coupling

The theory in this chapter is based on [4].

In the aircraft industry it is quite common in the preliminary design to model the wing as a slender beam to study the bend-twist characteristics (shear deformation is not considered). This idealized beam model for the composite wing is described by three stiffness parameters along the middle surface reference axis. The three stiffness parameters are the bending stiffness parameter EI , the torsional stiffness parameter GJ and the bend-twist coupling parameter K .

It is quite important to note that EI and GJ are not necessarily the bending and torsion stiffness of the beam since the reference axis is not necessarily the principal axis in general.

Figure 3.2.1 illustrates a beam segment with internal bending and torsional moments.

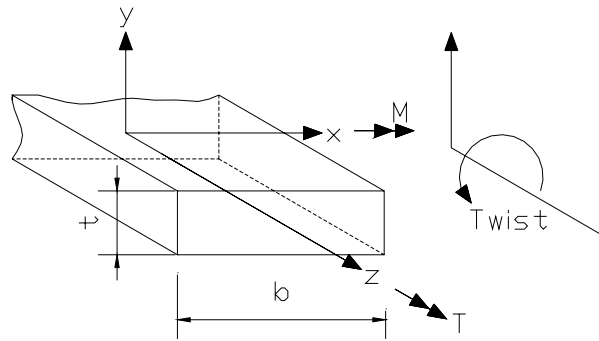


Figure 3.2.1 - A beam segment with internal bending moment, torsional moment and deformations.

The out-of-plan deflection or the two-dimensional displacement field $w(x,z)$, is assumed to vary linearly along the x -axis. The displacement field can be represented by a bending deflection $w(z)$ along the z -axis and a twisting $\phi(z)$ about the z -axis.

At any cross section of the composite beam the relation between the bending moment M , and the torsional moment T , the curvature $\partial^2 w / \partial z^2$ and the twisting rate $\partial \phi / \partial z$ can be expressed by:

$$\begin{pmatrix} M \\ T \end{pmatrix} = \begin{pmatrix} EI & -K \\ -K & GJ \end{pmatrix} \begin{pmatrix} \frac{\partial^2}{\partial z^2} w \\ \frac{\partial}{\partial z} \phi \end{pmatrix}$$

Equation 3.27

The definition of the coupling coefficient ψ is given as:

$$\psi = \frac{K}{\sqrt{EI GJ}} \quad \text{and} \quad -1 < \psi < 1$$

Equation 3.28

A coupling coefficient close to ± 1 indicate that the coupling is high while a coupling coefficient equal to zero indicates that there is no coupling between bending and torsion.

If it is assumed that the beam can be described as a two-dimensional laminate with a symmetric lay-up ($B=0$), the relation between the plate bending moments, torsional moment and curvatures can be determined by classical laminated plate theory as:

$$\begin{pmatrix} M_x \\ M_y \\ M_{xy} \end{pmatrix} = \begin{pmatrix} D_{11} & D_{12} & D_{16} \\ D_{12} & D_{22} & D_{26} \\ D_{16} & D_{26} & D_{66} \end{pmatrix} \begin{pmatrix} \kappa_x \\ \kappa_y \\ \kappa_{xy} \end{pmatrix}$$

If it is assumed that the plate moment M_y is equal to zero the three stiffness parameters in *Equation 3.27* can be determined by (The bending stiffnesses D_{ij} are given in *Equation 3.18*):

$$EI = b \cdot \left(D_{11} - \frac{D_{12}^2}{D_{22}} \right) \quad GJ = 4 \cdot b \cdot \left(D_{66} - \frac{D_{26}^2}{D_{22}} \right) \quad K = 2 \cdot b \cdot \left(D_{16} - \frac{D_{12} \cdot D_{26}}{D_{22}} \right)$$

Equation 3.29

3.2.1. Theoretical estimation of the stiffness parameters, and coupling coefficient

To gain some physical insight into the stiffness parameters EI , GJ and K , it is assumed that a beam can be described as a two-dimensional laminate, which has a lay-up of $[\theta]_s$ (single orientation).

The stiffness parameters are plotted below for a beam of E-glass and Carbon (IM). The width of the beam is 100mm and the thickness is 20mm.

The material data for E-glass and Carbon (IM) can be seen in *Table 3.2.1*:

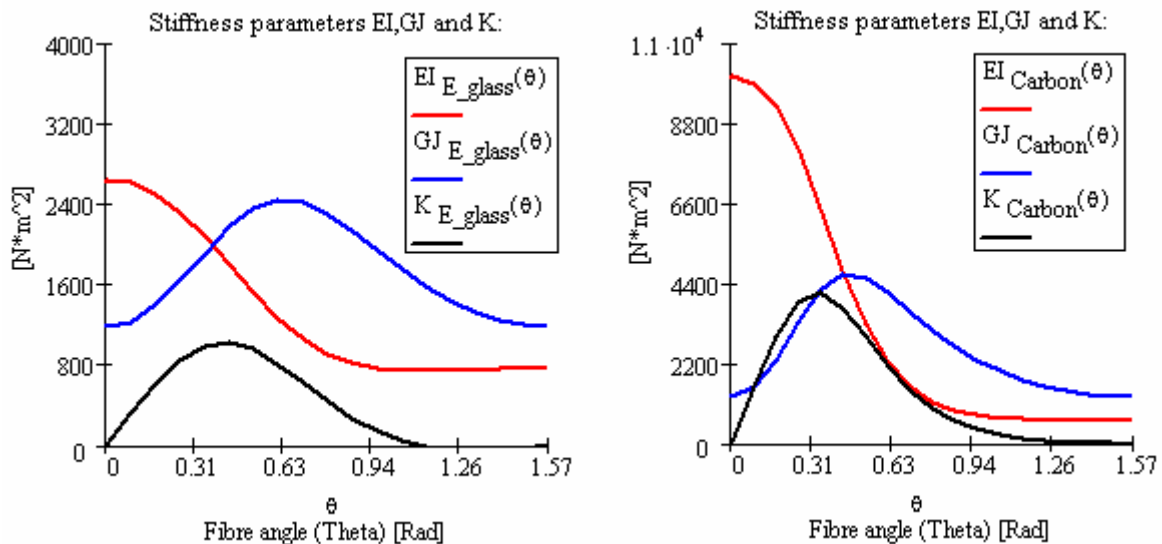


Figure 3.2.2- Stiffness parameters for E-glass and Carbon

The coupling coefficient ψ , is determined for the same beam as the stiffness parameters.

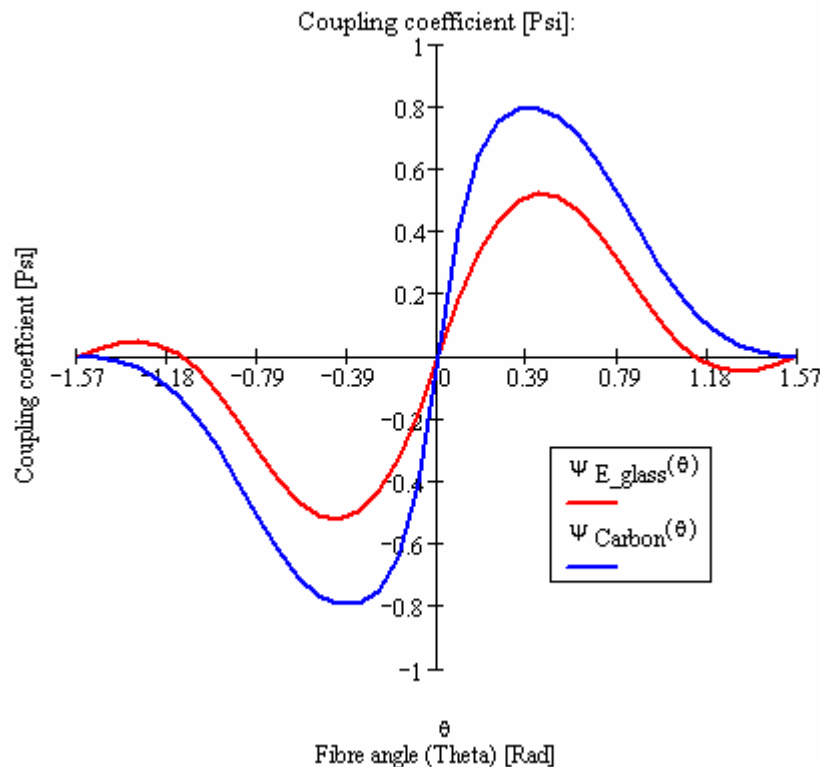


Table 3.2.1 – Material Properties for E-glass and Carbon (IM).

Fibre	E-glass	Carbon
E_1 [GPa]	49.874	151
E_2 [GPa]	11.58	9.4
G_{12} [GPa]	4.44	4.8
ν_{12}	0.303	0.31

Figure 3.2.3 - The coupling coefficients for E-glass and Carbon (IM)

The bend-twist coupling coefficient for both E-glass and Carbon has a maximum value when the fibre angle is around 25° . Carbon's coupling coefficient is around 35 percent larger than E-glass' at this fibre angle.

All indicates that the turbine blades in the future are going to be constructed in Carbon fibres, in contrast to today where the blades are constructed with E-glass. The reason for this is clear when one compare the two plots of the stiffness parameters. Carbon is very stiff which means that the turbine blades can be made lighter and longer. So in short, the bend-twist coupling is probably going to play a bigger role in the future!

3.3. Beam theories

Two beam theories/models are commonly use in structural mechanics. These theories are Bernoulli-Euler and Timoshenko beam theory. These two theories will in the following be presented.

3.3.1. Bernoulli-Euler beam theory

Bernoulli-Euler beam theory is also known as classical beam theory or engineering beam theory and is probably the most used beam theory. The model accounts for bending moments effects on stresses and deformation. The deformation due to transverse shear forces on beams is neglected. The fundamental assumption is that the cross sections remain plane and normal to the deformed longitudinal neutral axis as shown in *Figure 3.3.1*. The total rotation θ_y is due to bending alone. This rotation occurs about the neutral/principle axis in the x-direction. The neutral axis passes through the centroid of isotropic cross sections.

The assumptions of Bernoulli-Euler beam theory are listed below:

- Cross sections which are perpendicular to the undeformed neutral axis, also remains perpendicular to the deformed neutral axis.
- Cross sections remain straight in the deformed state.

The Bernoulli-Euler assumptions means that one is only working with one variable: Displacement.

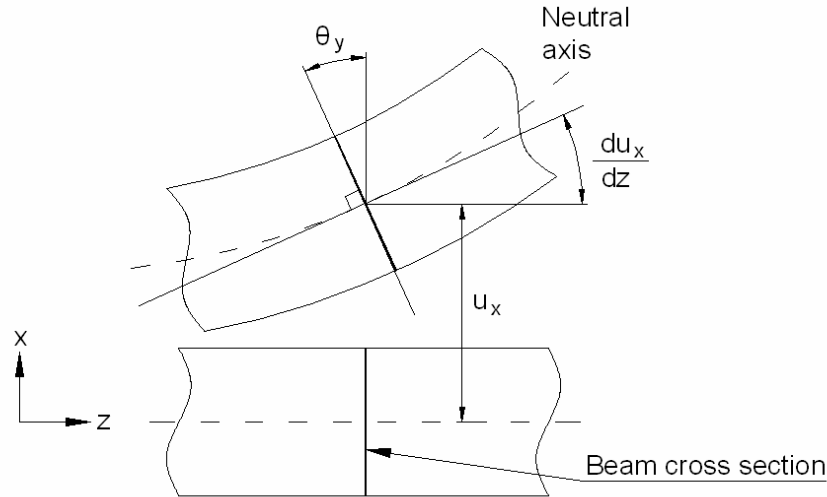


Figure 3.3.1 - Deformation of cross section, Bernoulli-Euler

The equations for a Bernoulli-Euler beam are:

$$u_z = -x\theta_y(z) \quad \theta_y(z) = \frac{d}{dz}u_x \quad \Rightarrow \quad u_z = -x\frac{d}{dz}u_x \quad \varepsilon_{zz} = \frac{d}{dz}u_z = -x\frac{d^2}{dz^2}u_x$$

Equation 3.30

If assuming that $\sigma_{yy} = \sigma_{xx} = \sigma_{zy} = \sigma_{yx} = 0$, then the stress strain relations are:

$$\varepsilon_{zz} = \frac{1}{E} \left[\sigma_{zz} - \nu \cdot (\sigma_{xx} + \sigma_{yy}) \right] \Rightarrow \varepsilon_{zz} = \frac{1}{E} \cdot \sigma_{zz} \Rightarrow \sigma_{zz} = -E \cdot x \cdot \frac{d^2}{dz^2} u_x$$

$$\theta_y \cdot dx = -du_z \Rightarrow \frac{d}{dz} u_x = \frac{d}{dx} u_z \Rightarrow \frac{d}{dx} u_z = \frac{d}{dz} u_x$$

$$\sigma_{zx} = G \left(\frac{d}{dx} u_z + \frac{d}{dz} u_x \right) \Rightarrow \sigma_{zx} = G \left(\frac{d}{dz} u_x + \frac{d}{dz} u_x \right) = 0$$

Equation 3.31

The bending moment can be expressed in terms of the displacement u_x :

$$\sigma_{zz} = -E \cdot x \cdot \frac{d^2}{dz^2} u_x \quad M = - \int_A x \cdot \sigma_{zz} dA = E \cdot \frac{d^2}{dz^2} u_x \cdot \int_A x^2 dA = E \cdot I \cdot \frac{d^2}{dz^2} u_x = E \cdot I \cdot \kappa_y \Rightarrow \sigma_{zz} = \frac{-M \cdot x}{I}$$

Equation 3.32

I is the area moment of inertia for the cross section with respect to the y -axis.

3.3.2. Timoshenko beam theory

This theory corrects/improves the classical beam theory with a first-order shear deformation effect.

The cross section remain plane in Timoshenko beam theory and rotate about the same neutral axis (x-axis) as the Bernoulli-Euler model, but the cross sections do not remain normal/perpendicular to the deformed longitudinal neutral axis (z-axis) as shown in *Figure 3.3.2*. This effect is produced by a transverse shear stress that is assumed to be constant over the cross section. In *Figure 3.3.2* is the slope θ_y due to bending and γ_x is due to shear deformation. So in short, the main difference between Bernoulli-Euler beam theory and Timoshenko beam theory is that the cross sections do not remain perpendicular to the deformed longitudinal neutral axis. One is now working with two variables: Displacement and rotation.

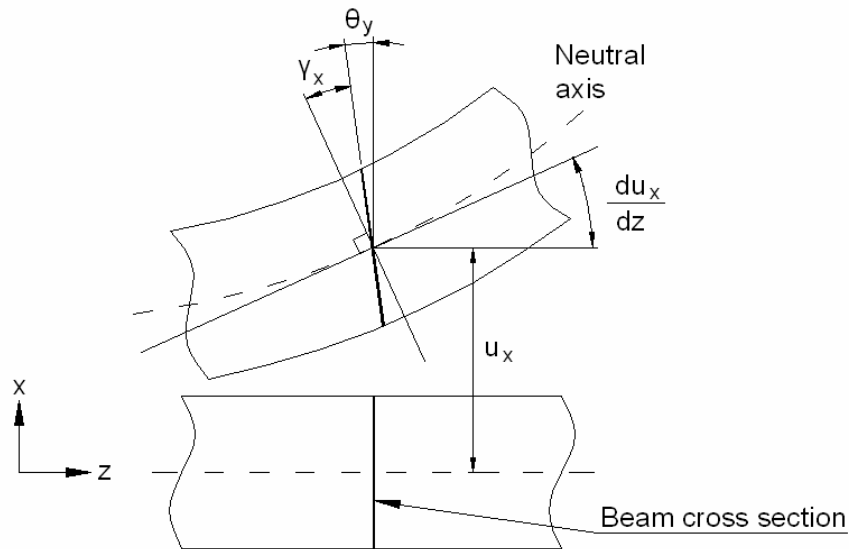


Figure 3.3.2 - Deformation of cross section, Timoshenko

The equations for a Timoshenko beam are:

$$u_z = -x\theta_y(z) \quad \theta_y(z) \neq \frac{d}{dz}u_x \quad \theta_y = \frac{d}{dz}u_x - \gamma_x \quad \kappa_y = \frac{d}{dz}\theta_y$$

Equation 3.33

If assuming that $\sigma_{yy} = \sigma_{xx} = \sigma_{zy} = \sigma_{yx} = 0$, then the stress strain relations are:

$$\sigma_{zz} = -E x \frac{d}{dz}\theta_y \quad \sigma_{zx} = G \left(\frac{d}{dx}u_z + \frac{d}{dz}u_x \right) = G \left[-\theta_y(z) + \frac{d}{dz}u_x \right]$$

Equation 3.34

It is important to note that the shear stress is assumed to be constant over the cross section. However, when a cross section is subjected to a shear force then the shear stress varies through the height of the cross section and the cross section does not remain plane, it warps. This warping is largest at the longitudinal neutral axis and zero at the outer fibers. This physical behavior is of course in conflict with the assumptions in Timoshenko beam theory. Therefore, must the theory be corrected and this is done by introducing the shear correction factor (k).

This shear correction factor is only dependent of shape and the material properties of the cross section. The shear correction factor can be found in literature for simple isotropic cross section.

$$\sigma_{zz} = -E \cdot x \frac{d}{dz} \theta_y \quad \sigma_{zx} = k \cdot G \left(-\theta_y(z) + \frac{d}{dz} u_x \right)$$

Equation 3.35

The constitutive equations are:

$$M = - \int_A x \sigma_{zz} dA = E \frac{d}{dz} \theta_y \cdot \int_A x^2 dA = E \cdot I \frac{d}{dz} \theta_y = E \cdot I \cdot \kappa_y$$

$$Q = - \int_A \sigma_{zx} dA = - \int_A k \cdot G \left(-\theta_y + \frac{d}{dz} u_x \right) dA = k \cdot G \cdot A \cdot \gamma_x$$

Equation 3.36

M is the bending part and Q is the shearing part of the constitutive equations.

Note that the shear effects are significant for short beams and beams of composite material, such as wind turbine blades. When determining natural frequencies for beam structures, then the shear effect becomes significant for frequencies in the higher range. The first mode shapes can often be determined by using Bernoulli-Euler beam theory but the results using this theory becomes inaccurate for the higher mode shapes and one has to include shear effects.

3.4. Torsion

Three isotropic torsional problems will be treated in this chapter.

Firstly, circular cross sections for which the cross-section does not warp during torsion.

Secondly, non-circular cross sections which will warp during torsion. The third case is a closed thin-walled cross section.

3.4.1. Circular cross section

The simplest case of torsion deformation is a circular bar subjected to pure torsion. Because of the symmetry of the cross section can it be proved that the cross section do not change shape as it rotate about its shear-center (the center of torsion). In other words, the cross sections remain plane and circular. Furthermore, if the angle of rotation is assumed to be small, then will neither the length nor the radius change during deformation.

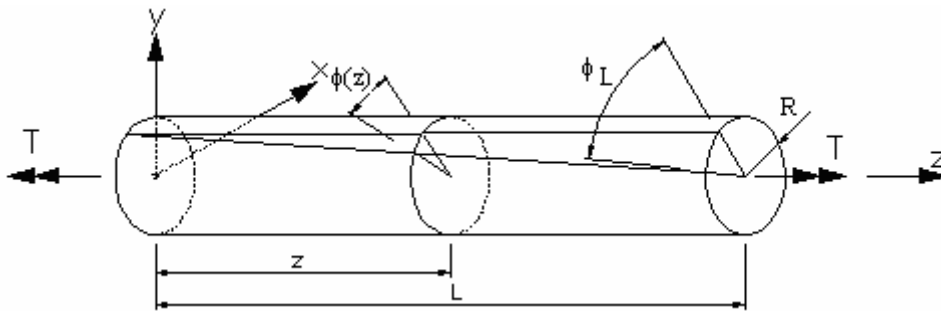


Figure 3.4.1- Circular cross section subjected to pure torsion

Figure 3.4.1 shows a prismatic bar with a massive circular cross section, of the length L subjected to a constant torsional moment (T).

Assuming that the cross section at $z = 0$ is fixed then the entire rotation takes place at $z = L$ as shown on the figure. At an arbitrary cross section ($z = z$) the twist angle is ϕ , and at $z + dz$ it is $\phi + d\phi$. The ratio $d\phi/dz$ is denoted by θ and is referred to as the angle of twist per unit length or the rate of twist:

$$\theta = \frac{d\phi}{dz}$$

Equation 3.37

For the case of pure torsion, the rate of twist is constant and is therefore equal to the total angle of twist divided by the length of the bar:

$$\theta = \frac{\phi_L}{L}$$

Equation 3.38

The displacement field that satisfies the state conditions for this case of torsion can be given as:

$$u_x = -y \cdot z \cdot \theta \quad u_y = x \cdot z \cdot \theta \quad u_z = 0$$

Equation 3.39

Note ($u_z = 0$), no out-of-plane displacement. In other words, the cross section does not warp when subjected to torsion.

The strain field for this case of torsion can be given as:

$$\begin{aligned}\epsilon_{xx} &= \frac{\partial}{\partial x} u_x = 0 & \epsilon_{yy} &= \frac{\partial}{\partial y} u_y = 0 & \epsilon_{zz} &= \frac{\partial}{\partial z} u_z = 0 \\ \gamma_{xy} &= \frac{\partial}{\partial x} u_y + \frac{\partial}{\partial y} u_x = 0 & \gamma_{xz} &= \frac{\partial}{\partial z} u_x + \frac{\partial}{\partial x} u_z = -y \cdot \theta & \gamma_{yz} &= \frac{\partial}{\partial z} u_y + \frac{\partial}{\partial y} u_z = x \cdot \theta\end{aligned}$$

Equation 3.40

This is a state of pure shear strain in the cross sectional plane. The resulting shear strain γ in the tangential direction is:

$$\gamma = \sqrt{\gamma_{xz}^2 + \gamma_{yz}^2} = r \cdot \theta$$

Equation 3.41

Assuming an isotropic Hooke's law for the state of pure shear stress:

$$\tau_{xz} = -y \cdot \theta \cdot G \quad \tau_{yz} = x \cdot \theta \cdot G$$

Equation 3.42

The resulting tangential shear stress τ is (the maximum shear stress will be at the outer boundary ($r = R$)):

$$\tau = \sqrt{\tau_{xz}^2 + \tau_{yz}^2} = r \cdot \theta \cdot G = \gamma \cdot G \quad \tau_{\max} = R \cdot \theta \cdot G$$

Equation 3.43

The equilibrium with the external torsional moment and the internal stress can be illustrated by the following example/sketch:

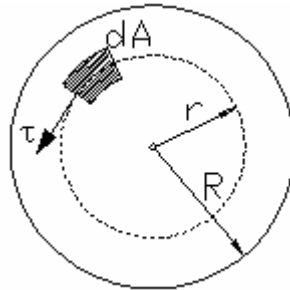


Figure 3.4.2-Determination of the resultant of the shear stress acting on a cross section

The shear force acting on the element is equal to $\tau \cdot dA$, where τ is the shear stress at radius r . The moment of this force acting about the shear center of the bar is $\tau \cdot dA \cdot r$. This can be written:

$$dM = \tau \cdot dA \cdot r = \frac{\tau_{\max}}{R} \cdot r^2 \cdot dA \quad T = \int_A \tau \cdot r \, dA = \frac{\tau_{\max}}{R} \cdot \int_A r^2 \, dA = \frac{\tau_{\max}}{R} \cdot I_p$$

Equation 3.44

I_p is the polar moment of inertia for a circular cross section. One can now derive the expression for the torsional stiffness (GI_p) as:

$$T = \frac{\tau_{\max}}{R} \cdot I_p \Rightarrow T = \frac{R \cdot \theta \cdot G}{R} \cdot I_p \Rightarrow GI_p = \frac{T}{\theta}$$

Equation 3.45

The torsional stiffness is in general referred to as GJ . The torsional stiffness has a material parameter G (shear modulus) and a cross section factor J , which is called the cross sectional torsion factor. Only for a circular cross section is $I_p = J$.

3.4.2. Non-circular cross section

A bar with a non-circular cross section will warp when subjected to torsion, which means that the assumption of the out-of-plane displacement ($u_z = 0$) is no longer valid. St. Venant made the following displacement field assumptions:

$$u_x = -y \cdot z \cdot \theta \quad u_y = x \cdot z \cdot \theta \quad u_z = \psi(x, y) \cdot \theta$$

Equation 3.46

$\psi(x, z)$ is the **warping function** and the displacement u_z , which describes the warping, is called the warping displacement. The warping is independent of z , which means that the warping is the same at each cross section. Furthermore, it is assumed that there is no distortion of the cross section. The strain field can be expressed by the displacement field:

$$\begin{aligned} \epsilon_{xx} &= \frac{\partial}{\partial x} u_x = 0 & \epsilon_{yy} &= \frac{\partial}{\partial y} u_y = 0 & \epsilon_{zz} &= \frac{\partial}{\partial z} u_z = 0 \\ \gamma_{xy} &= \frac{\partial}{\partial x} u_y + \frac{\partial}{\partial y} u_x = 0 & \gamma_{xz} &= \frac{\partial}{\partial z} u_x + \frac{\partial}{\partial x} u_z = \frac{\partial}{\partial x} \psi - y \cdot \theta & \gamma_{yz} &= \frac{\partial}{\partial z} u_y + \frac{\partial}{\partial y} u_z = \frac{\partial}{\partial y} \psi + x \cdot \theta \end{aligned}$$

Equation 3.47

With the resulting stress components:

$$\tau_{xz} = G \left(\frac{\partial}{\partial x} \psi - y \right) \cdot \theta \quad \tau_{yz} = G \left(\frac{\partial}{\partial y} \psi + x \right) \cdot \theta$$

Equation 3.48

In *Figure 3.4.3* below, are the non-zero stress components shown. The force equilibrium of a volume element gives the following three equations (the volume forces are disregarded).

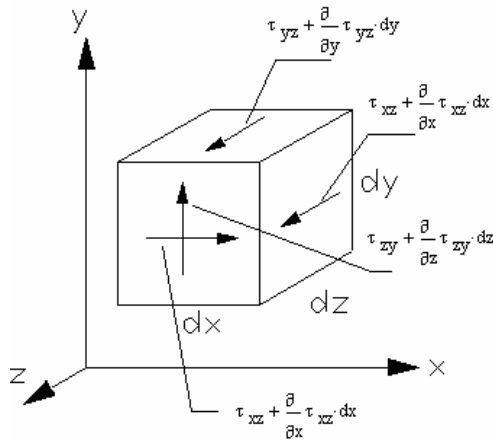


Figure 3.4.3 – Force equilibrium of a volume element

Equilibrium in the z-direction:

$$\left(\frac{\partial}{\partial y} \tau_{yz} \cdot dy \right) \cdot dx \cdot dz + \left(\frac{\partial}{\partial x} \tau_{xz} \cdot dx \right) \cdot dy \cdot dz = 0 \Rightarrow \frac{\partial}{\partial y} \tau_{yz} + \frac{\partial}{\partial x} \tau_{xz} = 0$$

Equation 3.49

Equilibrium in the y-direction:

$$\left(\frac{\partial}{\partial z} \tau_{yz} \cdot dz \right) \cdot dx \cdot dy = 0 \Rightarrow \frac{\partial}{\partial z} \tau_{yz} = 0$$

Equation 3.50

Equilibrium in the x-direction:

$$\left(\frac{\partial}{\partial z} \tau_{zx} \cdot dz \right) \cdot dx \cdot dz = 0 \Rightarrow \frac{\partial}{\partial z} \tau_{zx} \cdot dz = 0$$

Equation 3.51

By substituting Equation 3.48 into Equation 3.49 one gets the governing equation for the warping function:

$$G \cdot \theta \cdot \left(\frac{\partial^2}{\partial x^2} \psi + \frac{\partial^2}{\partial y^2} \psi \right) = 0$$

Equation 3.52

This can be rewritten as:

$$\frac{\partial^2}{\partial x^2} \psi + \frac{\partial^2}{\partial y^2} \psi = \Delta \cdot \psi(x, y) = 0$$

Equation 3.53

This is known as the Laplace's equation in two dimensions.

This equation is complicated to solve because of the boundary conditions, which are no surface tractions and that i.e. at boundary the following must be satisfied (n_x and n_y are the surfaces normal in the x- and y-direction).

$$\tau_{xz} n_x + \tau_{yz} n_y = 0$$

Equation 3.54

By using Equation 3.48 this can be rewritten:

$$\left(\frac{\partial}{\partial x} \psi - y \right) \cdot n_x + \left(\frac{\partial}{\partial y} \psi + x \right) \cdot n_y = 0$$

Equation 3.55

This equation describes the boundary conditions on the surface.

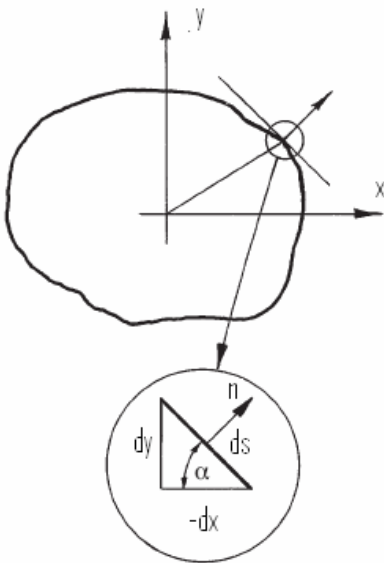


Figure 3.4.4 –surface normal

The surfaces normal n_x and n_y can be expressed by (see the sketch):

$$n_x = \sin(\alpha) = \frac{dy}{ds} \quad n_y = \cos(\alpha) = -\frac{dx}{ds}$$

Equation 3.56

By using these expressions for the normal, *Equation 3.55* takes the following form:

$$\left(\frac{\partial}{\partial x} \psi - y \right) \cdot \frac{dy}{ds} - \left(\frac{\partial}{\partial y} \psi + x \right) \cdot \frac{dx}{ds} = 0 \Rightarrow$$

$$\left(\frac{\partial}{\partial x} \psi \right) \cdot \frac{dy}{dx} - \frac{\partial}{\partial y} \psi = y \cdot \frac{dy}{dx} + x$$

Equation 3.57

The pure torsional problem involves solving *Equation 3.53* and *Equation 3.57*. Once $\psi(x,y)$ is known the shear stress can be determined by *Equation 3.48*. The equilibrium with the external torsional moment and the internal stress can be illustrated by the following example/sketch:

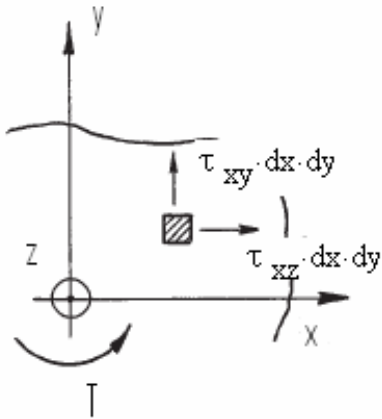


Figure 3.4.5 - External torsional moment

The external torsional moment can be determined by:

$$T = \int_A (-\tau_{xz}y + \tau_{yz}x) dA$$

Equation 3.58

By substituting the torsional moment with $T = G \cdot J \cdot \theta$, the following equation for J (cross sectional torsion factor) can be obtained:

$$J = \int_A \left[x^2 + y^2 + \left(\frac{\partial}{\partial y} \psi \right) \cdot x - \left(\frac{\partial}{\partial x} \psi \right) \cdot y \right] dA$$

Equation 3.59

It is possible to obtain the exact solution for ψ for simple cross sections, but very complicated. A more practical method to solve the pure torsional problem is to use Prandtl's **stress function** $\Phi(x,y)$. The two non-zero shear stress components described by the stress function:

$$\tau_{xz} = \frac{\partial}{\partial y} \Phi \quad \tau_{yz} = -\frac{\partial}{\partial x} \Phi$$

Equation 3.60

This simplifies the boundary conditions ($\tau_{xz} \cdot n_x + \tau_{yz} \cdot n_y = 0$) to the following:

$$\left(\frac{\partial}{\partial y} \Phi \right) \cdot \frac{dy}{ds} + \left(\frac{\partial}{\partial x} \Phi \right) \cdot \frac{dx}{ds} = \frac{d\Phi}{ds} = 0 \quad \Rightarrow \quad \Phi = \text{constant}$$

Equation 3.61

The stress function can be expressed by the warping function. This is done by substituting *Equation 3.48* into *Equation 3.60*:

$$\frac{\partial}{\partial x} \Phi = -G \cdot \left(\frac{\partial}{\partial y} \psi + x \right) \cdot \theta \quad \frac{\partial}{\partial y} \Phi = G \cdot \left(\frac{\partial}{\partial x} \psi - y \right) \cdot \theta$$

Equation 3.62

By differentiating and eliminating the warping function ψ (by derivation) then the following equation can be obtained (stress equilibrium):

$$\Delta \Phi = \frac{\partial^2}{\partial x^2} \Phi + \frac{\partial^2}{\partial y^2} \Phi = -2 \cdot G \cdot \theta$$

Equation 3.63

This equation is known as the Poisson differential equation. If one is able to solve the stress function, then the warping function is also solved.

By performing equilibrium with the external torsional moment and the internal stress, one can derive the following expression for the external torsional moment:

$$T = 2 \cdot \int \Phi \, dA$$

Equation 3.64

By substituting the torsional moment with $T = G \cdot J \cdot \theta$, the following equation for J (cross sectional torsion factor) can be obtained:

$$J = \left| \frac{2 \cdot \int \Phi \, dA}{G \cdot \theta} \right|$$

Equation 3.65

Equation 3.65 can be used to determine the cross sectional torsion factor and thereby the torsional stiffness for simple solid isotropic cross sections.

St. Venant's torsion problem can only be solved with numerical methods for more complicated cross sections. For a more detailed description on this topic see [5].

3.4.3. Closed thin-walled cross-section

A **thin-walled single-hole** tube with an arbitrary cross section is considered (see *Figure 3.4.6*). This tube is subjected to a torsional moment T and is able to warp. A small rectangular element described by $abcd$, of this tube is cut out and the shear stress acting on the faces on the element are considered. One can derive the following from force equilibrium:

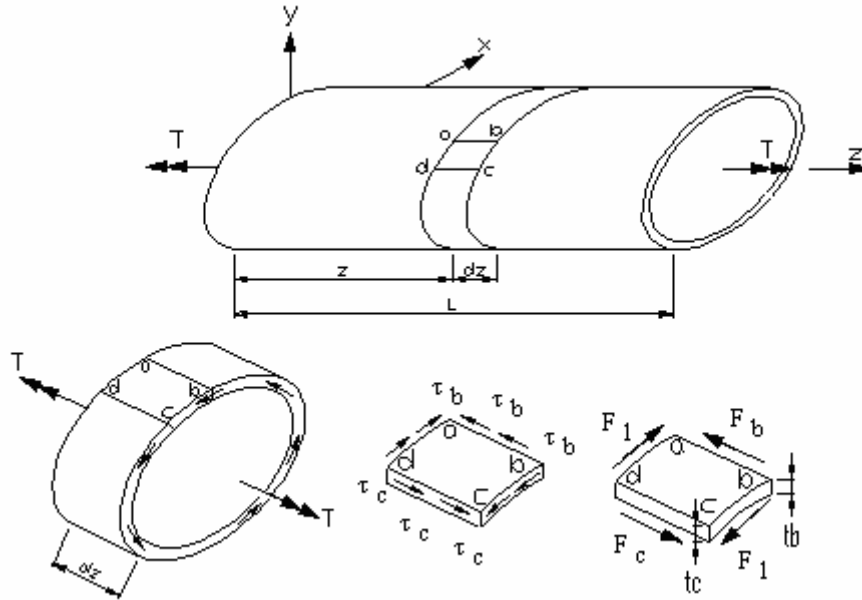


Figure 3.4.6 - Thin-walled tube of arbitrary cross sectional shape

$$F_b = \tau_b \cdot t_b \cdot dz \quad F_c = \tau_c \cdot t_c \cdot dz$$

Equation 3.66

From the equilibrium of the element in the longitudinal direction (z -direction) one can see that:

$$F_b = F_c \quad \text{or} \quad \tau_b \cdot t_b = \tau_c \cdot t_c = \tau \cdot t = \text{constant}$$

Equation 3.67

The product of the shear stress τ and the thickness t of tube is the same at every point on the cross section. This product is called the shear flow τt (note that this is only valid for thin-walled cross sections).

The next step is to determine the external torsional moment T , this is done by considering a cross section of the tube (see *Figure 3.4.7*).

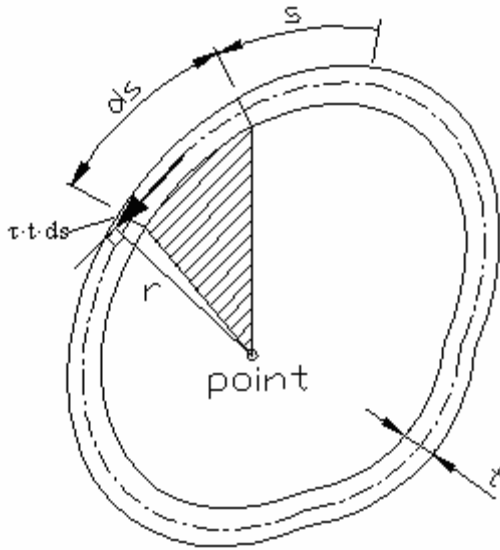


Figure 3.4.7 – Thin-walled cross section

The total shear force acting on the element of the area in Figure 3.4.7 is $\tau t ds$ and the moment of this force about any point within the tube is:

$$dT = \tau \cdot t \cdot r \cdot ds$$

Equation 3.68

The median line of the wall of the tube is shown with a dashed line in Figure 3.4.7. The total torsional moment produced by the shear stress is obtained by integrating along the median line of the cross section (L_0), which gives:

$$T = \tau \cdot t \cdot \int_0^{L_0} r ds$$

Equation 3.69

This integration can be difficult for complex cross sections, but can be solved “easily” by looking at the geometry.

The product $r \cdot ds$ represents twice the area of the shaded triangle shown in Figure 3.4.7 and therefore is the result of the integration the following:

$$\int_0^{L_0} r ds = 2 \cdot A_0$$

Equation 3.70

Note that A_0 is the area enclosed by the median line. The external torsional moment can now be expressed by:

$$T = \tau \cdot t \cdot 2 \cdot A_0$$

Equation 3.71

The maximum shear stress will of course occur where the wall thickness of the tube is smallest, which gives:

$$\tau = \frac{T}{t \cdot 2 \cdot A_0} \Rightarrow \tau_{\max} = \frac{T}{t_{\min} \cdot 2 \cdot A_0}$$

Equation 3.72

The cross sectional torsion factor J can be obtained by using strain energy theory. The strain energy of a thin-walled tube can be calculated by first finding the strain energy of an element and then integrating throughout the volume of the tube. The strain energy of an element is equal to the strain energy density times the volume (strain energy density for an element is equal to $u = \tau^2/2 \cdot G$ and the volume is equal to the area of the element $t \cdot ds$ times the length of element dz).

$$dU = \frac{\tau^2}{2 \cdot G} \cdot t \cdot ds \cdot dz = \frac{\tau \cdot t}{2 \cdot G} \cdot \frac{ds}{t} \cdot dz$$

Equation 3.73

The total strain energy is obtained by integrating dU throughout the volume of the tube, that is integrating ds from 0 to L_0 and dz from 0 to L . One can now derive the following expression for the strain energy:

$$U = \frac{\tau \cdot t \cdot L}{2G} \cdot \int_0^{L_0} \frac{1}{t} ds \quad \text{and} \quad \tau \cdot t = \frac{T}{2 \cdot A_0} \quad \Rightarrow \quad U = \frac{T^2 \cdot L}{8 \cdot G \cdot A_0^2} \cdot \int_0^{L_0} \frac{1}{t} ds$$

Equation 3.74

The work done by the torsional moment is equal to $W = T \cdot \phi_L / 2$ and W is equal to the strain energy $W = U$. Using the equation $\phi_L = (T \cdot L) / (G \cdot J)$ then the strain energy can be expressed by the following:

$$U = \frac{T^2 \cdot L}{2 \cdot G \cdot J}$$

Equation 3.75

By combining *Equation 3.74* and *Equation 3.75*, one can then derive the following expression for the cross sectional torsion factor J for a thin-walled cross section:

$$J = \frac{4 \cdot A_0^2}{\int_0^{L_0} \frac{1}{t} ds}$$

Equation 3.76

This equation is called Bredt's formula. In the special case that a cross section has a constant thickness t , the equation simplifies to:

$$J = \frac{4 \cdot t \cdot A_0^2}{L_0}$$

Equation 3.77

Thin-walled cross section has often several holes and in that case, the calculation of J (the cross sectional torsion factor) becomes more complicated. Pauli Pedersen has described a method/procedure in his book *Elasticity – Anisotropy – laminates* [5] for calculating the J for thin-walled isotropic cross sections. This method is described in the following.

The holes are numbered $n = 1, 2, 3, \dots, N$, where N is the total number of holes. It is assumed that the whole cross section has the same rotation when subjected to torsion and by rewriting *Equation 3.76* the following relation can be derived (note $J = T / (G \cdot \theta)$):

$$\theta_n = \theta = \frac{T_n}{4 \cdot G \cdot A_{0n}^2} \cdot \int_0^{L_{0n}} \frac{1}{t} ds \quad \Rightarrow \quad \int_0^{L_{0n}} \frac{1}{t} ds = \frac{\theta \cdot 4 \cdot G \cdot A_{0n}}{T_n}$$

Equation 3.78

For a special hole n , the integrated shear stress can be derived from the following by using *Equation 3.72* and *Equation 3.78*:

$$\int_0^{L_{0n}} \tau \, ds = \theta \cdot 2 \cdot G \cdot A_{0n}$$

Equation 3.79

One can derive an expression for the shear stress by using the stress function Φ . For an N -holed cross section are there a total of $N+1$ stress functions defined for the holes.

These are $\Phi_0, \Phi_1, \Phi_2, \dots, \Phi_N$, at the inner boundary of a hole n is the constant value of the stress function denoted Φ_n and at the outer surface/contour of the cross section is the stress function Φ_0 by definition set to zero (boundary condition). For a thin-walled cross section, it is reasonable to assume that the stress function vary linearly though the wall from hole to hole:

$$\tau_{nm} = \frac{\Phi_n - \Phi_m}{t_{nm}}$$

Equation 3.80

Where t_{nm} is the thickness of the wall between hole n and m . The approximated equation for the shear stress (*Equation 3.80*) is then inserted in *Equation 3.79*, which gives:

$$\int_0^{L_{0n}} \frac{\Phi_n - \Phi_m}{t_{nm}} \, ds = \sum_m \frac{\Phi_n - \Phi_m}{t_{nm}} \cdot S_{nm} = \theta \cdot 2 \cdot G \cdot A_{0n}$$

Equation 3.81

Where \sum_m is a summation over the m holes connected to hole n . Note that $t_{nm} = t_{mn}$ and $S_{nm} = S_{mn}$. This leads to a set of N linear equations and N unknowns, which are the stress functions.

The torsional moment T is calculated by using/rewriting *Equation 3.64*:

$$T = 2 \cdot \int \Phi \, dA = 2 \cdot \sum_n \Phi_n \cdot A_{0n}$$

Equation 3.82

The cross sectional torsion factor J for a thin-walled cross section with several holes can then be expressed by:

$$J = \frac{2 \left| \sum_n \Phi_n \cdot A_{0n} \right|}{G \theta}$$

Equation 3.83

An example of a three celled cross section is illustrated below in order to clarify this method:

Example: three-celled cross section

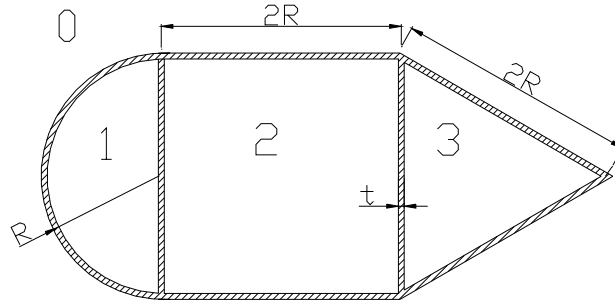


Figure 3.4.8 – Three-celled cross section

Figure 3.4.8 shows a three-celled cross section with a constant thickness t . The holes are numbered from one to three, zero represents the outside. The first step is to determine the four stress functions (note $\Phi_0=0$), this is done by using Equation 3.81:

$$\sum_m \frac{\Phi_n - \Phi_m}{t_{nm}} \cdot S_{nm} = \theta \cdot 2 \cdot G \cdot A_{0n}$$

When **hole one** is considered, the equation of the integrated shear stress is:

$$\frac{\Phi_1 - \Phi_0}{t_{10}} \cdot S_{10} + \frac{\Phi_1 - \Phi_2}{t_{12}} \cdot S_{12} = \theta \cdot 2 \cdot G \cdot A_{01}$$

When **hole two** is considered, the equation of the integrated shear stress is:

$$\frac{\Phi_2 - \Phi_0}{t_{20}} \cdot S_{20} + \frac{\Phi_2 - \Phi_1}{t_{21}} \cdot S_{21} + \frac{\Phi_2 - \Phi_3}{t_{23}} \cdot S_{23} = \theta \cdot 2 \cdot G \cdot A_{02}$$

When **hole three** is considered, the equation of the integrated shear stress is:

$$\frac{\Phi_3 - \Phi_0}{t_{30}} \cdot S_{30} + \frac{\Phi_3 - \Phi_2}{t_{32}} \cdot S_{32} = \theta \cdot 2 \cdot G \cdot A_{03}$$

The ratio between S_{nm} and t_{nm} are denoted ξ_{nm} :

$$\xi_{10} = \frac{\pi \cdot R}{t} \quad \xi_{12} = \frac{2 \cdot R}{t} \quad \xi_{20} = \frac{4 \cdot R}{t} \quad \xi_{30} = \frac{4 \cdot R}{t} \quad \xi_{23} = \frac{2 \cdot R}{t}$$

And the areas A_{0n} that are enclosed by the median lines can be calculated:

$$A_{01} = \frac{\pi \cdot R^2}{2} \quad A_{02} = (2 \cdot R)^2 \quad A_{03} = \sqrt{3} \cdot R^2$$

The three non-zero stress functions can be arranged in a matrix system:

$$\begin{pmatrix} \xi_{10} + \xi_{12} & -\xi_{12} & 0 \\ -\xi_{12} & \xi_{20} + \xi_{12} + \xi_{23} & -\xi_{23} \\ 0 & -\xi_{23} & \xi_{30} + \xi_{23} \end{pmatrix} \cdot \begin{pmatrix} \Phi_1 \\ \Phi_2 \\ \Phi_3 \end{pmatrix} = \theta \cdot 2 \cdot G \cdot \begin{pmatrix} A_{01} \\ A_{02} \\ A_{03} \end{pmatrix}$$

The solution of this matrix system is simple since the matrix $[\xi]$ is invertible. The solution of the system is:

$$\begin{pmatrix} \Phi_1 \\ \Phi_2 \\ \Phi_3 \end{pmatrix} = \theta \cdot 2 \cdot G \cdot \begin{pmatrix} \xi_{10} + \xi_{12} & -\xi_{12} & 0 \\ -\xi_{12} & \xi_{20} + \xi_{12} + \xi_{23} & -\xi_{23} \\ 0 & -\xi_{23} & \xi_{30} + \xi_{23} \end{pmatrix}^{-1} \cdot \begin{pmatrix} A_{01} \\ A_{02} \\ A_{03} \end{pmatrix}$$

When the three stress functions are known, then the cross sectional torsion factor J can be determined by *Equation 3.83*:

$$J = \frac{2 \cdot \left| \sum_n \Phi_n \cdot A_{0n} \right|}{G \cdot \theta}$$

$J = 0.00318\text{m}^4$ if R is equal to 0.25m and the thickness is equal to 0.01m.

Limitations of the method to determine the cross sectional torsion factor J

The method for determining the cross sectional torsion factor J assumes that the cross section is isotropic and thin-walled. The cross section of a wind turbine blade is not isotropic, which means that the shear modulus G vary and the equations above are no longer valid.

4. The Beam Property Extraction (BPE) method by Malcolm and Laird

The theory in this chapter is primarily based on the paper *Identification and use of blade physical properties* [2] by David J. Malcolm and Daniel L. Laird.

A complete FE-model of a wind turbine blade typically consists of thousands of composite shell elements and also solid elements for some FE-models.

The FE-models are very complex since they are used for examining stresses/strains, local and global deflections etc. But the FE-models are too detailed for aeroelastic analysis, so these analyses are normally based on a series of equivalent three-dimensional beam elements that represents the full blade.

The beam elements must accurately represent the real full blade behavior such as shear deformation, bend-twist coupling, offsets between the elastic and shear centers etc.

4.1. Extraction of the equivalent beam properties

Since a wind turbine blade has a big cross sectional variation when going from the root to the tip, then the equivalent beam elements will also have widely different cross sectional properties.

The full wind turbine blade can be described by dividing the blade into several beam elements (with constant cross sectional properties).

4.1.1. Stiffness matrix K

The section stiffness matrices for the beam elements can be determined by applying a series of static loads at the tip of the blade. The blade is divided into a number of elements, one can then determine the stiffness matrices by the elements internal forces/moments and their relative displacements/rotations.

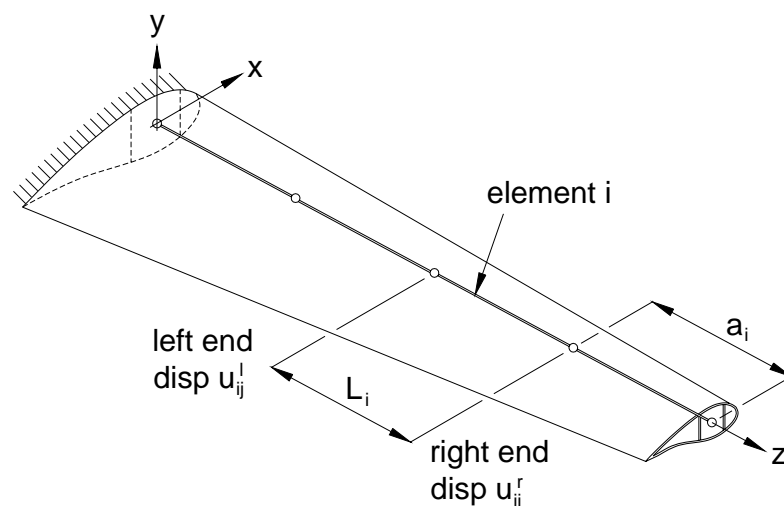


Figure 4.1.1 - Equivalent beam element for a 3D blade model

The relative displacements and rotations can be determined by:

$$\begin{aligned} u_{ix}^{rl} &= u_{ix}^r - u_{ix}^l - \theta_{iy}^l \cdot L & u_{iy}^{rl} &= u_{iy}^r - u_{iy}^l + \theta_{ix}^l \cdot L & u_{iz}^{rl} &= u_{iz}^r - u_{iz}^l \\ \theta_{ix}^{rl} &= \theta_{ix}^r - \theta_{ix}^l & \theta_{iy}^{rl} &= \theta_{iy}^r - \theta_{iy}^l & \theta_{iz}^{rl} &= \theta_{iz}^r - \theta_{iz}^l \end{aligned}$$

Equation 4.1

L_i is the length of element i .

Since the locations of the elastic and shear centers are not known, one must then select a global reference coordinate system and a global reference axis along the blade. The longitudinal pitch axis is an obvious choice for reference, but other locations can also be used.

After selecting a reference, then the static loads can be applied with respect to the reference.

The relative deflections and rotations shall also be determined with respect to the reference.

The series of static loads consists of two transverse forces (F_x and F_y), a axial force (F_z), two pure bending moments (M_x and M_y) and finally a torsional moment (M_z).

The elements stiffness matrices (K_i) are calculated in the following way:

$$\begin{aligned} F_i &= K_i \cdot U_i \quad \Leftrightarrow \quad \begin{pmatrix} F_x & 0 & 0 & 0 & 0 & 0 \\ 0 & F_y & 0 & 0 & 0 & 0 \\ 0 & 0 & F_z & 0 & 0 & 0 \\ 0 & -F_y \cdot a_i & 0 & M_x & 0 & 0 \\ F_x \cdot a_i & 0 & 0 & 0 & M_y & 0 \\ 0 & 0 & 0 & 0 & 0 & M_z \end{pmatrix} = K_i \cdot \begin{pmatrix} u_{ix} & u_{iy} & u_{iz} & \theta_{ix} & \theta_{iy} & \theta_{iz} \\ F_x & F_x & F_x & F_x & F_x & F_x \\ u_{ix} & u_{iy} & u_{iz} & \theta_{ix} & \theta_{iy} & \theta_{iz} \\ F_x & F_x & F_x & F_x & F_x & F_x \\ u_{ix} & u_{iy} & u_{iz} & \theta_{ix} & \theta_{iy} & \theta_{iz} \\ F_x & F_x & F_x & F_x & F_x & F_x \\ u_{ix} & u_{iy} & u_{iz} & \theta_{ix} & \theta_{iy} & \theta_{iz} \end{pmatrix} \\ &\Leftrightarrow \quad K_i = \begin{pmatrix} F_x & 0 & 0 & 0 & 0 & 0 \\ 0 & F_y & 0 & 0 & 0 & 0 \\ 0 & 0 & F_z & 0 & 0 & 0 \\ 0 & -F_y \cdot a_i & 0 & M_x & 0 & 0 \\ F_x \cdot a_i & 0 & 0 & 0 & M_y & 0 \\ 0 & 0 & 0 & 0 & 0 & M_z \end{pmatrix} \cdot \begin{pmatrix} F_x & F_y & F_z & M_x & M_y & M_z \\ u_{ix} & u_{iy} & u_{iz} & \theta_{ix} & \theta_{iy} & \theta_{iz} \\ F_x & F_x & F_x & F_x & F_x & F_x \\ u_{ix} & u_{iy} & u_{iz} & \theta_{ix} & \theta_{iy} & \theta_{iz} \\ F_x & F_x & F_x & F_x & F_x & F_x \\ u_{ix} & u_{iy} & u_{iz} & \theta_{ix} & \theta_{iy} & \theta_{iz} \\ F_x & F_x & F_x & F_x & F_x & F_x \\ u_{ix} & u_{iy} & u_{iz} & \theta_{ix} & \theta_{iy} & \theta_{iz} \end{pmatrix}^{-1} \end{aligned}$$

Equation 4.2

The a_i vector contains the lengths from the blade tip to the right ends of the different elements. The internal moments on the elements from the two transverse forces are calculated by using the a_i vector:

$$a_i = (a_1 \ a_2 \ \dots \ a_n)^T$$

4.1.2. Constitutive matrix k

The section constitutive matrix (k) is the relationship between the six forces/moments and the six strains. The constitutive matrix can be determined from the element stiffness matrix (K) and the geometry of the element.

The strains and the relation between the internal force resultants (f^z) and the six section strains are:

$$\varepsilon = \begin{pmatrix} \gamma_x \\ \gamma_y \\ \varepsilon_z \\ \kappa_x \\ \kappa_y \\ \kappa_z \end{pmatrix} = \begin{pmatrix} \frac{\partial}{\partial z} u_x - \theta_y & \frac{\partial}{\partial z} u_y + \theta_x & \frac{\partial}{\partial z} u_z & \frac{\partial}{\partial z} \theta_x & \frac{\partial}{\partial z} \theta_y & \frac{\partial}{\partial z} \theta_z \end{pmatrix}^T \quad f^z = \begin{pmatrix} F_x \\ F_y \\ F_z \\ M_x \\ M_y \\ M_z \end{pmatrix} = k \cdot \varepsilon$$

Equation 4.3

The terms $du_x/dz - \theta_y$ and $du_y/dz + \theta_x$ are the differences between the slopes of the neutral axes and the rotations of the cross sections (Timoshenko beam theory).

One can obtain the six displacements at the right element end relative to the left element end by integrating the slopes:

$$u^{rl} = \int_0^L \begin{pmatrix} \frac{\partial}{\partial z} u_x & \frac{\partial}{\partial z} u_y & \frac{\partial}{\partial z} u_z & \frac{\partial}{\partial z} \theta_x & \frac{\partial}{\partial z} \theta_y & \frac{\partial}{\partial z} \theta_z \end{pmatrix}^T dz = \int_0^L \begin{pmatrix} \gamma_x + \theta_y \\ \gamma_y - \theta_x \\ \varepsilon_z \\ \kappa_x \\ \kappa_y \\ \kappa_z \end{pmatrix} dz = \int_0^L k^{-1} \cdot f^z dz + \int_0^L \begin{pmatrix} \theta_y \\ -\theta_x \\ 0 \\ 0 \\ 0 \\ 0 \end{pmatrix} dz$$

Equation 4.4

The section forces (f^z) can be determined from statics in terms of the forces at the right element end along the element, z :

$$f^z = \begin{bmatrix} 1 & 0 & 0 & 0 & 0 & 0 \\ 0 & 1 & . & . & . & . \\ 0 & . & 1 & . & . & . \\ 0 & -(L-z) & . & 1 & . & . \\ (L-z) & . & . & . & 1 & . \\ 0 & . & . & . & . & 1 \end{bmatrix} \cdot f^r = D_z \cdot f^r$$

Equation 4.5

The second term in Equation 4.4 can be written as:

$$\begin{pmatrix} \theta_y \\ -\theta_x \\ 0 \\ 0 \\ 0 \\ 0 \end{pmatrix} = \int_0^z \begin{pmatrix} \kappa_y \\ -\kappa_x \\ 0 \\ 0 \\ 0 \\ 0 \end{pmatrix} dz = \int_0^z \begin{pmatrix} 0 & 0 & 0 & 0 & 1 & 0 \\ 0 & . & . & -1 & . & . \\ 0 & . & . & . & . & . \\ 0 & . & . & . & . & . \\ 0 & . & . & . & . & . \\ 0 & . & . & . & . & . \end{pmatrix} \cdot \varepsilon dz = \int_0^z E \cdot \varepsilon dz = \int_0^z E \cdot k^{-1} \cdot f^z dz = E \cdot k^{-1} \cdot \int_0^z D_z \cdot f^r dz$$

$$\Leftrightarrow \begin{pmatrix} \theta_y \\ -\theta_x \\ 0 \\ 0 \\ 0 \\ 0 \end{pmatrix} = E \cdot k^{-1} \cdot \begin{bmatrix} z & 0 & 0 & 0 & 0 & 0 \\ 0 & z & . & . & . & . \\ 0 & . & z & . & . & . \\ 0 & -z \left(L - \frac{z}{2} \right) & . & z & . & . \\ z \left(L - \frac{z}{2} \right) & . & . & . & z & . \\ . & . & . & . & . & z \end{bmatrix} \cdot f^r = E \cdot k^{-1} \cdot G_z \cdot f^r$$

Equation 4.6

Equation 4.4 can now be rewritten as:

$$u^{rl} = k^{-1} \cdot \int_0^L D_z \cdot f^r dz + E \cdot k^{-1} \cdot \int_0^L G_z \cdot f^r dz$$

$$\Leftrightarrow \quad u^{\text{rl}} = k^{-1} \cdot \begin{pmatrix} L & 0 & 0 & 0 & 0 & 0 \\ 0 & L & . & . & . & . \\ 0 & . & L & . & . & . \\ 0 & \frac{-L^2}{2} & . & L & . & . \\ \frac{L^2}{2} & . & . & . & L & . \\ 0 & . & . & . & . & L \end{pmatrix} \cdot f^{\text{r}} + E \cdot k^{-1} \cdot \begin{pmatrix} \frac{L^2}{2} & 0 & 0 & 0 & 0 & 0 \\ 0 & \frac{L^2}{2} & . & . & . & . \\ 0 & . & \frac{L^2}{2} & . & . & . \\ 0 & \frac{-L^3}{3} & . & \frac{L^2}{2} & . & . \\ \frac{L^3}{3} & . & . & . & \frac{L^2}{2} & . \\ 0 & . & . & . & . & \frac{L^2}{2} \end{pmatrix} \cdot f^{\text{r}} = (k^{-1} \cdot H + E \cdot k^{-1} \cdot Q) \cdot f^{\text{r}}$$

Equation 4.7

By using Equation 4.2, one can now write:

$$u^{\text{rl}} = K^{-1} \cdot f^{\text{r}} \quad \Leftrightarrow \quad K^{-1} \cdot f^{\text{r}} = (k^{-1} \cdot H + E \cdot k^{-1} \cdot Q) \cdot f^{\text{r}} \quad \Leftrightarrow \quad K^{-1} = k^{-1} \cdot H + E \cdot k^{-1} \cdot Q$$

$$\Leftrightarrow \quad K^{-1} \cdot Q^{-1} = k^{-1} \cdot H \cdot Q^{-1} + E \cdot k^{-1}$$

Equation 4.8

The constitutive matrix (k) can now be determined by using Lyapunov's method.

Equation 4.8 can be solved by using MatLab that has a built-in Lyapunov program/solver.

4.1.3. Elastic center

The elastic center can be defined as the cross section location with the following properties:

An axial force F_z through the elastic center will give an axial strain without additional moments about the x- and y-axis.

Figure 4.1.2 shows an example of the relationship between the axis origin and the elastic center:

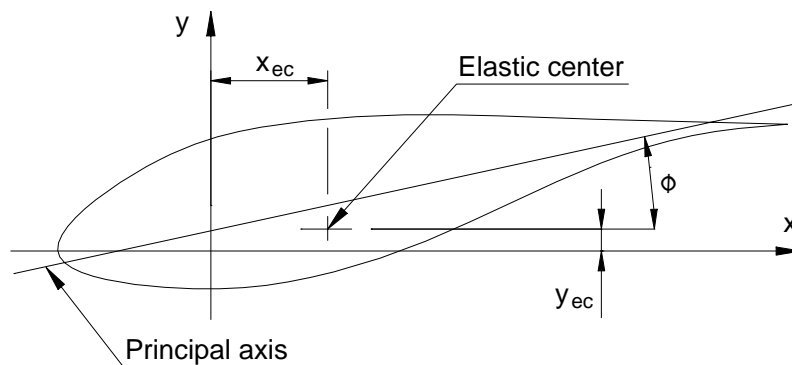


Figure 4.1.2 - Location of elastic center and principal axes

$$F_Z = k_{33} \cdot \varepsilon_Z \quad M_X = F_Z \cdot y_{ec} = k_{43} \cdot \varepsilon_Z \quad M_Y = -F_Z \cdot x_{ec} = k_{53} \cdot \varepsilon_Z \quad \Rightarrow \quad y_{ec} = \frac{k_{43}}{k_{33}} \quad x_{ec} = \frac{-k_{53}}{k_{33}}$$

Equation 4.9

When using the definition above for the location of the elastic center, then there will be zero coupling between axial strain and curvatures, when the axes origin is transferred to the elastic center.

4.1.4. Principal axes rotation

A principal axis can be defined as a direction about which an applied curvature will result in a moment about that axis and zero moment about the perpendicular axis.

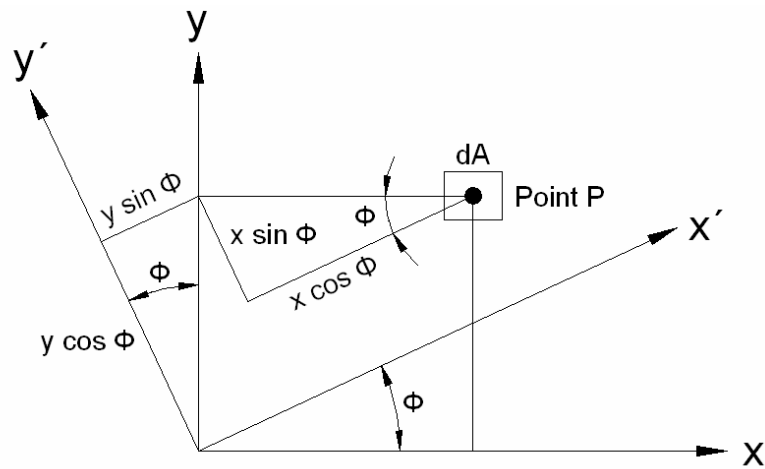


Figure 4.1.3 - Rotation of the coordinate system

The x' , y' coordinates for point P can be obtained in terms of the x , y coordinates (see Figure 4.1.3):

$$x' = x \cdot \cos(\phi) + y \cdot \sin(\phi) \quad y' = -x \cdot \sin(\phi) + y \cdot \cos(\phi)$$

Equation 4.10

Suppose that the area dA is located at point P, then the area moments of inertia in the rotated coordinate system are:

$$I_{x'} = \int y'^2 dA = I_Y \cdot \sin^2(\phi) + I_X \cdot \cos^2(\phi) - 2 \cdot I_{XY} \cdot \sin(\phi) \cdot \cos(\phi)$$

$$I_{y'} = \int x'^2 dA = I_Y \cdot \cos^2(\phi) + I_X \cdot \sin^2(\phi) + 2 \cdot I_{XY} \cdot \sin(\phi) \cdot \cos(\phi)$$

$$I_{x'y'} = \int x' \cdot y' dA = I_{XY} [\cos^2(\phi) - \sin^2(\phi)] + (I_X - I_Y) \cdot \sin(\phi) \cdot \cos(\phi)$$

Equation 4.11

The area moments of inertia for the rotated coordinate system can now be rewritten:

$$\begin{aligned}
 2 \cdot \cos^2(\phi) &= 1 + \cos(2\phi) & 2 \cdot \sin^2(\phi) &= 1 - \cos(2\phi) & 2 \cdot \sin(\phi) \cdot \cos(\phi) &= \sin(2\phi) & \Rightarrow \\
 I_{x'} &= \frac{I_x + I_y}{2} + \frac{I_x - I_y}{2} \cdot \cos(2\phi) - I_{xy} \cdot \sin(2\phi) & I_{y'} &= \frac{I_x + I_y}{2} - \frac{I_x - I_y}{2} \cdot \cos(2\phi) + I_{xy} \cdot \sin(2\phi) \\
 I_{x'y'} &= \frac{I_x - I_y}{2} \cdot \sin(2\phi) + I_{xy} \cdot \cos(2\phi)
 \end{aligned}$$

Equation 4.12

The three area moments of inertia are functions of the angle ϕ . The extreme values of the area moments of inertia (I_1 and I_2) are called the principal moments of inertia and the corresponding angles define the principal directions. The two principal directions are perpendicular to each other.

The angle, at which the moment of inertia is at its maximum value, can be determined by setting $dI_{x'}/d\phi$ equal to zero:

$$\frac{\partial}{\partial \phi} I_{x'} = 0 \quad \Rightarrow \quad (I_x - I_y) \cdot (-\sin(2\phi)) - 2 \cdot I_{xy} \cdot \cos(2\phi) = 0 \quad \Leftrightarrow \quad \tan(2\phi) = \frac{2 \cdot I_{xy}}{I_y - I_x}$$

Equation 4.13

This angle also corresponds to the rotation for which the product of inertia $I_{x'y'}$ is zero.

The constitutive matrix (k) can now be substituted into the last term of *Equation 4.13* and the principal axis rotation can be determined:

$$\tan(2\phi) = \frac{2 \cdot k_{45}}{k_{44} - k_{55}} \quad \Leftrightarrow \quad \phi = \frac{1}{2} \cdot \tan^{-1} \left(\frac{2 \cdot k_{45}}{k_{44} - k_{55}} \right)$$

Equation 4.14

4.1.5. Shear center

According to Malcolm and Laird, the shear center is defined as the location on the cross section with the following properties: By imposing a lateral strain γ_x while all other strains are restrained to be zero, then this will result in a lateral force F_x , through the shear center but a resulting torsional moment M_z that is equal to zero. This can be written as:

$$F_x = k_{11} \cdot \gamma_x \quad M_z = -F_{x'} \cdot y_{sc} = k_{61} \cdot \gamma_x \quad \Rightarrow \quad y_{sc} = \frac{-k_{61}}{k_{11}}$$

Equation 4.15

Similarly it can be shown:

$$F_y = k_{22} \cdot \gamma_y \quad M_z = F_y \cdot x_{sc} = k_{62} \cdot \gamma_y \quad \Rightarrow \quad y_{sc} = \frac{k_{62}}{k_{22}}$$

Equation 4.16

4.1.6. Translation and rotation of coordinates

The relationship between the six forces/moments and the six strains in a xyz-coordinate system (the global reference coordinate system) can be written as:

$$\begin{pmatrix} F_x \\ F_y \\ F_z \\ M_x \\ M_y \\ M_z \end{pmatrix} = \begin{pmatrix} k_{11} & k_{12} & k_{13} & k_{14} & k_{15} & k_{16} \\ k_{21} & k_{22} & k_{23} & k_{24} & k_{25} & k_{26} \\ k_{31} & k_{32} & k_{33} & k_{34} & k_{35} & k_{36} \\ k_{41} & k_{42} & k_{43} & k_{45} & k_{45} & k_{46} \\ k_{51} & k_{52} & k_{53} & k_{54} & k_{55} & k_{56} \\ k_{61} & k_{62} & k_{63} & k_{64} & k_{65} & k_{66} \end{pmatrix} \begin{pmatrix} \gamma_x \\ \gamma_y \\ \varepsilon_z \\ \kappa_x \\ \kappa_y \\ \kappa_z \end{pmatrix}$$

Equation 4.17

This relation between the forces/moments and strains in the xyz-coordinate system can be transformed to an arbitrary location (x'y'z'-coordinate system). The relation between the forces/moments in the xyz-coordinate system and the forces'/moments' in the x'y'z'-coordinate system can be illustrated as:

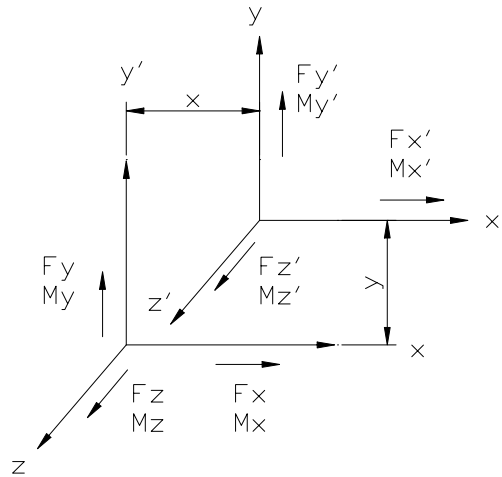


Figure 4.1.4 – Translations of coordinates

The relation between the forces'/moments' in the x'y'z'-coordinate and strains' can be written as:

$$\begin{pmatrix} F'_x \\ F'_y \\ F'_z \\ M'_x + y \cdot F'_z \\ M'_y - x \cdot F'_z \\ M'_z - y \cdot F'_x + x \cdot F'_y \end{pmatrix} = k \cdot \begin{pmatrix} \gamma'_x + y \cdot \kappa'_x \\ \gamma'_y - x \cdot \kappa'_y \\ \varepsilon'_z - y \cdot \kappa'_x + x \cdot \kappa'_y \\ \kappa'_x \\ \kappa'_y \\ \kappa'_z \end{pmatrix}$$

Equation 4.18

By adding and subtracting columns and rows, then Malcolm and Laird determined the following translations transformations matrix:

$$\begin{pmatrix} F'_x \\ F'_y \\ F'_z \\ M'_x \\ M'_y \\ M'_z \end{pmatrix} = k' \cdot \begin{pmatrix} \gamma'_x \\ \gamma'_y \\ \varepsilon'_z \\ \kappa'_x \\ \kappa'_y \\ \kappa'_z \end{pmatrix} \quad k' = T_{\text{trans}} = \begin{pmatrix} T_1 & T_2 \\ T_3 & T_4 \end{pmatrix}$$

Equation 4.19

Where T_1 , T_2 , T_3 and T_4 are given by the following:

$$\begin{aligned} T_1 &= \begin{pmatrix} k_{11} & k_{12} & k_{13} \\ k_{21} & k_{22} & k_{23} \\ k_{31} & k_{32} & k_{33} \end{pmatrix} \quad T_2 = \begin{pmatrix} k_{14} - y \cdot k_{13} & k_{15} + x \cdot k_{13} & k_{16} + y \cdot k_{11} - x \cdot k_{12} \\ k_{24} - y \cdot k_{23} & k_{25} + x \cdot k_{23} & k_{26} + y \cdot k_{21} - x \cdot k_{22} \\ k_{34} - y \cdot k_{33} & k_{35} + x \cdot k_{33} & k_{36} + y \cdot k_{31} - x \cdot k_{32} \end{pmatrix} \\ T_3 &= \begin{pmatrix} k_{41} - y \cdot k_{31} & k_{42} - y \cdot k_{32} & k_{43} - y \cdot k_{33} \\ k_{51} + x \cdot k_{31} & k_{52} + x \cdot k_{32} & k_{53} + x \cdot k_{33} \\ k_{61} + x \cdot k_{11} - y \cdot k_{21} & k_{62} + y \cdot k_{12} - x \cdot k_{22} & k_{63} + y \cdot k_{13} - x \cdot k_{23} \end{pmatrix} \\ T_4 &= \begin{bmatrix} k_{44} - y \cdot k_{43} - y \cdot (k_{34} - y \cdot k_{33}) & k_{45} + x \cdot k_{43} - y \cdot (k_{35} + x \cdot k_{33}) & \begin{bmatrix} (k_{46} + y \cdot k_{41} - x \cdot k_{42}) \dots \\ + y \cdot (k_{36} + y \cdot k_{31} - x \cdot k_{32}) \cdot -1 \end{bmatrix} \\ k_{54} - y \cdot k_{53} + x \cdot (k_{34} - y \cdot k_{33}) & k_{55} + x \cdot k_{53} + x \cdot (k_{35} + x \cdot k_{33}) & \begin{bmatrix} (k_{56} + y \cdot k_{51} - x \cdot k_{52}) \dots \\ + x \cdot (k_{36} + y \cdot k_{31} - x \cdot k_{32}) \end{bmatrix} \\ \begin{bmatrix} k_{64} - y \cdot k_{63} \dots \\ + y \cdot (k_{14} - y \cdot k_{13}) - x \cdot (k_{24} - y \cdot k_{23}) \end{bmatrix} & \begin{bmatrix} k_{65} + x \cdot k_{63} \dots \\ + y \cdot (k_{15} + x \cdot k_{13}) - x \cdot (k_{25} + x \cdot k_{23}) \end{bmatrix} & \begin{bmatrix} (k_{66} + y \cdot k_{61} - x \cdot k_{62}) \dots \\ + y \cdot (k_{16} + y \cdot k_{11} - x \cdot k_{12}) \dots \\ + x \cdot (k_{26} + y \cdot k_{21} - x \cdot k_{22}) \cdot -1 \end{bmatrix} \end{bmatrix} \end{aligned}$$

Equation 4.20

The constitutive matrix k can also be rotated to an arbitrary orientation by using the following rotation transformation matrix:

$$R = \begin{pmatrix} \cos(\phi) & \sin(\phi) & 0 & 0 & 0 & 0 \\ -\sin(\phi) & \cos(\phi) & 0 & 0 & 0 & 0 \\ 0 & 0 & 1 & 0 & 0 & 0 \\ 0 & 0 & 0 & \cos(\phi) & \sin(\phi) & 0 \\ 0 & 0 & 0 & -\sin(\phi) & \cos(\phi) & 0 \\ 0 & 0 & 0 & 0 & 0 & 1 \end{pmatrix} \quad k' = R \cdot k \cdot R^T$$

Equation 4.21

4.2. Insight into the 3D Timoshenko model

The theory in this chapter is based on the book; *Nonlinear composite beam theory* by D. Hodges [8]. The cross sectional constitutive law in terms of the stiffness coefficients can be written as:

$$\begin{pmatrix} F \\ M \end{pmatrix} = \begin{pmatrix} A & B \\ B^T & D \end{pmatrix} \cdot \begin{pmatrix} \gamma \\ \kappa \end{pmatrix}$$

Where A, B and D are 3x3 cross-sectional stiffness sub-matrices of the 6x6 constitutive matrix (k) (these matrices are not same as found in lamination theory). The inverse, in terms of cross-sectional flexibility matrices, can be expressed as:

$$\begin{pmatrix} \gamma \\ \kappa \end{pmatrix} = \begin{pmatrix} R & Z \\ Z^T & T \end{pmatrix} \cdot \begin{pmatrix} F \\ M \end{pmatrix}$$

Where R, Z and T are 3x3 cross-sectional flexibility sub-matrices of the 6x6 flexibility matrix (s).

For an isotropic prismatic beam, with a double symmetric cross section and the reference coordinate system located and orientated as the elastic center (for an isotropic beam with a double symmetric cross section is the elastic center and the shear center located at the same point/location) will there be no off diagonal terms. The constitutive matrix for this case:

$$k = \begin{pmatrix} GA \cdot k_x & 0 & 0 & 0 & 0 & 0 \\ 0 & GA \cdot k_y & 0 & 0 & 0 & 0 \\ 0 & 0 & AE & 0 & 0 & 0 \\ 0 & 0 & 0 & EI_x & 0 & 0 \\ 0 & 0 & 0 & 0 & EI_y & 0 \\ 0 & 0 & 0 & 0 & 0 & GJ \end{pmatrix}$$

The shear center and elastic center will not have the same location if the beam is not double symmetric. If the reference coordinate system is not located in the shear center or the elastic center and if the reference coordinate system is not rotated as the principle axes then there will be some off-diagonal terms. The offset from the elastic center (x_{ec} , y_{ec}) and the shear center (x_{sc} , y_{sc}) forms the matrix (z):

$$z = \begin{pmatrix} 0 & 0 & y_{sc} \\ 0 & 0 & -x_{sc} \\ -y_{ec} & x_{ec} & 0 \end{pmatrix} \quad A = \begin{pmatrix} GA \cdot k_{xx} & GA \cdot k_{xy} & 0 \\ GA \cdot k_{xy} & GA \cdot k_{yy} & 0 \\ 0 & 0 & AE \end{pmatrix}$$

The off-diagonal terms in the matrix (A) are due to the rotation of the cross section (reference coordinate system).

The relation between the B- and A- matrix can be written as:

$$B = A \cdot z = \begin{pmatrix} 0 & 0 & GA \cdot k_{xx} y_{sc} - GA \cdot k_{xy} x_{sc} \\ 0 & 0 & GA \cdot k_{xy} y_{sc} - GA \cdot k_{yy} x_{sc} \\ -AE \cdot y_{ec} & AE \cdot x_{ec} & 0 \end{pmatrix}$$

According to D. H. Hodges, it can be shown, based on forming a column matrix $M_c = T^{-1} \cdot \kappa$ of the torsional moment at the shear center and the bending moment at the elastic center, that $M_c = M - z^T \cdot F$ and furthermore that:

$$R = A^{-1} + z \cdot T \cdot z^T \quad Z = -z \cdot T \quad D = T^{-1} + z^T \cdot A \cdot z$$

The equations for R, Z and D are valid even if A and T are fully populated, as long as B has the form $B = A \cdot z$.

The equations for A, B, R, Z and D was tested with the analytical BPE-model described in chapter 4.4 and compare with the analytical obtained constitutive matrix (k) and flexibility matrix (s). All equations proved to be right, as expected.

The constitutive matrix k can be fully populated for a composite beam. Some of the couplings will be described in the following. All terms which are not placed in the diagonal of the constitutive matrix are in theory couplings. These couplings can come from geometry and the lay-up of beam structure:

$$\begin{pmatrix} F_x \\ F_y \\ F_z \\ M_x \\ M_y \\ M_z \end{pmatrix} = \begin{pmatrix} k_{11} & k_{12} & k_{13} & k_{14} & k_{15} & k_{16} \\ k_{21} & k_{22} & k_{23} & k_{24} & k_{25} & k_{26} \\ k_{31} & k_{32} & k_{33} & k_{34} & k_{35} & k_{36} \\ k_{41} & k_{42} & k_{43} & k_{44} & k_{45} & k_{46} \\ k_{51} & k_{52} & k_{53} & k_{54} & k_{55} & k_{56} \\ k_{61} & k_{62} & k_{63} & k_{64} & k_{65} & k_{66} \end{pmatrix} \cdot \begin{pmatrix} \gamma_x \\ \gamma_y \\ \varepsilon_z \\ \kappa_x \\ \kappa_y \\ \kappa_z \end{pmatrix}$$

Extension-bend couplings

The extension-bend couplings (shown with red boxes) have been described above (see equation chdfh). The couplings are introduced because the reference coordinate system is not located at the elastic center. An axial strain ε_z will therefore result in an axial force F_z and in one or two bending moments (M_x and M_y). A curvature (κ_x or κ_y) will result in an axial force F_z and in a bending moment (M_x or M_y).

Shear-twist couplings

The shear-twist couplings (shown with black boxes) have been described above (see equation hsdhw). The couplings are introduced because the reference coordinate system is not located at the shear center. A lateral strain (γ_x or γ_y) will therefore result in a torsional moment (M_z) and a twist rate (κ_z) will result in one or two lateral forces (F_x and F_y).

Shear-shear couplings

The shear-shear couplings (shown with yellow boxes) create a coupling between the two lateral forces (F_x and F_y). A shear strain will result in two lateral forces if the constitutive matrix has a shear-shear coupling.

The shear-shear couplings are introduced because the orientation of the reference coordinate system is not orientated according to the principle axes.

Bend-bend couplings

The bend-bend couplings (shown with green boxes) create a coupling between the two bending moments (M_x and M_y). A bending curvature will result in two bending moments if the constitutive matrix has a bend-bend coupling.

The bend-bend couplings can be introduced because the orientation of the reference coordinate system is not orientated according to the principle axes or if the reference coordinate system is not located at the elastic center.

Bend-twist couplings

The bend-twist couplings (shown with blue boxes) create couplings between bending and torsion. A bending curvature will result in a bending moment but also a torsional moment if the constitutive matrix has a bend-twist coupling.

The bend-twist coupling is created by the material properties. Off axis laminates will create this coupling.

Extension-twist coupling

The extension-twist coupling (shown with brown boxes) creates a coupling between extension and twist. An axial strain will result in a torsional moment if the constitutive matrix has an extension-twist coupling and twist rate will result in an axial force.

The extension-twist coupling is created by the material properties.

4.3. Extraction of the equivalent beam properties for a 4x4 matrix

In this work, a simpler beam model has also been used. This model is not described by Malcolm and Laird. The model is a 4x4 constitutive matrix, which do not take the location of the shear center and shear deformation into consideration. The relation between force/moments and strains can be written as:

$$\begin{pmatrix} F_z \\ M_x \\ M_y \\ M_z \end{pmatrix} = \begin{pmatrix} k_{11} & k_{12} & k_{13} & k_{14} \\ k_{21} & k_{22} & k_{23} & k_{24} \\ k_{31} & k_{32} & k_{33} & k_{34} \\ k_{41} & k_{42} & k_{43} & k_{44} \end{pmatrix} \begin{pmatrix} \varepsilon_z \\ \kappa_x \\ \kappa_y \\ \kappa_z \end{pmatrix}$$

Only four load cases are required in order to determine the stiffness matrix K. The loads are an axial force (F_z), two pure bending moments (M_x and M_y) and finally a torsional moment (M_z). The relative displacements and rotations (u_z , r_x , r_y and r_z) of the four load cases are calculated according to *Equation 4.1*. The stiffness matrix is given as:

$$K = F \cdot U^{-1} \quad \text{where} \quad F = \begin{pmatrix} F_z & 0 & 0 & 0 \\ 0 & M_x & 0 & 0 \\ 0 & 0 & M_y & 0 \\ 0 & 0 & 0 & M_z \end{pmatrix}$$

Equation 4.22

U is the relative displacement matrix for a given beam element (column 1 from load case 1 and column 2 is from load case 2 ...etc.) and K is the stiffness matrix for that element.

The constitutive matrix k is determined by:

$$s = K^{-1} \cdot H^{-1} \quad k = s^{-1} \quad H = \begin{pmatrix} L & 0 & 0 & 0 \\ 0 & L & 0 & 0 \\ 0 & 0 & L & 0 \\ 0 & 0 & 0 & L \end{pmatrix}$$

Equation 4.23

The terms in the diagonal in the H-matrix is the length of a given beam element and k is the constitutive matrix for that element.

The constitutive matrix k can also be determined in an alternative way (According to D. H.Hodges), which requires that one known the 6x6 constitutive matrix from *Equation 4.17*. The constitutive matrix in the 4x4 model is obtained by striking the first and second columns and rows from the inverse of the 6x6 model and inverting the resulting 4x4 matrix. This is illustrated below:

$$\begin{pmatrix} \gamma_x \\ \gamma_y \\ \varepsilon_z \\ \kappa_x \\ \kappa_y \\ \kappa_z \end{pmatrix} = \begin{pmatrix} s_{11} & s_{12} & s_{13} & s_{14} & s_{15} & s_{16} \\ s_{21} & s_{22} & s_{23} & s_{24} & s_{25} & s_{26} \\ s_{31} & s_{32} & s_{33} & s_{34} & s_{35} & s_{36} \\ s_{41} & s_{42} & s_{43} & s_{44} & s_{45} & s_{46} \\ s_{51} & s_{52} & s_{53} & s_{54} & s_{55} & s_{56} \\ s_{61} & s_{62} & s_{63} & s_{64} & s_{65} & s_{66} \end{pmatrix} \begin{pmatrix} F_x \\ F_y \\ F_z \\ M_x \\ M_y \\ M_z \end{pmatrix} \quad k_{4 \times 4} = \begin{pmatrix} s_{33} & s_{34} & s_{35} & s_{36} \\ s_{43} & s_{44} & s_{45} & s_{46} \\ s_{53} & s_{54} & s_{55} & s_{56} \\ s_{63} & s_{64} & s_{65} & s_{66} \end{pmatrix}^{-1}$$

Equation 4.24

The relation between the forces'/moments' in the x'y'z'-coordinate and strains' can be written as:

$$\begin{pmatrix} F'_z \\ M'_x \\ M'_y \\ M'_z \end{pmatrix} = k' \cdot \begin{pmatrix} \varepsilon'_z \\ \kappa'_x \\ \kappa'_y \\ \kappa'_z \end{pmatrix}$$

Equation 4.25

The transformed matrix k' is:

$$k' = T_{\text{trans}} = \begin{bmatrix} k_{11} & (k_{12} - \nu \cdot k_{11}) & (k_{13} + \mu \cdot k_{11}) & k_{14} \\ (k_{21} - \nu \cdot k_{11}) & [k_{22} + \nu \cdot (\nu \cdot k_{11} - k_{21} - k_{12})] & (k_{23} + \mu \cdot k_{21} - \nu \cdot k_{13} - \nu \cdot \mu \cdot k_{11}) & (k_{24} - \nu \cdot k_{14}) \\ (k_{31} + \mu \cdot k_{11}) & (k_{32} + \mu \cdot k_{12} - \nu \cdot k_{31} - \mu \cdot \nu \cdot k_{11}) & [k_{33} + \mu \cdot (k_{31} + k_{13} + \mu \cdot k_{11})] & (k_{34} + \mu \cdot k_{14}) \\ k_{41} & (k_{42} - \nu \cdot k_{41}) & (k_{43} + \mu \cdot k_{41}) & k_{44} \end{bmatrix}$$

Equation 4.26

The transformation (rotation) matrix is just a sub-matrix of the 6x6 transformation (rotation) matrix (see Equation 4.21). The rotated constitutive matrix k' is determined by:

$$k' = r \cdot k \cdot r^T \quad r = \begin{pmatrix} 1 & 0 & 0 & 0 \\ 0 & \cos(\phi) & \sin(\phi) & 0 \\ 0 & -\sin(\phi) & \cos(\phi) & 0 \\ 0 & 0 & 0 & 1 \end{pmatrix}$$

The elastic center is determined by (same theory as for 6x6 model):

$$x_{ec} = -\frac{k_{31}}{k_{11}} \quad y_{ec_i} = \frac{k_{21}}{k_{11}}$$

Equation 4.27

The rotation of the principle axes are determined by:

$$\phi = \operatorname{atan}\left(\frac{2 \cdot s_{23}}{s_{22} - s_{33}}\right) \cdot \frac{1}{2}$$

Equation 4.28

The rotation/orientation of the principle axes are defined in the following way: An applied moment will result in a curvature above that axis and zero curvature about the perpendicular axis.

4.4. Analytical validation of the Beam Property Extraction (BPE) method

An analytical 3D model was created to validate the BPE-method which is described in the paper *Identification and Use of Blade Physical Properties* by David J. Malcolm and Daniel L. Laid [2]. This analytical model was chosen to be a 20meter long cantilever steel beam, with a rectangular cross section. The reason for choosing a beam with this geometry was that the beam properties were reasonable simple to determine by hand calculations.

In *Figure 4.4.1* is the geometry of the beam model illustrated. The rectangular tube was divided into five equivalent beam elements. The reference coordinate system was moved 250mm in the x-direction and -62.5mm in the y-direction. The coordinate system was then rotated -10° about the z-axis (this is the same as rotating the tube/cross-section +10° about the z-axis). The three relative displacements and rotations were calculated with respect to this reference coordinate system. The loads were also applied in this reference.

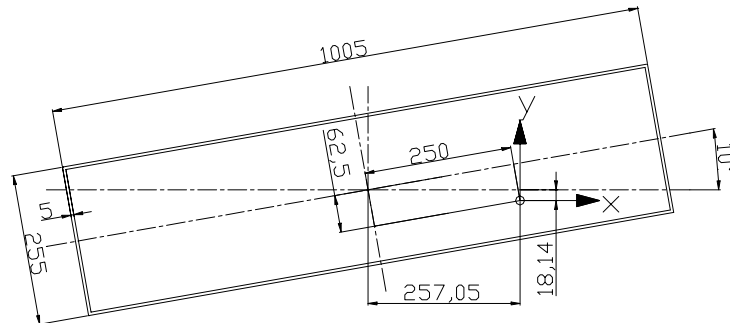


Figure 4.4.1 – Sketch of the analytical model.

The analytical validation of the BPE-method works by calculating the analytical deflections and rotations at the reference coordinate system and then see if this results in the correct analytical constitutive matrix (k), and by that also validating the methods for determining the location and orientation of the principle axes and the location of the elastic center and shear center.

The deflections of the reference are determined by calculating the deflections of the elastic axis (which also is the shear center in this case).

By performing some transformations, one can determine the deflections according to the reference coordinate system (the rotations at the elastic axis is the same as the rotations at the reference coordinate system since the deformed cross section is assumed to remain plane).

The distance from the reference coordinate system to the elastic axis is calculated:

$$\begin{aligned} \text{dist}_x &= 250\text{mm} & \text{dist}_y &= -62.5\text{mm} & \phi &= 10\text{deg} \\ \text{dist}'_x &= \text{dist}_x \cdot \cos(\phi) - \text{dist}_y \cdot \sin(\phi) & \text{dist}'_x &= 257.05\text{mm} \\ \text{dist}'_y &= \text{dist}_x \cdot \sin(\phi) + \text{dist}_y \cdot \cos(\phi) & \text{dist}'_y &= -18.14\text{mm} \end{aligned}$$

As stated before, the stiffness matrix is determined by performing six load cases (the load cases are the following: F_x , F_y , F_z , M_x , M_y and M_z). The three forces (F_x , F_y , F_z) results in the following internal moments:

$$\begin{aligned} M_{y_Fx}(z) &= F_x \cdot (L - z) & T_{z_Fx} &= -F_x \cdot \text{dist}'_y & (\text{moments from } F_x) \\ M_{x_Fy}(z) &= -F_y \cdot (L - z) & T_{z_Fy} &= F_y \cdot \text{dist}'_x & (\text{moments from } F_y) \\ M_{x_Fz} &= F_z \cdot \text{dist}'_y & M_{y_Fz} &= -F_z \cdot \text{dist}'_x & (\text{moments from } F_z) \end{aligned}$$

4.4.1. Cross sectional properties for the analytical model

One of the first steps in creating the analytical model is to calculate the beam properties. The **moments of inertia** (I_{xx} and I_{yy}) are calculated for a rotation angle equal to zero.

The two area moments of inertia are used to create a 2x2 symmetric inertia matrix (I). By using the transformation matrix (R) then it is possible to determine the inertia matrix as a function of ϕ . The rotated inertia matrix is called (I') and the inverse of this matrix is called (I'_{inv}):

$$I = \begin{pmatrix} I_{xx} & 0 \\ 0 & I_{yy} \end{pmatrix} \quad R = \begin{pmatrix} \cos(\phi) & -\sin(\phi) \\ \sin(\phi) & \cos(\phi) \end{pmatrix} \quad I' = R \cdot I \cdot R^T \quad I' = \begin{pmatrix} I'_{xx} & I'_{xy} \\ I'_{xy} & I'_{yy} \end{pmatrix} \quad I'_{\text{inv}} = I'^{-1}$$

Equation 4.29

The **sectional torsion factor** is calculated by (the equation for J is taken from [6]):

$$J = \frac{2 \cdot t^2 \cdot b^2 \cdot h^2}{b \cdot t + h \cdot t}$$

Equation 4.30

t is the wall thickness, b is width of the tube and h is the height of the tube.

The **shear deformations factors** are calculated by (the equation for k_y and k_x is taken from [7]):

$$k = \frac{10 \cdot (1 + \nu) \cdot (1 + 3 \cdot m)^2}{(12 + 72 \cdot m + 150 \cdot m^2 + 90 \cdot m^3) + \nu \cdot (11 + 66 \cdot m + 135 \cdot m^2 + 90 \cdot m^3) + 10 \cdot n^2 \cdot [(3 + \nu) \cdot m + 3 \cdot m^2]}$$

$$m = \frac{b \cdot t_1}{h \cdot t} \quad n = \frac{b}{h}$$

Equation 4.31

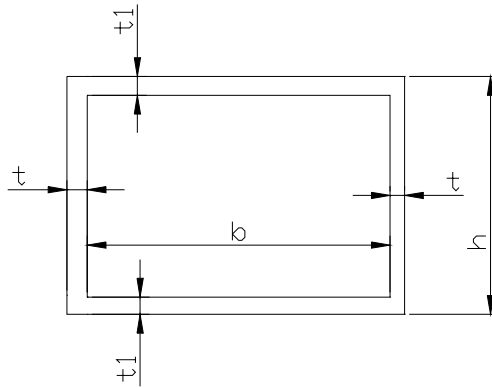


Figure 4.4.2 – Dimensions for calculating the shear correction factors

The two shear deformation factors (k_{xx} and k_{yy}) are calculated for a rotation angle equal to zero. It is possible to determine the 2x2 shear deformation matrix for any arbitrary rotation angle (φ) of cross section by using the rotation transformation matrix. The rotated shear deformation factor matrix is called (k'_s) and the inverse of this matrix is called (k'_{s_inv}):

$$k_s = \begin{pmatrix} k_{xx} & 0 \\ 0 & k_{yy} \end{pmatrix} \quad k'_s = R \cdot k_s \cdot R^T \quad k'_s = \begin{pmatrix} k'_{xx} & k'_{xy} \\ k'_{xy} & k'_{yy} \end{pmatrix} \quad k'_{s_inv} = k'^{-1}$$

Equation 4.32

It is now possible to calculate the three deflections and rotations of the elastic axis. These results are then used to calculate the deflections and rotations of the reference. This is done by using a transformation procedure (this will be illustrated later).

The next chapter illustrates how the deflections and rotations for the six load cases are calculated at the elastic axis and how these results are transformed to the reference coordinate system.

4.4.2. The six load cases for the analytical model

The BPE-method works by performing six different load cases. These six different load cases are performed by applying the loads at the tip end of the beam. The six load cases involves three forces (F_x , F_y , F_z) and three moments (M_x , M_y , M_z).

Load case $F_x(1)$

The transverse force (F_x) results in a bending moment above the y-axis ($M_{y_{Fx}}$) and a torsional moment ($T_{z_{Fx}}$). The load case is illustrated below.

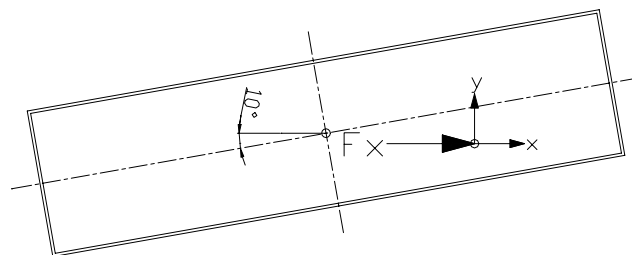


Figure 4.4.3 – Load case $F_x(1)$

The load results in the following deflections and rotations of the elastic axis:

$$\begin{aligned}
 u_{x_Fx}(z) &= \frac{1}{E} \cdot I'_{\text{inv}2,2} \cdot \int_0^z \int_0^z M_{y_Fx}(z) dz dz + \int_0^z \frac{F_x}{GA} \cdot k'_{\text{inv}1,1} dz & \theta_{y_Fx}(z) &= \frac{1}{E} \cdot I'_{\text{inv}2,2} \cdot \int_0^z M_{y_Fx}(z) dz \\
 u_{y_Fx}(z) &= -\frac{1}{E} \cdot I'_{\text{inv}1,2} \cdot \int_0^z \int_0^z M_{y_Fx}(z) dz dz + \int_0^z \frac{F_x}{GA} \cdot k'_{\text{inv}1,2} dz & \theta_{x_Fx}(z) &= \frac{1}{E} \cdot I'_{\text{inv}1,2} \cdot \int_0^z M_{y_Fx}(z) dz \\
 \theta_{z_Fx}(z) &= \frac{T_{z_Fx} z}{GJ}
 \end{aligned}$$

Equation 4.33

$u_{x_Fx}(z)$ and $u_{y_Fx}(z)$ are the deflections in the x- and y-direction. $\theta_{x_Fx}(z)$ and $\theta_{y_Fx}(z)$ are the bending slopes about the x- and y-axis. $I'_{\text{inv}2,2}$ is equal to $I'_{\text{inv}yy}$, $I'_{\text{inv}1,2}$ is equal to $I'_{\text{inv}xy}$ (the same goes for $k'_{\text{inv}22}$ and $k'_{\text{inv}12}$).

The deflections and rotations are now calculated at the elastic axis and then assembled in a displacements vector:

$$u1 = \begin{pmatrix} u_{x_Fx}(z) & u_{y_Fx}(z) & 0 & \theta_{x_Fx}(z) & \theta_{y_Fx}(z) & \theta_{z_Fx}(z) \end{pmatrix}^T$$

The deflections are determined at the reference coordinate system by performing the following transformation:

$$R_z = \begin{pmatrix} \cos(\theta_z) & -\sin(\theta_z) & 0 \\ \sin(\theta_z) & \cos(\theta_z) & 0 \\ 0 & 0 & 1 \end{pmatrix} \quad R_y = \begin{pmatrix} \cos(\theta_y) & 0 & \sin(\theta_y) \\ 0 & 1 & 0 \\ -\sin(\theta_y) & 0 & \cos(\theta_y) \end{pmatrix} \quad R_x = \begin{pmatrix} 1 & 0 & 0 \\ 0 & \cos(\theta_x) & -\sin(\theta_x) \\ 0 & \sin(\theta_x) & \cos(\theta_x) \end{pmatrix} \quad R_{zyx} = R_z \cdot R_y \cdot R_x$$

$$p_{\text{neutral}} = \begin{pmatrix} u_x & u_y & u_z \end{pmatrix}^T \quad p_{\text{dist}} = \begin{pmatrix} \text{dist}'_x & \text{dist}'_y & 0 \end{pmatrix}^T \quad \Delta p = R_{zyx} p_{\text{dist}} - p_{\text{dist}} \quad p_{\text{ref}} = p_{\text{neutral}} + \Delta p$$

Equation 4.34

The rotation transformation matrix (R_{zyx}) is only valid for small rotations angles. It is therefore very important that the forces and moments used in the analytical model are very small.

The new displacements vector for load case (F_x), at the reference coordinate system is:

$$u1_{\text{ref}} = \begin{pmatrix} p_{\text{ref}1} & p_{\text{ref}2} & p_{\text{ref}3} & \theta_x & \theta_y & \theta_z \end{pmatrix}^T$$

The same transformation method for determining the displacements vector at the reference coordinate system is used for all six load cases.

Load case F_y (2)

The transverse force (F_y) results in a bending moment about the x-axis (M_{x_Fy}) and a torsional moment (T_{z_Fy}). The load case is illustrated below:

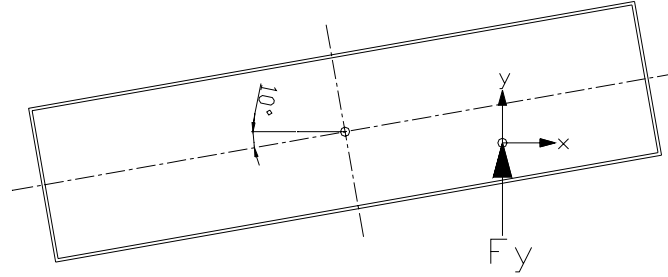


Figure 4.4.4 – Load case F_y (2)

The load case results in the following deflections and rotations of the elastic axis.

$$\begin{aligned}
 u_{x_Fy}(z) &= \frac{1}{E} \cdot I'_{inv1,2} \cdot \int_0^z \int_0^z M_{x_Fy}(z) dz dz + \int_0^z \frac{F_y}{G \cdot A} \cdot k'_{inv1,2} dz & \theta_{y_Fy}(z) &= \frac{1}{E} \cdot I'_{inv1,2} \cdot \int_0^z M_{x_Fy}(z) dz \\
 u_{y_Fy}(z) &= -\frac{1}{E} \cdot I'_{inv1,1} \cdot \int_0^z \int_0^z M_{x_Fy}(z) dz dz + \int_0^z \frac{F_y}{G \cdot A} \cdot k'_{inv2,2} dz & \theta_{x_Fy}(z) &= \frac{1}{E} \cdot I'_{inv1,1} \cdot \int_0^z M_{x_Fy}(z) dz \\
 \theta_{z_Fy}(z) &= \frac{T_{z_Fy} \cdot z}{G \cdot J}
 \end{aligned}$$

Equation 4.35

The deflections and rotations are now calculated at the elastic axis and then assembled in a displacements vector:

$$u2 = \begin{pmatrix} u_{x_Fy}(z) & u_{y_Fy}(z) & 0 & \theta_{x_Fy}(z) & \theta_{y_Fy}(z) & \theta_{z_Fy}(z) \end{pmatrix}^T$$

The same transformation method as illustrated for load case F_x (1) is used to determine the displacements vector at the reference coordinate system.

Load case F_z (3)

The axial force (F_z) results in two bending moments (M_{x_Fz} and M_{y_Fz}) about the x- and y-axis. The load case is illustrated below:

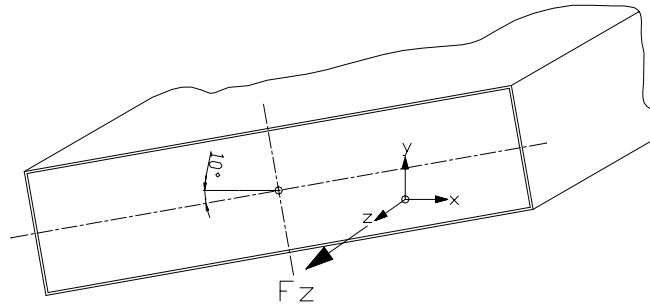


Figure 4.4.5- Load case F_z (3)

The load case results in the following deflections and rotations of the elastic axis:

$$\begin{aligned}
 u_{x_Fz}(z) &= \frac{1}{E} \cdot I'_{inv2,2} \cdot \int_0^z \int_0^z M_{y_Fz} dz dz + \frac{1}{E} \cdot I'_{inv1,2} \cdot \int_0^z \int_0^z M_{x_Fz} dz dz \\
 u_{y_Fz}(z) &= -\frac{1}{E} \cdot I'_{inv1,1} \cdot \int_0^z \int_0^z M_{x_Fz} dz dz - \frac{1}{E} \cdot I'_{inv1,2} \cdot \int_0^z \int_0^z M_{y_Fz} dz dz \quad u_{z_Fz}(z) = \frac{F_z \cdot z}{A \cdot E} \\
 \theta_{x_Fz}(z) &= \frac{1}{E} \cdot I'_{inv1,1} \cdot \int_0^z M_{x_Fz} dz + \frac{1}{E} \cdot I'_{inv1,2} \cdot \int_0^z M_{y_Fz} dz \\
 \theta_{y_Fz}(z) &= \frac{1}{E} \cdot I'_{inv2,2} \cdot \int_0^z M_{y_Fz} dz + \frac{1}{E} \cdot I'_{inv1,2} \cdot \int_0^z M_{x_Fz} dz
 \end{aligned}$$

Equation 4.36

The deflections and rotations are now calculated at the elastic axis and then assembled in a displacements vector:

$$u3 = \left(u_{x_Fz}(z) \quad u_{y_Fz}(z) \quad u_{z_Fz}(z) \quad \theta_{x_Fz}(z) \quad \theta_{y_Fz}(z) \quad 0 \right)^T$$

The same transformation method as illustrated for load case Fx (1) is used to determine the displacements vector at the reference coordinate system.

Load case M_x (4)

The pure bending moment about the x-axis is illustrated below:

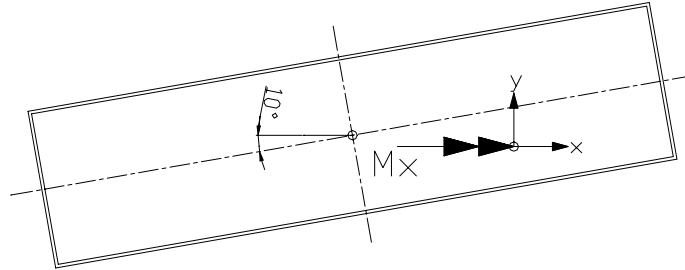


Figure 4.4.6 – Load case M_x (4)

The load case results in the following deflections and rotations of the elastic axis:

$$\begin{aligned}
 u_{x_Mx}(z) &= \frac{1}{E} \cdot I'_{inv1,2} \cdot \int_0^z \int_0^z M_x dz dz & \theta_{y_Mx}(z) &= \frac{1}{E} \cdot I'_{inv1,2} \cdot \int_0^z M_x dz \\
 u_{y_Mx}(z) &= -\frac{1}{E} \cdot I'_{inv1,1} \cdot \int_0^z \int_0^z M_x dz dz & \theta_{x_Mx}(z) &= \frac{1}{E} \cdot I'_{inv1,1} \cdot \int_0^z M_x dz
 \end{aligned}$$

Equation 4.37

The deflections and rotations are now calculated at the elastic axis and then assembled in a displacements vector:

$$u4 = \begin{pmatrix} u_{x_Mx}(z) & u_{y_Mx}(z) & 0 & \theta_{x_Mx}(z) & \theta_{y_Mx}(z) & 0 \end{pmatrix}^T$$

The same transformation method as illustrated for load case Fx is used to determine the displacements vector at the reference coordinate system.

Load case M_y (5)

The pure bending moment above the y-axis is illustrated below:

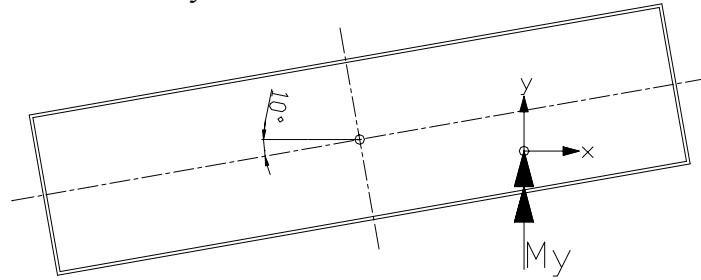


Figure 4.4.7 – Load case M_y (5)

The load case results in the following deflections and rotations of the elastic axis:

$$\begin{aligned} u_{x_My}(z) &= \frac{1}{E} \cdot I'_{inv_{2,2}} \cdot \int_0^z \int_0^z M_y dz dz & \theta_{y_My}(z) &= \frac{1}{E} \cdot I'_{inv_{2,2}} \cdot \int_0^z M_y dz \\ u_{y_My}(z) &= -\frac{1}{E} \cdot I'_{inv_{1,2}} \cdot \int_0^z \int_0^z M_y dz dz & \theta_{x_My}(z) &= \frac{1}{E} \cdot I'_{inv_{1,2}} \cdot \int_0^z M_y dz \end{aligned}$$

Equation 4.38

The deflections and rotations are now calculated at the elastic axis and then assembled in a displacements vector:

$$u5 = \begin{pmatrix} u_{x_My}(z) & u_{y_My}(z) & 0 & \theta_{x_My}(z) & \theta_{y_My}(z) & 0 \end{pmatrix}^T$$

The same transformation method as illustrated for load case Fx (1) is used to determine the displacements vector at the reference coordinate system.

Load case M_z (6)

The torsional moment (M_z) is illustrated below:

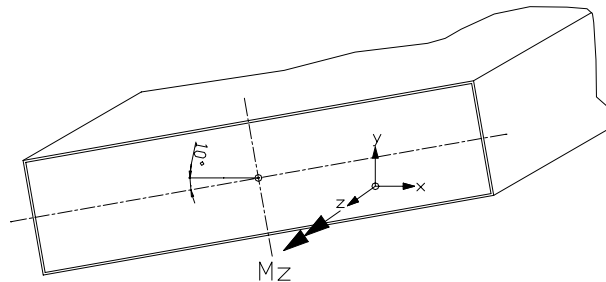


Figure 4.4.8 – Load case M_z (6)

The load case results in the following rotation of the elastic axis:

$$\theta_{z_Mz}(z) = \frac{M_{z_z}}{GJ}$$

The deflections and rotations are now calculated at the elastic axis and then assembled in a displacements vector:

$$u_6 = \begin{pmatrix} 0 & 0 & 0 & 0 & 0 & \theta_{z_Mz}(z) \end{pmatrix}^T$$

The same transformation method as illustrated for load case Fx (1) is used to determine the displacements vector at the reference coordinate system

Now, all the deflections and rotations are calculated at the five cross sections (the tube is divided into five beam elements). The deflections and rotations are zero at fixed end.

As stated before, the relative displacements and rotations are determined by:

$$\begin{aligned} u_{ix}^{rl} &= u_{ix}^r - u_{ix}^l - \theta_{iy}^l \cdot L & u_{iy}^{rl} &= u_{iy}^r - u_{iy}^l + \theta_{ix}^l \cdot L & u_{iz}^{rl} &= u_{iz}^r - u_{iz}^l \\ \theta_{ix}^{rl} &= \theta_{ix}^r - \theta_{ix}^l & \theta_{iy}^{rl} &= \theta_{iy}^r - \theta_{iy}^l & \theta_{iz}^{rl} &= \theta_{iz}^r - \theta_{iz}^l \end{aligned}$$

L_i is the length of element i .

As stated before, the quarter of the beam element Timoshenko stiffness matrices (K_i) is calculated in the following way (U_{ei} is the displacements matrix (6x6) and F_i is the load matrix (6x6)):

$$K_i = F_i \cdot (U_{ei})^{-1}$$

Note that the stiffness matrix is described with respect to the reference coordinate system and not the elastic axis. The constitutive matrix (k_i) is determined by solving the equation below via Lyapunov's method:

$$(K_i)^{-1} \cdot (Q_i)^{-1} = (k_i)^{-1} \cdot H_i \cdot (Q_i)^{-1} + E \cdot (k_i)^{-1}$$

The constitutive matrix is like the stiffness matrix described with respect to the reference coordinate system. One of the five (all identical in this case) analytical constitutive matrix (k) is shown below:

$$k_i = \begin{pmatrix} 747.4 & 112.3 & 0 & -0 & 0 & -42.4 \\ 112.3 & 130.5 & 0 & -0 & 0 & -35.6 \\ 0 & 0 & 2625 & 47.6 & 674.8 & -0 \\ 0 & -0 & 47.6 & 44.6 & -34.1 & 0 \\ 0 & 0 & 674.8 & -34.1 & 471.6 & -0 \\ -42.4 & -35.6 & -0 & 0 & -0 & 50.3 \end{pmatrix} \cdot 10^6 \quad s_i = (k_i)^{-1} \quad s_i = \begin{pmatrix} 1.5 & -1.2 & -0 & -0 & -0 & 0.4 \\ -1.2 & 10.4 & 0 & 0 & 0 & 6.4 \\ -0 & -0 & 0.7 & -1.6 & -1.1 & 0 \\ 0 & 0 & -1.6 & 27.4 & 4.3 & -0 \\ 0 & 0 & -1.1 & 4.3 & 4 & 0 \\ 0.4 & 6.4 & 0 & -0 & 0 & 24.8 \end{pmatrix}$$

The analytical constitutive matrix is symmetric as expected. The off diagonal terms are due to the location and rotation of the reference coordinate system. A more thorough description of these off axes terms will be presented later.

4.4.3. Analytical validation of the method for determining the elastic center

As stated before, the **elastic center** according to Malcolm and Laird is determined by:

$$x_{ec_i} = -\frac{(k_i)_{5,3}}{(k_i)_{3,3}} \quad y_{ec_i} = \frac{(k_i)_{4,3}}{(k_i)_{3,3}} \quad \Rightarrow \quad x_{ec_i} = -0.25705 \quad y_{ec_i} = 0.01814$$

The location of the elastic center calculated by this method is correct (x_{ec} [m] and y_{ec} [m] are the distances from the reference coordinate system to the elastic center).

4.4.4. Analytical validation of the method for determining the shear center

As stated before, the **shear center** according to Malcolm and Laird is determined by:

$$x_{sc_i} = \frac{(k_i)_{6,2}}{(k_i)_{2,2}} \quad y_{sc_i} = \frac{-(k_i)_{6,1}}{(k_i)_{1,1}} \quad \Rightarrow \quad x_{sc_i} = -0.27266 \quad y_{sc_i} = 0.05674$$

Since the location of the elastic center and the shear center is the same, then the result for the location of shear center determined by this method is not correct! (x_{sc} [m] and y_{sc} [m] are the distances from the reference coordinate system to the shear center).

Malcolm and Laird defines the shear center as the location on the cross section with the following properties: A lateral strain (γ_x) is imposed, will all other strains are zero and that restraints include a lateral force (F_x), through the shear center but zero additional torque (M_z):

$$F_x = k_{11} \cdot \gamma_x \quad M_z = -F_x \cdot y_{sc} = k_{61} \cdot \gamma_x \quad \Rightarrow \quad y_{sc} = \frac{-k_{61}}{k_{11}}$$

And similiary!

$$F_y = k_{22} \cdot \gamma_y \quad M_z = F_y \cdot x_{sc} = k_{62} \cdot \gamma_y \quad \Rightarrow \quad x_{sc} = \frac{k_{62}}{k_{22}}$$

These two equations are only correct if the orientation of the principle axes is identical to the orientation of the reference axes. If the orientation of the axes is not identical then the imposed lateral strain (γ_x) will result in two lateral forces (F_x) and (F_y). The lateral force (F_y) is due to the off axis term (k_{21}), which will be different from zero if the orientations are not identical. A lateral strain (γ_y) will similarly result in two lateral forces. This is illustrated below.

The lateral strain (γ_x) that is imposed result in two lateral forces (F_x) and (F_y), through the shear center but zero additional torsional moment (M_z):

$$F_x = k_{11} \cdot \gamma_x \quad F_y = k_{21} \cdot \gamma_x \quad M_z = -F_x \cdot y_{sc} + F_y \cdot x_{sh} = k_{61} \cdot \gamma_x \Rightarrow -k_{11} \cdot y_{sc} + k_{21} \cdot x_{sh} = k_{61} \quad \text{Equation 4.39}$$

The lateral strain (γ_y) that is imposed result in two lateral forces (F_x) and (F_y), through the shear center but zero additional torsional moment (M_z).

$$F_x = k_{12} \cdot \gamma_y \quad F_y = k_{22} \cdot \gamma_y \quad M_z = -F_x \cdot y_{sc} + F_y \cdot x_{sh} = k_{62} \cdot \gamma_y \Rightarrow -k_{12} \cdot y_{sc} + k_{22} \cdot x_{sh} = k_{62} \quad \text{Equation 4.40}$$

This gives two equations and two unknowns. The location to the shear center for any rotation angle (φ) can be found by:

$$x_{sc} = \frac{(k_{62} \cdot k_{11} - k_{12} \cdot k_{61})}{(-k_{12}^2 + k_{22} \cdot k_{11})} \quad y_{sc} = \frac{(-k_{61} \cdot k_{22} - k_{12} \cdot k_{62})}{(-k_{12}^2 + k_{22} \cdot k_{11})} \Rightarrow x_{sc_i} = -0.25705 \quad y_{sc_i} = 0.01814$$

$$\text{Equation 4.41}$$

Summary

The method for determine the shear center described by Malcolm and Laird is only valid if the reference coordinate system has the same orientation as the principle axes. The modified Equation 4.12 is valid for any arbitrary orientation of the reference coordinate system.

An alternative method for calculating the location of the shear center is described in [8].

It is assumed that the following relation between the strains and the forces is known:

$$\begin{pmatrix} F_x \\ F_y \\ F_z \\ M_x \\ M_y \\ M_z \end{pmatrix}_i = s_i \cdot \begin{pmatrix} \gamma_x \\ \gamma_y \\ \epsilon_z \\ \kappa_x \\ \kappa_y \\ \kappa_z \end{pmatrix}_i \Rightarrow \begin{pmatrix} \gamma_x \\ \gamma_y \\ \epsilon_z \\ \kappa_x \\ \kappa_y \\ \kappa_z \end{pmatrix}_i = \begin{pmatrix} s_{11} & s_{12} & s_{13} & s_{14} & s_{15} & s_{16} \\ s_{21} & s_{22} & s_{23} & s_{24} & s_{25} & s_{26} \\ s_{31} & s_{32} & s_{33} & s_{34} & s_{35} & s_{36} \\ s_{41} & s_{42} & s_{43} & s_{44} & s_{45} & s_{46} \\ s_{51} & s_{52} & s_{53} & s_{54} & s_{55} & s_{56} \\ s_{61} & s_{62} & s_{63} & s_{64} & s_{65} & s_{66} \end{pmatrix}_i \begin{pmatrix} F_x \\ F_y \\ F_z \\ M_x \\ M_y \\ M_z \end{pmatrix}_i$$

To obtain the shear center location, it is sufficient to assume that there are two transverse forces at the tip of a cantilever beam (F_x and F_y). The two forces will result in two bending moments (M_x and M_y) and a torsional moment (M_z):

$$M_x = -F_y \cdot (L - z) \quad M_y = F_x \cdot (L - z) \quad M_z = F_y \cdot x_{sc} - F_x \cdot y_{sc}$$

According to the definition of the shear center, one needs to find (x_{sc}) and (y_{sc}) in order to locate a position where an application of the transverse forces result in zero twist, that is ($\kappa_z = 0$).

This can be written in terms of loading and stiffness as:

$$\begin{aligned}\kappa_z = 0 &= F_x \cdot s_{61} + F_y \cdot s_{62} + M_x \cdot s_{64} + M_y \cdot s_{65} + M_z \cdot s_{66} \quad \Rightarrow \\ 0 &= F_x \cdot s_{61} + F_y \cdot s_{62} - F_y \cdot (L - z) \cdot s_{64} + F_x \cdot (L - z) \cdot s_{65} + (F_y \cdot x_{sc} - F_x \cdot y_{sc}) \cdot s_{66} \quad \Rightarrow \\ 0 &= F_x [s_{61} + (L - z) \cdot s_{65} - y_{sc} \cdot s_{66}] + F_y [s_{62} - (L - z) \cdot s_{64} + x_{sc} \cdot s_{66}]\end{aligned}$$

Since this equation is valid for any arbitrary (F_x and F_y), then the location of shear center can be obtained by:

$$\begin{aligned}0 &= s_{61} + (L - z) \cdot s_{65} - y_{sc} \cdot s_{66} \quad \Rightarrow \quad y_{sc} = \frac{s_{61}}{s_{66}} + \frac{s_{65}}{s_{66}} \cdot (L - z) \\ 0 &= s_{62} + (L - z) \cdot s_{64} - x_{sc} \cdot s_{66} \quad \Rightarrow \quad x_{sc} = \frac{s_{62}}{s_{66}} + \frac{s_{64}}{s_{66}} \cdot (L - z)\end{aligned}$$

Equation 4.42

This demonstrates that the position of the shear center varies linearly with respect to the axial coordinate and is therefore not a cross-sectional property for beams with bending-twist coupling (s_{64} is the flapwise bend-twist coupling and s_{65} is the edgewise bend-twist coupling).

However, if there is no bending-twist coupling, then the shear center becomes a cross-sectional property, and the use of the location of the shear center provides a reference line that decouples bending and twist, which makes it a popular choice for a reference.

One can modify the definition of the shear center for beams with bending-twist coupling (composite beams) by only considering the twist caused by the shear forces and excluding the twist produced by the bending moment (through the bending-twist coupling).

In such cases will the second term in *Equation 4.42* drop out, and the shear center becomes a cross-sectional property by this modified definition. The modified definition is shown below:

$$x_{sc} = \frac{s_{62}}{s_{66}} \quad y_{sc} = \frac{s_{61}}{s_{66}} \quad \Rightarrow \quad x_{sc_i} = -0.25705 \quad y_{sc_i} = 0.01814$$

Equation 4.43

The location of the shear center for the analytical model calculated by this method is correct.

Comment

All three methods for determine the shear center can be used but the method described by Malcolm and Laird is only valid if the reference coordinate system has the same orientation as the principle axes. The modified method (see *Equation 4.12*) and the method described by D. H. Hodges (see *Equation 4.43*) are valid for an arbitrary orientation of the reference coordinate system, which makes these methods more flexible.

4.4.5. Analytical validation of the method for determining the orientation of the principle axes

As stated before, the principle axis is defined by Malcolm and Laird as the direction about which an applied curvature will result in a moment about that axis and zero moment about the perpendicular axis. The rotation of the principle axis is given by:

$$\phi = \operatorname{atan}\left(\frac{2 \cdot k_{45}}{k_{44} - k_{55}}\right) \cdot \frac{1}{2} \Rightarrow \phi_i = 4.532 \text{deg}$$

Since the rotation of the reference coordinate system is 10° then the result is not correct.

The method described by Malcolm and Laid is only valid if the reference coordinate system is placed at the elastic axis (some times also referred to as the tension center). The terms (k_{44} , k_{45} , k_{55}) in the constitutive matrix are dependent of the location of the reference coordinate system. If the rotation of the reference coordinate system in the analytical model is set to zero, then will the term (k_{45}) only be equal to zero when the reference coordinate system has the same location as the elastic axis.

If the constitutive matrix is transformed to the elastic axis, then will the method described by Malcolm and Laid method give the correct rotation of the reference coordinate system.

An alternative method for calculating the orientation of the reference coordinate system

By defining the principle axis as a direction about which an applied moment will result in a curvature about that axis and zero curvature about the perpendicular axis, can the rotation of the principle axis be determined by (note that (s) is the inverted of (k)):

$$\phi = \operatorname{atan}\left(\frac{2 \cdot s_{45}}{s_{44} - s_{55}}\right) \cdot \frac{1}{2} \Rightarrow \phi_i = 10 \text{deg}$$

Equation 4.44

The result is correct since the rotation of the reference coordinate system is 10° .

The terms (s_{44} , s_{45} , s_{55}) in the inverted constitutive matrix are independent of the location of the reference coordinate system and the rotation of the reference coordinate system can therefore be determined for an arbitrary point on the cross section.

4.4.6. Translation an rotation transformation of the constitutive matrix (k)

When the correct orientation angle (ϕ) and offset from the reference coordinate system is obtained then is the order of transformation not important. This means that one can perform the translation transformation and then the rotation transformation or the other way around and the result will be the same.

The translation and rotation transformation according to Malcolm and Laid was tested on the analytical model and gave exact results. The constitutive matrix is shown below, translated and rotated to the location and orientation of the principle axis:

$$k = \begin{pmatrix} 767.2 & 0 & 0 & 0 & 0 & 0 \\ -0 & 110.7 & -0 & -0 & -0 & -0 \\ 0 & 0 & 2625 & -0 & -0 & 0 \\ -0 & -0 & 0 & 35.6 & 0 & 0 \\ -0 & 0 & 0 & 0 & 306.3 & 0 \\ -0 & 0 & 0 & 0 & 0 & 40.4 \end{pmatrix} \cdot 10^6 \quad \text{Which is the same as:} \quad k = \begin{pmatrix} GA \cdot k_x & 0 & 0 & 0 & 0 & 0 \\ 0 & GA \cdot k_y & 0 & 0 & 0 & 0 \\ 0 & 0 & AE & 0 & 0 & 0 \\ 0 & 0 & 0 & EI_x & 0 & 0 \\ 0 & 0 & 0 & 0 & EI_y & 0 \\ 0 & 0 & 0 & 0 & 0 & GJ \end{pmatrix}$$

As illustrated by the constitutive matrices above, the analytical model is able to compute the correct constitutive matrix.

4.4.7. Summary and conclusion of the analytical model

It can be concluded that in order to obtain correct results for the method described by Malcolm and Laird then one must follow some steps in a specific order.

The following steps must be followed:

- To determine the location of the shear center then the constitutive matrix must be transformed (rotated) to the orientation of the principle axis.
- To determine the rotation of the principle axis then the constitutive matrix must be transformed (translation) to the location of the elastic axis.

The steps can be illustrated by the following flowchart.

Compute location of elastic axis ► Transformation (translation) to location of elastic axis ►
Compute orientation of principle axis ► Transformation (rotation) to orientation of principle
axis ► Compute location of shear center.

The orientation of the principle axis, the location of the elastic axis and the shear center can be determined directly from the modified equations (*Equation 4.12*, *Equation 4.14* and *Equation 4.44*) without using any transformations. This makes the system more flexible.

4.5. Numerical validation of the Beam Property Extraction (BPE) method

The analytical validation of the BPE-method showed that the exact three displacements and rotations would give the exact constitutive matrix (k) referring to the reference coordinate system. By performing the translation and rotation transformation it is possible to obtain the constitutive matrix for an arbitrary location and rotation of the cross section. In short, the exact displacements and rotations give the exact constitutive matrix.

Each cross section in the FE-model will potentially have hundreds of degrees-of-freedom and all these degrees-of-freedom shall be described by the six degrees-of-freedom (the three displacements and rotations) of the reference coordinate system.

Two different methods for determining the three displacements and rotations were tested in this work. The two methods are:

- A least squares algorithm
- Multiple Point Constrain element (MPC-element)

The two methods listed above were tested on a shell FE-model of the rectangular steel tube from the analytical model and a shell model of the blade section. These two FE-models are described later on.

4.5.1. Least squares algorithm (displacements and rotations)

The least squares algorithm can be divided into three steps, which are listed below:

1. Determining the rotation above the z-axis (twist-angle)
2. Determining the rotation above the x-and y-axes (the two bending slopes)
3. Determining the displacements at the reference coordinate system

Step 1 (Twist-angle)

The rotation about the z-axis (twist-angle (r_z)) can be calculated by two different methods (called method-1 and method-2). Both methods work by using linear least squares regression, which creates a line with the best fit through a number of points. The lines have the following equation: $y(x) = \alpha \cdot x + b$. The line is fitted by finding α and b values that minimize the squared residuals (vertical distance between the points and the line).

Method-1: In short, the z-rotation of the cross section is determined by fitting a linear least squares regression curve through the deformed and undeformed cross section.

The difference between the slopes for the two curves is then equal to the twist angle. The theory of linear least squares regression is shown below:

$$F = \begin{pmatrix} 1 & x_1 \\ 1 & x_2 \\ \dots & \dots \\ 1 & x_n \end{pmatrix} \quad \begin{pmatrix} b \\ \alpha \end{pmatrix} = (F^T \cdot F)^{-1} \cdot F^T \cdot \begin{pmatrix} y_1 \\ y_2 \\ \dots \\ y_n \end{pmatrix} \quad y(x) = \alpha \cdot x + b \quad \Rightarrow \quad r_z = \text{atan}(\alpha_{\text{deformed}}) - \text{atan}(\alpha_{\text{undeformed}})$$

Equation 4.45

x_i and y_i are the nodal coordinates. α is the slope and b is the intersection value with the y-axis. r_z is the rotation above the z-axis (twist angle).

The method was tested on the cross section from the FE-model of the rectangular tube. This undeformed cross section was rotated (the nodes) by using the rotation transformation matrix and the result from method-1 was compared with the actual rotation angle. The deviation was of a considerable size (11.7% deviation with a 5° rotation), but it can be shown that this deviation between the actual rotation angle and the twist-angle obtained by method-1 is more or less a constant value. The method is very accurate if using a deviation constant (k_d).

This is illustrated in the following.

In the plot below is the cross section of the rectangular tube rotated 5° and the least squares curve determined by method-1 is compared with the exact curve (the exact curve has a slope equal to 5°):

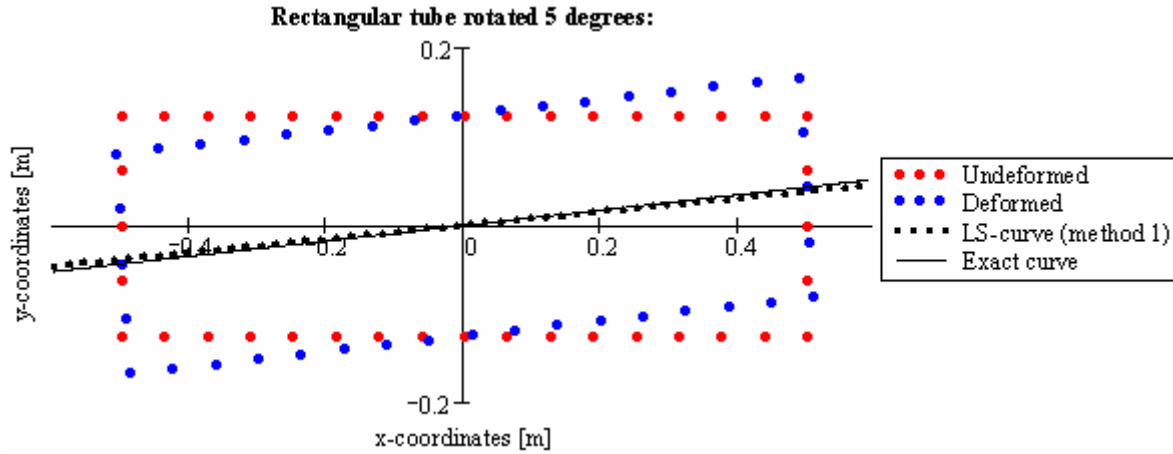


Figure 4.5.1 – Method-1, Least squares method on the rectangular tube.

As illustrated in Figure 4.5.1 is there a deviation between the slopes from the LS-curve and the exact curve. This deviation is 11.7% which is unacceptable.

In Figure 4.5.2 is the deviation between the exact rotation angles and the angles obtained by method-1 plotted in the interval $(-5^\circ \leq \theta \leq 5^\circ)$.

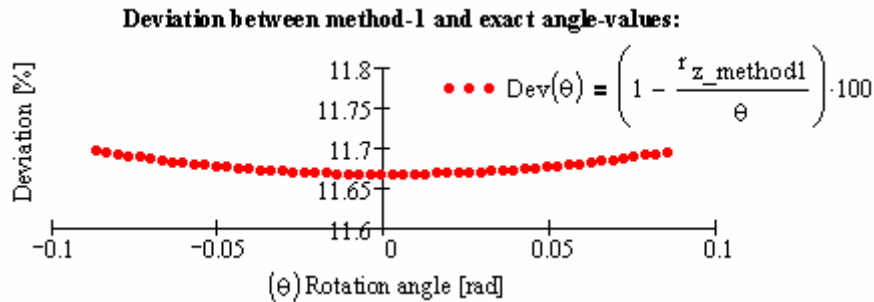


Figure 4.5.2 – Method-1, deviation of twist-angle

Figure 4.5.2 shows that the deviation between the results from method-1 and the exact rotation angles is almost a constant value in the plotted interval. This means that by adding a deviation constant (k_d) then can this method give a precise estimate of the twist angle.

The deviation constant is calculated by:

$$k_d = \left[\frac{\sum_{n=1}^n \left(\frac{r_{z_method1}}{\theta} \right)}{n} \right]^{-1} \quad r_{z_kd} = r_{z_method1} \cdot k_d$$

Equation 4.46

θ is the exact rotation angles, $r_{z_method1}$ is the rotation angles obtained by method-1 and n is the number of calculated angles. r_{z_kd} is the modified rotation angle which gives a very precise estimate of the twist angle. The maximum deviation with the modified method-1, in the plotted interval was 0.022% which is acceptable.

Method-1 was also tested on a cross section from the FE-model of the blade section and the conclusion was the same. For a cross section at radial position R17 was the deviation before the correction 3.15% with a rotation angle of 5° . After correction (modified method-1) was the maximum deviation 0.02% in the interval $-5^\circ \leq \theta \leq 5^\circ$.

The nodes of the cross section are shown below in the undeformed and deformed state (rotated 5°):

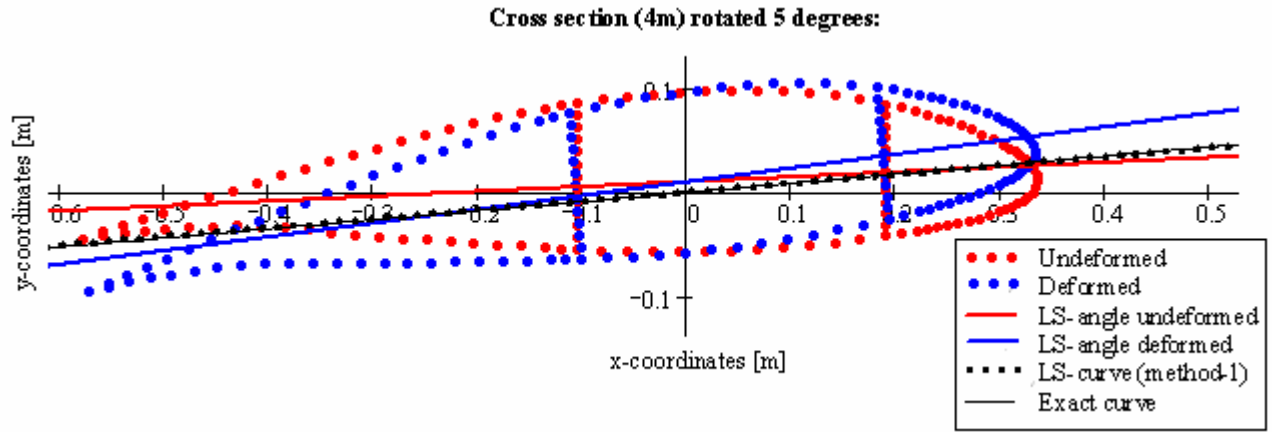


Figure 4.5.3 – Method-1, Least squares method on a cross section from blade section.

There is a small deviation (see Figure 4.5.3) between the result from method-1 (LS-curve) and the exact curve, which has a slope equal to 5° . This deviation is 3.15% as mentioned earlier. By performing the correction will the deviation become very small (0.02%), which is acceptable.

Method-2: The z-rotation of the cross section is determined by fitting a linear least squares regressions curve through the deformed x-coordinates and the relative displacements in the y-direction ($dy = y_{\text{deformed}} - y_{\text{undeformed}}$). The slope of the curve is then equal to the twist angle. For this assumption to be valid then must the rotation angle be small. The theory of linear least squares regression is shown below (note that dy is equal to the relative displacement in the y-direction):

$$F = \begin{pmatrix} 1 & x_1 \\ 1 & x_2 \\ \dots & \dots \\ 1 & x_n \end{pmatrix} \quad \begin{pmatrix} b \\ \alpha \end{pmatrix} = (F^T \cdot F)^{-1} \cdot F^T \cdot \begin{pmatrix} dy_1 \\ dy_2 \\ \dots \\ dy_n \end{pmatrix} \quad y(x) = \alpha \cdot x + b \quad \Rightarrow \quad r_z = \text{atan}(\alpha_{\text{deformed}})$$

Method-2 was tested on the rectangular tube cross section and a cross section from the blade section. Method-2 gave reasonable accurate results for both cross sections. The results from these two tests will be presented in the following.

In the plot below are the nodes from a cross section of the rectangular tube rotated 5° and the least squares curve determined by method-2 is compared with the exact curve (the exact curve has a slope equal to 5°):

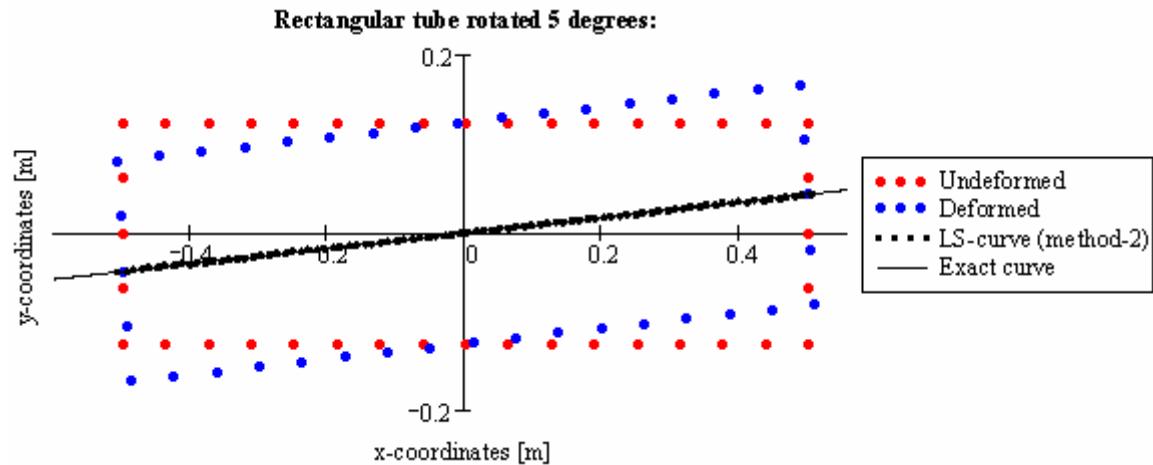


Figure 4.5.4 - Method-2, Least squares method on the rectangular tube.

The deviation (see Figure 4.5.5) between the slopes from the LS-curve and the exact curve is very small (0.04%), which is acceptable.

Below is the deviation between the angles obtained by method-2 and the exact rotation angles plotted in the interval $-5^\circ \leq \theta \leq 5^\circ$.

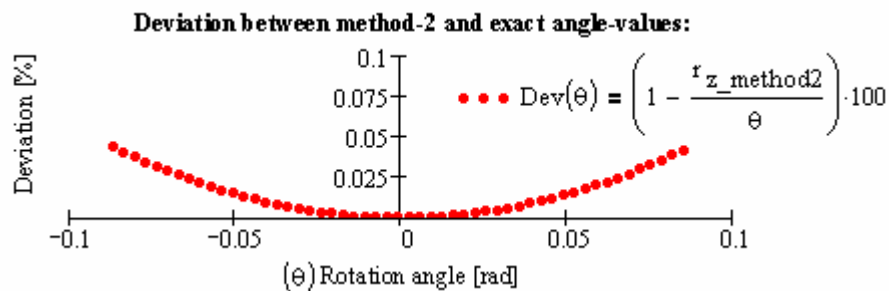


Figure 4.5.5 - Method-2, deviation of twist-angle

As one can see on the plot above, the deviation between the result from method-2 and the exact value becomes larger as rotation becomes larger. But this method is very accurate for small rotations. The maximum deviation in the plotted interval is 0.04%.

Method-2 was also tested on the cross section from the blade section and showed to be reasonable accurate. The maximum deviation in the interval $-5^\circ \leq \theta \leq 5^\circ$ was 0.2%, which is acceptable.

Comment on the two methods for determine the twist angle

Both methods showed that they were capable of estimating the rotation angle with a reasonable accuracy. Both methods are only valid for small rotation angles, because the accuracy decreases as the rotation angle increases. Method-1 is very sensitive to local deformation of the cross section, since this will affect the deviation constant. If the beam has a varying cross section like the blade section then it is necessary to determine a deviation constant for each cross section, which is going to be evaluated. Method-2 is less sensitive to local deformations of the cross section and the method is less depended on the shape of the cross section (no deviation constant).

Step 2 (bending slopes: rotation above the x- and y-axis)

The rotations about the x- and y-axis are determined by using a linear multiple regression plane, which has the following equation: $z(x,y) = b + r_y \cdot x + r_x \cdot y$.

The two variables x and y describes a plane in the three-dimensional (x,y,z) space. r_y and r_x are the rotation above the y- and x-axis and b is the intersection with the z-axis. To make the plane come as close as possible to the points in the aggregate, then the values of r_y , r_x and b that minimize the sum of the squared residuals are found. This is illustrated below in matrix form:

$$F = \begin{pmatrix} 1 & x_1 & y_1 \\ 1 & x_2 & y_2 \\ \dots & \dots & \dots \\ 1 & x_n & y_n \end{pmatrix} \quad \begin{pmatrix} b \\ r_y \\ r_x \end{pmatrix} = (F^T \cdot F)^{-1} \cdot F^T \cdot \begin{pmatrix} z_1 \\ z_2 \\ \dots \\ z_n \end{pmatrix} \quad z(x,y) = b + r_y \cdot x + r_x \cdot y$$

One can now calculate the three relative rotations of each beam element from the global x-,y- and z-rotations, that were determined by the least squares algorithm. This can be done by combining step 1 and 2.

The combination of the two steps is shown below for the rectangular tube that is subjected to an axial force (F_z) located 250mm in the x-direction and 62.5mm in the y-direction from the elastic axis. This will result in bending about both axes and extension of the tube.

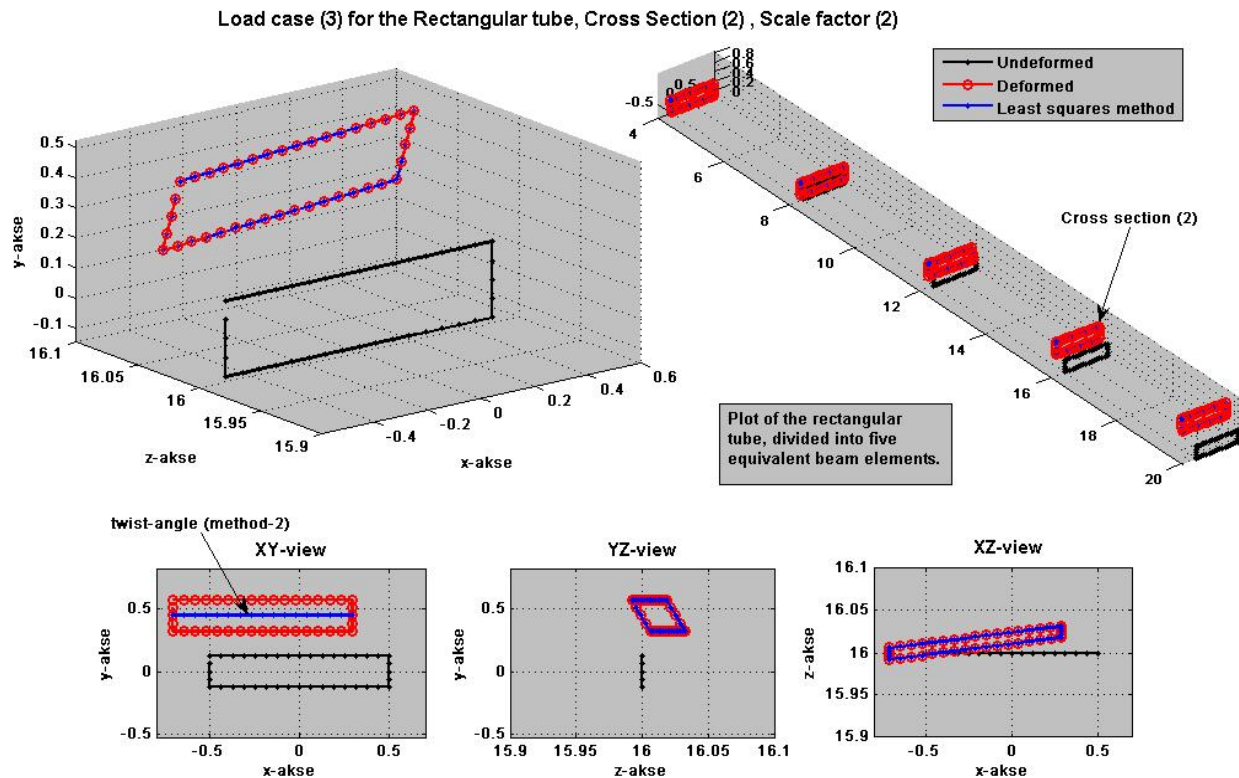


Figure 4.5.6 – Load case 3

Step 3 (displacements at the reference coordinate system)

It is necessary to obtain the deflections at the reference coordinate system as illustrated by the analytical validation of the BPE-method. In the least squares algorithm are the three deflections at the reference coordinate system determined by evaluating four points/nodes on the cross section. The four nodes create two lines in the three-dimensional space and the reference coordinate system is placed at the intersection between the two lines. The cross section in the undeformed state is plane and the lines will therefore intersect, but this is probably not the case for the deformed cross section. This problem is solved by using a least squares method, which determines the location of the reference coordinate system on the deformed cross section. This is illustrated in the following.

The first step is to calculate the location of the reference coordinate system in the undeformed state. This is done by choosing four points on the cross section and then determining two parametric equations that are described by the four points. This is illustrated in the following for cross section (2) subjected to load case 3, which is an axial force (note that the scale factor is equal to 1 in this case).

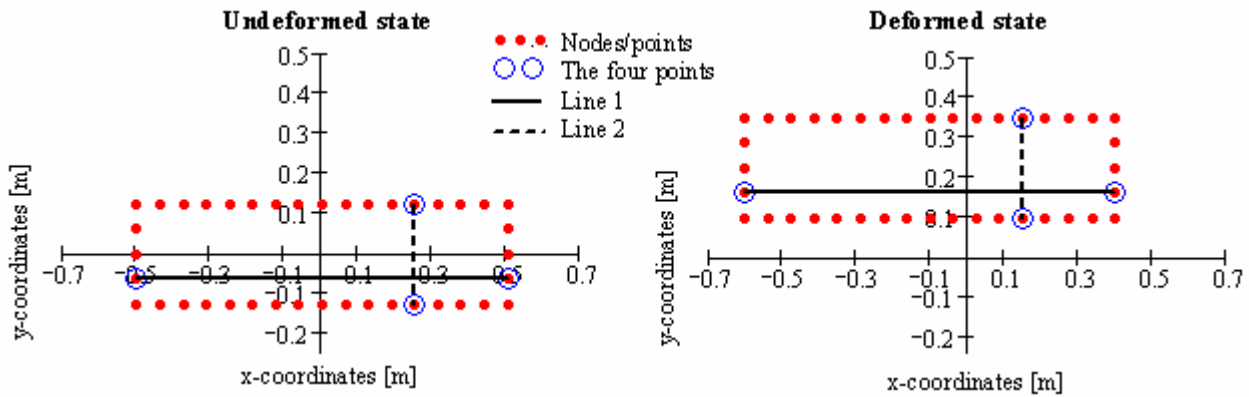


Figure 4.5.7 – Undeformed and deformed state

p_a , p_b , p_c and p_d are the four chosen points. r_1 and r_2 are the direction vectors. $l_1(t_1)$ and $l_2(t_2)$ are the parametric equations for the two lines, which is plotted above (undeformed state).

$$r_1 = p_b - p_a \quad r_2 = p_d - p_c \quad k_1 = p_b \quad k_2 = p_c \quad \Rightarrow \quad l_1(t_1) = r_1 \cdot t_1 + k_1 \quad l_2(t_2) = r_2 \cdot t_2 + k_2$$

The two parameters can be determined by solving the following equation. When the parameters are determined then can the intersection between the two lines be found. This is also the location of the reference coordinate system in the undeformed state.

$$a_m \cdot t = b_m \quad \Rightarrow \quad a_m^T \cdot a_m \cdot t = a_m^T \cdot b_m \quad \Rightarrow \quad t = (a_m^T \cdot a_m)^{-1} \cdot (a_m^T \cdot b_m)$$

$$a_m = (r_1 \quad -r_2) \quad b_m = k_2 - k_1 \quad \Rightarrow \quad t = \begin{pmatrix} -0.75 \\ 0.75 \end{pmatrix} \Rightarrow \quad l_1(t_1) = \begin{pmatrix} 0.25 \\ -0.0625 \\ 16 \end{pmatrix} \quad l_2(t_2) = \begin{pmatrix} 0.25 \\ -0.0625 \\ 16 \end{pmatrix}$$

The method for determining the location of the reference coordinate system in the deformed state is more or less the same. The three points P_a , P_b , P_c and P_d are now used to describe the two parametric equations for the two lines. The two parameters are again determined (T_1 and T_2) by solving the equation and these parameters are put into the parametric equations, which gives the following:

$$\begin{aligned}
 L_1(T_1) &= R_1 \cdot T_1 + K_1 & L_2(T_2) &= R_2 \cdot T_2 + K_2 & L_1(T_1) &= \begin{pmatrix} 0.145549 \\ 0.162198 \\ 16.011112 \end{pmatrix} & L_2(T_2) &= \begin{pmatrix} 0.145549 \\ 0.162198 \\ 16.011113 \end{pmatrix} \\
 L_T &= \frac{L_1(T_1) + L_2(T_2)}{2} & \text{disp} &= L_T - l_T & L_T &= \begin{pmatrix} 0.145549 \\ 0.162198 \\ 16.011113 \end{pmatrix} & \text{disp} &= \begin{pmatrix} -0.104451 \\ 0.224698 \\ 0.011113 \end{pmatrix}
 \end{aligned}$$

L_T is the location of the reference coordinate system in the deformed state and l_T is the location in the undeformed state. The difference between the two locations is equal to the relative displacements of the cross section.

The method described for determining the location of the reference coordinate system was tested on the rectangular tube. Results from the six FE-analyses (the six load cases) were used to determine the relative displacements at the reference coordinate system and it showed an excellent agreement with the analytical results from the analytical model.

Summary on the least squares algorithm

Method-2 was used for determining the z-rotation. Method-2 was chosen instead of Method-1 because it is less sensitive to local deformation of the cross section etc.

One can obtain very accurate results with Method-2 as long as one is operating with small rotations.

The linear multiple regression plane was used with success to determine the x- and y-rotations. The method described above evaluates only 4 points in the cross section and is therefore sensitive towards local deformations of the cross sections.

4.5.2. MPC-element (displacements and rotations)

Another way of determining the cross sectional displacements and rotations is by using a MPC-RBE3 element. The RBE3 element creates a link between one dependent node and a number of independent nodes.

RBE3 is a linear interpolation element, which means that the displacement and rotation of the dependent node is govern by the independent nodes on the cross section.

All cross sectional displacements and rotations are therefore obtained from the RBE3 elements.

Note that the RBE3 element does not create a rigid region like the RBE2 element.

A RBE3 element is shown on the picture below on the outer surface FE-model. The dependent node is created in the center of the spar and then linked to all the surrounding nodes in the cross section.

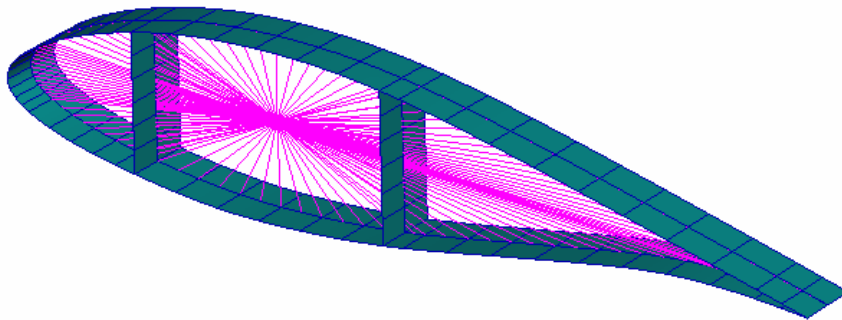


Figure 4.5.8 - RBE3 MPC-element

4.5.3. Comparison between least squares algorithm and MPC element

The FE-model of the rectangular steel tube was subjected to the six load cases, which are shown below. The reference coordinate system is placed in the lower right corner (250mm in the x-direction and -62.5mm in the y-direction compared to the elastic axis).

The following six loads were applied and analyzed:

$$F_x = 30 \cdot 10^3 \cdot N \quad F_y = 5 \cdot 10^3 \cdot N \quad F_z = 1 \cdot 10^6 \cdot N \quad M_x = 0.5 \cdot 10^5 \cdot N \quad M_y = 5 \cdot 10^5 \cdot N \quad M_z = 2 \cdot 10^5 \cdot N$$

The deflections and rotations from these load cases are assembled in displacement matrices (U_i) for each cross section. The displacement matrix for cross section 2 (U_2) will be analyzed in the following. This cross section is located 16m from the fixed end and 4m from the rigid loading end (tip) because this will minimize the affect from the rigid ends. The displacement matrices determined by the least squares algorithm and the MPC-element are shown below and compared with the analytical displacement matrix:

The first column is load case 1 (LC1), the second column is load case 2 (LC2)...etc. The first three rows are the displacements of the reference coordinate system in the x-,y- and z-direction. The last three rows are the rotations about the x-,y- and z-axis:

LC1	LC2	LC3	LC4	LC5	LC6	
0.184566	0.000031	-0.104485	0	0.20897	0.004952	ux
0.000186	0.264854	0.225006	-0.180005	0	0.01981	uy
-0.004702	0.001688	0.011118	-0.001406	-0.00653	0	uz
0	-0.027001	-0.028126	0.022501	0	0	rx
0.018807	0	-0.013061	0	0.026121	0	ry
0.000743	0.000495	0	0	0	0.079238	rz

Figure 4.5.9 - Analytical displacements matrix (U_2)

By comparing this displacement matrix with the analytical matrix, it is easy to see that there is some noise in this matrix. Some of the noise could be a result of distortion and warping of the rectangular tube, which is not accounted for in the analytical model. The red boxes indicate some of noise:

LC1	LC2	LC3	LC4	LC5	LC6	
0.184405	0.000028	-0.104451	0.000006	0.208829	0.004858	ux
0.000188	0.264382	0.224698	-0.17975	-0.000007	0.020327	uy
-0.004698	0.001687	0.011113	-0.001404	-0.006527	0.000055	uz
-0.000027	-0.02694	-0.028083	0.022473	-0	-0	rx
0.018788	-0.000028	-0.013057	-0	0.026089	0	ry
0.000766	0.00051	0	0	0	0.080711	rz

Figure 4.5.10 - Least Squares algorithm displacements matrix (U_2)

By comparing this displacement matrix with the analytical matrix, it is easy to see that the two matrices have the same structure (zeros at the same locations). It looks like there is no noise in this matrix, or it is very limited because it has these analytical zeros.

LC1	LC2	LC3	LC4	LC5	LC6	
0.184429	0.000032	-0.104429	-0	0.208858	0.005072	ux
0.00019	0.26442	0.22474	-0.179792	0	0.020288	uy
-0.0047	0.001685	0.011112	-0.001405	-0.006529	0	uz
-0	-0.026967	-0.028107	0.022485	-0	-0	rx
0.018798	0	-0.013057	-0	0.026114	-0	ry
0.000761	0.000507	-0	0	-0	0.081152	rz

Figure 4.5.11 - MPC-element displacements matrix (U_2)

There is a bit of noise in the displacement matrix from the least squares algorithm method which later will influence the BPE-method. The displacements and rotations from the RBE3 element are in very good agreement with the analytical model.

4.5.4. The numerical results of the BPE-method

The BPE-method has already been validated by the analytical model. It can be concluded that the analytical displacements and rotations gives the analytical constitutive matrix for the rectangular steel tube.

The numerical validation of the BPE-method is performed by comparing the results from a series of FE-analyses. The displacements and rotations at a number of cross sections along the FE-models are computed by using the MPC-RBE3 element. Some of the FE-models that were tested are presented in the following. These FE-models are:

1. A shell model of the rectangular steel tube from the analytical model.
2. A shell model of a three cell asymmetric isotropic profile with a constant cross section.
3. The final FE-model of the original blade section.
4. A modified FE-model of the final blade section (bend-twist blade section).

1) FE-model of a rectangular steel tube

An MSC.Patran/Nastran FE-model of the rectangular steel tube was created. The reference coordinate system was moved 250mm in the x-direction and -62.5mm in the y-direction and the tube was then rotated 10° like the analytical model. The structure was meshed with 20 elements circumferentially and 50 longitudinally (see *Figure 4.5.12*). The elements were 8-node quadrilateral shell elements, which were located in the material mid-thickness. The 20m long tube was divided into five equal beam elements, from which the beam properties were calculated.

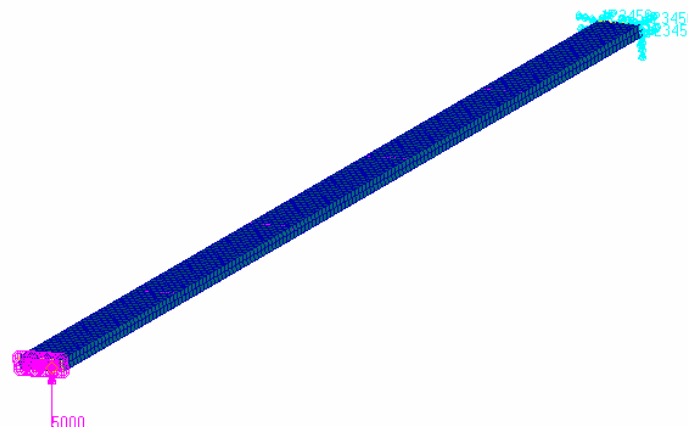


Figure 4.5.12 – FE-model of the rectangular tube

In *Figure 4.5.13* are the five constitutive matrices computed by the numerical BPE-method. Note that all matrices are multiplied by 10^{-6} :

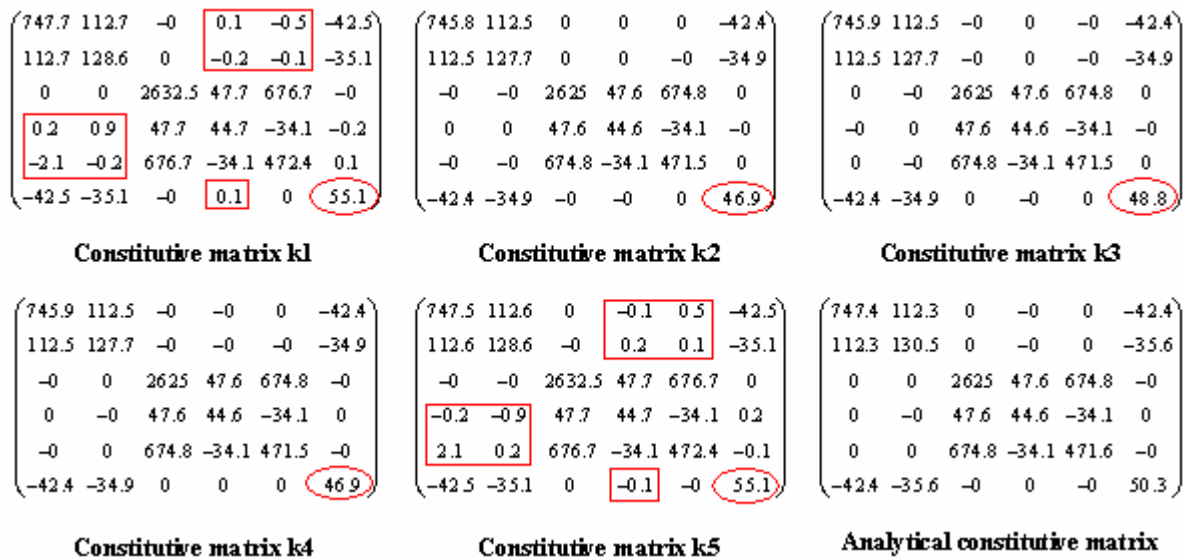


Figure 4.5.13 – Constitutive matrices from the rectangular tube

Comment

k_1 is the constitutive matrix for the tip beam element and k_5 is beam element at the fixed end (the steel tube is 20m long and divided into five beam elements of equal length). The analytical constitutive matrix is shown in the lower right corner.

The red boxes in Figure 4.5.13 indicate noise due to the two rigid ends (loading MPC-element and the fixed end). This noise is probably primarily caused by the increasing warping resistance near the rigid ends, which also has a significant affect on the torsional stiffness shown with red ellipses in Figure 4.5.13. Near the two rigid ends are the torsional stiffnesses too high because the twist angle is too small. The best result is seen in the beam element in the middle (k_3), which also was expected because the affects from the boundary conditions are smallest for this element.

Numerical results - location of elastic center, shear center and orientation of principle axes:

	x-direction (Xec), location of elastic center [m]	y-direction (Yec), location of elastic center [m]	x-direction (Xsc), location of shear center [m]	x-direction (Ysc), location of shear center [m]	Orientation of principle axes [degrees]
BPE-element 1	-0,2570549	0,0181383	-0,2570548	0,0181380	10,0000372
BPE-element 2	-0,2570549	0,0181383	-0,2570551	0,0181379	10,0000390
BPE-element 3	-0,2570549	0,0181383	-0,2570550	0,0181379	10,0000388
BPE-element 4	-0,2570550	0,0181383	-0,2570551	0,0181379	10,0000376
BPE-element 5	-0,2570550	0,0181383	-0,2570549	0,0181380	10,0000386
Analytical	-0,2570549	0,0181384	-0,2570549	0,0181384	10,0000000

Table 4.5.1 – Numerical results for the rectangular tube

Location of the elastic center, shear center and orientation of principle axes are determined by Equation 4.9, Equation 4.43, Equation 4.44.

There is an excellent agreement between the numerical and analytical/correct results, as one can see in Table 4.5.1.

For the rectangular steel tube, it can be concluded that one is able to determine the location of the elastic center, shear center and the orientation of the principle axes by using the BPE-method.

Stiffness parameters determined by the BPE-method.

$$k_{3_BPE} = \begin{bmatrix} 765.69 & 0 & -0 & 0 & -0 & 0 \\ 0 & 107.89 & 0 & 0 & -0 & -0 \\ -0 & 0 & 2625 & 0 & 0 & -0 \\ 0 & 0 & 0 & 35.55 & 0 & 0 \\ -0 & -0 & 0 & 0 & 306.25 & 0 \\ 0 & -0 & -0 & 0 & 0 & 39.08 \end{bmatrix} \cdot 10^6$$

$$k_{analytical} = \begin{bmatrix} 767.2 & 0 & 0 & 0 & 0 & 0 \\ 0 & 110.7 & 0 & 0 & 0 & 0 \\ 0 & 0 & 2625 & 0 & 0 & 0 \\ 0 & 0 & 0 & 35.55 & 0 & 0 \\ 0 & 0 & 0 & 0 & 306.26 & 0 \\ 0 & 0 & 0 & 0 & 0 & 40.38 \end{bmatrix} \cdot 10^6$$

Figure 4.5.14 – Comparison of numerical and analytical constitutive matrix**Comment**

The constitutive matrix for beam element number three is transformed (translation) to the elastic center and transformed (rotated) according to the principle axes. The diagonal in the blue box shows the shear stiffnesses in the x- and y-direction ($G A k_x$ and $G A k_y$ [N]). The diagonal in the green box shows the following cross sectional properties; $A E$ [N], $E I_x$ [$N m^2$], $E I_y$ [$N m^2$] and $G J$ [$N m^2$].

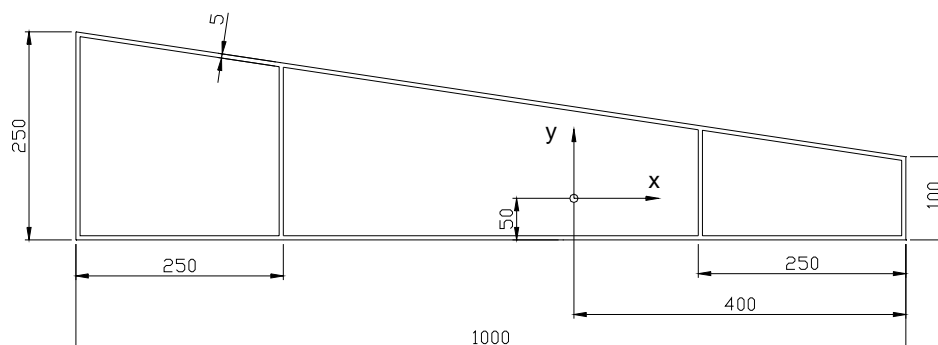
By comparing the numerical result with the analytical, one can concluded that the agreement is good. There is a small deviation between (3.2%) the numerical and analytical torsional stiffness, which can be due to boundary conditions as mentioned before. Note that the torsional stiffness parameter is dependent on the location of the reference coordinate system, which can be seen by comparing *Figure 4.5.13* (before transformation (translation and rotation)) and *Figure 4.5.14* (after transformation (translation and rotation)).

The deviation between the numerical and analytical shear stiffness in the y-direction is 2.5%, which is reasonable small.

It can be concluded that the BPE-method is in good agreement with analytical results when the rectangular steel tube is analyzed.

2) Three cell asymmetric isotropic profile

A MSC.Patran/Nastran FE-model of a three cell asymmetric aluminum ($E = 70$ GPa and $\nu = 0.3$) profile was created. The geometry and the location of the reference coordinate system can see in *Figure 4.5.15*:

**Figure 4.5.15 – Geometry of the three cell profile**

The structure was meshed with 48 elements circumferentially and 400 longitudinally. The two shear-webs were meshed with 5 elements in the height. The elements were 8-node quadrilateral

shell elements, which were located in the material mid-thickness. The 20m long tube was divided into ten equal beam elements, from which the beam properties were calculated. The FE-model of the structure can be seen below:

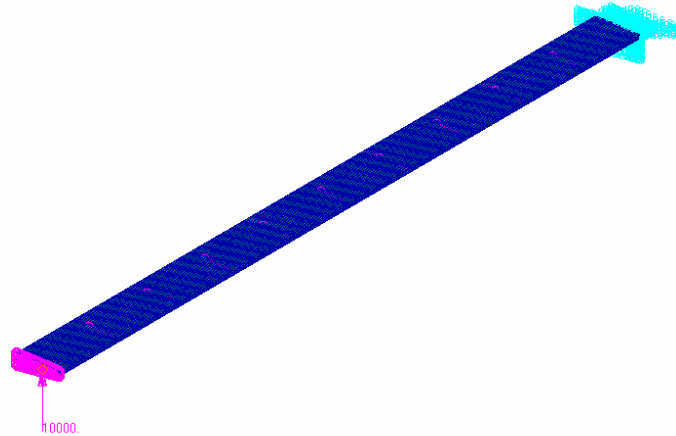


Figure 4.5.16 – FE-model of the three cell profile

The following constitutive matrices were determined by the BPE-method:

$$k_5 = \begin{pmatrix} 242.33 & -18.04 & 0 & -0 & 0 & -7.09 \\ -18.03 & 69.05 & 0 & -0 & 0 & -16.09 \\ -0 & 0 & 948.92 & 38.39 & 127.7 & 0 \\ -0 & 0 & 38.39 & 8.66 & 12.36 & -0 \\ -0 & -0 & 127.7 & 12.36 & 112.99 & 0 \\ -7.09 & -18.16 & -0 & -0 & -0 & 11.96 \end{pmatrix} \cdot 10^6$$

Figure 4.5.17 - Constitutive matrix k_5 referring to reference coordinate system

$$k_{trans_5} = \begin{pmatrix} 244.1 & -3.93 & 0 & 0 & 0 & 0.88 \\ -3.92 & 67.28 & 0 & -0 & 0 & -7.48 \\ -0 & 0 & 948.92 & -0 & 0 & -0 \\ -0 & 0 & 0 & 6.52 & -0 & -0 \\ -0 & 0 & 0 & 0 & 96.39 & -0 \\ 1.06 & -9.54 & 0 & -0 & -0 & 8.23 \end{pmatrix} \cdot 10^6$$

Figure 4.5.18 - Constitutive matrix k_5 (transformed to elastic center and rotated to the principle axis).

$$k_{trans_5} = \begin{pmatrix} 244.1 & -3.93 & 0 & 0 & 0 & -0.18 \\ -3.92 & 67.28 & 0 & -0 & 0 & 2.06 \\ -0 & 0 & 948.92 & 1.97 & -134.4 & -0 \\ -0 & 0 & 1.97 & 6.53 & -0.28 & 0 \\ -0 & 0 & -134.4 & -0.28 & 115.42 & 0 \\ 0 & -0 & 0 & -0 & -0 & 7.17 \end{pmatrix} \cdot 10^6$$

Figure 4.5.19 - Constitutive matrix k_5 (transformed to shear center and rotated according to the principle axis).

$$k_{5_4x4_bpe} = \begin{pmatrix} 948.92 & 0 & 0 & 0 \\ 0 & 6.52 & 0 & 0 \\ 0 & 0 & 96.39 & 0 \\ 0 & 0 & 0 & 7.17 \end{pmatrix} \cdot 10^6$$

$$k_{4x4_analytical} = \begin{pmatrix} 945.40 & 0 & 0 & 0 \\ 0 & 6.50 & 0 & 0 \\ 0 & 0 & 96.45 & 0 \\ 0 & 0 & 0 & 7.20 \end{pmatrix} \cdot 10^6$$

Figure 4.5.20 – Classical 4x4 constitutive matrices.

Comment to Figure 4.5.17

One of the middle beam elements (element five) is picked out. The constitutive matrix for this element is shown in Figure 4.5.17 with respect to the reference coordinate system.

The constitutive matrix is not completely symmetric because k_{62} and k_{26} , shown with red ellipses in the matrix, do not have the same values. The matrix should theoretical be completely

symmetric. The terms k_{16} , k_{26} , k_{61} and k_{62} indicate that the reference coordinate system is not located in the shear center. The BPE-method will compute the wrong location of the shear center if these terms are not correct and a transformation of the constitutive matrix to the shear center will result in some errors.

Comment to Figure 4.5.18

The constitutive matrix for beam element five, when transformed (translation) to the elastic center and transformed (rotated) according to the principle axes, is shown in *Figure 4.5.18*. The transformation has made the terms k_{16} , k_{26} , k_{61} and k_{62} more asymmetric. The deviation between k_{26} and k_{62} has increased and k_{16} and k_{61} are no longer identical. This is indicated by the red boxes. When the constitutive matrix is transformed according to the principle axes, then should k_{12} and k_{21} be equal to zero but this is not the case. These terms are shown with red ellipses.

Comment to Figure 4.5.19

The constitutive matrix, when transformed (translation) to the shear center and transformed (rotated) according to the principle axes, is shown in *Figure 4.5.19*.

As stated before, a transformation of the constitutive matrix to the shear center will result in some errors if the terms k_{16} , k_{26} , k_{61} and k_{62} are not completely correct (symmetric). Since the location of the shear center is determined by k_{61} and k_{62} (see *Equation 4.15* and *Equation 4.16*), then these terms are zero in the transformed matrix. The terms k_{16} and k_{26} should in theory also be equal to zero but this is not the case because of the asymmetric (the terms are shown with a red box).

In the 6x6 constitutive matrix is the term k_{66} dependent of the location of the reference coordinate system. The term will be equal to the torsional stiffness (GJ) if the reference coordinate system is located in the shear center. To transform the constitutive matrix to the shear center and compute the correct torsional stiffness, then all terms in the following equation must be correct:

$$GJ = k'_{66} = k_{66} + v \cdot k_{61} - \mu \cdot k_{62} + v \cdot (k_{16} + v \cdot k_{11} - \mu \cdot k_{12}) - \mu \cdot (k_{26} + v \cdot k_{21} - \mu \cdot k_{22})$$

The equation above is taken from the transformation matrix.

Since the terms k_{16} , k_{26} , k_{61} , k_{62} , k_{12} and k_{21} are subjected to some uncertainties, then is the torsional stiffness determined by the BPE-method also subjected to some uncertainties.

The blue boxes and ellipses in the figure indicate that the reference coordinate system is not located at the elastic center but at the shear center determined by the BPE-method.

The elastic center and shear center will not have same location because the profile is asymmetric, and the terms in the blue boxes and ellipses should therefore not be equal to zero.

Comment to Figure 4.5.20

In *Figure 4.5.20* is the matrix in the top the classical 4x4 constitutive matrix which is transformed (translation) to the elastic center and transformed (rotated) according to the principle axes. Note that the classical constitutive matrix is determined by *Equation 4.23*.

In *Figure 4.5.20* is the matrix in the bottom the classical 4x4 analytical constitutive matrix.

The axial stiffness AE and the bending stiffnesses EI_x and EI_y are determined by using the CAD program Pro/Engineer. The location of the elastic center and the orientation of the principle axes can also be determined by Pro/E, which is used in the comparison between the results from the BPE-method and analytical results in *Table 4.5.2*.

The torsional stiffness GJ in the analytical matrix is determined by using *Equation 3.83* (note that this equation is an approximated method for determining the torsional stiffness).

By comparing the two matrices in *Figure 4.5.20* then one can conclude that there is excellent agreement between the results from the BPE-4x4-method and the analytical results.

It can also be concluded that the torsional stiffness determined by the BPE-4x4-method is identical to the torsional stiffness determined by the BPE-6x6-method when the constitutive matrix is transformed to the shear center (see term k_{66} in *Figure 4.5.19* and term k_{44} in *Figure 4.5.20*). This could be a coincidence!

Note that the torsional stiffness in the 4x4 constitutive matrix does not depend on the location of the reference coordinate system (see *Equation 4.26*).

Numerical results - location of elastic center, “shear center” and orientation of principle axes.

	x-direction (Xec), location of elastic center [m]	y-direction (Yec), location of elastic center [m]	x-direction (Xsc), location of shear center [m]	x-direction (Ysc), location of shear center [m]	Orientation of principle axes [degrees]
BPE-element 5	-0,1345790	0,0404545	-0,2759276	0,0497661	-4,6091052
BPE-4x4-element 5	-0,1345790	0,0404545	??	??	-4,6091052
Analytical	-0,1349886	0,0404848	??	??	-4,6080000

Table 4.5.2

Comment to *Table 4.5.2*

By comparing the results from the BPE-6x6- and BPE-4x4-method, it can be concluded that the two methods gives the same results for the location of the elastic center and orientation of the principle axes. By comparing the results from the BPE-methods and analytical results (from Pro/E) then it can be concluded that there is excellent agreement between the results.

Only the BPE-6x6-method can compute the location of the shear center and the result is as mentioned before subjected to some uncertainties.

3) The final FE-model of the original blade section

One of the primary aims of this work was to create a FE-model of the blade section, which can describe the static response correctly. Three different FE-models were created and their responses have been compared with experimental results from static testing. The best model was select and used for the BPE-method. The final FE-model of the blade section is in short created by using solid hex 20 elements as core material and 8-node quadrilateral shell elements as the solid laminates. These shell elements are placed in the mid-thickness of the laminates. A detailed description of this model can be found in chapter 6. The experimental testing of the blade section is described in chapter 5. The final FE-model is shown below in. The reference coordinate system is placed in the center of spar.

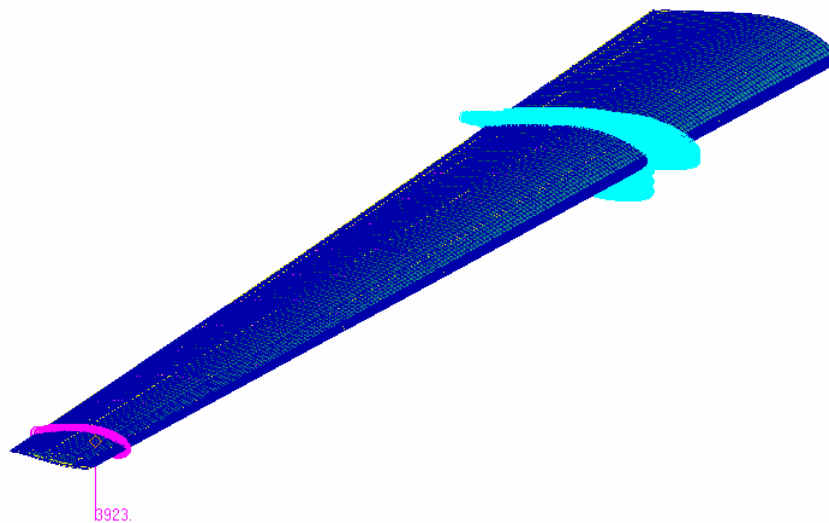


Figure 4.5.21 – FE-model of the original blade section

The blade section is divided into seven beam elements:

- Beam element 1, 6.057m – 5.607m
- Beam element 2, 5.607m – 4.607m
- Beam element 3, 4.607m – 3.607m
- Beam element 4, 3.607m – 2.607m
- Beam element 5, 2.607m – 1.607m
- Beam element 6, 1.607m – 0.607m
- Beam element 7, 0.607m – 0.000m

(0.0m = R12.827m for the 23m blade (measured from the hub)).

Numerical results - location of elastic center, “shear center” and orientation of principle axes from the BPE-6x6-method:

BPE-6x6-method	x-direction (Xec), location of elastic center [m]	y-direction (Yec), location of elastic center [m]	x-direction (Xsc), location of shear center [m]	x-direction (Ysc), location of shear center [m]	Orientation of principle axes [degrees]
BPE-element 1	-0,030679	-0,002106	0,012362	0,010672	4,078
BPE-element 2	-0,031869	-0,002083	0,031528	0,013233	3,820
BPE-element 3	-0,033006	-0,002458	0,012372	0,021082	3,476
BPE-element 4	-0,034225	-0,002149	0,024876	0,021177	3,117
BPE-element 5	-0,038277	-0,001612	0,049214	0,019389	2,665
BPE-element 6	-0,042044	-0,001007	0,079807	-0,016598	2,126
BPE-element 7	-0,046685	-0,000450	0,070049	-0,042334	1,461

Table 4.5.3

Numerical results - location of elastic center, “shear center” and orientation of principle axes from the BPE-6x6-method:

BPE-4x4-method	x-direction (Xec), location of elastic center [m]	y-direction (Yec), location of elastic center [m]	Orientation of principle axes [degrees]
BPE-element 1	-0,030626	-0,002175	4,078
BPE-element 2	-0,031694	-0,002071	3,820
BPE-element 3	-0,032812	-0,002412	3,476
BPE-element 4	-0,034104	-0,002226	3,117
BPE-element 5	-0,038153	-0,001729	2,665
BPE-element 6	-0,041975	-0,001116	2,126
BPE-element 7	-0,046551	-0,000424	1,461

Table 4.5.4

Comment

By comparing the results from the two BPE-methods it can be concluded that the location of elastic center and the orientation of the principle axes are almost identical. As stated before, the location of the shear center is subjected to some uncertainties because the terms k_{16} , k_{26} , k_{61} and k_{62} are not completely symmetric/identical ($k_{16} = k_{61}$ and $k_{26} = k_{62}$).

Stiffness parameters determined by the BPE-6x6-method.

The results of the stiffness parameters from the BPE-method are shown in Table 4.5.5.

The axial stiffness AE (k_{33}), the flapwise bending stiffness EI_x (k_{44}), edgewise bending stiffness EI_y (k_{55}), bend-twist coupling between flapwise bending and torsion K_f (k_{64} or k_{46}), bend-twist coupling between edgewise bending and torsion K_e (k_{65} or k_{56}), shear stiffness GAk_x (k_{11}), shear stiffness GAk_y (k_{22}) are for each element determined at the location of the elastic center and orientated according to the principle axes. The torsional stiffness GJ (k_{66}) is for each element determined at the location of the shear center.

Note that for beams with couplings, one is not able to compute the generally stiffness terms such as axial-, flapwise-, edgewise-, torsional stiffnesses because these terms are coupled. This means that the terms in the constitutive matrix are not equal to stiffness known from simple beam theory. Since the original blade section has limited coupling, it can be assumed that the terms in the diagonal of the constitutive matrix are equal to the stiffness known from beam theory and the terms k_{46} , k_{64} , k_{56} and k_{65} are equal to the bend-twist couplings (which are of limited size).

BPE-6x6-method	Axial stiffness $AE \cdot 10^6$ [Nm ²]	Flapwise bending stiffness $EI_x \cdot 10^6$ [Nm ²]	Edgewise bending stiffness $EI_y \cdot 10^6$ [Nm ²]	Torsional stiffness $GJ \cdot 10^6$ [Nm ²]	Bend-twist coupling (flap + torsion) $K_f \cdot 10^6$ [Nm ²]	Bend-twist coupling (Edge + torsion) $K_e \cdot 10^6$ [Nm ²]	Shear stiffness $GAk_x \cdot 10^6$ [N]	Shear stiffness $GAk_y \cdot 10^6$ [N]
BPE-element 1	297,408	0,469	5,486	0,304	-0,022	0,013	38,933	8,741
BPE-element 2	343,986	0,782	7,437	0,418	-0,030	-0,014	36,879	10,187
BPE-element 3	425,033	1,372	10,669	0,698	-0,019	-0,017	40,932	12,026
BPE-element 4	515,632	2,352	14,767	0,911	-0,035	0,040	46,159	10,203
BPE-element 5	562,391	3,490	19,290	1,430	-0,073	0,149	50,583	12,102
BPE-element 6	604,993	4,960	24,482	1,970	-0,053	0,272	57,616	14,652
BPE-element 7	650,138	6,413	29,617	2,435	0,328	0,117	75,517	17,657

Table 4.5.5

Stiffness parameters determined by the BPE-4x4-method.

All stiffnesses are determined at the location of the elastic center and orientated according to the principle axes. Note that the 6x6-model and 4x4-model cannot in general be compared, but since the blade section has a limited coupling and the torsional stiffness in 6x6-model is determined at the location of shear center, then it can be assumed that a comparison is valid.

BPE-4x4-method	Axial stiffness $AE \cdot 10^6$ [Nm ²]	Flapwise bending stiffness $EI_x \cdot 10^6$ [Nm ²]	Edgewise bending stiffness $EI_y \cdot 10^6$ [Nm ²]	Torsional stiffness $GJ \cdot 10^6$ [Nm ²]	Bend-twist coupling (flap + torsion) $K_f \cdot 10^6$ [Nm ²]	Bend-twist coupling (edge + torsion) $K_e \cdot 10^6$ [Nm ²]
BPE-element 1	297,888	0,462	5,480	0,304	-0,011	0,023
BPE-element 2	343,983	0,729	7,340	0,418	0,008	0,011
BPE-element 3	424,764	1,321	10,568	0,698	0,012	0,017
BPE-element 4	515,539	2,294	14,689	0,911	0,002	0,077
BPE-element 5	562,221	3,425	19,209	1,430	0,004	0,198
BPE-element 6	604,778	4,880	24,398	1,972	0,083	0,309
BPE-element 7	648,887	6,409	29,616	2,432	0,364	0,198

Table 4.5.6

Comment

The stiffness terms AE , EI_x , EI_y and GJ computed by both models are almost identical. The bend-twist couplings computed by the two methods are not in generally good agreement but these couplings are also of limited size and are therefore subjected to some uncertainties.

The blade section has a limited coupling and the stiffness terms in the constitutive matrix can therefore be compared with the stiffness known from simple beam theory. In the following are the flapwise bending stiffness EI_{x_bpe} and the edgewise bending stiffness EI_{y_bpe} computed by the BPE-method at the center of the spar. It is assumed that these values will be reasonable close to a flapwise bending stiffness EI_{x_beam} and edgewise bending stiffness EI_{y_beam} determined by classical beam theory. It is also assumed that the torsional stiffness GJ_{bpe} computed by the BPE-method at the shear center will be reasonable close to a torsional stiffness determined by classical beam theory.

The stiffnesses determined by the BPE-method and the stiffnesses determined by classical beam theory are compared in the following. The first and last BPE-elements are not considered because these elements are influenced by the boundary conditions. The classical stiffnesses are determined by the relative rotations and the moment distribution over the elements. This can be written as:

$$L_z^T = (0 \ 1 \ 2 \ 3 \ 4 \ 5)m \quad i = 1..rows(L_z)$$

$$EI_{flap_i} = \frac{-\int_{L_{z_i}}^{L_{z_{i+1}}} M_x(z) dz}{r_{x_{i+1}} - r_{x_i}} \quad EI_{edge_i} = \frac{\int_{L_{z_i}}^{L_{z_{i+1}}} M_y(z) dz}{r_{y_{i+1}} - r_{y_i}} \quad GJ_i = \frac{-T \cdot (L_{z_{i+1}} - L_{z_i})}{r_{z_{i+1}} - r_{z_i}}$$

$M_x(z)$ and $M_y(z)$ is the flapwise- and edgewise moment distribution and T is the constant torsional moment:

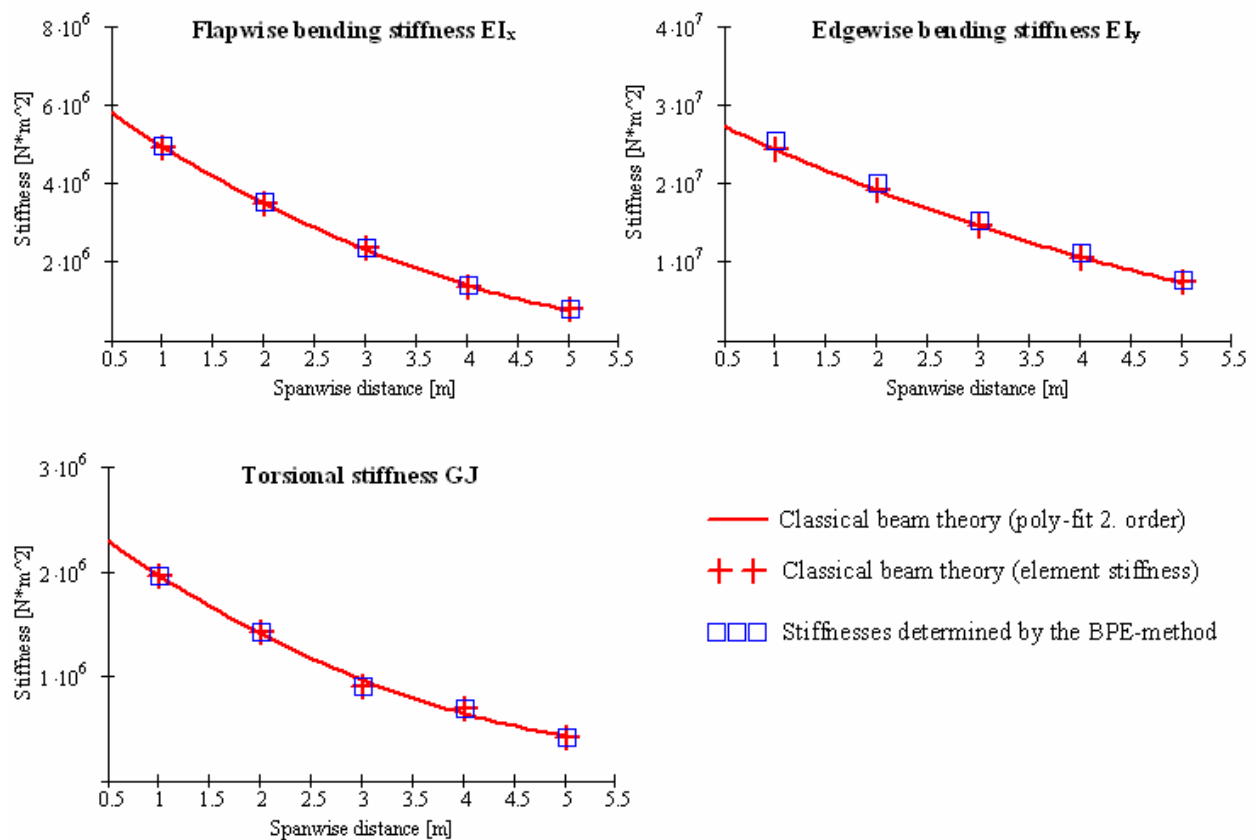


Figure 4.5.22 – Comparison of stiffness terms

Comment

By comparing the element stiffnesses determined by classical beam theory and the BPE-method, it can be concluded that there is general good agreement between the results. The edgewise bending stiffness determined by the BPE-method is bit stiffer near the fixed end, but the deviation is reasonable small.

4) A modified FE-model of the final blade section (bend-twist blade section).

The original blade section is modified by adding some additional angled UD layers on the suction and pressure side of the aerodynamic profile, which will introduce bend-twist couplings. A detailed description of the FE-model can found in chapter 6.

Numerical results - location of elastic center, “shear center” and orientation of principle axes from the BPE-6x6-method:

BPE-6x6-method	x-direction (Xec), location of elastic center [m]	y-direction (Yec), location of elastic center [m]	x-direction (Xsc), location of shear center [m]	x-direction (Ysc), location of shear center [m]	Orientation of principle axes [degrees]
BPE-element 1	-0,055468	-0,003985	0,005517	0,007510	4,090
BPE-element 2	-0,062705	-0,004101	0,014441	0,014231	3,725
BPE-element 3	-0,066523	-0,004326	0,032515	0,025381	3,355
BPE-element 4	-0,070871	-0,003995	0,037429	0,030571	2,897
BPE-element 5	-0,079361	-0,003360	0,099673	0,025951	2,307
BPE-element 6	-0,088254	-0,002992	0,192903	-0,016921	1,624
BPE-element 7	-0,099774	-0,002007	0,173019	-0,033992	0,986

Numerical results - location of elastic center, “shear center” and orientation of principle axes from the BPE-4x4-method:

BPE-4x4-method	x-direction (Xec), location of elastic center [m]	y-direction (Yec), location of elastic center [m]	Orientation of principle axes [degrees]
BPE-element 1	-0,051415	-0,003819	4,090
BPE-element 2	-0,055705	-0,003762	3,725
BPE-element 3	-0,059346	-0,004117	3,355
BPE-element 4	-0,064305	-0,003985	2,897
BPE-element 5	-0,072624	-0,003336	2,307
BPE-element 6	-0,081062	-0,002499	1,624
BPE-element 7	-0,093676	-0,000808	0,986

Comment

By comparing the orientation of the principle axes determined by the two BPE-methods, it can be concluded that there is an excellent agreement between the results. The location of the elastic center is in general good agreement, except the computed distance in the y-direction for BPE-element 7, which seems to deviate when compared with the other results.

Stiffness parameters determined by the BPE-6x6-method.

The results of the stiffness parameters from the BPE-method are shown in the table below. The axial stiffness AE (k_{33}), the flapwise bending stiffness EI_x (k_{44}), the edgewise bending stiffness EI_y (k_{55}), the bend-twist coupling between flapwise bending and torsion K_f (k_{64} or k_{46}), the bend-twist coupling between edgewise bending and torsion K_e (k_{65} or k_{65}), the shear stiffness GAk_x (k_{11}), the shear stiffness GAk_y (k_{22}) are for each element determined at the location of the elastic center and orientated according to the principle axes. The torsional stiffness GJ (k_{66}) is for each element determined at the location of the shear center.

Since this blade section is highly coupled, the stiffness terms cannot be compared with the stiffnesses known from classical beam theory.

BPE-6x6-method	Axial stiffness $AE \cdot 10^6$ [Nm ²]	Flapwise bending stiffness $EI_x \cdot 10^6$ [Nm ²]	Edgewise bending stiffness $EI_y \cdot 10^6$ [Nm ²]	Torsional stiffness $GJ \cdot 10^6$ [Nm ²]	Bend-twist coupling (flap + torsion) $K_f \cdot 10^6$ [Nm ²]	Bend-twist coupling (Edge + torsion) $K_e \cdot 10^6$ [Nm ²]	Shear stiffness $GA_{Kx} \cdot 10^6$ [N]	Shear stiffness $GA_{Ky} \cdot 10^6$ [N]
BPE-element 1	431,472	0,763	10,023	0,539	-0,145	-0,008	86,872	11,012
BPE-element 2	499,575	1,194	14,157	0,694	-0,223	-0,019	87,770	11,932
BPE-element 3	603,947	1,992	20,655	1,119	-0,306	-0,084	97,799	13,771
BPE-element 4	714,285	3,258	29,035	1,569	-0,430	0,016	109,008	12,526
BPE-element 5	781,927	4,782	38,710	2,564	-0,731	0,281	117,479	15,064
BPE-element 6	847,152	6,655	50,786	3,310	-0,928	0,780	125,824	18,449
BPE-element 7	944,462	8,286	64,951	3,951	-0,379	0,467	146,283	21,959

Table 4.5.7

Comment

The additional angled UD layers should in theory create a flapwise bend-twist coupling.

The real modified blade section was experimentally tested and it was concluded that by adding these angled UD layers then a measurable bend-twist coupling was obtained.

The same load cases were performed experimentally and numerically on the blade section and it was concluded that the numerical response was in good agreement with the experiments.

It was therefore concluded that the FE-model was able to model the bend-twist coupled behavior.

The results of the BPE-method also shows that the modified blade section has a measurable flapwise bend-twist coupling K_f .

If BPE-element 7 is not considered, it can be concluded that the bend-twist coupling decreases smoothly from the tip end to the fixed end, which also was expected. The reason that BPE-element 7 deviates is probably due to the increasing warping resistance near the fixed end, which increases the torsional stiffness and thereby minimizes the bend-twist coupling.

Stiffness parameters determined by the BPE-4x4-method.

All stiffnesses are determined at the location of the elastic center. Note that the 6x6-model and 4x4-model cannot in general be compared.

Since this blade section is highly coupled, the stiffness terms cannot be compared with the stiffness known from classical beam theory.

BPE-4x4-method	Axial stiffness $AE \cdot 10^6$ [Nm ²]	Flapwise bending stiffness $EI_x \cdot 10^6$ [Nm ²]	Edgewise bending stiffness $EI_y \cdot 10^6$ [Nm ²]	Torsional stiffness $GJ \cdot 10^6$ [Nm ²]	Bend-twist coupling (flap + torsion) $K_f \cdot 10^6$ [Nm ²]	Bend-twist coupling (edge + torsion) $K_e \cdot 10^6$ [Nm ²]
BPE-element 1	418,060	0,753	9,841	0,538	-0,121	0,011
BPE-element 2	475,371	1,113	13,537	0,692	-0,132	0,043
BPE-element 3	574,029	1,891	19,855	1,120	-0,182	0,038
BPE-element 4	683,966	3,140	28,108	1,567	-0,288	0,193
BPE-element 5	749,158	4,620	37,601	2,564	-0,462	0,450
BPE-element 6	810,367	6,437	49,432	3,345	-0,468	0,758
BPE-element 7	878,269	8,243	63,965	3,937	-0,208	0,417

Table 4.5.8

Stiffness parameters determined for the simple beam model with bend-twist coupling.

The stiffness terms in *Table 4.5.9* are terms from the “*Simple composite beam model with bend-twist coupling*”, described in chapter 3. The stiffness terms are determined by using load case M_x and M_z from the BPE-method.

The 4x4-model and the 2x2-model cannot in general be compared but since both models are independent of the location of the shear center, then a comparison can be assumed to be valid. Note that for the 2x2-model it is assumed that the reference coordinate system is orientated according to principle axes. The 2x2-model can be illustrated as:

$$\begin{pmatrix} M_x \\ M_z \end{pmatrix} = \begin{pmatrix} EI_x & -K_f \\ -K_f & GJ \end{pmatrix} \cdot \begin{pmatrix} \frac{\partial^2}{\partial z^2} w \\ \frac{\partial}{\partial z} \phi \end{pmatrix} \Rightarrow \begin{pmatrix} \frac{\partial^2}{\partial z^2} w \\ \frac{\partial}{\partial z} \phi \end{pmatrix} = \begin{pmatrix} D_{inv11} & D_{inv12} \\ D_{inv21} & D_{inv22} \end{pmatrix} \cdot \begin{pmatrix} M_x \\ M_z \end{pmatrix}$$

Equation 4.47

The inverted stiffness terms are determined by:

$$D_{inv11} = \left(\int M_x dz \right)^{-1} \cdot \Delta r_{x_mx} \quad D_{inv21} = \left(\int M_x dz \right)^{-1} \cdot \Delta r_{z_mx}$$

$$D_{inv22} = \left(\int M_z dz \right)^{-1} \cdot \Delta r_{z_mz} \quad D_{inv12} = \left(\int M_z dz \right)^{-1} \cdot \Delta r_{x_mz}$$

Equation 4.48

The stiffness terms are then computed by inverting the flexibility matrix (D_{inv}).

2x2-model with bend-twist coupling	Flapwise bending stiffness $EI_x \cdot 10^6$ [Nm ²]	Torsional stiffness $GJ \cdot 10^6$ [Nm ²]	Bend-twist coupling (flap + torsion) $K_f \cdot 10^6$ [Nm ²]
BPE-element 1	0,756	0,538	-0,122
BPE-element 2	1,117	0,692	-0,133
BPE-element 3	1,897	1,120	-0,183
BPE-element 4	3,147	1,566	-0,289
BPE-element 5	4,627	2,559	-0,463
BPE-element 6	6,442	3,333	-0,470
BPE-element 7	8,246	3,941	-0,212

Table 4.5.9

Comment

By comparing the stiffness terms (EI_x , GJ and K_f) in the two tables (*Table 4.5.8* and *Table 4.5.9*), it can be concluded that there is a general good agreement between the results from the 4x4-model and the 2x2-model. The bend-twist coupling is decreasing near the tip end, but that does not mean that the coupling coefficient ψ is decreasing.

The coupling coefficient is defined as:

$$\psi = \frac{K_f}{\sqrt{E I_x \cdot G J}} \quad -1 < \psi < 1$$

A coupling coefficient close to ± 1 indicate that the beam is highly coupled, while a coupling coefficient equal to zero indicates that there is no coupling between bending and torsion. In *Table 4.5.10* is the coupling coefficient ψ determined for the 2x2-model.

2x2-model with bend-twist coupling	(Flapwise) The coupling coefficient ψ
BPE-element 1	-0,191
BPE-element 2	-0,151
BPE-element 3	-0,125
BPE-element 4	-0,130
BPE-element 5	-0,135
BPE-element 6	-0,101
BPE-element 7	-0,037

Table 4.5.10

The coupling coefficients have negative sign because the bend-twist coupling introduces a negative twist when bended.

5. Experimental testing of the blade section

The aim of the experimental testing is to validate the FE-model. This is going to be done by comparing the experimental and numerical results. Three deflections and rotations for a number of cross sections along the blade section are going to be calculated from the experimental data. These deflections and rotations are going to be compared with the results from numerical models.

One of the primary aims of the master thesis is to determine the torsional stiffness parameter (GJ) and the bend-twist coupling parameter (K) for the blade section, since these parameters are primarily subjected to uncertainties. These parameters will therefore also be of great interest in the experimental testing.

The FE-analyses done in the pre-project and in the start of master thesis showed that the bend-twist coupling for the original blade section was so small that it was not possible to determine. An interesting question is therefore: Will the experimental results show the same? If that was the case, then there has been a discussion about adding some additional angled UD-ply on the suction and pressure side which will increase the coupling coefficient!

The reason for modifying the blade section is that the bend-twist coupling has to be of a considerably size, so it can be determined experimentally and by FEA. The comparison between these two results will give an idea about whether a simple FE-model can model this coupling correct.

5.1. The test rig

The test rig was designed during the pre-project and assembled at DTU's laboratory in the beginning of the master-thesis. The test rig at DTU is shown below. The picture from Pro/Engineer shows three hydraulic presses, but only two presses are going to be used. The reason why three presses are shown is just to indicate all the possible placements for the presses.

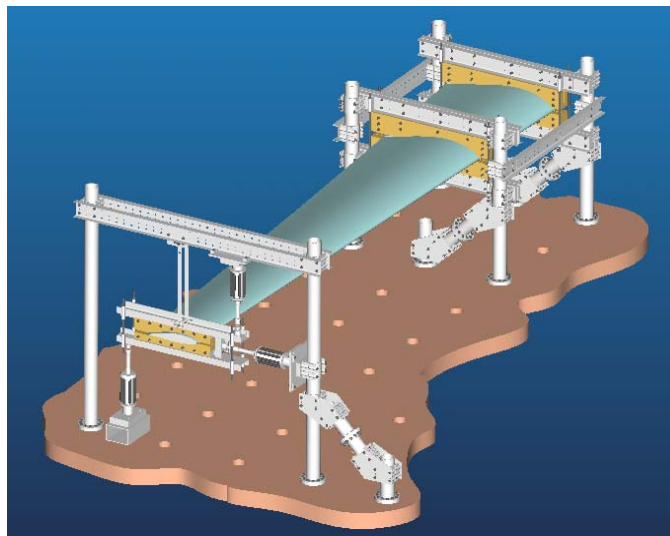


Figure 5.1.1: The test rig

5.1.1. The principle construction of the test rig

The test rig is basically made of two separate systems, one part is the pre-setup in the laboratory and the other part is the blade section with the clamps. The idea behind having two separate systems is that the systems can be assembled independently of each other and to a certain degree be modified independently of each other. The two systems are shown below:

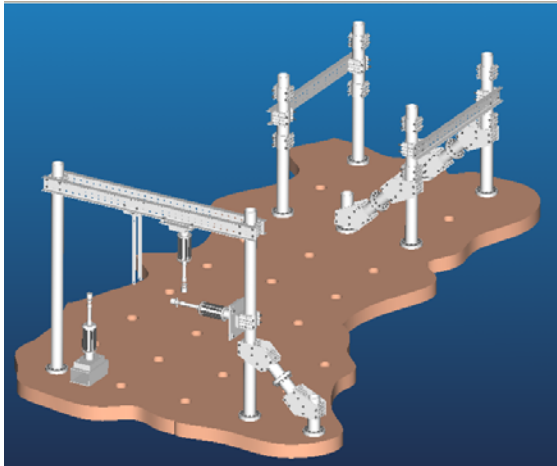


Figure 5.1.2- The pre-setup in the laboratory

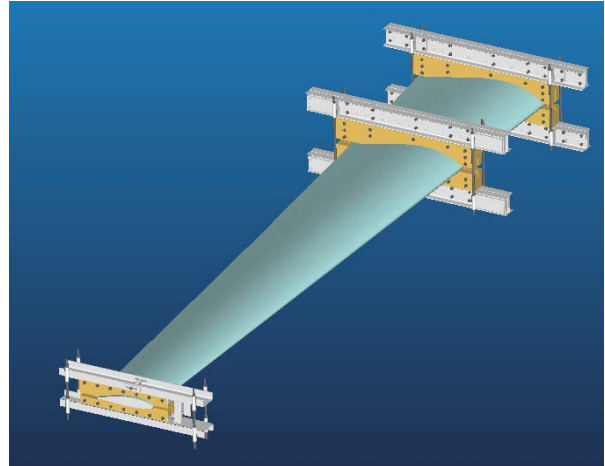


Figure 5.1.3- The blade section with clamps

The pre-setup in the laboratory

The entire pre-setup at the laboratory at DTU is made of standard components from the laboratory. These standard components are steel columns, UNP-profiles with mounting holes, friction-clamps and horizontal supports. The concrete floor in the laboratory is fitted with mounting holes for the vertical steel columns and horizontal supports. A steel column is able to withstand a horizontal force of 500 kN and moment of 50 kNm.

The components for the test rig were dimensioned by doing conservative strength and stiffness calculations in order to have a sufficient stiffness and safety.

The blade section with clamps

This system is made of three sub-systems, the two clamps that create the rigid connection (*clamp 1 and 2*), the tip clamp (*clamp 3*) and finally the blade section.

Clamp 1 and 2 are constructed of four standard UNP-profiles from the laboratory, where steel strips clamped between these profiles creates the mounting device for the contour-cut upper and lower part of plywood. These contour-cut parts are each made of six plywood plates that are stacked together to form the upper or lower part.

A rubber cushion is going to be placed between the contour-cut parts and the blade surface, the rubber levels any crookedness between the surfaces of the clamp and the blade. The rubber also provides a good contact between blade section and the clamps.

The upper and lower part of a clamp is bolted together with four M24 thread bars. These four thread bars run through the two types of brackets, which are shown below. To avoid any twisting and movement of the upper and lower part relative to each other, then each of the thread bars is fitted with four lock nuts. Bracket 2 is partly constructed for the bolted connection between the upper and lower part of the clamps, but bracket 2 also is the joint between the blade section with clamps and the pre-setup. Bracket 2 is constructed with four M20 thread holes, and with these holes one can bolt the clamps to the steel columns by using the friction-clamps.

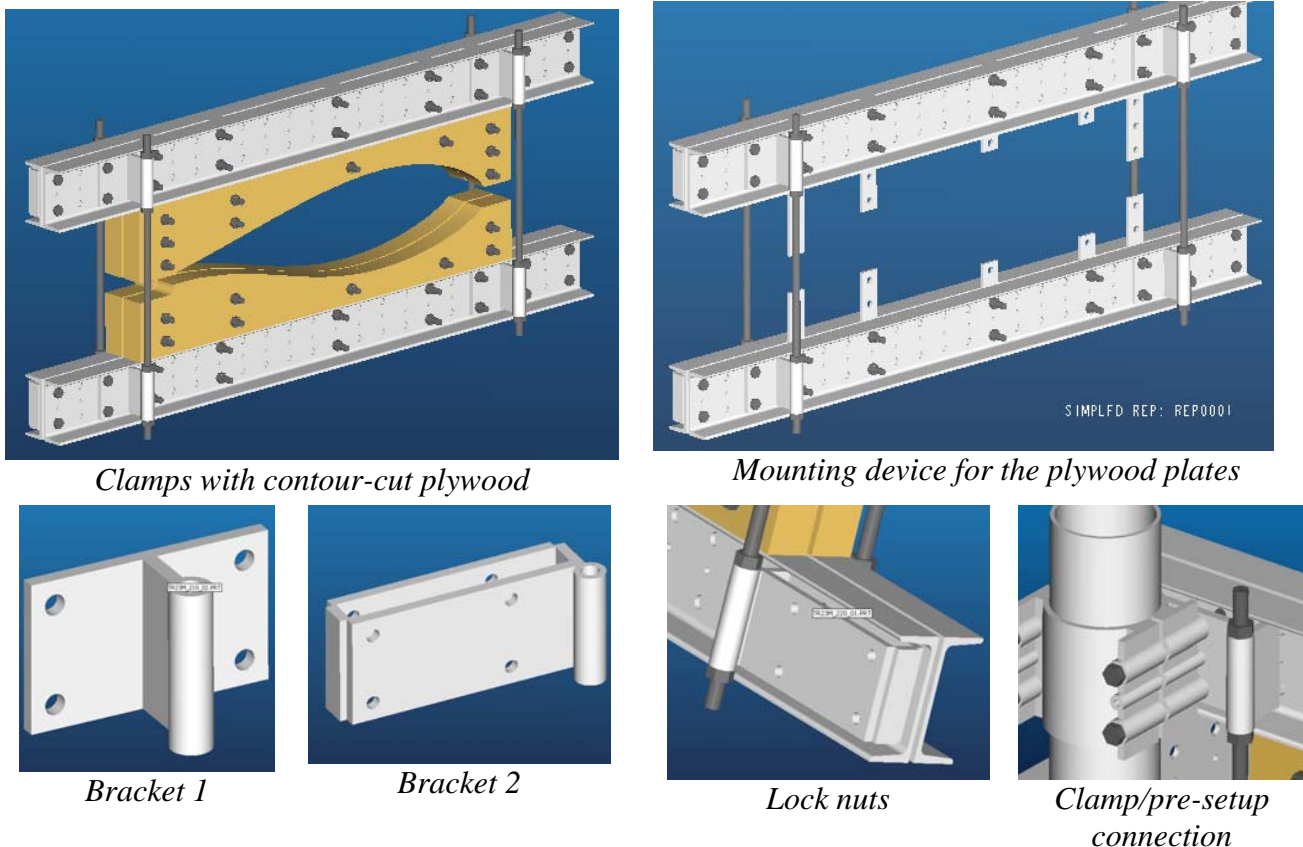


Figure 5.1.4 - Assembled clamp and its components

Clamp 3 is basically built in the same way as clamp 1 and 2.

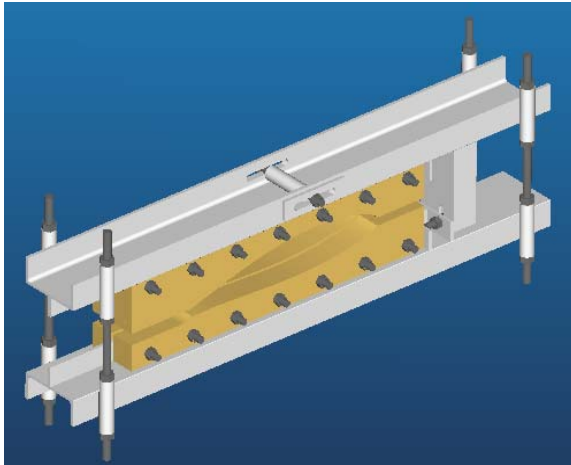
Here are the primary components the upper and lower part which are made of two standard UPE-profiles with a steel strip welded on. These steel strips stiffen the UPE-profiles, but they also function as mounting devices for the contour-cut plywood plates.

The upper and lower part are bolted together in pretty much the same way as clamp 1 and 2.

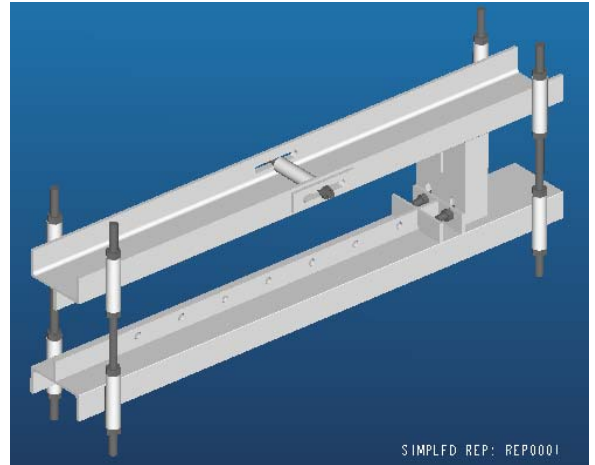
At the middle of the upper UPE-profile, a slit is made in the webs and in this slit a M20 bolt can be fastened, creating the lock-system which is going to be used during the locked torsion test.

This lock-system is also going to be used when the blade section is going to be bended more than 125mm, which is the maximum stroke length of the hydraulic presses. The method for bending the blade section more than 125mm is described later in the report (see 7.3.2).

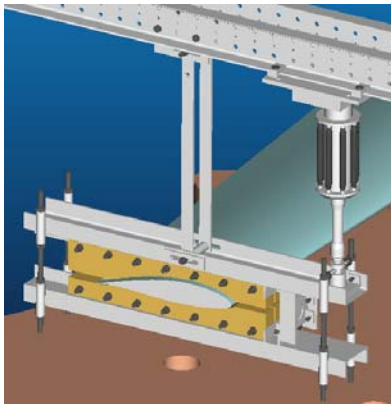
When the clamp is locked it is able to rotate and move in the horizontal plane (in a circular arc movement) but not in the vertical plane. This lock-system can be seen below. The hydraulic presses are able to rotate some few degrees in both ends because they are fitted with spherical joints. This rotation is important when the bend-twist coupling is going to be measured. To be absolutely sure that the hydraulic presses are applying the forces in the right places, then a fixing-unit is constructed and placed inside the UPE-profiles. These fixing-units can be placed inside the top UPE-profile, the vertical UPE-profile and in the lower UPE-profile.



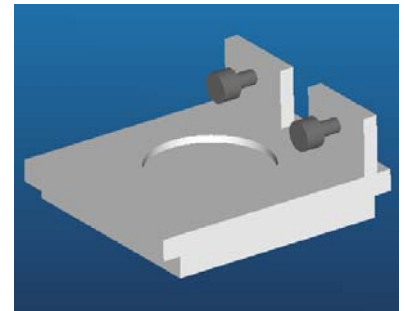
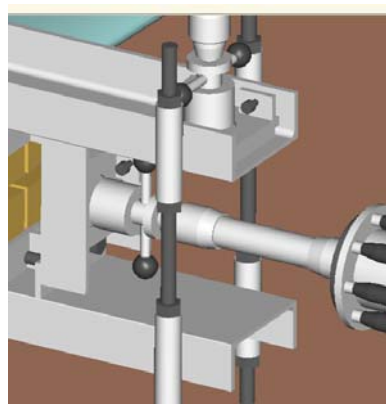
Clamp 3 with contour-cut plywood



Clamp 3 without the contour-cut plywood



The lock-system



The fixing-unit that guides the hydraulic presses

Figure 5.1.5 - Assembled load clamp (clamp 3)

Stiffening of the trailing edge at the spar at the blade tip:

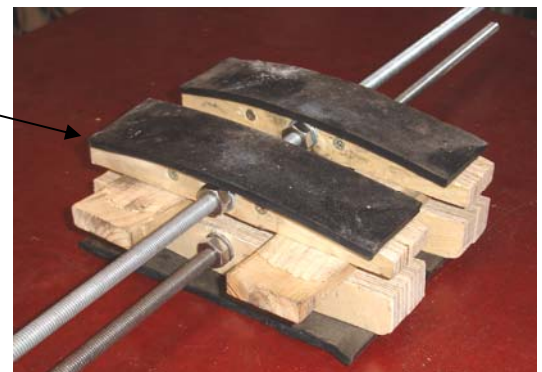


Figure 5.1.6 – Stiffening of load clamp (clamp 3)

5.1.2. The five test methods

The test rig at DTU can perform five different tests which are used to validate the FEM of the blade section. The five different tests are:

- *Flapwise bending*
- *Flapwise bending and torsion*
- *Edgewise bending*
- *Pure torsion*
- *Locked torsion*

Flapwise bending

The point load is applied at the center of the spar at the blade tip. The center of gravity for the load clamp (*clamp 3*) is located at the center of the spar where the force is applied and the weight of the clamp will therefore not produce at torsional moment. The blade is pre-bended before measuring which eliminates the effect of the weight of clamp and the blade section. The measuring equipment is then set to “zero” in the pre-bended condition.

If the flapwise bending is going to exceed 125mm (*tip deflection*), then the test must be done in some steps, because the maximum stroke length of the hydraulic presses are 125 mm.

Step 1: The tip end of the blade section is bended 125mm, which is the maximum stroke length of the press.

Step 2: Clamp 3 is locked in the position 125mm over the starting point by using the locking-system (the locking-system can be seen in *Figure 5.1.5*). The press is unloaded and the spindle is moved the 125mm.

Step 3: Clamp 3 is then released from the locking-system.

Step 4: The tip end can now be bended an additional 125mm (the maximum deflection of the tip end is 250mm).



Figure 5.1.7 - Flapwise bending

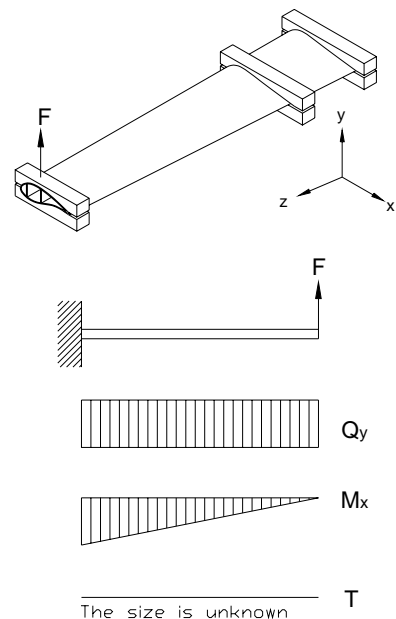


Figure 5.1.8

Test advantages:

- This test is easy to perform in the laboratory, since the point load is simple to create with the hydraulic presses from the laboratory.

Test disadvantages:

- This load type will give shear-extension coupling (probably of very limited size).
- The location of the shear center is not known and therefore is the size of the torsional moment not known (the torsional moment is equal to shear force multiplied with the distance to the shear center).

Flapwise bending and torsion

This test is a combination of flapwise bending and torsion. The point load is applied at a distance from the center of the spar (0.695m), which creates a bending moment and a torsional moment. The blade is pre-bended before measuring which eliminates the effect of the weight of clamp and the blade. The measuring equipment is then set to “zero” in the pre-bended condition.

This test can also be carried out in several steps like the flapwise bending test, if it should be of interest to deform the tip more than 125mm.



Figure 5.1.9 - Flapwise bending and torsion

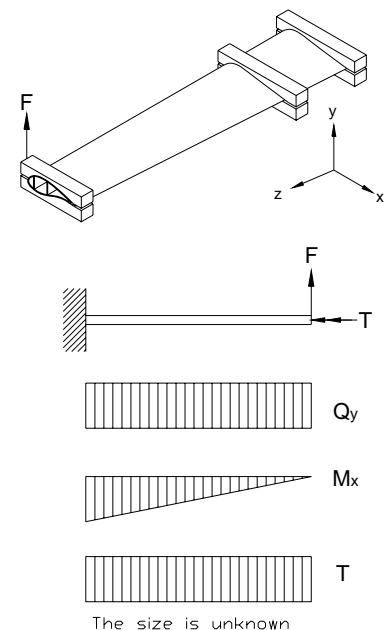


Figure 5.1.10

Test advantages:

- This test is easy to perform in the laboratory, since the point load is simple to create with the hydraulic presses from the laboratory.

Test disadvantages:

- This load type will give shear-extension coupling (probably of very limited size).
- The location of the shear center is not known and therefore is the size of the torsional moment not known (the torsional moment is equal to shear force multiplied with the distance to the shear center).

Edgewise bending

The load is applied horizontally in the center of the spar at the blade tip. The measuring equipment is set to “zero” in the pre-bended stage. The picture below shows three hydraulic presses but only the horizontal press is being used.

The edgewise bending test is carried out by placing the press head in the fixing-unit, which is placed in the vertical UPE-profile. The fixing-unit is fitted with a central hole which works as a guidance for the press under the deformation of blade section.



Figure 5.1.11: Edgewise bending

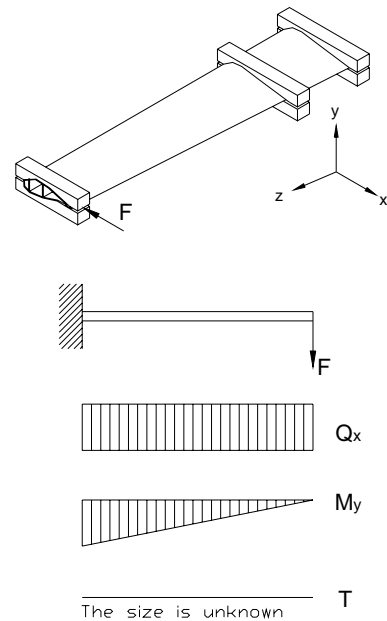


Figure 5.1.12

Test advantages:

- This test is easy to perform in the laboratory, since the point load is simple to create with the hydraulic presses from the laboratory.

Test disadvantages:

- This load type will give shear-extension coupling (probably of very limited size).
- The location of the shear center is not known and therefore is the size of the torsional moment not known (the torsional moment is equal to shear force multiplied with the distance to the shear center).
- The test rig is not very rigid in the horizontal plan, which can result in some problems with the boundary conditions.

Pure torsion

The pure torsion test is performed by using two hydraulic presses that create a force couple. The two point loads are placed at a distance from the center of the spar (0.695m), which creates the torsional moment. The blade is pre-twisted before measuring which eliminates the effect of the weight of clamp and the blade. The measuring equipment is then set to “zero” in the pre-twisted condition.

The applied forces from the two presses must be equal in order to create the correct torsional moment (it is not required that the presses travel/stroke are equal).

This test is performed very slowly, because it can be troublesome to control the two presses manually.



Figure 5.1.13 - Pure Torsion

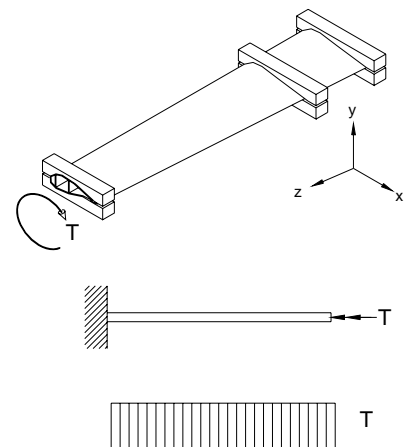


Figure 5.1.14

Test advantages:

- This test method is in theory probably the optimal method for determining the torsional stiffness and the bend-twist coupling.

Test disadvantages:

- The torsional moment is very difficult to apply in reality since the blade/tip must be able to move freely, which is required in order to measure the induced bending deflection.

Locked torsion

In the locked torsion test is the clamp locked in a given point that cannot move in the vertical plane. The clamp can rotate and move in the horizontal plane since the steel strip is able to rotate in both ends. The movement in the horizontal plane is not 100% free because this movement is a circular arc. The point load is applied at a distance from the centre of the spar (0.695m), which creates a torsional moment.

In this test is the locking-system used to force the tip end to rotate about a point directly over the center of spar.

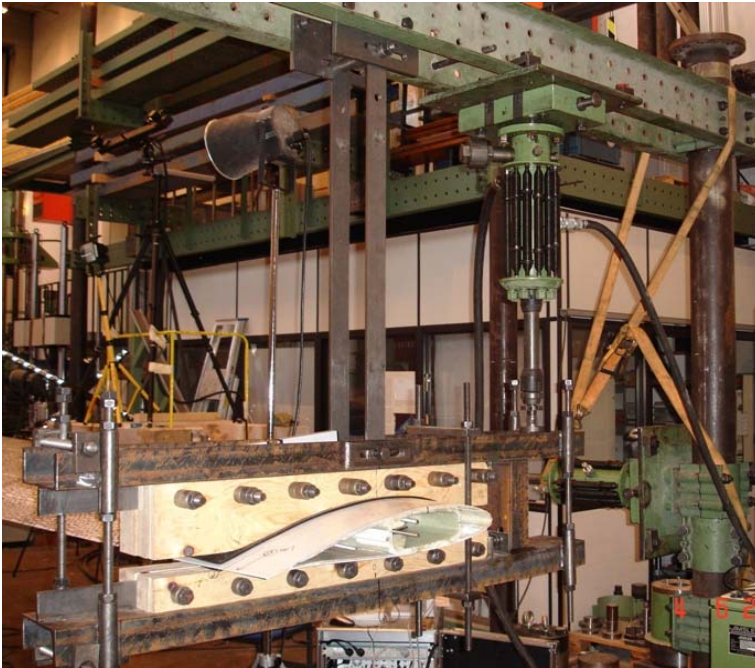


Figure 5.1.15 - Locked torsion

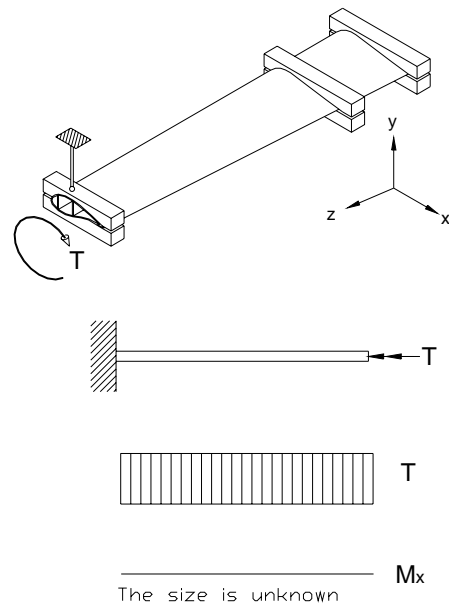


Figure 5.1.16

Test advantages:

- Unlike the pure torsion test is this test easy to perform in the laboratory, since the blade tip is locked and this means that the torsional moment is simple to create.
- If the bend-twist coupling is of limited size, is this method a simple way to determine the torsional stiffness.

Test disadvantages:

- If the bend-twist coupling is of a considerable size then will blade tip “try” to move in the vertical plan, but this is not possible because of the locking-system. An induced force will therefore be absorbed in the locking-systems two steel trips and that complicates the analysis.
- The tip will try to rotate about a type of “global shear center” and the chosen rotational point is probably not 100% identical to this point. This will probably create some strange behaviour near the loading clamp.

5.2. Measuring method for the original blade section

All measuring of the original blade section were done with the 3D optical ARAMIS 2M system (2M = two mega-pixel cameras).

The deformation measuring system ARAMIS records an object/surface under load using CCD cameras. To measure the 3D deformation of an object, two cameras are needed. For each stage of load, the 3D coordinates of the object surface are calculated on the basis of digital image processing, delivering also the 3D displacement and the surface strain.

For the ARAMIS system to do this then a pattern (typically black spray on a white background) has to be applied to the object/surface and a common starting point has to be selected in the right and the left image (the two images/pictures are captured by the two cameras). The system is then able to calculate a 3D area/surface. This makes the system ideal for validating FE calculations. All measuring of the blade section is done according to the guidelines from ARAMIS.

Since the measuring surfaces on the blade section are of a considerable size then the pattern could not be created by spraying black paint on the surface. A rougher pattern was needed. Some tests were performed to develop a pattern, which could be used on the blade section. The best result was obtained by applying dim black spots of a size around 6.6mm on the surface, see picture below:

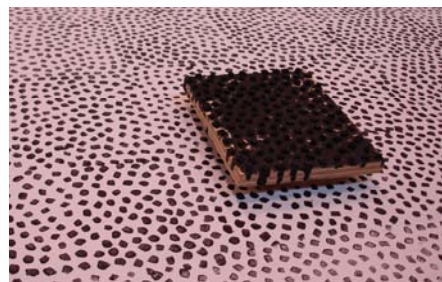


Figure 5.2.1 – Measuring pattern

For the ARAMIS system to capture as much of the blade surface as possible, then the two cameras had to look down on the surface. A simple platform for the ARAMIS equipment was created. This arrangement can be seen in picture below:



Figure 5.2.2 – Camera setup

The blade deflections (u_x , u_y and u_z) were measured with the 3D optical ARAMIS system. The ARAMIS system is not capable of covering the entire 6m blade and the blade was therefore divided into the following four measuring areas:

- Area 1: 0.00 – 0.93 m (0.00 = R12.827 m for the 23m blade (measured from the hub))
- Area 2: 0.93 – 2.63 m.
- Area 3: 2.63 – 4.33 m.
- Area 4: 4.33 – 6.03 m.

The measuring of the four areas was done by moving the ARAMIS equipment along the blade section, which means that four measuring stations along blade section were used. The force from the hydraulic cylinder was obtained from a digital signal from the hydraulic pump station which was loaded into the ARAMIS system. These signals showed the pressure/force that was applied and the ARAMIS results for the four areas were then assembled to create a complete measuring area/surface of 6m (the entity blade section). Each area was divided into 3-5 cross sections from which the displacements were obtained. For each load case were 5 images/pictures generated. Images 1 show the undeformed area, images 2 show the deformed area with 25% of the load etc. and finally, image 5 show the deformed area with 100% of the load.

One can easily determine if the blade response is linear or non-linear from this “loading history”. Each load case was performed 3 times to ensure that the data was consistent. The first time the test was performed is called run 1, second time is called run 2 and third time is called run 3. The four undeformed areas are shown below:

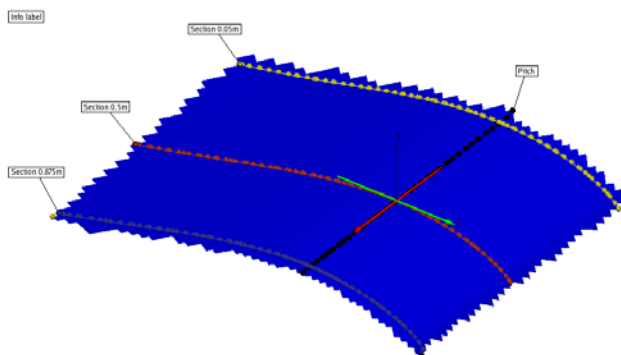


Figure 5.2.3: Area 1 (undeformed stage)

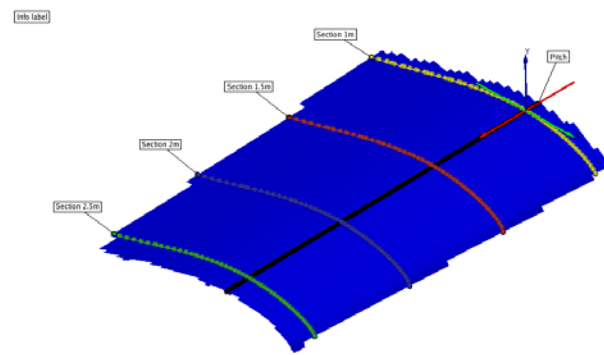


Figure 5.2.4: Area 2 (undeformed stage)

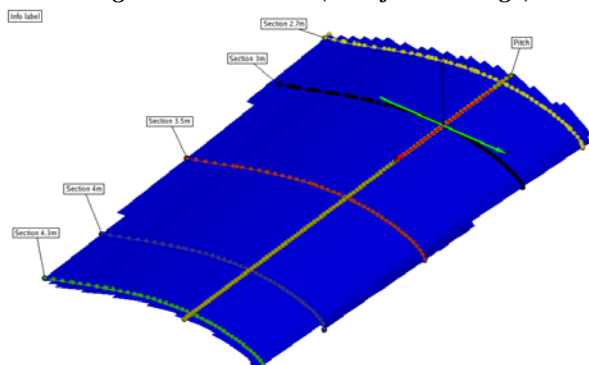


Figure 5.2.5: Area 3 (undeformed stage)

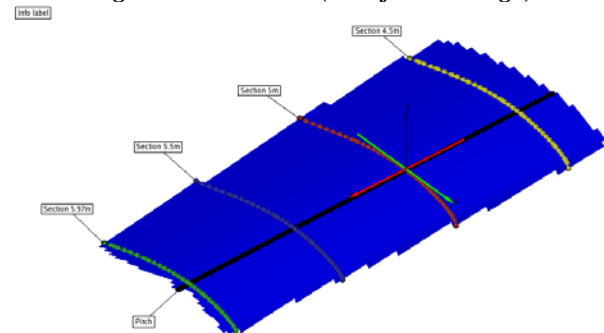


Figure 5.2.6: Area 4 (undeformed stage)

The deformed areas that are shown below are for the combination of the flapwise bending and torsion test, for 100% of the load (image 5). The displacements are shown for the y- direction:

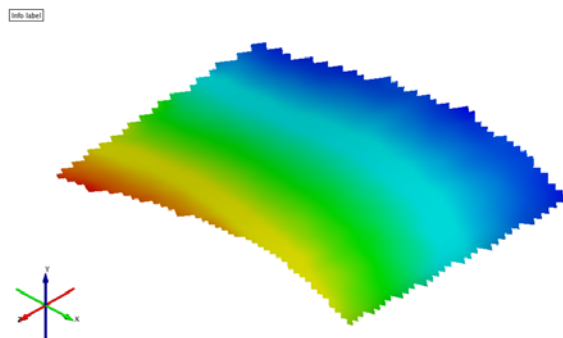


Figure 5.2.7: Area 1 (flap+torsion)

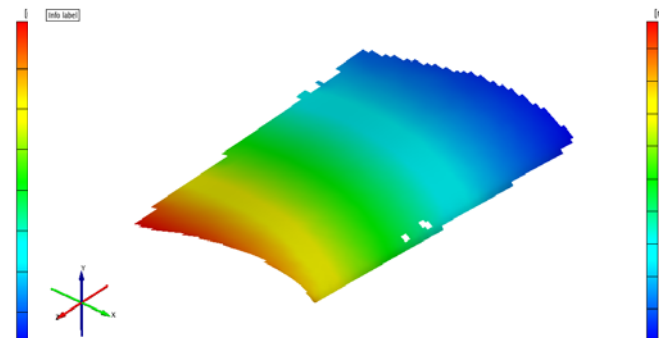


Figure 5.2.8: Area 2 (flap+torsion)

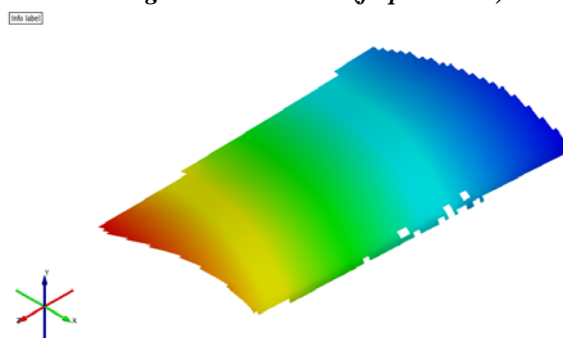


Figure 5.2.9: Area 3 (flap+torsion)

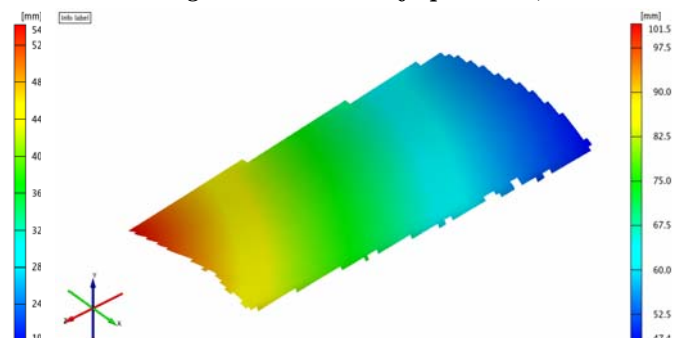


Figure 5.2.10: Area 4 (flap+torsion)

5.3. Experimental determination of the deflections and rotations

The following eleven cross sections were chosen:

- Cross section 0.5 m (R13.327 for the 23m blade)
- Cross section 1.0 m
- Cross section 1.5 m
- Cross section x.x m
- Cross section 4.5 m
- Cross section 5.0 m
- Cross section 5.5 m (R18.327 for the 23m blade)

The deflections and rotations were calculated for the eleven cross sections. The undeformed and deformed cross sections are plotted below for the flapwise bending and torsion test:

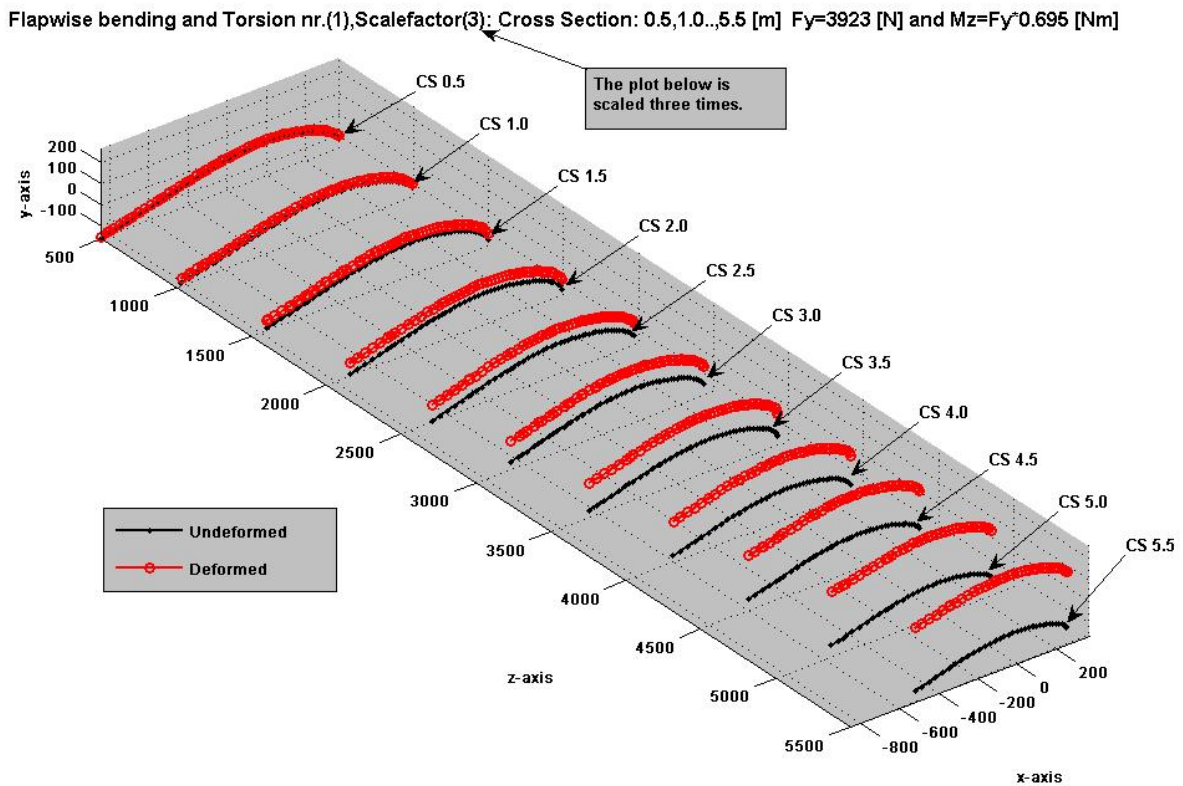


Figure 5.3.1: Flap + torsion

Displacements

The three displacements were calculated as average values. It means that all the relative nodal/point displacements are summed up and then divided by the number of nodes/points. (Δx , Δy and Δz = relative displacements).

$$u_x = \frac{\sum_{i=1}^n \Delta x_i}{n} \quad u_y = \frac{\sum_{i=1}^n \Delta y_i}{n} \quad u_z = \frac{\sum_{i=1}^n \Delta z_i}{n}$$

Rotation about the z-axis (r_z)

The rotation about the z-axis (twist-angle (r_z)) can be calculated by two different methods. Both methods work by linear least squares regression.

The first method for the experimental calculation of the twist angle is illustrated below:

The theory of linear least squares regression is shown below:

$$F = \begin{pmatrix} 1 & x_1 \\ 1 & x_2 \\ \dots & \dots \\ 1 & x_n \end{pmatrix} \quad \begin{pmatrix} b \\ r_z \end{pmatrix} = (F^T \cdot F)^{-1} \cdot F^T \cdot \begin{pmatrix} dy_1 \\ dy_2 \\ \dots \\ dy_n \end{pmatrix}$$

$$y(x) = r_z \cdot x + b$$

r_z is the rotation about the z-axis (twist-angle).

dy is the difference between the deformed and undeformed y-values.

x_i are the deformed x-values.

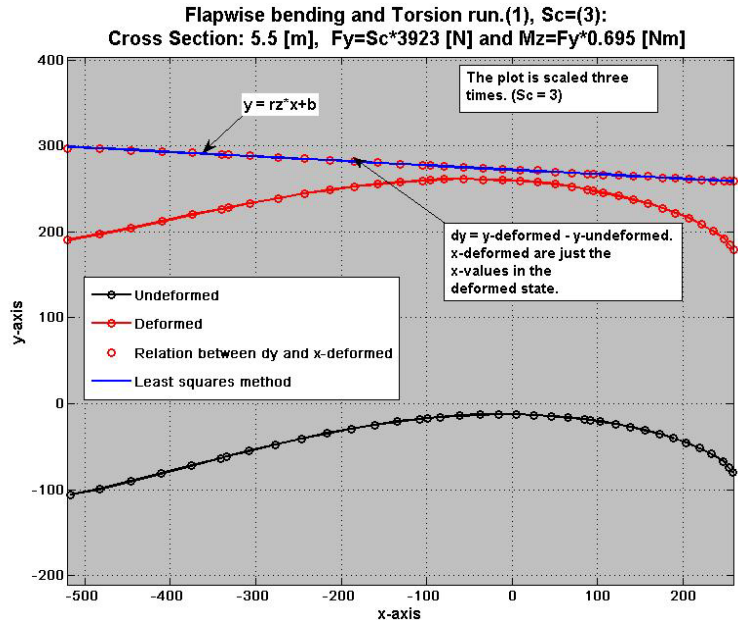


Figure 5.3.2 - Plot of twist-angle

This method for determining the twist angle was tested on several cross sections and showed to be very accurate for small twist angles.

This method was also compared with another method, which in short worked by fitting a linear least squares curve through the deformed and undeformed cross section. The difference between the slopes for the two curves is then equal to the twist angle, see illustration below:

The theory of linear least squares regression is shown below:

$$F = \begin{pmatrix} 1 & x_1 \\ 1 & x_2 \\ \dots & \dots \\ 1 & x_n \end{pmatrix} \quad \begin{pmatrix} b \\ r_z \end{pmatrix} = (F^T \cdot F)^{-1} \cdot F^T \cdot \begin{pmatrix} y_1 \\ y_2 \\ \dots \\ y_n \end{pmatrix}$$

$$y(x) = r_z \cdot x + b$$

$r_{z2} - r_{z1}$ is the rotation about the z-axis (twist-angle).

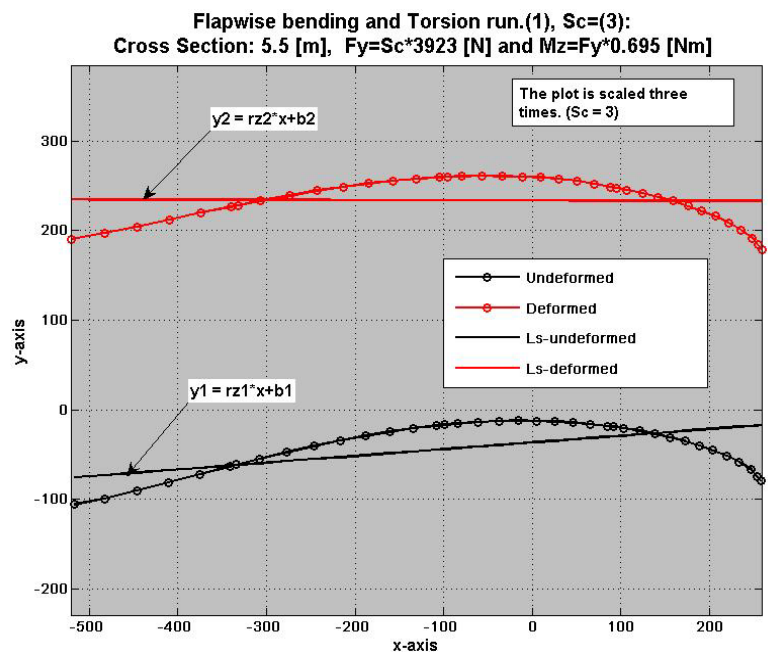


Figure 5.3.3 - Plot of twist-angle

Comment on the two methods for determining the twist angle

The two methods were tested on several deformed cross sections for which the twist angle was known and the results from the two methods showed that both methods were very accurate but the first method was slightly better and was therefore used.

Rotations about the x- and y-axis (r_x and r_y)

The rotations about the x- and y-axis were calculated by fitting a multiple regression plane through the deformed cross section. Below is it illustrated how the two rotation-angles were calculated (For a more detailed description, see chapter 4):

The theory of multiple regression is shown below:

$$F = \begin{pmatrix} 1 & x_1 & y_1 \\ 1 & x_2 & y_2 \\ \vdots & \vdots & \vdots \\ 1 & x_n & y_n \end{pmatrix}$$

$$\begin{pmatrix} b \\ r_y \\ r_x \end{pmatrix} = (F^T \cdot F)^{-1} \cdot F^T \cdot \begin{pmatrix} z_1 \\ z_2 \\ \vdots \\ z_n \end{pmatrix}$$

$$z(x, y) = b + r_y \cdot x + r_x \cdot y$$

r_y is the rotation about y.
 r_x is the rotation about x.

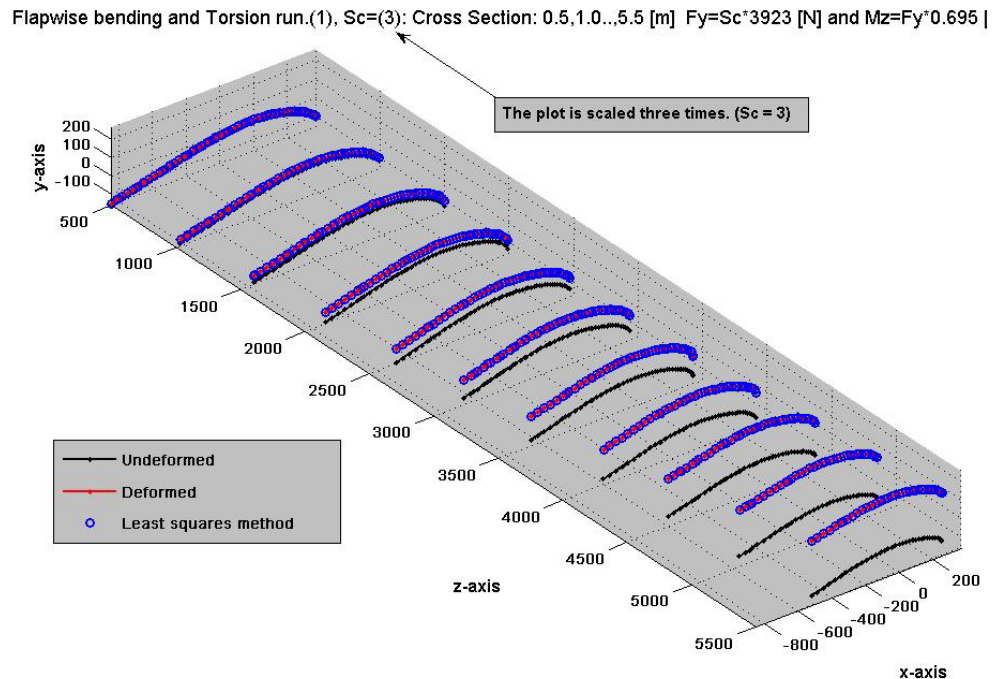


Figure 5.3.4 - 3D plot of multiple regressions planes

The blue points/o's are plotted on the multiple regressions planes, which can be seen on the plot above.

Each cross section will potentially have hundreds of degrees-of-freedom in reality, but by using the described method then each cross section can now be described by three displacements and three rotations. In this way is each cross section now described by a single set of displacements and rotations and that is a big step towards a 3D beam model.

The idea is to do the same for the FE-model and in this way can the displacements and rotations for each cross section be compared with results from the “experimental cross sections”.

5.3.1. Boundary conditions

The blade section is of course not fully fixed since the test rig is not infinite rigid.

The ARAMIS equipment was used to investigate the deformed surface of the blade section near the “fixed end”. The undeformed and deformed surfaces near the “fixed end” are plotted below. The images are from the flapwise bending and torsion test:

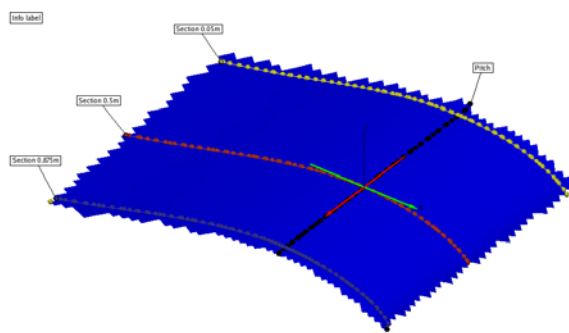


Figure 5.3.5: Undeformed surface near the Boundary condition.

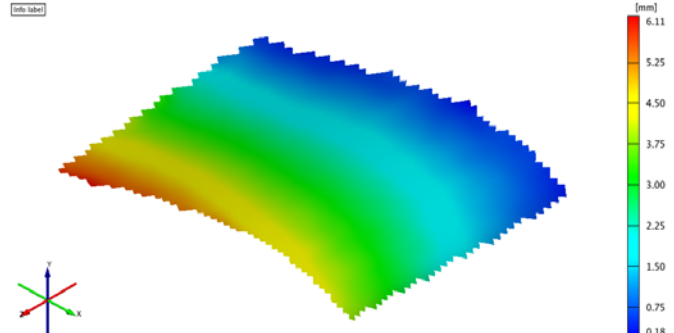


Figure 5.3.6: Displacement in the y-direction near the Boundary condition.

One can see that there is a small displacement in the y-direction near the boundary (see *Figure 5.3.6*), which means that the blade section cannot be assumed to be a cantilever beam.

The experimental and numerical results can only be compared if the experimental and numerical boundary conditions are the same. The problem with the boundary conditions can be solved in following ways:

- One can model the test rig boundary conditions by measuring the deflections of the clamps with the Aramis equipment. These deflections can then be applied to the FE-model.
- One can also model the test rig boundary conditions by modeling the clamps. To get a realistic FE-model of the clamps, one must model the plywood plates and the steel profiles and then use contact elements to model the contact between the clamps and the blade section.
- Finally, one can solve the test rig boundary condition problem by using the Aramis experimental data to determine all the cross sectional displacements and rotations via least squares algorithms.
One can create a fully fixed and clamped boundary condition by subtracting the measured deflections and rotations of the cross section where one wants the fixed end, from all the other cross sections.

The last method was chosen since this is the simplest and probably also the most precise method. The cross section near the “fixed end” was chosen to be cross section 0.5 m (R13.327 for the 23m blade). The last method was chosen because it involves simple FE-modeling since one can use a “standard” fixed boundary condition where all nodal displacements and rotations are set to zero. Furthermore, the last method is very flexible because one can select an “arbitrary” location for the fixed end from the measured cross sections along the blade section.

Another problem with the boundary conditions in the experiments is near the load clamp (clamp 3). It is impossible to apply a load without introducing some local deformations, which will affect the results. As mentioned earlier, the tip end of the blade section was stiffened in the spar and in the trailing edge to avoid local deformations. Besides the internal stiffening, then was the local deformations “completely” removed by not considering the last half meter that was measured.

The experimental and numerical results are compared by obtaining the cross sectional displacements and rotations in the same manner. The FE-model was fully fixed in the cross section where clamp 2 is located and the loads were of course applied at the location of clamp 3, but the first and last half meter are not considered which is identical to the way that the experimental data are analyzed. The problems with the rigid ends for the FE-model are at the same time minimized.

There is a considerable problem with rigid ends in the FE-model. This is because the ends restraints warping which increases the stiffnesses (especially the torsional stiffness).

It is shown below how the deflections and rotations for the different cross sections are calculated (L_e is the length of the beam elements).

$$L_e = (0 \ 500 \ 500 \ 500 \ 500 \ 500 \ 500 \ 500 \ 500 \ 500 \ 500)^T \cdot \text{mm}$$

$$u_{x_i} = u_{x_i} - u_{x_1} - r_y \cdot \sum_{i=1}^i L_{e_i}$$

$$u_{y_i} = u_{y_i} - u_{y_1} + r_x \cdot \sum_{i=1}^i L_{e_i}$$

$$u_{z_i} = u_{z_i} - u_{z_1}$$

$$r_{x_i} = r_{x_i} - r_{x_1}$$

$$r_{y_i} = r_{y_i} - r_{y_1}$$

$$r_{z_i} = r_{z_i} - r_{z_1}$$

5.4. Experimental results for the five test methods

Five tests were performed and for each test were the three displacements and rotations determined for a number of cross sections along the blade section.

In the following will the displacements and rotations for cross section 0.5 m be subtracted from all the other cross section, which means that the new fixed end is placed 0.5m from the original fixed end (0.5m from clamp 2).

Flapwise bending

The flapwise bending was performed with a point load of 3923 [N] placed 5.607m from cross section 0.5 m. This results in a bending moment and a shear force distribution described as described earlier. Each load case was performed 3 times to ensure that the data is consistent. The first time the test is performed is called run 1, second time is called run 2 and third time is called run 3:

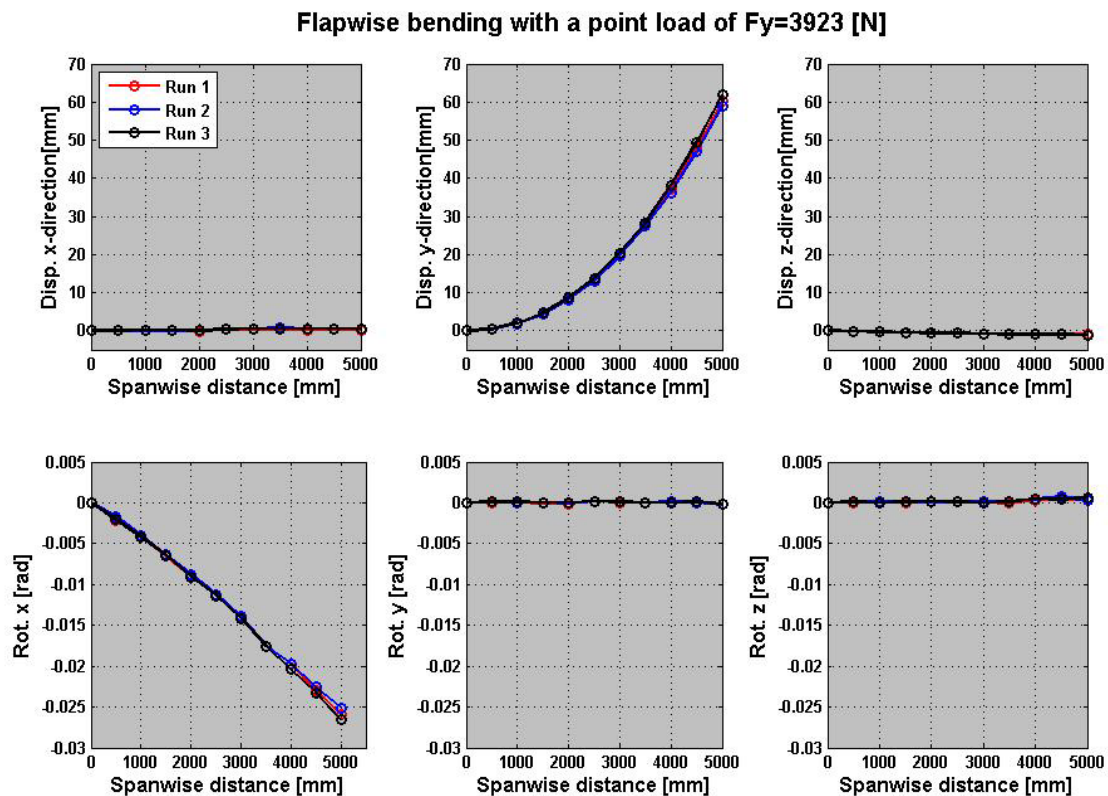


Figure 5.4.1 – Results from flapwise bending

Comment

The data for the three runs are reasonable consistent, as one can see on the plots of the displacements and rotations.

The test results more or less only in a displacement in the y-direction and a rotation about the x-axis (bending slope), which also was expected.

As mentioned earlier, the location of the shear center is not known, which means that the shear force placed in the center of the spar can result in a small torsional moment! If it is assumed that the shear center is placed in middle of spar then will this flapwise bending test indicate that the bend-twist coupling is equal or close to zero, since the bending moment do not result in a twist angle (rotation about the z-axis) of blade section.

Flapwise bending and Torsion

The flapwise bending and torsion test was performed with a point load of 3923 [N] placed 5.607m from cross section 0.5 m and at a distance of 0.695m from the center of the spar. This results in a bending moment, torsional moment and shear force distribution as described earlier:

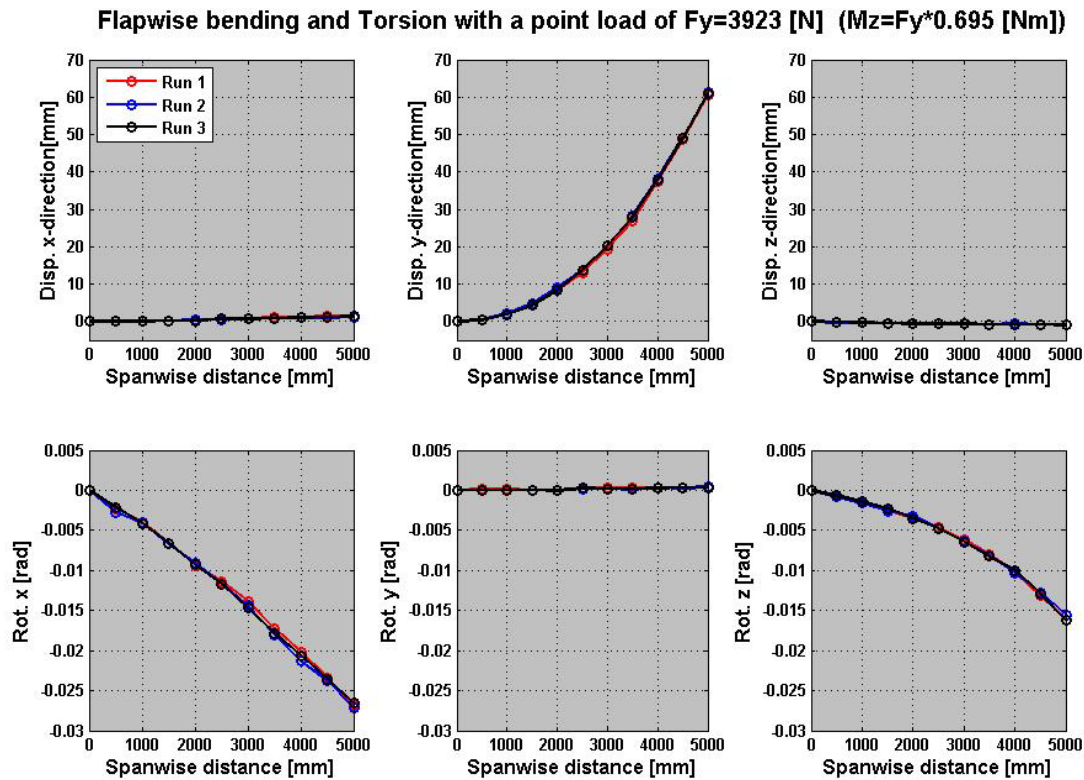


Figure 5.4.2 – Results from flapwise bending and torsion

Comment

The data for the three runs are reasonable consistent, as one can see on the plots of the displacements and rotations.

The test results in a displacement in the y-direction, rotation about the x-axis (bending slope) and rotation about the z-axis (twist angle).

The “tip deflection” in the y-direction is close to 60 mm, which also was the case for the flapwise bending test. This indicates again that the bend-twist coupling is equal or close to zero, since a bend-twist coupling would result in a different deflection in the y-direction (twist induced bending).

Edgewise bending

The edgewise bending test was performed with a horizontal point load of 4903 [N] placed 5.607m from cross section 0.5m. This results in a bending moment and shear force distribution as described earlier:

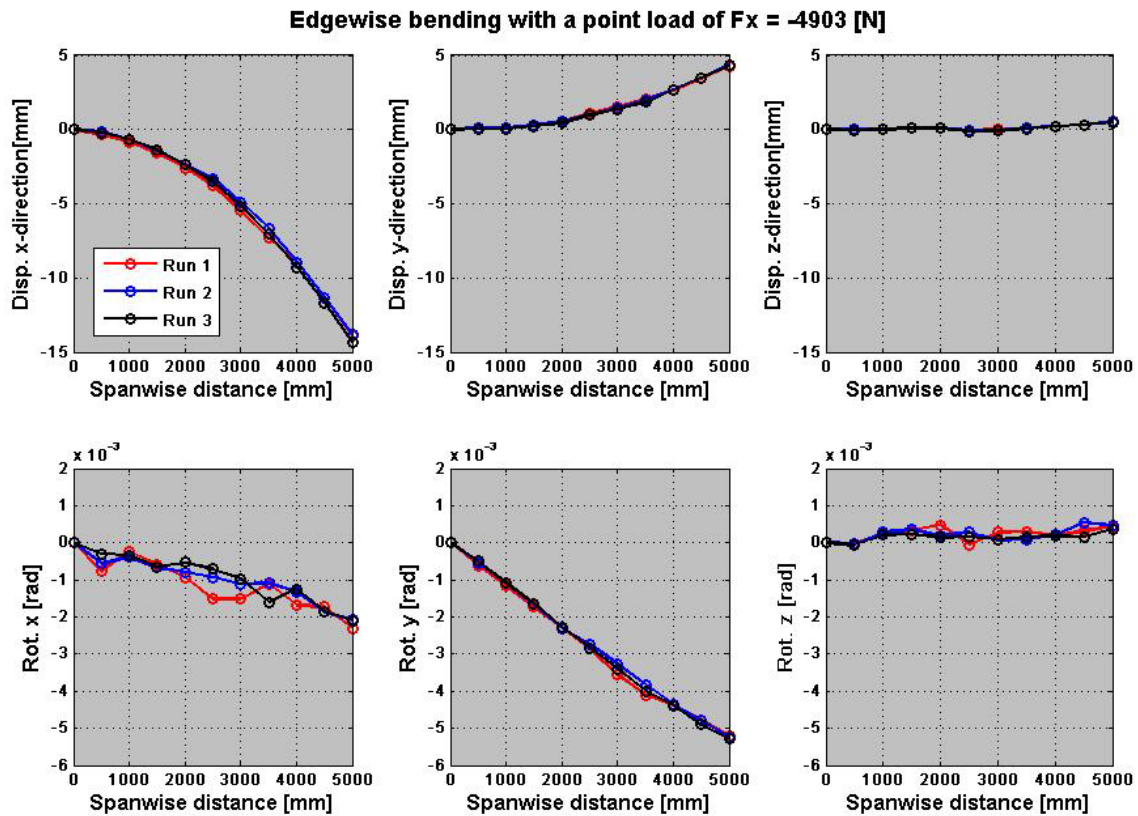


Figure 5.4.3 – Results from edgewise bending

Comment

The data for the three runs are reasonable consistent, as one can see on the plots of the displacements and rotations.

The test results in a displacement in the x-direction as expected but also a small displacement in the y-direction. The deflections in the two directions produce of course a rotation about the y-axis and a small rotation about the x-axis. The displacement in the y-direction could be a result of the orientation of principle axes. If the principle axes are orientated as illustrated in *Figure 5.4.4* then would a force in the global x-direction result in a bending moment about the principle x- and y-axis and this will make blade section bend in both directions.

One has to remember that edgewise bending stiffness is about five times larger than the flapwise bending stiffness and this could be the reason why the flapwise bending test did not indicate that the principle axes are rotated compared with the global coordinates.

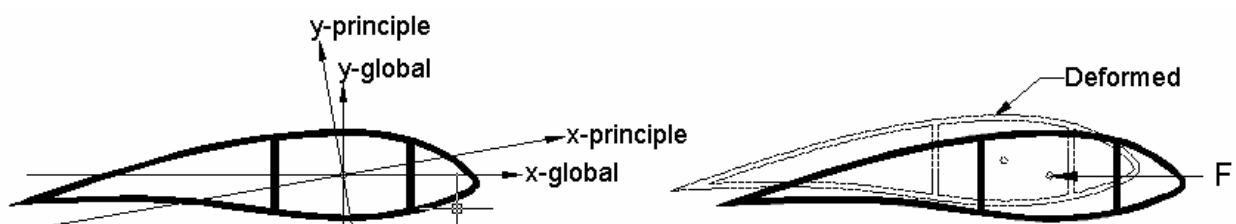


Figure 5.4.4: Orientation of the principle axes.

Pure Torsion

The pure torsion test was performed by applying a force couple at the tip end. This force couple creates a torsional moment of 3408 [Nm]:

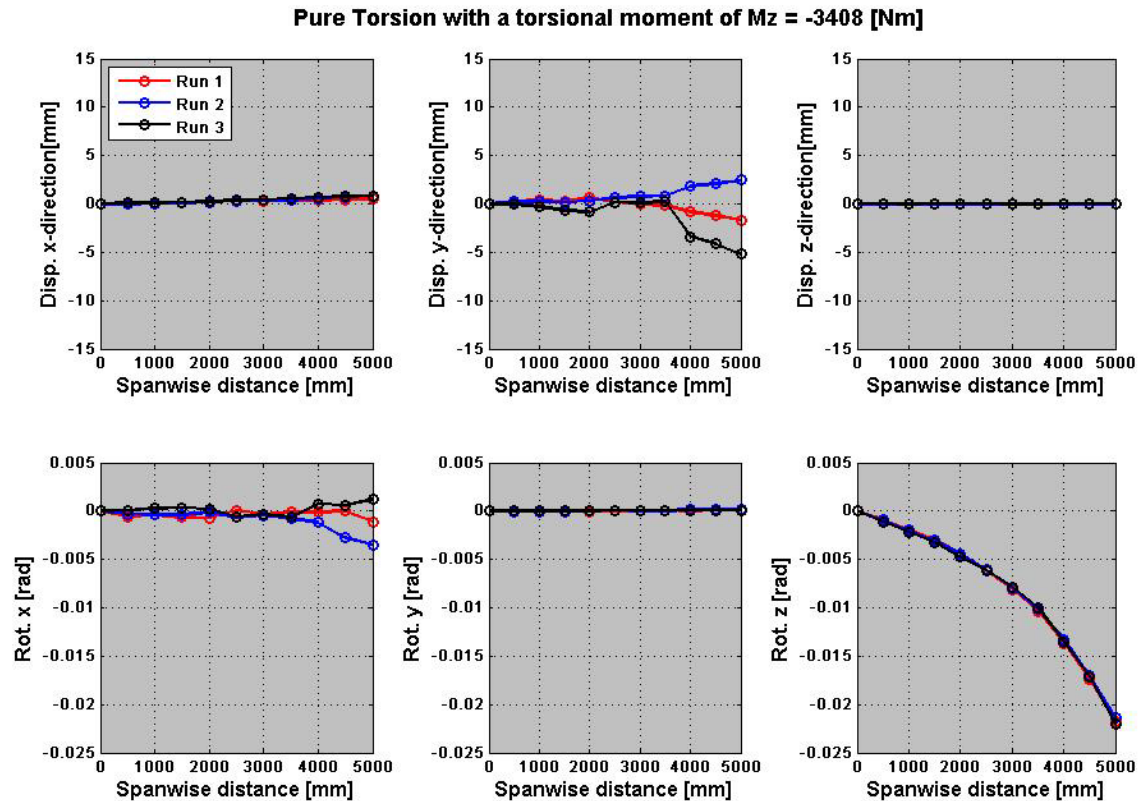


Figure 5.4.5 – Results from pure torsion

Comment

As expected, this test was not easy to perform because the two hydraulic presses should produce forces of equal size and still should the blade tip be able to move freely, which is required in order to measure the twist-induced bending deflection.

The data for the three runs are not consistent, as one can see on the plots of the displacements and rotations.

The results of the displacement in the y-direction and the rotation about the x-axis are not satisfying because there are large deviations between these values. The deviations are a result of the very difficult control of the two hydraulic presses.

The result of the twist angle for this test is good and this test method could probably be used for determining the torsional stiffness (if it is assumed that the bend-twist coupling is of limited size).

Locked Torsion

In the locked torsion test was clamp 3 locked in a point directly over the center of the spar. The blade tip was able to rotate about this point and the blade tip could move in the horizontal plane. A force of 4904 [N] was applied at a distance of 0.695m from the rotation point and that creates a torsional moment of 3408 [Nm]:

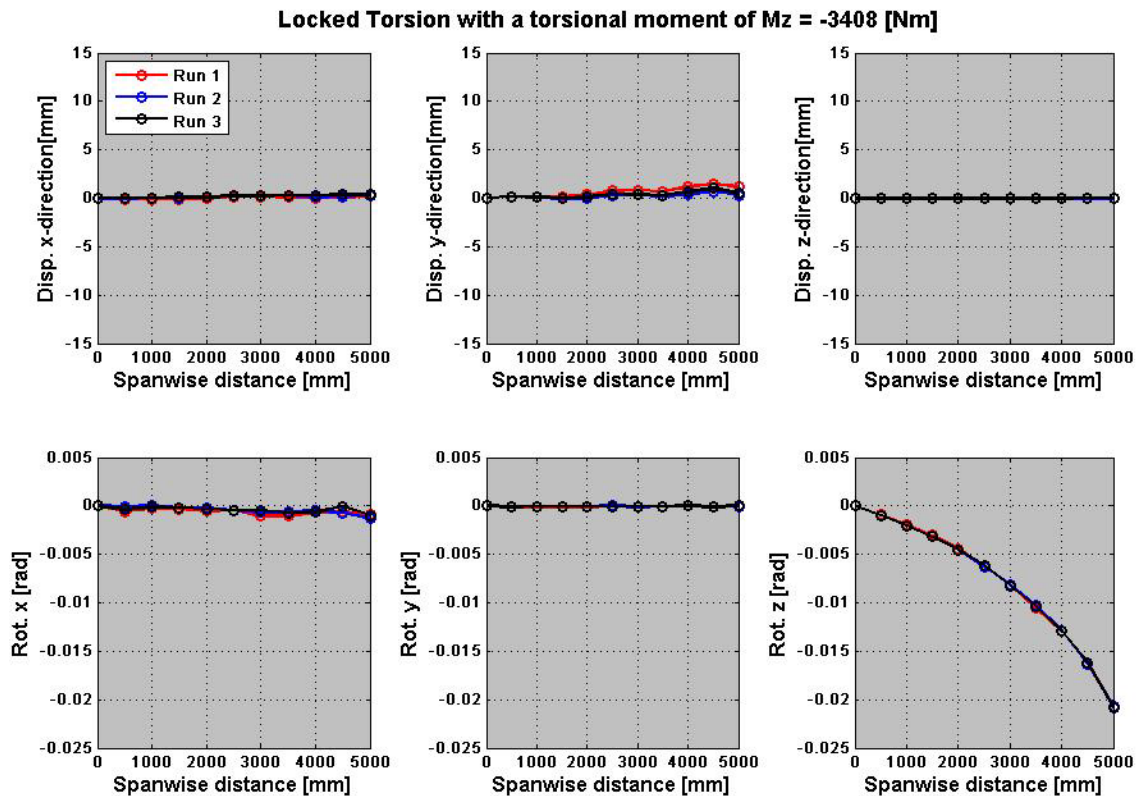


Figure 5.4.6 – Results from locked torsion

Comment

The torsional moment was unlike the pure torsion test easy to apply in the locked torsion test with the equipment available in the laboratory. The data for the three runs are reasonable consistent, as one can see on the plots of the displacements and rotations.

As expected, it is only the twist angle which is not equal to zero. The twist angle at the tip is equal to -0.021 [rad], which also was the result from the pure torsion test. This test can be used to determine the torsional stiffness for the blade section if the bend-twist coupling is of limited size. If a bend-twist coupling exist in the blade then it is necessary to measure the induced bending force at the tip end. This force can be measured by mounting strain-gauges on the locking system.

5.5. Bend-twist coupling for the original blade section

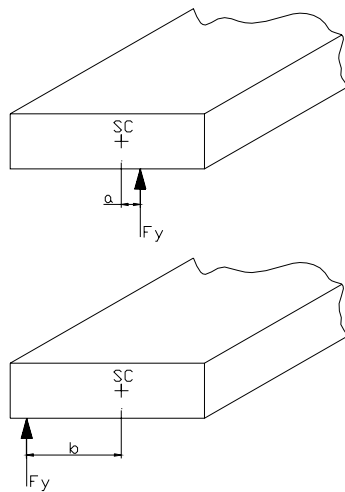
Five different tests were performed, but only the flapwise bending test and the combined flapwise bending and torsion test will be analyzed in the following calculation of the bend-twist coupling for the original blade section.

The bend-twist coupling is determined by only looking at the flapwise bending and flapwise bending and torsion test as mentioned earlier. The idea is that the flapwise bending test is subtracted from the flapwise bending and torsion test and the result of that is pure torsion (the principle of superposition).

If a bend-twist coupling exist, then the blade will twist but also bend because of the coupling (twist induced bending) if it is subjected to a pure torsional moment. The size of the torsional moment is in theory unknown because the location of the shear center is not known.

This problem with the location of the shear center is illustrated in the figure below.

For the principle of superposition to be valid, then the response of the blade must be linear!



Flapwise bending test: $M_{b_f} = F_y \cdot (L - z)$ $T_f = F_y \cdot a$

Flapwise bending and torsion test: $M_{b_ft} = F_y \cdot (L - z)$ $T_{ft} = -F_y \cdot b$

flapwise bending and torsion - flapwise bending = pure torsion =>

$$T_{\text{pure_torsion}} = -F_y \cdot (a + b)$$

This is just an example to illustrate the principle of superposition and the problem with the location of the shear center.

Figure 5.5.1: Flapwise bending and torsion

5.5.1. Linear response test

The response of the blade must be linear for the principle of superposition to be valid. The three displacements and rotations for cross section 5.0m (load case: flapwise bending and torsion) are plotted below.

Each load case was performed by generating 5 images/pictures of the measuring area. Picture 1 show the undeformed area, picture 2 shows the deformed area with 25% of the load etc. and finally, picture 5 shows the deformed area with 100% of the load. One can easily determine if the blade response is linear or non-linear with this “loading history”.

The deflections and rotations near the “fixed end” are not subtracted in the plot below:

Flapwise bending and Torsion, with a point load of $F_y=0\ldots3923\text{[N]}$ and a moment of $M_z=F_y\cdot0.695\text{[N}\cdot\text{m]}$

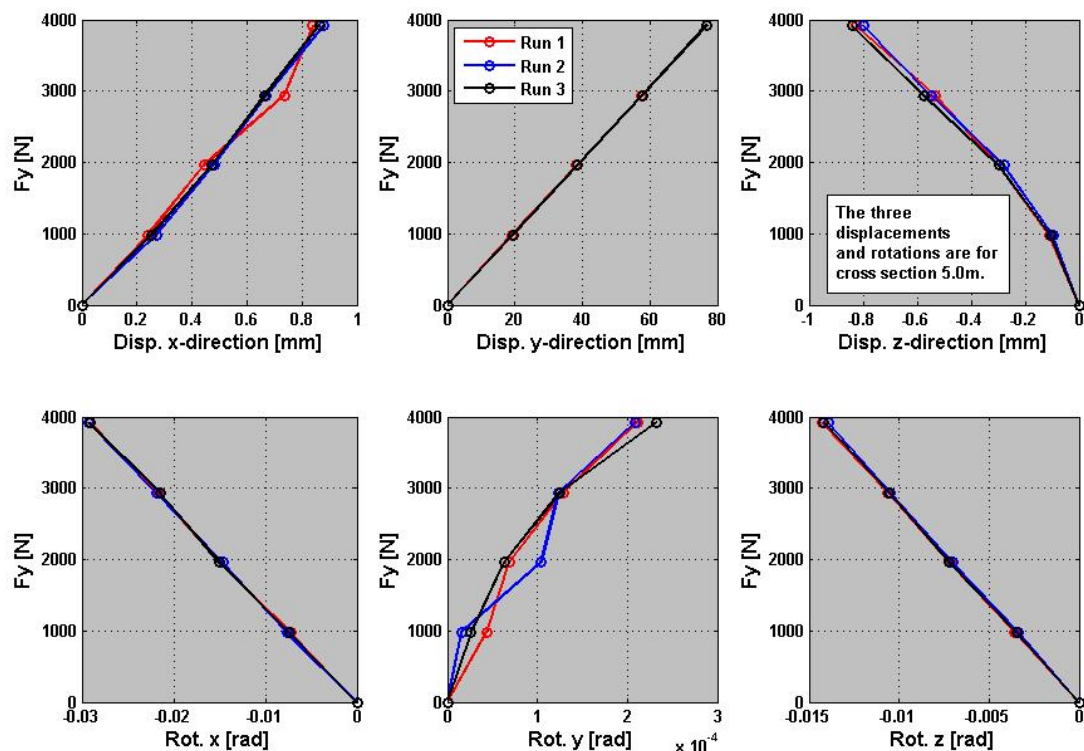


Figure 5.5.2 – Linear response for flapwise bending and torsion

Conclusion for the linear response test

The combined flapwise bending and torsion test showed that the displacement in the y-direction and the rotations about the x- and y-axis are completely linear.

The displacement in the x- and z-direction and the rotation about the y-axis are not completely linear, but the values are also very small and therefore very sensitive to any “measuring noise”. It can be concluded that the response of the blade is linear and this means that superposition can be used.

Note, the response of all five experiments was analyzed and they all showed perfect linearity.

5.5.2. Superposition

The displacements and rotations in the two plots below are all average values that are calculated from the three runs:

Flapwise bending and Torsion with a point load of $F_y=3923$ [N] ($M_z=F_y \cdot 0.695$ [Nm]) (average va

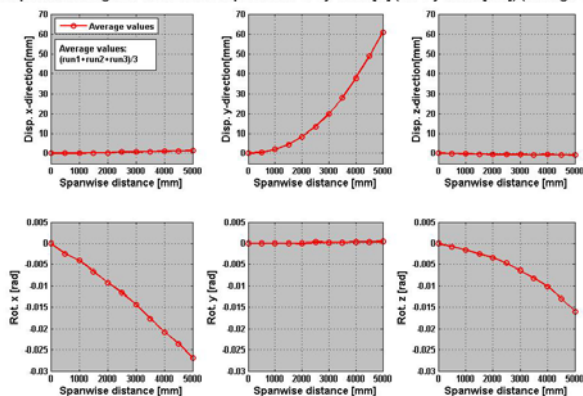


Figure 5.5.3 – Flapwise bending and torsion

Flapwise bending with a point load of $F_y=3923$ [N] (average values)

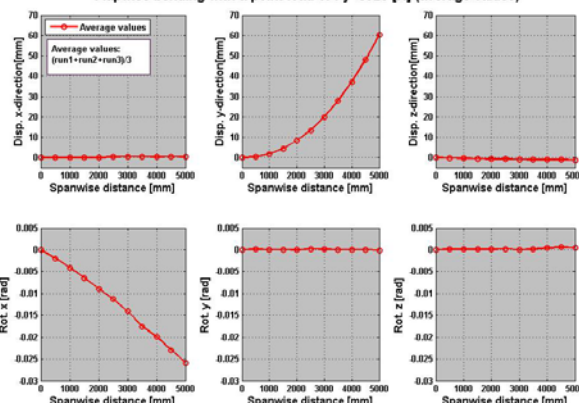


Figure 5.5.4 – Flapwise bending

The measured deflections and rotations from the flapwise bending test subtracted from the combined flapwise bending and torsion test, are shown below. In this way, one can see if the blade has a bend-twist coupling or not! The plots below are the results from the superposition (the flapwise bending test is subtracted from the flapwise bending and torsion test).

The deflections and rotations near the “fixed end” are subtracted and the deflections and rotations are all average values of the three runs:

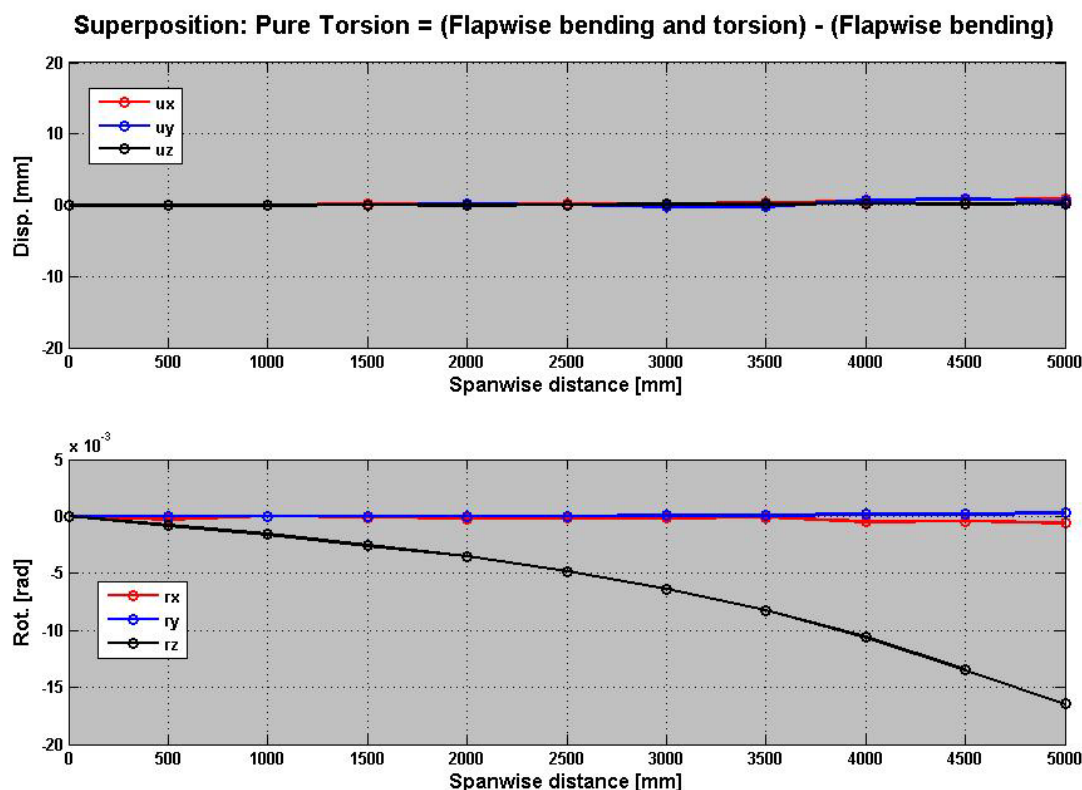


Figure 5.5.5 - Superposition

Comment

One can see that the blade section is twisting but not bending. This means that the bend-twist coupling is close to zero which also was expected. It can therefore be concluded that the **Bend-twist coupling ≈ 0** .

As mentioned earlier, one of primary aims of this work was to model bend-twist coupled behavior correct when using FEM. This was of course very difficult to validate since the bend-twist coupling on the actual blade was of limited size!

The “problem” with the nonexistent bend-twist coupling was solved by adding some additional angled UD-ply on the outer blade-surface.

5.6. The bend-twist coupled blade section (modified blade section)

One of the aims with this project was to create a FE-model that was capable of modeling correct bend-twist coupled behaviour. The FE-models response was validated by experimental static testing. The original blade section was modified and four layers of UD1200 were laminated on the pressure and suction side to create a measurable flapwise bend-twist coupling. The additional layers were laminated as shown below:

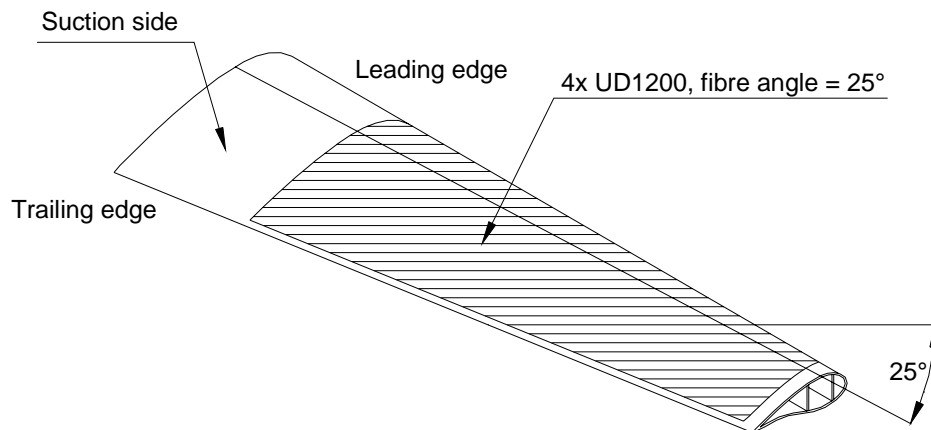


Figure 5.6.1 - Fiber orientation for the extra UD material

The extra layers were laminated onto the blade section by a vacuum infusion process. The area between the two clamps was not laminated with extra UD-layers since it is only the behaviour of the cantilever part of the blade section that is interesting. The blade section was laminated with an overlap of 0.5m at clamp 2.

The leading edge area, the trailing edge area and the tip area was not laminated because vacuum bags and resin lines for the infusion process were mounted here. The leading and trailing edge areas for the vacuum bags and resin lines are 100mm wide.

The optimal fiber angle of 25° was determined by trial and error using FEM.

The optimal fiber angle was determined from the outer surface FE-model with layers of UD1600 material. The optimal fiber angle is subjected to some uncertainties because the outer surface model is not capable of modeling correct torsional behaviour, but only the outer surface model was created at the time when it was decided that extra UD layers were going to be laminated on the blade.

The optimal fiber angle is also subjected to some uncertainties because the UD properties that were used for determining the optimal fiber angle, were the mechanical properties taken from the UD1600 layers used in the spar caps.

It is not possible to achieve the same “high” mechanical properties for the extra UD layers as for the spar cap UD layers when using a vacuum infusion process.

Four extra layers of UD material was chosen because the stiffnesses increases significantly when extra layers are added. The increase in bending and torsional stiffness means that one must apply greater loads in order to obtain the same deflections as for the original blade. So “only” four layers of extra UD material was laminated onto the blade section to avoid overloading of the testrig.

The following set of material data from Vestas Wind Systems A/S was used for the UD layers:

$$E_1 = 34000 \text{ N/mm}^2 \quad E_2 = 8200 \text{ N/mm}^2 \quad G_{12} = 4500 \text{ N/mm}^2 \quad \nu_{12} = 0.29$$

The material data for the extra UD layers is a good estimate but not exact mechanical properties. The picture below shows the blade section after being modified with the extra UD layers:



Figure 5.6.2 – Extra UD lamination

5.6.1. Experimental results for the modified blade section

All the measuring of the modified blade section was performed with the 3D optical ARAMIS 4M system (this system is of course more accurate then the 2M system which was used on the original blade section).

Only two different tests were performed on the modified blade section. These two tests were the flapwise bending test and the combined flapwise bending and torsion test. The reason for reducing the experimental testing to these two tests was that the primary aim was to investigate the additional angled UD layers affect on the bend-twist coupling. The experimental testing of the original blade section showed that the two test methods were usable for determining if the blade section had a bend-twist coupling or not.

Flapwise bending

The flapwise bending test was performed with a point load of 9808[N] placed 5.607m from cross section 0.5m. The flapwise bending test for the modified blade section was performed in the same way as the test for the original blade section:

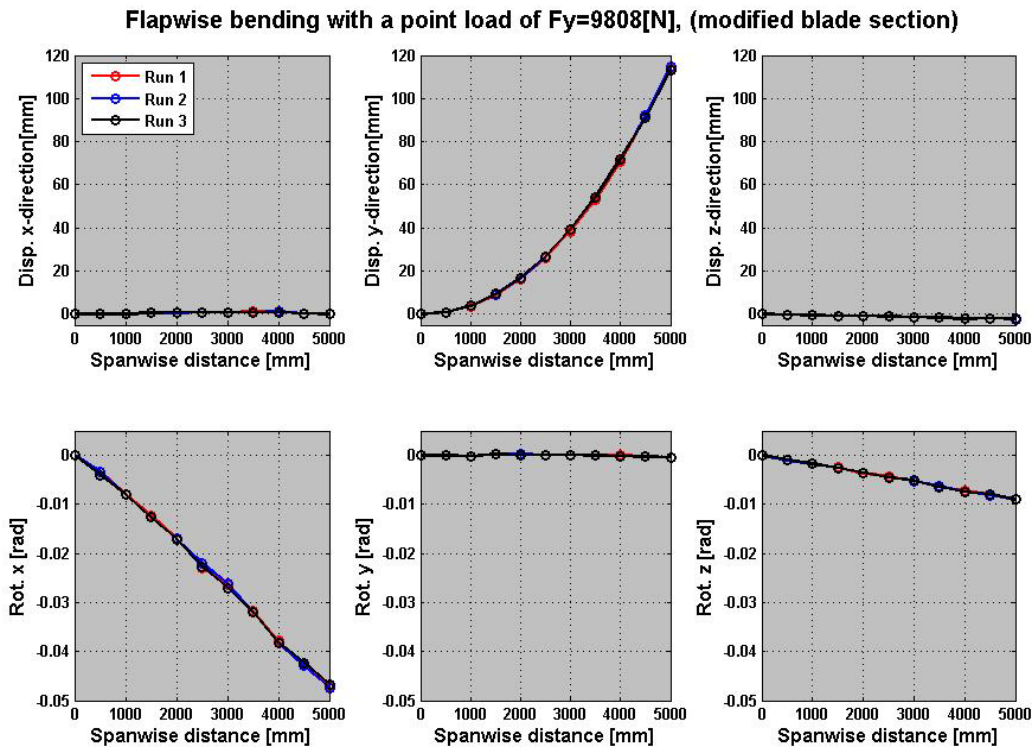


Figure 5.6.3 – Results from flapwise bending (modified blade)

Comment

The data for the three runs are consistent, as one can see on the plots of the displacements and rotations.

The interesting part of the plot is the subplot of the rotation about the z-axis. The z-rotation was more or less equal to zero for the original blade section. The z-rotation indicates that the modified blade section now has a measurable bend-twist coupling.

Flapwise bending and torsion

The flapwise bending and torsion test was performed with a point load of 9808[N] placed 5.607m from cross section 0.5m and at a distance of 0.695m from the center of the spar.

The flapwise bending and torsion test for the modified blade section was performed in the same way as the test for the original blade section:

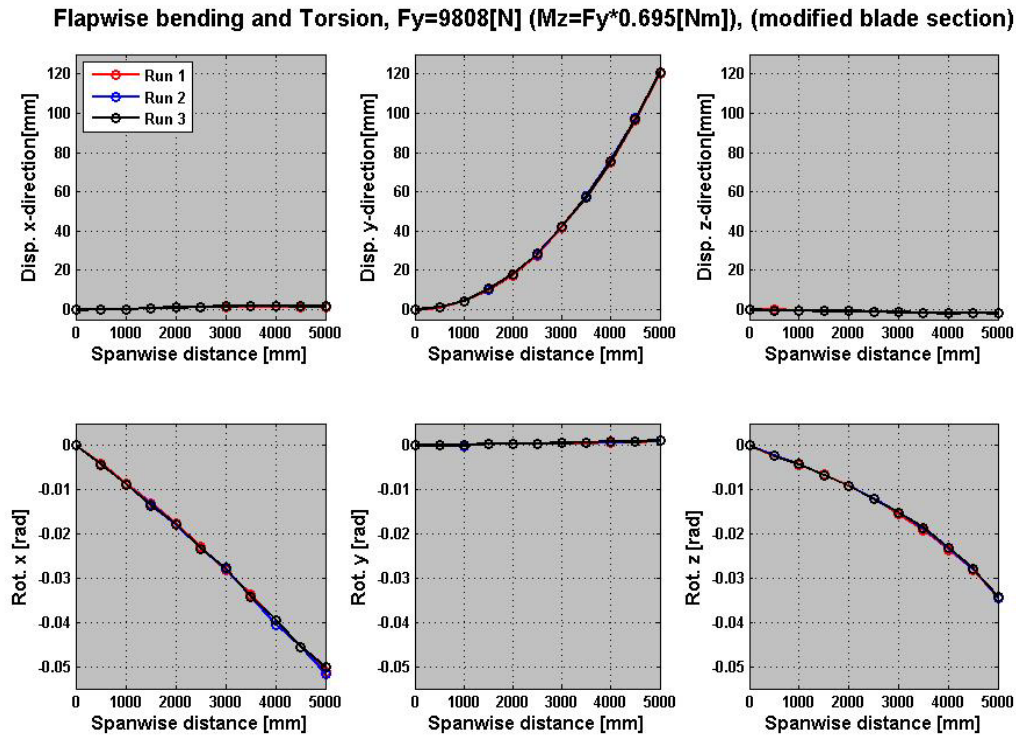


Figure 5.6.4 – Results from flapwise bending and torsion (modified blade)

Comment

The data for the three runs are consistent, as one can see on the plots of the displacements and rotations.

The test results in a deflection in the y-direction, rotation about the x-axis (bending slope) and rotation about the z-axis (twist angle).

The “tip deflection” in the y-direction is close to 120mm, which is a bit higher than the result for the flapwise bending test. Again, this indicates that the bend-twist coupling is of a measurable size because a bend-twist coupling will change the y-deflection (twist induced bending).

5.6.2. Bend-twist coupling for the modified blade section

Again is the bend-twist coupling determined (is there a bend-twist coupling or not?) by using the principle of superposition. The flapwise bending test is subtracted from the flapwise bending and torsion test, which results in pure torsion.

If there is a bend-twist coupling and the blade section is subjected to a pure torsional moment, then the blade will twist but also bend due to the bend-twist coupling (twist induced bending). As mentioned before, the size of the torsional moment in theory unknown because the location of the shear center is unknown.

Linear response test for the modified blade section

The modified blade section was deformed significantly more than the original blade section, so the affect of the bend-twist coupling was easy to see and measure. It is therefore necessary to investigate if the response is still linear when the deformation is about twice as much as for the original blade section. Again, the response must be linear for the principle of superposition to be valid.

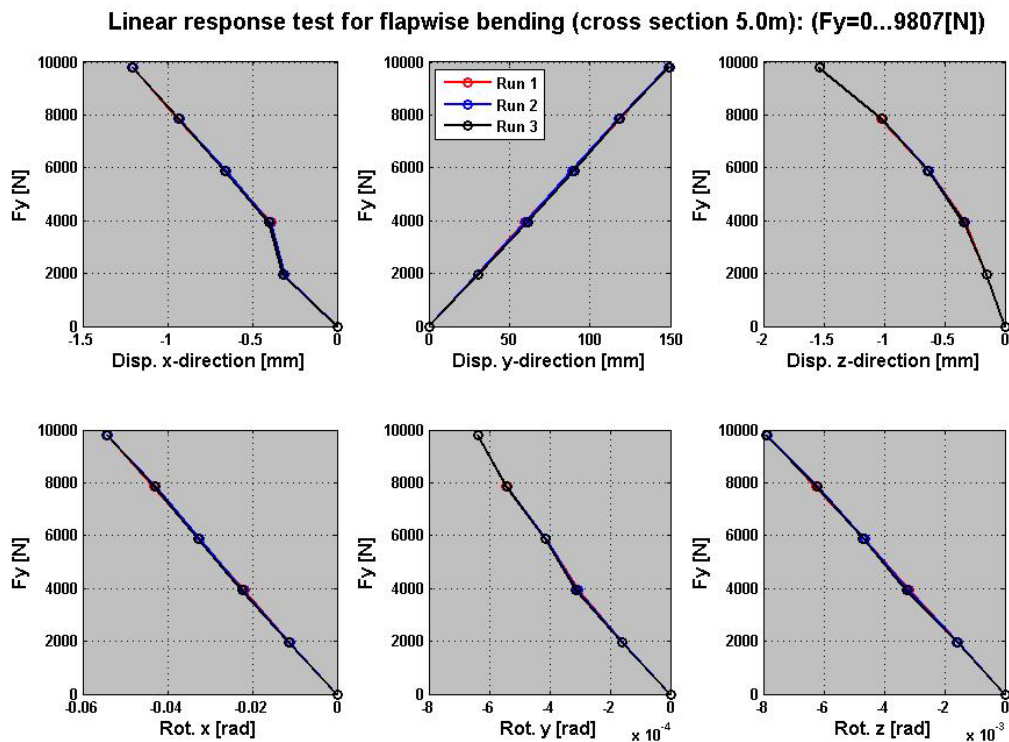


Figure 5.6.5 – Linear response test for the modified blade

Comment

The flapwise bending test shows that the displacement in the y-direction and the rotations about the x- and z-axis are completely linear.

The displacements in the x- and z-direction and the rotation about the y-axis are not completely linear, but these values are also very small and therefore very sensitive to any “measuring noise”. It can be concluded that the response of the blade is linear and this means that superposition can be used.

Superposition

On the plots below are the measured deflections and rotations from the flapwise bending test subtracted from the combined flapwise bending and torsion test. In this way one can see if the blade has a bend-twist coupling or not!

The displacements and rotations in the two plots below are average values, which are calculated from the three runs:

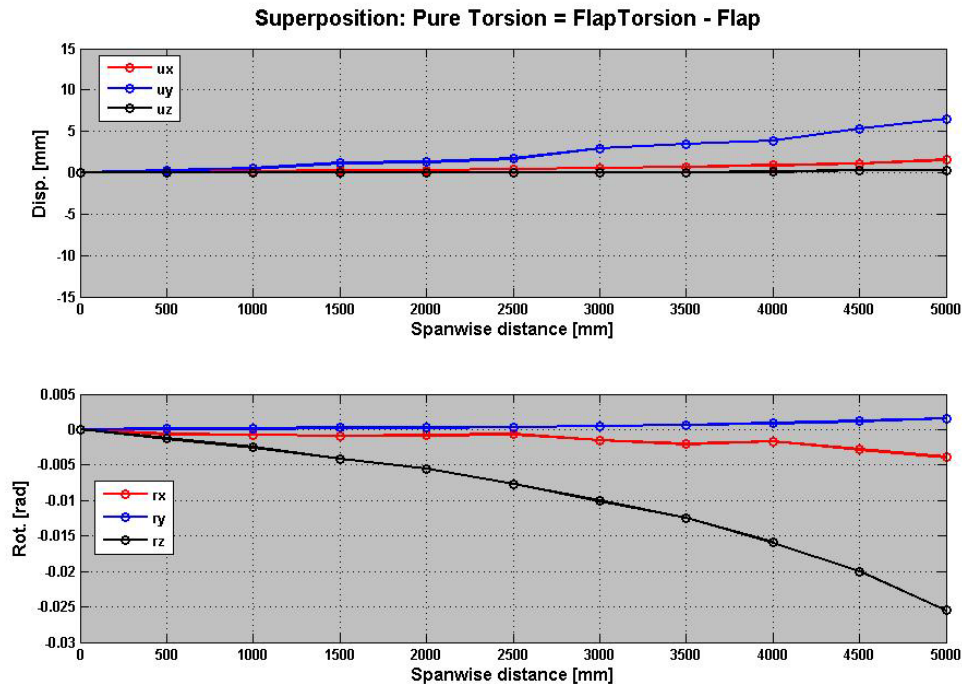


Figure 5.6.6 – Superposition for the modified blade

Comment

It can be concluded from the result of the superposition that the pure torsional moment induces bending of the blade section and it can therefore be concluded that the bend-twist coupling is of a measurable size. The twist-induced bending is 6.5mm and the twist-induced bending slope (rotation about the x-axis) is about -0.005[rad] at the tip end.

6. Finite Element Modeling

First, a general description of the blade section is presented in this chapter. The finite element models of the original and modified blade section are then presented.

6.1. Blade section description

To obtain a reliable determination of the torsion stiffness and the bend-twist couplings using FEM, the FE-model must be validated by experimental results. As described earlier, experimental results are going to be obtained by testing a section of a real wind turbine blade.

The experimental work done in this project was carried out on an 8.4m blade section taken from a 23m wind turbine blade provided by Vestas Wind Systems A/S.

The 8.4m blade section goes from radial position R10.8 to R19.2 (see *Figure 6.1.1*).

The design of the test rig for the experimental work and the selection of the blade section was done in the pre-project “Torsional Performance of Large Wind Turbine Blades – Experimental Test Design”, by Berring, P. and Knudsen, H.

Only a general description of the blade section selection is presented here, a more detailed description is presented in the pre-project.

The overall requirements for selecting the blade section were:

- The root section has a very complex geometry, meaning that the section is highly non-linear and much more complex to model and analyze in FEM.
The root section is furthermore the strongest part of the blade, which requires greater forces and with it a stronger testrig. So a blade section close to the tip is preferable.
- In order to apply beam theories, the selected section must be slender.
- By selecting a blade section with a relatively simple lay-up, one is able to keep the FE-model more simple in terms of modeling and analyzing, in contrasts to selecting a section with discontinuities in the overall lay-up like local reinforcements etc.

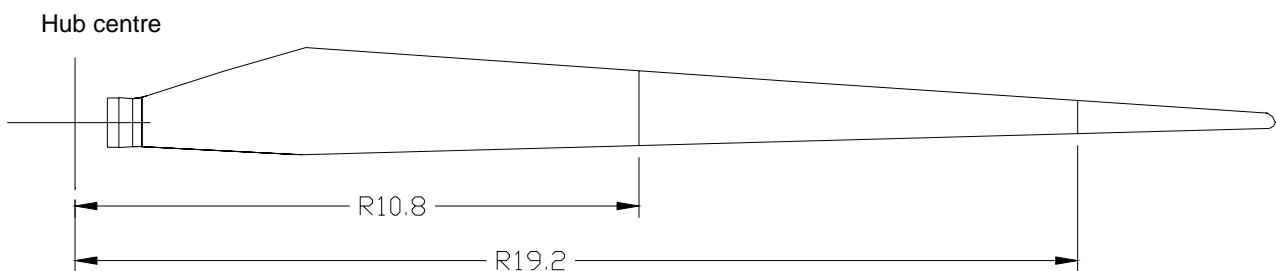


Figure 6.1.1 - 23m wind turbine blade

6.1.1. Blade section layout

The 23m wind turbine blade is constructed of fiberglass (E-glass/Epoxy) UD-, Biax-, Triax-layers, PMI and PVC sandwich core material and an outer surface Gelcoat.

A UD-layer is a unidirectional lamina with only 0° fibers. The UD “number”, for example UD1200 means that the UD weights 1200 gram/m².

A Biax-layer is stacked with $+45^\circ/-45^\circ$ fibers and the plies weights the same. The Biax “number”, for example Biax600 means that the Biax weights 600 gram/m².

A Triax900-layer is stacked with $0^\circ/+45^\circ/-45^\circ$ fibers and it weights 425/230/230 gram/m².

The Triax900-layer is always stacked with the 0° layer closest to the sandwich core.

The following material data was provided by Vestas Wind Systems A/S:

The E_1 , E_2 , G_{12} and ν_{12} values for Biax and Triax are all apparent properties.

	E_1 [MPa]	E_2 [MPa]	G_{12} [MPa]	ν_{12}	t [mm]	ρ [g/cm ³]
UD 1600	39 874	11 580	4440	0,303	1,2	1,91
UD 1200	39 874	11 580	4440	0,303	0,9	1,91
Biax 1800	11 885	11 885	10 838	0,55	1,5	1,85
Biax 600	11 885	11 885	10 838	0,55	0,5	1,85
Biax 450	11 885	11 885	10 838	0,55	0,38	1,83
Biax 300	11 885	11 885	10 838	0,55	0,25	1,83
Triax 900	22 555	11 230	6555	0,46	0,8	1,81
PVC (isotropic)	130	-	-	0,3	10 - 20	0,08
PMI (isotropic)	150	-	-	0,3	10	0,11
Adhesive (iso.)	2000	-	-	0,3	5	1,2
Gelcoat (iso.)	2000	-	-	0,3	1	1,5

The blade section’s layout is shown below in *Figure 6.1.2* and in the following tables:

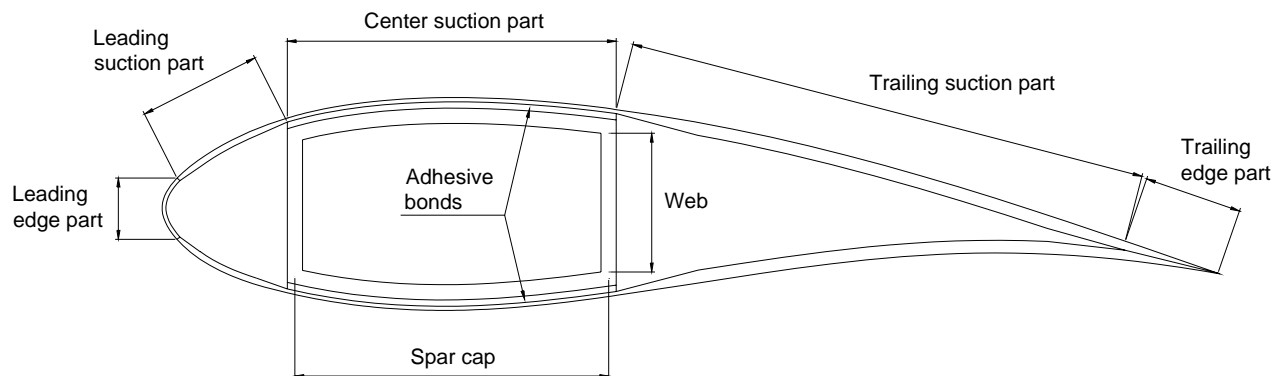


Figure 6.1.2 - Laminated parts of the blade section

Leading edge part:

Layer:	Orientation:	Number:	Radial position:
Gelcoat	-	1	R10.8 – R19.2
Biax 300	0°	1	R10.8 – R19.2
Triax 900	Aligned with TE	1	R10.8 – R19.2
Triax 900	Aligned with TE	1	R10.8 – R19.2
Biax 600	0°	1	R10.8 – R19.2
Biax 1800	0°	1	R10.8 – R19.2

Leading pressure and suction part:

Layer:	Orientation:	Number:	Radial position:
Gelcoat	-	1	R10.8 – R19.2
Triax 900	Aligned with TE	1	R10.8 – R19.2
PVC 5mm	-	1	R10.8 – R19.2
Triax 900	Aligned with TE	1	R10.8 – R19.2

Center pressure and suction part:

Layer:	Orientation:	Number:	Radial position:
Gelcoat	-	1	R10.8 – R19.2
Triax 900	Aligned with TE	1	R10.8 – R19.2
Biax 450	0°	1	R10.8 – R19.2
Triax 900	Aligned with TE	1	R10.8 – R19.2

Trailing pressure and suction part:

Layer:	Orientation:	Number:	Radial position:
Gelcoat	-	1	R10.8 – R19.2
Triax 900	Aligned with TE	1	R10.8 – R19.2
PVC 20mm	-	1	R10.8 – R12.06
PVC 20-15mm	-	1	R12.06 – 13.12
PVC 15mm	-	1	R13.12 – 15.24
PVC 15-10mm	-	1	R15.24 – 16.4
PVC 10mm	-	1	R16.4 – R19.2
Triax 900	Aligned with TE	1	R10.8 – R19.2

Trailing edge part:

Layer:	Orientation:	Number:	Radial position:
Gelcoat	-	1	R10.8 – R19.2
Biax 300	Aligned with TE	1	R10.8 – R19.2
Triax 900	Aligned with TE	1	R10.8 – R19.2
Triax 900	Aligned with TE	1	R10.8 – R19.2
Biax 600	Aligned with TE	1	R10.8 – R12.06

Spar caps:

Layer:	Orientation:	Number:	Radial position:
Biax 450	0°	1	R10.8 – R19.2
UD 1600	0°	4	R10.8 – R19.2
Biax 450	0°	1	R10.8 – R19.2
UD 1600	0°	2	R10.8 – R19.2
UD 1600	0°	2	R10.8 – R17.7
Biax 450	0°	1	R10.8 – R19.2
UD 1600	0°	2	R10.8 – R16.4
UD 1600	0°	2	R10.8 – R19.2
Biax450	0°	1	R10.8 – R19.2
Biax 600	0°	1	R10.8 – R19.2

Webs:

Layer:	Orientation:	Number:	Radial position:
Biax 600	0°	1	R10.8 – R19.2
Biax 600	0°	1	R16.4 – R19.2
Biax 450	0°	1	R10.8 – R19.2
Biax 450	0°	1	R16.4 – R19.2
Biax 600	0°	1	R10.8 – R17.7
Biax 600	0°	1	R16.4 – R19.2

PMI 10mm	0°	1	R10.8 – R16.4
Biax 600	0°	1	R10.8 – R19.2
Biax 600	0°	1	R16.4 – R19.2
Biax 450	0°	1	R10.8 – R19.2
Biax 450	0°	1	R16.4 – R19.2
Biax 600	0°	1	R10.8 – R17.7
Biax 600	0°	1	R16.4 – R19.2

As described earlier, the material data for Biax and Triax are all apparent properties.

All FE-models were analyzed with real material properties in order to capture potential couplings. All couplings on laminate level are neglected when one determines the apparent properties since one is only using values from the A-matrix (the laminate bend-twist coupling is for example in the D-matrix).

In order to calculate the real properties, a 150x200mm piece of the spar cap from the blade section was cut out and then analyzed by Vestas Wind Systems A/S.

Vestas Wind Systems A/S performed a laminate “burn-off” test in order to determine the fiber mass fraction. A fiber mass fraction of 0.7 was obtained from the test.

One can determine the fiber volume fraction from the mass fraction and the fiber/matrix densities:

$$v_i = \frac{\frac{w_i}{\rho_i}}{\sum_i \frac{w_i}{\rho_i}} \Rightarrow v_f = \frac{\frac{w_f}{\rho_f}}{\frac{w_f}{\rho_f} + \frac{w_m}{\rho_m}}$$

v_f is the fiber volume fraction, w_f and w_m are the fiber and matrix mass fractions, ρ_f and ρ_m are the fiber and matrix densities.

The mechanical properties can be determined by using the micromechanics model *Rule of Mixtures*:

$$E_1 = E_f v_f + E_m v_m \quad E_2 = \frac{1}{\left(\frac{v_f}{E_f} + \frac{v_m}{E_m} \right)} \quad G_{12} = \frac{1}{\left(\frac{v_f}{G_f} + \frac{v_m}{G_m} \right)} \quad v_{12} = v_f v_f + v_m v_m$$

E_f and E_m are the fiber and matrix E-modulus, G_f and G_m are the fiber and matrix G-modulus, v_f and v_m are the fiber and matrix Poisson's ratio.

The *Rule of Mixtures* (ROM) solutions are widely used as first approximations because of the simplicity. The E_1 result from ROM generally agrees with more sophisticated models and experimental results. The E_2 and G_{12} results are on the other hand significantly lower than those predicted by more sophisticated models and from experiments.

Another more sophisticated and accurate model is the Halpin-Tsai semi-empirical relation. The Halpin-Tsai model takes fiber geometry, packing geometry and loading conditions into account. These geometries/conditions are expressed by the factor ξ_1 .

The Halpin-Tsai semi empirical relation for the longitudinal modulus and Poisson's ratio is:

$$E_1 = E_{f1} \cdot v_f + E_m \cdot v_m \quad v_{12} = v_f \cdot v_f + v_m \cdot v_m$$

E_{f1} is the fiber modulus in the longitudinal direction.

The Halpin-Tsai semi-empirical relation for the transverse modulus is:

$$E_2 = E_m \cdot \frac{1 + \xi_1 \cdot \eta_1 \cdot v_f}{1 - \eta_1 \cdot v_f} \quad \text{where} \quad \eta_1 = \frac{\left(\frac{E_{f2}}{E_m} \right) - 1}{\left(\frac{E_{f2}}{E_m} \right) + \xi_1}$$

E_{f2} is the fiber modulus in the transverse direction (in case that the fiber is anisotropic).

A similar relation exists for the in-plane shear modulus:

$$G_{12} = G_m \cdot \frac{1 + \xi_2 \cdot \eta_2 \cdot v_f}{1 - \eta_2 \cdot v_f} \quad \text{where} \quad \eta_2 = \frac{\left(\frac{G_f}{G_m} \right) - 1}{\left(\frac{G_f}{G_m} \right) + \xi_2}$$

Obtaining accurate values for ξ is the most difficult part of using Halpin-Tsai relation.

The following approximated values can be used:

$\xi_1 = 2$ for E_2 , $\xi_2 = 1$ for G_{12} for circular and square fibers in a square array. These values give good results for $v_f < 0.9$.

The following mechanical properties were determined by the Halpin-Tsai model and Laminator and used in the FE-models:

$$E_1 = 39850 \text{ N/mm}^2 \quad E_2 = 12240 \text{ N/mm}^2 \quad G_{12} = 3686 \text{ N/mm}^2 \quad v_{12} = 0.2977$$

6.2. FEM description

A structure can be mathematically model from a series of discrete finite elements. Each finite element has an analytically defined relationship between force and displacement.

This relationship, also called stiffness, of each element can be assembled to create a stiffness matrix for the whole structure. Then the response of the entire structure can be determined from the prescribed loads and boundary conditions. The particular arrangement of elements is called a mesh.

The finite element method is characterized by the simple relationship between a force vector (F), the stiffness matrix (K) and a displacement vector (U):

$$F = K \cdot U$$

The FE method provides an approximate solution because the method is based on *finite* elements.

Linear finite element analysis:

When working with linear finite element analysis, then the stiffness of the structure is assumed to remain constant during the analysis. This is an approximation in most cases because even small deflections in a structure are likely to introduce some change in stiffness.

However, this approximation is valid in many cases where the results are therefore acceptable.

This linear assumption provides the following benefits:

- The principle of superposition can be used.
- The results can be scaled.
- The loading sequence is not important.
- The past loading history of the structure is not important.

The linear assumption, that the structural stiffness remains constant during the analysis means that:

- The material properties must remain constant. Material yielding and plastic deformation cannot be analyzed correctly since the material stiffness is depending on the strain.
- The linear analysis is invalid if structure undergoes large deflections. Large deflections can affect the stiffness significantly because of changes in the structural shape.
- The linear analysis is invalid if the structural stiffness changes because of contact between parts of the structure.

Many engineering problems cannot be analyzed accurately with linear FEM which means that one must turn to nonlinear FEM.

Nonlinear finite element analysis:

A nonlinear finite element analysis is different from a linear analysis in that the stiffness of structure in a nonlinear analysis is not assumed to be constant during the analysis.

The nonlinear analysis is an extension of the linear analysis since it is based on the same type of matrix solution technique and employs the same types of elements, material models and boundary conditions, although the solution is an incremental-iterative process.

The sources of nonlinearity can be classified into the following three main categories:

- **Material nonlinearity.**
Many materials exhibit an elastic response for small deformations – the material return to its original shape when the load is removed. The elastic stiffness, Young's modulus (E -modulus), is constant for small strain values for a particular material at a particular temperature. Many metallic materials like steel undergoes some form of yielding followed by plastic flow at higher strain values (plasticity). Such nonlinear material behaviour cannot be modeled using linear FEM because once the yield point is reached then the stiffness changes as the deformation increases. Nonlinear FEM must therefore be used.
Other materials like rubber and elastic polymers are elastic, since there is no permanent deformation after loading and unloading but they do not have a constant stiffness since their stress-strain behaviour is not constant. Such materials must also be modeled using nonlinear FEM.
- **Geometry nonlinearity.**
The stiffness of the structure is assumed to be independent of the magnitude of the displacements when using linear FEM. However, for real structures, this is not necessarily the case.
In general terms, geometric nonlinearity covers all situations where a change in the orientation or in the geometry of a structure leads to a change in its response. Geometric nonlinearity can also arise when a structure undergoes large rotations and when structural instabilities such as postbuckling behaviour occur.
- **Boundary nonlinearity.**
The basis of the FE method is that a set of loads is applied to a structure with a given stiffness and a set of displacements is derived.
The constraints or boundary conditions on the structure are important factors when determining the resulting deformation.
It is assumed that the boundary conditions on the structure remain constant when using linear FEM. However, there are situations where this assumption is not valid; the most important are the analysis of contact and frictional sliding.

The stiffness matrix is not constant during a nonlinear FEM analysis which means that the stiffness matrix may need to be recalculated many times over the course of the analysis. An iterative-incremental solution technique is normally used. The load is applied in incremental stages and equilibrium is then found at each increment by using an iterative scheme. The solution proceeds with changes to the stiffness at each increment until the final load has been reached.

The linear assumption that the structural stiffness remains constant during the analysis was valid in this work and the final FE-model of the blade section was validated by using linear FEM. As described earlier, all the experimental load cases were analyzed with respect to linearity.

All the applied loads were moderate and the experiments never came near failure of the blade section.

The loading history was recorded for every experimental load case and from this one can see that all the displacements and rotations are linear related to the loads. Or in other words, the experimental deflections/rotations were so small that the structural stiffness remained constant during the experiments. Furthermore, no phenomena like local buckling etc. were observed with the Aramis equipment or from the blade response plots.

Linear FEM was also used for the BPE-method because the method is based on classical linear beam theory and the linear stiffness method with the relation $F = KU$.

Furthermore, flapwise bending of the outer surface shell model was analyzed using nonlinear FEM. The FE-model was analyzed with a load of same magnitude as used in the experiments and the nonlinear analysis came up with the same result as the linear analysis.

6.2.1. FEM models

Three FE-models were created and analyzed during this project:

1. Outer surface shell model – using shell element offset.
2. Mid-thickness shell model.
3. Combined shell/solid model.

The combined shell/solid model is presented in this chapter with a detailed description and the two other models are only described briefly.

The reason for this is that many of the modeling procedures are the same for the three models. Furthermore, the outer surface model and the mid-thickness model are not capable of modeling correct torsional behaviour which makes these models “uninteresting” (see the comparisons between the num. and exp. results in chapter 7).

The three FE-models were created by using the MSC.Patran Command Language (PCL). PCL is a programming language that is an integrated part of the MSC.Patran system. The advantages of using PCL are:

- Automated generation of geometry, mesh etc.
- Ideal for parametric modelling/studies.
- Easy modification of the model (refine mesh etc).
- Time saving.
- MSC.Patran may be customized. For example, the user can write a custom PCL function that generates a specialized failure criterion.

The following input files (session files) were created for each FE-model:

- ***Geometry.***
- ***Surface and solid.***
- ***Mesh.***
- ***Loads and boundary conditions.***
- ***Layup.***

Outer surface shell model

The first FE-model of the blade section was a shell model based on the outer surface meaning that the shell elements were located on the physical outer surface of the aerodynamic shell. The outer surface model is a “classical” wind turbine FE-model that uses shell element offset.

A rough outer surface model was created during the pre-project. This rough model was improved during this work in the following ways:

- Real composite material properties were added instead of apparent properties. All laminas were created in Laminate Modeler and the overall layup was modified.
- A more realistic representation of the chamfered sandwich core regions in the trailing part of the blade section was created.
- The element topology was changed from 4-noded to 8-noded shell elements.

The chamfered sandwich cores were modified and modeled by dividing each sandwich panel into four smaller panels (see *Figure 6.2.1*). Region 1 and 3 was created with half the core thickness of Region 2. Region 4 was created with a quarter of the core thickness of Region 2.

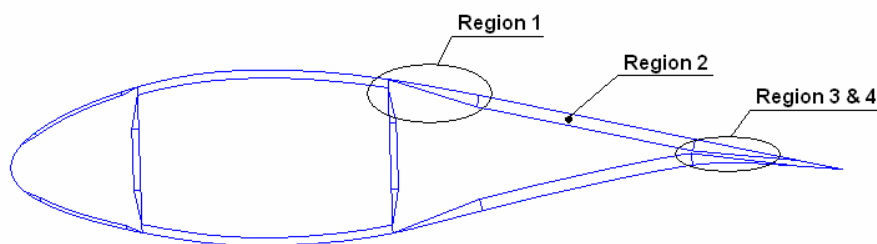


Figure 6.2.1 - Sandwich core regions

The original outer surface FE model can be seen in *Figure 6.2.2* with the simplified sandwich panels:

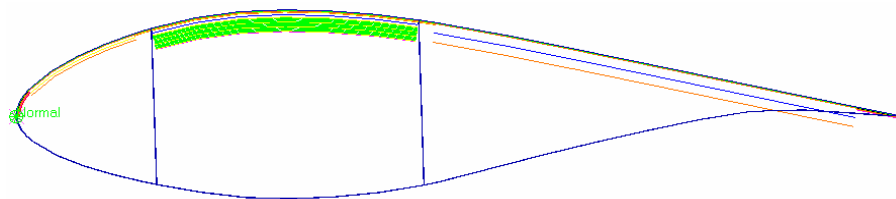


Figure 6.2.2 - Original outer surface FE model

The new improved outer surface model is shown below with the modified sandwich panels and with the material offset from the physical outer surface of the blade section:

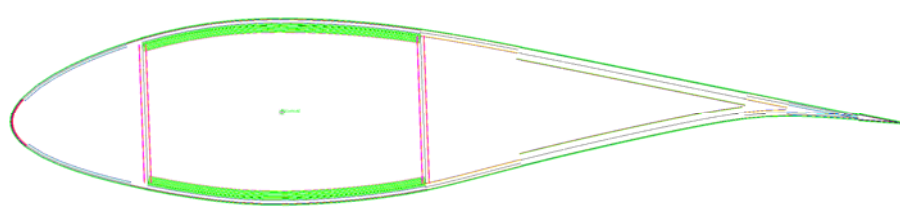


Figure 6.2.3 – Modified outer surface FE-model with material offset

The outer surface model was in excellent agreement with the experimental results when flapwise bending was compared (see chapter 7).

The outer surface model was also in relative good agreement with the experimental results when edgewise bending was compared.

But the agreement between the outer surface model and the experimental results was really poor when torsion was compared. The major part of the disagreement in torsional performance is associated with the layered shell element offset. This problem is described in the paper “Finite Element Modeling of Wind Turbine Blades” by Laird, D.L., Montoya, F.C. and Malcolm, D.J. (LMM) [9]. The results and conclusions from this paper are presented in the following chapter.

Finite element modeling problems

The typical way of modeling a wind turbine blade with the finite element method is by using layered shell elements with an offset. The outer surface or airfoil on a wind turbine blade has a well defined geometry which makes it an obvious location for the shell elements.

The bending response of the blade is of primary interest, but with the continuous development of larger wind turbine blades which result in lower torsion frequencies, then the future blades will be getting closer to the limit of flutter, where flapwise bending and torsion vibrations couple together in a dramatic instability.

In order to determine the flutter speed for a new blade design, then a correct modeling of the torsional response/stiffness and the bend-twist coupling is critical.

A correct torsional modeling is also critical for the future blade designs which will incorporate bend-twist coupling. The bend-twist coupling can for example be used for load reduction, because the blade will twist when it is bended which alter the angle of attack and with it the aerodynamic forces.

However, correct modeling of bend-twist couplings and torsion stiffness based on FEM is subjected to some uncertainties, when numerical results are compared to experimental modal analyses of blades. The major part of this disagreement is associated with the layered shell element offset.

LMM created numerous numerical models to test the accuracy of shell elements with offset in bending and in torsion. LMM tested the accuracy on a cantilevered hollow tube made of aluminum (see *Figure 6.2.4*).

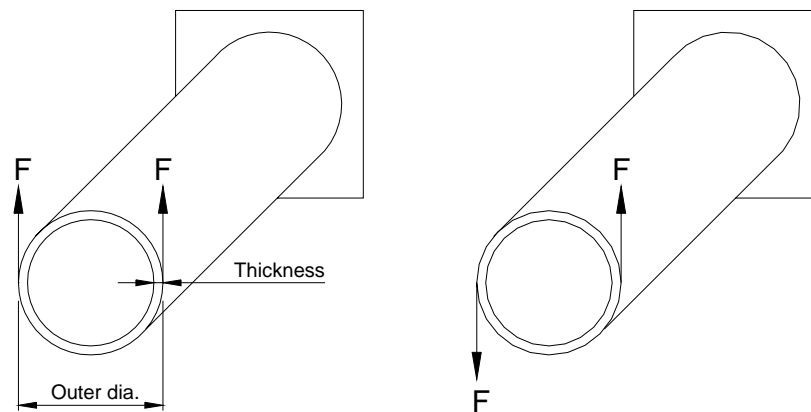


Figure 6.2.4 - Cantilever tube with bending load and torsional load

A hollow tube was selected since the analytical solutions exist for this geometry. The cylinder was modeled with three different element configurations:

- 8-node layered shell with nodes at the material mid-thickness (default element formulation).
- 8-node layered shell with nodes at the outer surface.
- 20-node structural solid element.

The two shell element configurations have nodal locations at two different radii in order to represent the same hollow cylinder. The two forces (F) that creates the torsional loading were scaled to obtain the same torsional moment.

The cylinder was analyzed with a bending load and a torsional load. The bending stress and shear stress was then compared to the analytical result for the following three cases:

- Varying element aspect ratio (no. of elements, radius/thickness, length/diameter = constant).
- Varying number of elements (aspect ratio, radius/thickness, length/diameter = constant).
- Varying radius/thickness ratio (no. of elements, aspect ratio, length = constant).

The element aspect ratio is defined as the axial element length divided by the element width.

Bending test

The bending load was applied as illustrated in *Figure 6.2.4*. The maximum normal (bending) stress was then determined at the mid-span of the hollow tube in order to avoid influence from boundary conditions etc. The tube was modeled with a rigid region at the free end to avoid local distortion where the loads are applied.

The normal/bending stress in the tube can be determined analytically from the following equation:

$$\sigma = \frac{M \cdot x}{I}$$

Equation 6.1

σ is the maximum normal stress due to bending. M is the bending moment. I is the cross sectional area moment of inertia and x is the greatest distance from the neutral axis.

Bending case 1

The first bending case involved varying the element aspect ratio while keeping the number of elements constant at 19200, the radius/thickness ratio constant at 10 and the length/diameter ratio constant at 10. The results can be seen in *Figure 6.2.5*.

The normal stresses from the FE-model are compared to the analytical solution at the mid-span to avoid effects from the boundary conditions and the rigid end.

As one can see, all element configurations had relatively good performance. The solid element model is the most accurate of the three configurations which also was expected, but all configurations had acceptable errors.

The outer surface model performed slightly better than the mid-thickness model, so this study showed no shell offset problems when determining the normal stresses.

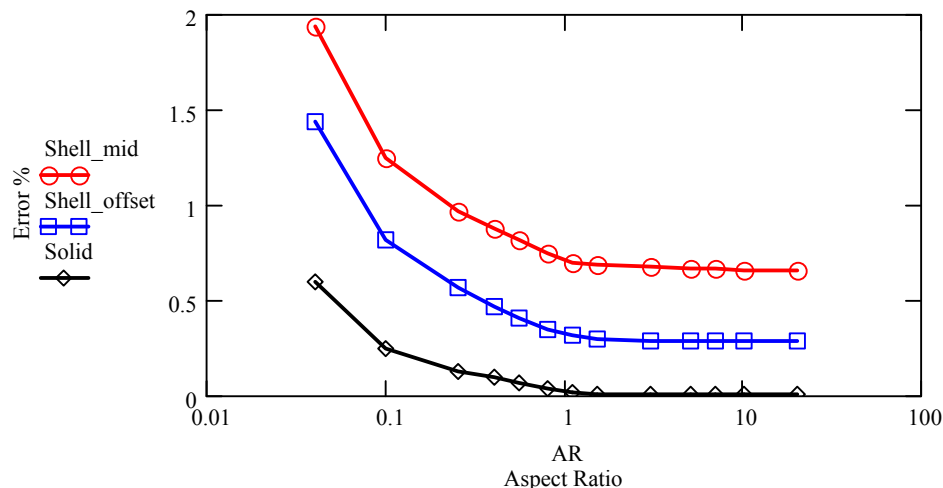


Figure 6.2.5 - Error in normal stress as a function of the aspect ratio

Bending case 2

The second bending case involved varying the number of elements while keeping the aspect ratio constant at 1.1, the radius/thickness ratio constant at 7.5 and the length/diameter ratio constant at 13.3. The results can be seen in *Figure 6.2.6*.

Again, the solid element model is the most accurate of the three configurations which also was expected and again was the performance of the outer surface model slightly better than the mid-thickness model.

The errors converge to a value near zero for the solid model and the outer surface model while the mid-thickness model converges to an error of 0.9%.

Surprisingly, the error stays below 6% for the three element configurations when the mesh discretization is extremely coarse.

Bending case 2 showed no problems with determining the normal stresses when working with shell element offset.

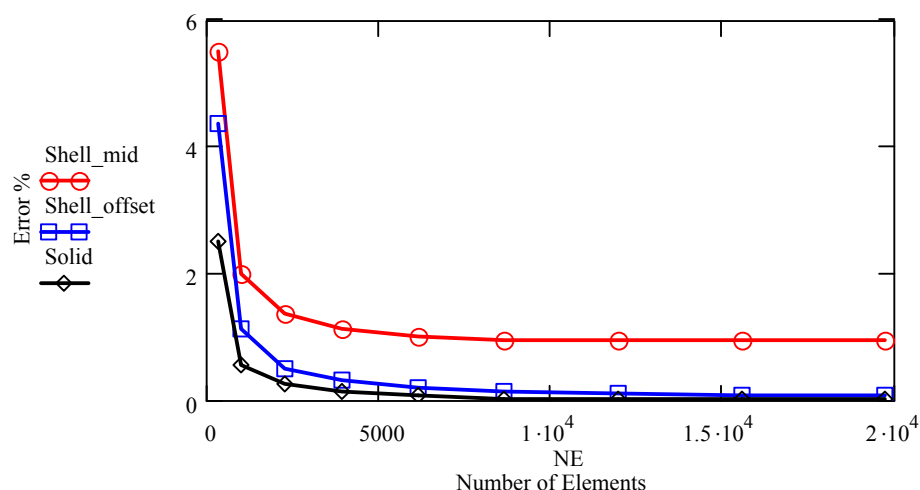


Figure 6.2.6 – Error in normal stress as a function of the number of elements

Bending case 3

The third bending case involved varying the radius/thickness ratio while keeping the aspect ratio constant at 3.4, the number of elements constant at 2880 and the length of the tube constant at 20. The results can be seen in Figure 6.2.7.

All element configurations performed well and converged to the analytical solution when the radius/thickness ratio was more than 5.

The most interesting results were for the outer surface model. The accuracy is excellent for ratios above 5 but for ratios below 5, the accuracy degrades quickly. This is very important in the FE analysis of wind turbine blades for the leading edge. The blade will not in general have small radius/thickness ratios but regions of the leading edge can have radius/thickness ratios as low as 2. This error could significantly affect the results of edgewise bending.

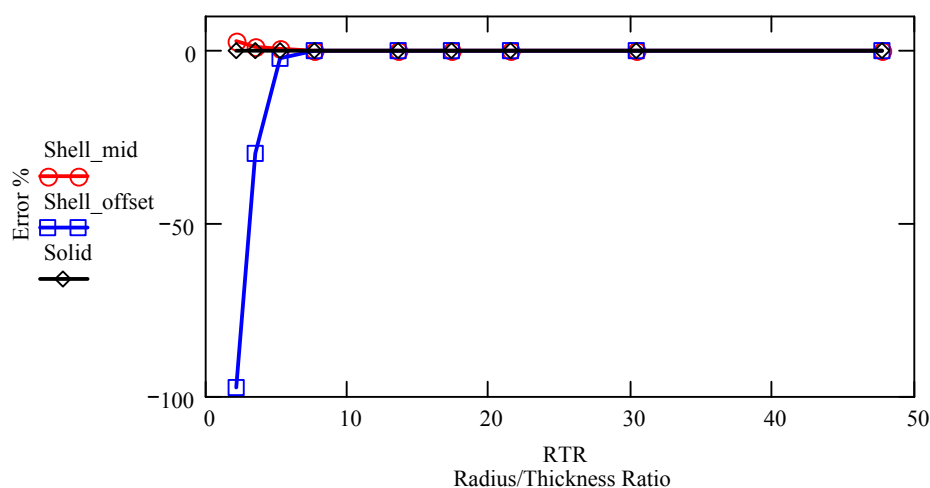


Figure 6.2.7 - Error in normal stress as a function of the radius/thickness ratio

Torsional test

The cantilever tube was subjected to a force couple that generates a torsional load (see *Figure 6.2.4*). The tube was modeled with a rigid region at the free end to avoid local distortion where the loads are applied. As mentioned earlier, the forces (F) were scaled for each element configuration so that one has the same torsional moment.

The shear stress in the tube can be determined analytically from the following equation:

$$\tau = \frac{T \cdot r}{J}$$

Equation 6.2

τ is the maximum shear stress due to torsion. T is the torsional moment. J is the cross sectional polar moment of inertia and r is the outer radius of the tube.

Torsional case 1

The first torsional case involved varying the element aspect ratio while keeping the number of elements constant at 19200, the radius/thickness ratio constant at 10 and the length/diameter ratio constant at 10. The results can be seen in *Figure 6.2.8*.

The shear stresses from the FE-model are compared to the analytical solution at the mid-span to avoid effects from the boundary conditions and the rigid end.

As one can see, both the solid elements and the mid-thickness shell elements performed well at the range studied. The shell model based on the outer surface performed poorly in most of the range.

Only at aspect ratios over approx. 10 did the outer surface model start to perform well, but creating FE-models with such high aspect ratios to fix the offset problem is not a good solution. It is recommended in most FE-codes that one does not operate with aspect ratios greater than 10-12 when working with 8-noded quad elements.

The error is 40% for an aspect ratio of 1 which is the ideal element ratio! As one can see, the study clearly indicates that there is a problem with using shell offset.

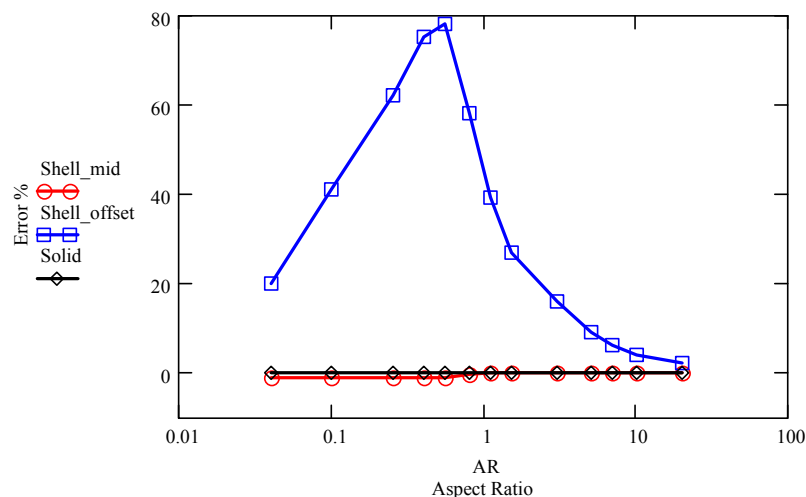


Figure 6.2.8 - Error in shear stress as a function of the aspect ratio

Torsional case 2

The second torsional case involved varying the number of elements while keeping the aspect ratio constant at 1.1, the radius/thickness ratio constant at 7.5 and the length/diameter ratio constant at 13.3. The results can be seen in *Figure 6.2.9*.

Again, both the solid elements and the mid-thickness shell elements performed well at the range studied and again did the shell model based on the outer surface performed poorly.

The error increased with greater numbers of elements which was unexpected since a finer mesh normally gives more accurate results. This behaviour further indicates the problems with shell offset when working with torsional loading.

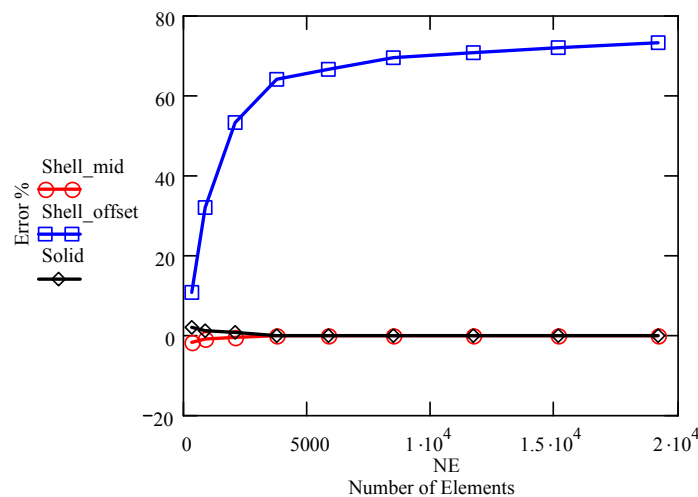


Figure 6.2.9 - Error in shear stress as a function of the number of elements

Torsional case 3

The third torsional case involved varying the radius/thickness ratio while keeping the aspect ratio constant at 3.4, the number of elements constant at 2880 and the length of the tube constant at 20. The results can be seen in *Figure 6.2.10*.

Again, both the solid elements and the mid-thickness shell elements performed well at the range studied and again did the shell model based on the outer surface performed poorly.

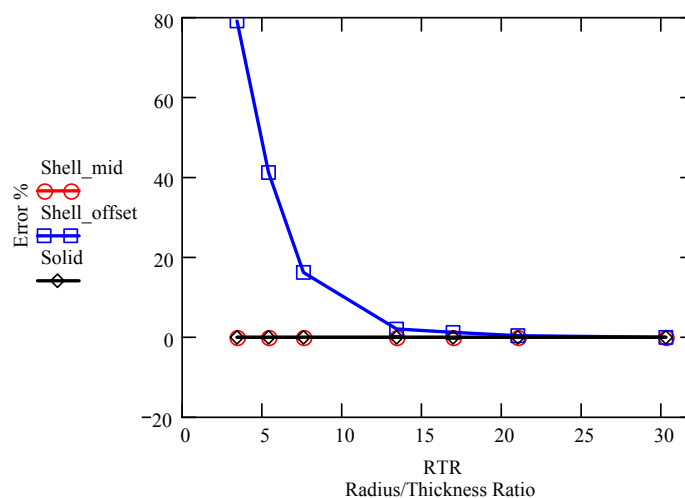


Figure 6.2.10 - Error in shear stress as a function of the radius/thickness ratio

Conclusion

It can be concluded from the LMM studies that wind turbine blade models that uses layered shell element offset are inaccurate for determining the torsional stiffness and the shear stress due to torsional loading. Inaccurate results may also be obtained in bending for cases of very low radius/thickness ratio.

LMM analyzed the circular tube with ANSYS and LMM has confronted ANSYS with these problems with shell element offset. The cylinder with the torsional load was reproduced in COSMOS, NASTRAN and ABAQUS in order to determine if this was only an ANSYS problem. LMM and ANSYS concluded that the problem appears to be a general limitation in the FEA theory.

The results from the bending tests were generally good except for the case of very low radius/thickness ratio. The only region with such low radius/thickness ratios is the leading edge at the near the tip of the wind turbine blade.

The leading edge does not play an important role in flapwise bending, but the edgewise bending results could be significantly affected by the sensitivity to low radius/thickness ratios.

The shear stress results due to torsional loading were extremely poor when working with shells with offset. It appears that this element configuration is not adequate for determining shear stresses, torsional stiffness or coupling coefficients for bend-twist coupled blades.

Comparison between offset and mid-thickness configuration

Two FE-models were created to investigate the difference in torsional and bending stiffnesses when analyzing an outer surface shell model and a mid-thickness shell model.

The aim of this study was to give an idea of the inaccuracy that one is dealing with when working with FE-models that are based on shell elements on the outer surface of the blade (offset).

The two FE-models have the same constant cross section and layup as the 23m Vestas blade at R10.7. Only difference between the two models is that one is based on shell elements at the outer surface of the aerodynamic shell and the other model is based on shell elements that are located at the material mid-thickness.

The outer surface FE-model is created from the geometry of the aerodynamic shell, this geometry is taken from a Pro/E CAD model provided by Vestas Wind Systems A/S.

The webs were created from the geometry of the mandrel. The geometry of the mandrel is also included in the CAD model of the aerodynamic shell (see *Figure 6.2.11*).

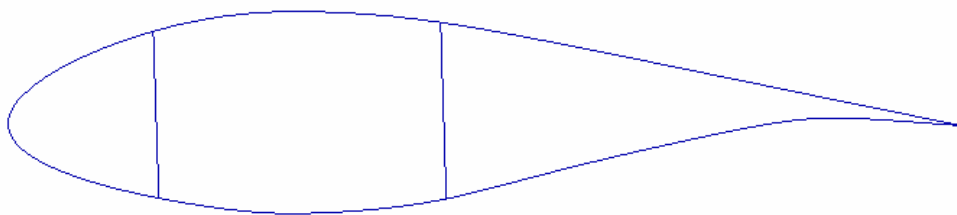


Figure 6.2.11 - Outer surface FE-model

The outer surface FE-model was created with the following offset:

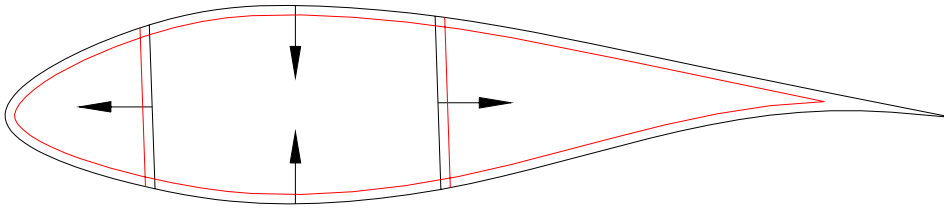


Figure 6.2.12 - Offset for the outer surface FE-model

The mid-thickness FE-model was also created from the geometry of the aerodynamic shell. When looking at a wind turbine blade cross section, one can see that the material thicknesses vary a lot. The trailing part of the blade is very thick since it is a sandwich construction and the spar caps are also thick because of the many UD-layers etc. So the web/cap/leading/trailing thicknesses are not constant and one must therefore calculate all the different mid-thicknesses in order to create a usable FE-model that does not involve shell element offset.



Figure 6.2.13 - Cross section picture of the real blade at R10.7

As one can see in *Figure 6.2.13*, the trailing part of the blade is a sandwich construction. The sandwich panels do not have a constant thickness because the ends are chamfered in order to create smooth transitions when nearing the trailing edge and when nearing the spar. The real panel has a maximum core thickness of 20mm and this was modeled by using four different thicknesses. Four areas were modeled in order to create the four different thicknesses, which can represent the sandwich panels in the trailing part of the blade (see *Figure 6.2.14*). The areas closest to the spar have a core thickness of 10mm, the next areas have a core thickness of 20mm, the next areas have a core thickness of 10mm and the areas closest to the trailing edge have a core thickness of 5mm. The webs are also sandwich constructions. The web panels do not have a constant thickness because the ends are chamfered in order to create smooth transitions between the spar caps and the webs. In this case, the webs have not been modeled with the chamfered ends but as a sandwich panel with constant core thickness.

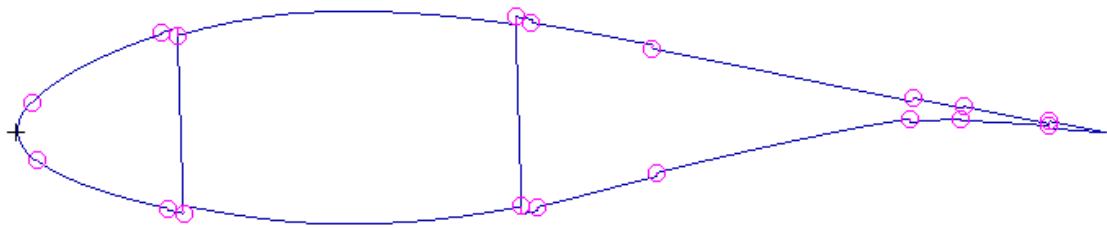


Figure 6.2.14 – Mid-thickness shell model with rigid elements

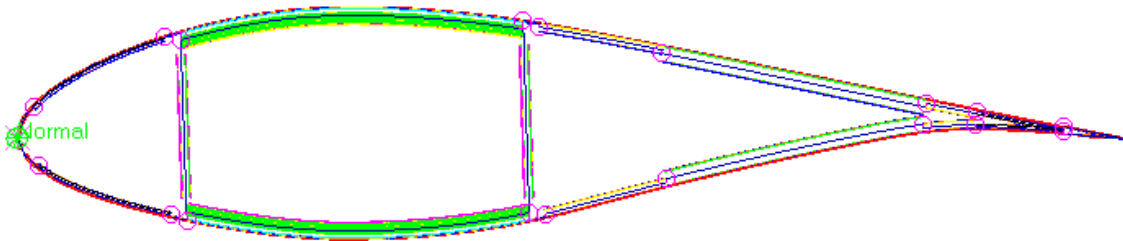


Figure 6.2.15 - Mid-thickness shell model material visualization (Laminate Modeler)

The different material thicknesses in the cross section imply that the aerodynamic shell will not have a continuous surface like the outer surface FE-model. The discontinuous surfaces are connected by rigid (fixed) elements (see *Figure 6.2.16*). A rigid element is capable of transferring all displacements and rotations from one node to another without deforming (rigid).

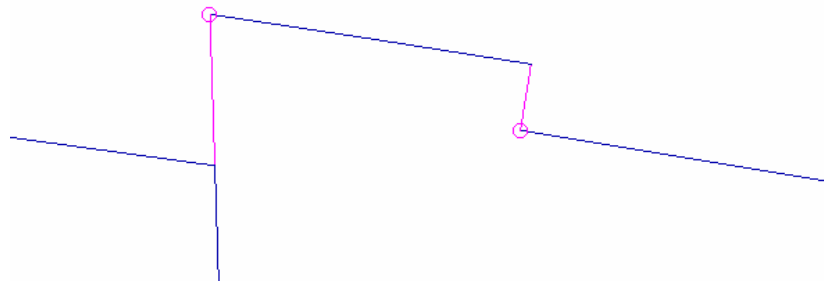


Figure 6.2.16 - Rigid elements (pink) connecting spar corner and trailing sandwich panel

Both FE-models were modeled with a length of 5m. Both FE-models were fixed in one end and a torsional moment of 5000 Nm was applied at the other end. The torsional moment was applied at the center of the spar via a MPC-RBE2 element. The RBE2 element creates a rigid end section that avoids local distortion of the blade where the load is applied.

Four MPC-RBE3 elements were created and connected to the surrounding nodes in the cross sections at 1m, 2m, 3m and 4m. The RBE3 elements' dependent node was placed in the center of the spar and from these nodes the cross-sectional rotations were determined. The RBE3 element does not create a rigid section like the RBE2 element so it has no influence on the behaviour of the FE-model.

The torsional stiffness of the blade is determined by:

$$GJ(z) = \frac{T \cdot z}{\theta(z)}$$

Equation 6.3

T is the torsional moment, z is the spanwise distance and $\theta(z)$ is the twist angle. The results from the torsional analyses are shown below:

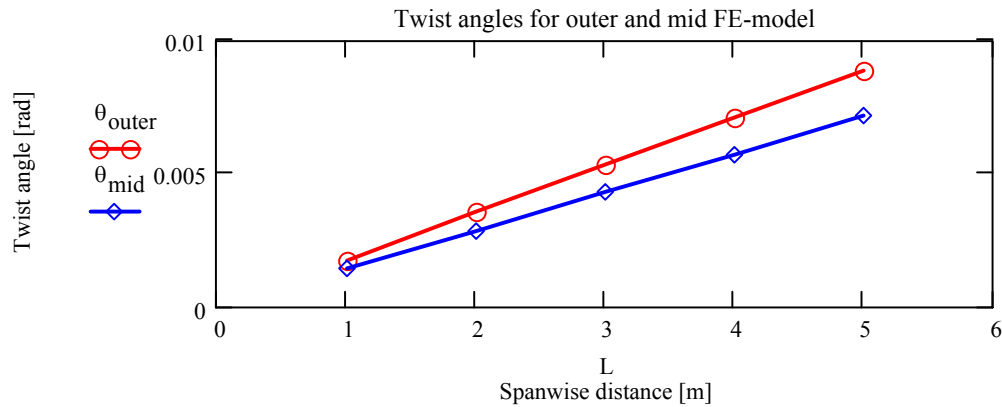


Figure 6.2.17

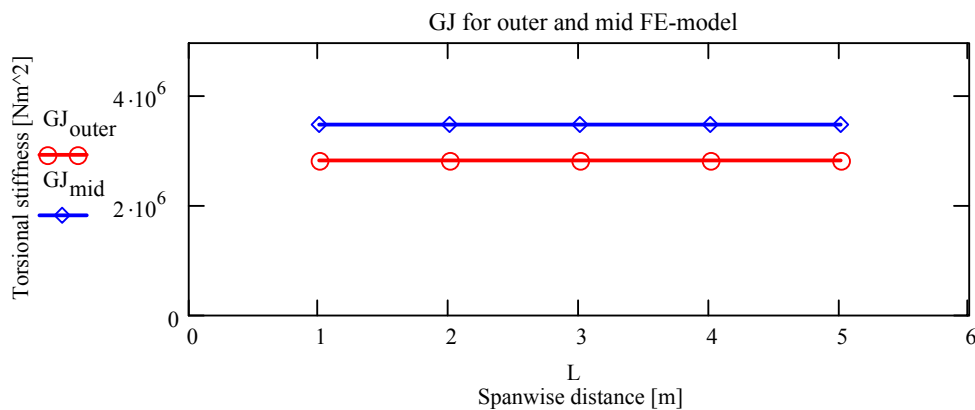


Figure 6.2.18

Conclusion

There is a significant difference between the two FE-models, as one can see in *Figure 6.2.17* and *Figure 6.2.18*. The torsional stiffness deviation is about 19%, with the outer surface FE-model being the most flexible.

Together with the paper "Finite Element Modeling of Wind Turbine Blades" by Laird, D.L., Montoya, F.C. and Malcolm, D.J., this study further indicates the major torsional problem with the current FE-models of wind turbine blades that are based on the outer surface.

Bending loads were also analyzed but no significant difference was observed.

So a shell FE-model without element offset was needed for accurate torsional results!

Mid-thickness shell model

A complete shell FE-model of the blade section without shell element offset was created to obtain accurate numerical torsional results.

The mid-thickness shell model of the blade section is an extension of the mid-thickness model that was created with the constant cross section.

The mid-thickness model generation is a bit complicated because one must calculate all the varying mid-thickness locations. The different mid-thickness locations results in a discontinuous FE-model and is more time consuming to create than the outer surface model.

The curve geometry of the mid-thickness model was created from the following seven cross sections:

- Cross section 1 = R10.70.
- Cross section 2 = R12.06.
- Cross section 3 = R13.12.
- Cross section 4 = R15.24.
- Cross section 5 = R16.40.
- Cross section 6 = R17.70.
- Cross section 7 = R19.30.

From Pro/Engineer files of the 25 m blade provided by Vestas Wind Systems A/S, the dimensions of the seven different cross sections were measured.

Each cross section was created from twelve points (see *Figure 6.2.19*); one at the leading edge (106), one at the trailing edge (101), four at the connections between the spar webs and the blade shells (103, 105, 107 and 109), two at the top and the bottom of the spar (104 and 108), and finally four points to describe the rear part of the blade (102, 110, 111 and 112):

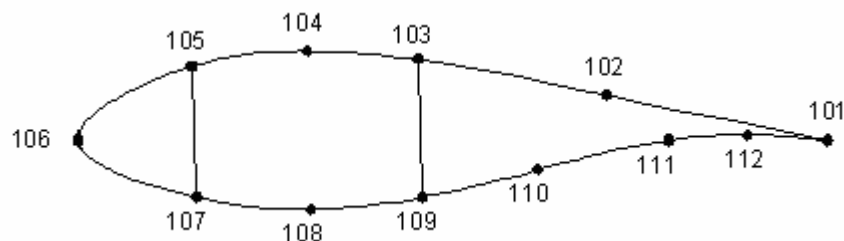


Figure 6.2.19 – Point locations and numbering

The aerodynamic shell was created by creating a curve spline through the twelve points.

The spline is the physical outer geometry of the blade, which is the inside of the moulds for the upper and lower blade shells.

The two spar webs were created by connecting point 105/107 and 103/109 with two straight curves. The two curves are the outer geometry of the mandrel on which the spar is constructed.

The sandwich panels and the spar caps were then created by offsetting the curve geometry of the aerodynamic shell (see *Figure 6.2.20*):

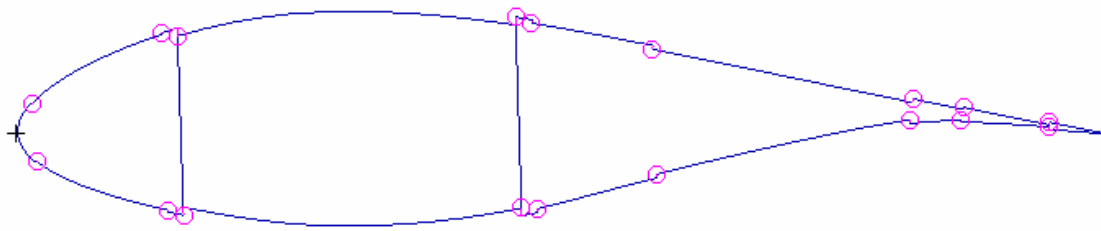


Figure 6.2.20 – Mid-thickness illustration

The nodes on the meshed surfaces were then connected by MPC-Rigid (fixed) elements. Rigid elements were created along and across the blade to connect the discontinuous regions (see *Figure 6.2.21*). The rigid element across the spar cap was created because of a UD ply drop-off which changes the location of the mid-thickness:

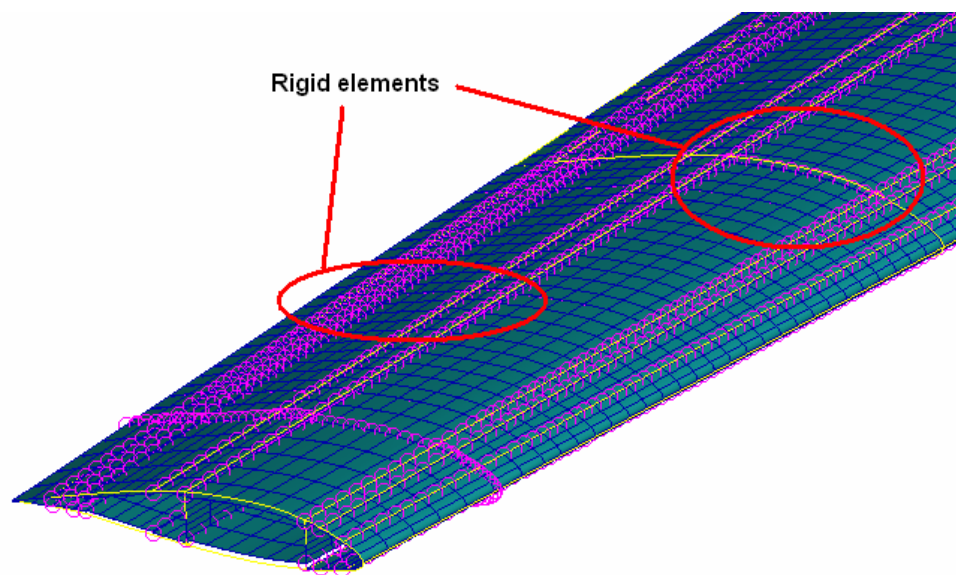


Figure 6.2.21 – Rigid elements

The picture below is generated by MSC Laminate Modeler and shows the “extruded” material. It is very important to check these visualized pictures of the layup in order to see if the model is created correct.

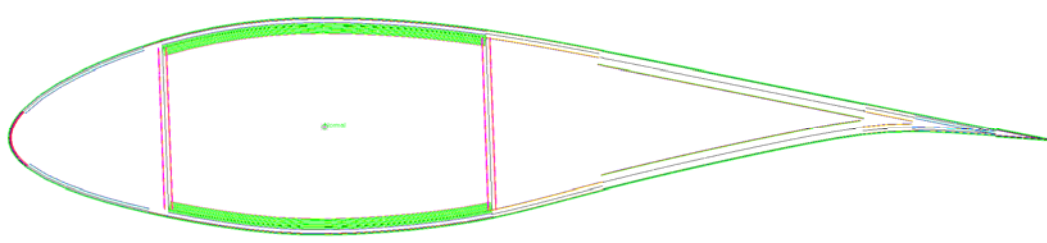


Figure 6.2.22 – Material thickness

The mid-thickness model was an improvement of the outer surface model in terms of the torsional results but the mid-thickness model was not in good agreement with the experimental results when flapwise and edgewise bending was compared (see chapter 7).

Shell/solid model

Because of the bad performance by the mid-thickness model, then was a combined shell/solid model created.

Much of the material thickness discontinuity in the blade cross section is due to sandwich panels and instead of modeling these with a mid-thickness shell configuration, then the core material and adhesive bonds were modeled with solid elements in the shell/solid FE-model.

Geometry creation

The FE-model of the blade section was created from the following seven cross sections:

- Cross section 1 = R10.70.
- Cross section 2 = R12.06.
- Cross section 3 = R13.12.
- Cross section 4 = R15.24.
- Cross section 5 = R16.40.
- Cross section 6 = R17.70.
- Cross section 7 = R19.30.

From Pro/Engineer files of the 25 m blade provided by Vestas Wind Systems A/S, the dimensions of the seven different cross sections were measured.

Each cross sections was created from twelve points (see *Figure 6.2.23*); one at the leading edge (106), one at the trailing edge (101), four at the connections between the spar webs and the blade shells (103, 105, 107 and 109), two at the top and the bottom of the spar (104 and 108), and finally four points to describe the rear part of the blade (102, 110, 111 and 112).

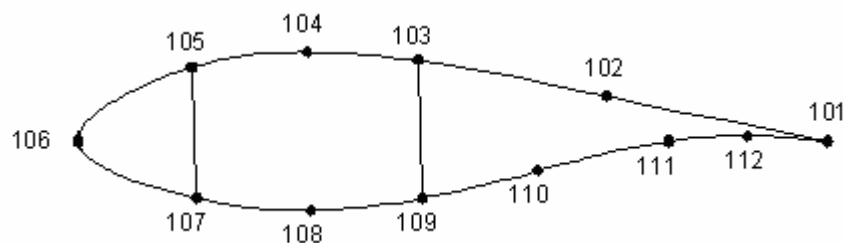


Figure 6.2.23 - Location of the twelve cross sectional points

The aerodynamic shell was created by a curve spline through the twelve points.

The spline is the outer physical geometry of the blade, which is the inside of the moulds for the upper and lower blade shells.

The two spar webs were created by connecting point 105/107 and 103/109 with two straight curves. The two curves are the outer geometry of the mandrel on which the spar is constructed.

The sandwich panels and the spar caps were then created by offsetting the curve geometry of the aerodynamic shell and the spar webs (see *Figure 6.2.24*).

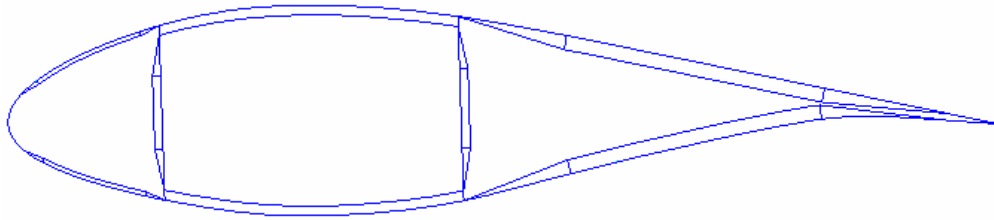


Figure 6.2.24 - Cross section curves

The seven cross sections were then connected with longitudinal spline curves (see *Figure 6.2.25*).

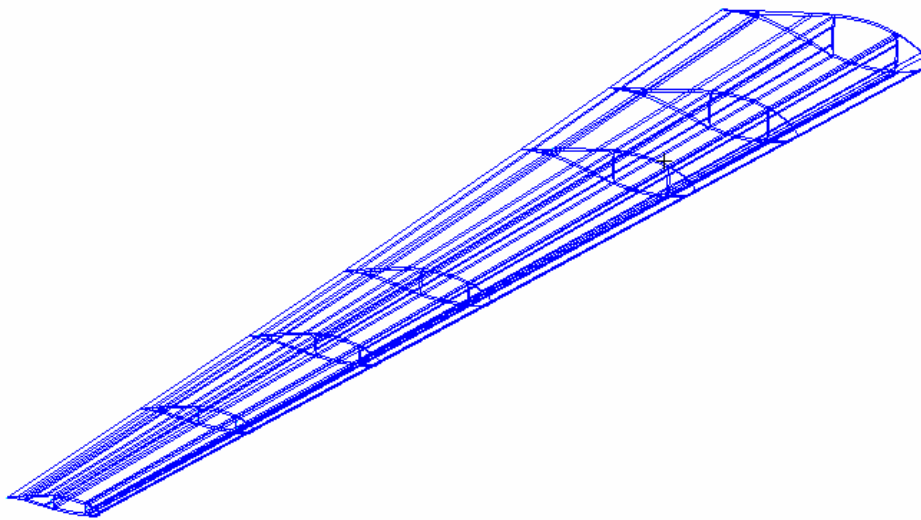


Figure 6.2.25 - Complete curve geometry

Surface and solid creation

All surfaces were created from the longitudinal spline curves and the cross section curves. All surfaces were therefore created from four edges which is very important in order to create the correct double curvature. The surfaces represent the following:

- Outer aerodynamic surface (outer sandwich skins).
- Inner sandwich skins in the leading and trailing part of the blade.
- Leading and trailing edge.
- Web sandwich skins.
- Spar caps.

After creating the surfaces were the solids created. All solids were created from two opposing surfaces. The solids represent the following:

- Sandwich core in the leading and trailing part of the blade.
- Sandwich core in the webs.
- Adhesive bonds between the aerodynamic shell and the spar.

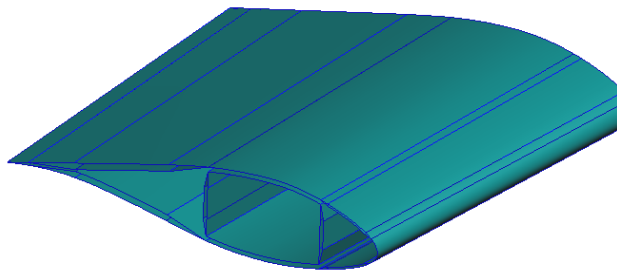


Figure 6.2.26 - Surfaces

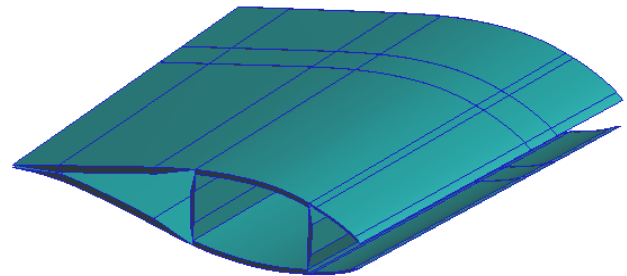


Figure 6.2.27 - Solids

Mesh creation

The surfaces were meshed with 8-noded shell elements (Quad8) and the solids were meshed with 20-noded solid elements (Hex20).

A Quad4/Hex8 configuration reduces the number of DOF's, but this configuration was not used because of the limited aspect ratios and possible problems with shear locking.

It is recommended that one stays below aspect ratios of 2 when working with Quad4/Hex8 and this becomes a “problem” when meshing the leading edge.

The leading edge requires a fine mesh because of the great curvature, it is of course possible to mesh with Quad4 elements but since the element length can only be twice the element width, then one is forced to use an unnecessary fine mesh along the blade which seriously increases the solving time.

The maximum aspect ratio for Quad8/Hex20 is 10-12 which mean that one can mesh the leading edge with longer elements and thereby reduce the number of elements in the longitudinal blade direction.

The mesh density of the blade section was determined from a flapwise-, edgewise- and torsional convergence test by examining the cross sectional displacements and rotations.

All convergence tests were carried out with the blade being fixed at R12.877 and with the loads applied at R18.934 via a MPC-RBE2 element.

The converged solution or final displacements/rotations was determined by examining each cross section at every half meter. The twelve cross sectional displacements and rotations were obtained by using MPC-RBE3 (see “Loads and boundary conditions”).

In general, a relative coarse mesh can give accurate global displacement results for a FE-model but a much finer mesh is required for analyzing stresses and strains in the structure.

When analyzing stresses and strains, one can determine the required mesh density by examining the stress contour lines and the stress discontinuities between elements.

A contour plot that displays significant interelement discontinuities warns that a finer mesh is needed.

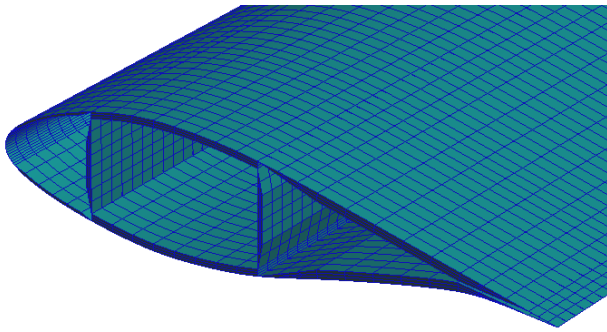


Figure 6.2.28 - Meshed blade section at R10.8

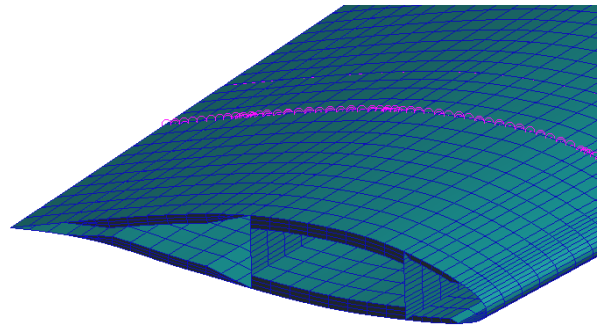


Figure 6.2.29 - Meshed blade section at R19.2

The shell/solid FE-model used a mesh of 74 elements circumferentially, 175 elements longitudinally and 3 solid elements through the thickness of the sandwiches and the adhesive bonds and had 600.000 degrees of freedom (DOF).

The convergence tests showed that it was necessary to have 3 solid elements through the thickness in order to model accurate shear deformation.

Solid wedge elements were automatically created by MSC.Patran in the regions where the solids are chamfered.

A fine mesh of 18 elements was used in the leading edge to avoid shape warnings from MSC.

The Quad8/Hex20 aspect ratios were kept below 7 to avoid poor FE results.

The FE-model used thick shell formulation which is automatically enabled when working with composite materials in MSC.

Loads and boundary conditions

As described earlier, one has three options regarding modeling of the experimental boundary conditions:

- One can model the test rig boundary conditions by measuring the deflections of the clamps with the Aramis equipment. These deflections can then be applied to the FE-model.
- One can also model the test rig boundary conditions by modeling the clamps. To get a realistic FE-model of the clamps, one must model the plywood plates and the steel profiles and then use contact elements to model the contact between the clamps and the blade section.
- Finally, one can solve the test rig boundary condition problem by using the Aramis experimental data to determine all the cross sectional displacements and rotations via least squares algorithms.
One can create a fully fixed and clamped boundary condition by subtracting the measured deflections and rotations of the cross section where one wants the fixed end, from all the other cross sections.

The last method was chosen because this is the simplest and probably also the most precise method.

The fixed end of the blade section cannot warp when the blade is subjected to torsion or bending. The torsional stiffness increases considerably when this out-of-plane distortion is restrained. The test rig used for the experimental work cannot restrain warping 100%, so the following numerical studies were carried out:

- a) Comparison of the flapwise bending stiffnesses when the fixed end was placed at R10.7 and at R12.877.
- b) Comparison of the edgewise bending stiffnesses when the fixed end was placed at R10.7 and at R12.877.
- c) Comparison of the torsional stiffnesses when the fixed end was placed at R10.7 and at R12.877.

Case (a) and (b) showed that the flapwise and edgewise bending stiffnesses are more or less unaffected by the position of the fixed end. The stiffness variations were below 0.1%.

Case (c) showed that the torsional stiffness decreased approximately 2.5% when the fixed end was moved from R12.877 to R10.7. The size of the model (DOF's) and the solving time was increased significantly when the boundary condition was moved from R12.877 to R10.7 and the profit was relatively small, so the fixed end was placed at R12.877 (clamp 2 location).

A load application node was created at the blade tip in the center of the spar and a MPC-RBE2 element was used to transfer the forces/moments to the surrounding nodes on the cross section (see *Figure 6.2.30*). RBE2 is a rigid element so local distortion of the blade is avoided where the loads are applied.

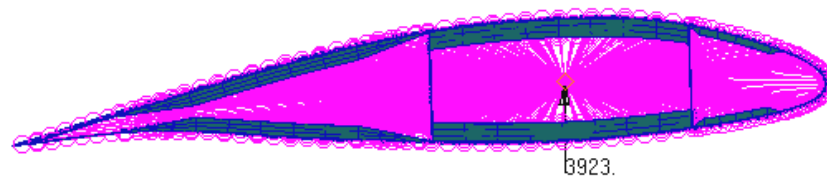


Figure 6.2.30 - RBE2 element for load applications

Twelve nodes were created along the blade in the center of the spar. The nodes were created at the same locations along the z-axis as the cross sections from the experiments.

Twelve MPC-RBE3 elements were created with the spar center node as the dependent node.

The dependent node is connected to the surrounding nodes on the cross section.

RBE3 is a linear interpolation element, which means that the displacement and rotation of the dependent node is govern by the independent nodes on the cross section.

All cross sectional displacements and rotations are therefore obtained from the RBE3 elements.

Note that the RBE3 element does not create a rigid region like the RBE2 element.

The twelve RBE3 elements and their locations are shown below:

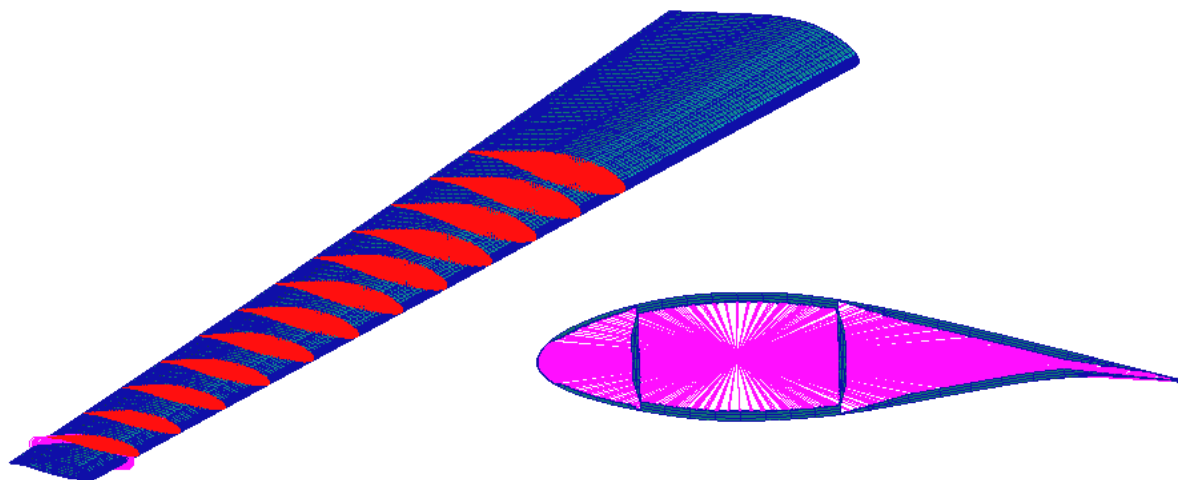


Figure 6.2.31 – RBE3 elements along the blade and a RBE3 element in a cross section.

Layup creation

The FE-model was “laminated” with the build-in program MSC Laminate Modeler.

Laminate Modeler models the lay-up by entering each ply in the same stack sequence as it would be placed in the mould and on the spar mandrel (see *Figure 6.2.32*).

The initial application point, fiber orientation and extent of each ply are specified and Laminate modeler then determines the fiber orientations over the full extent of the ply.

When all plies are modeled and stacked into a laminate, then Laminate Modeler determines the equivalent properties of the lay-up at every shell element.

A exploded view of the spar cap layup is shown below:

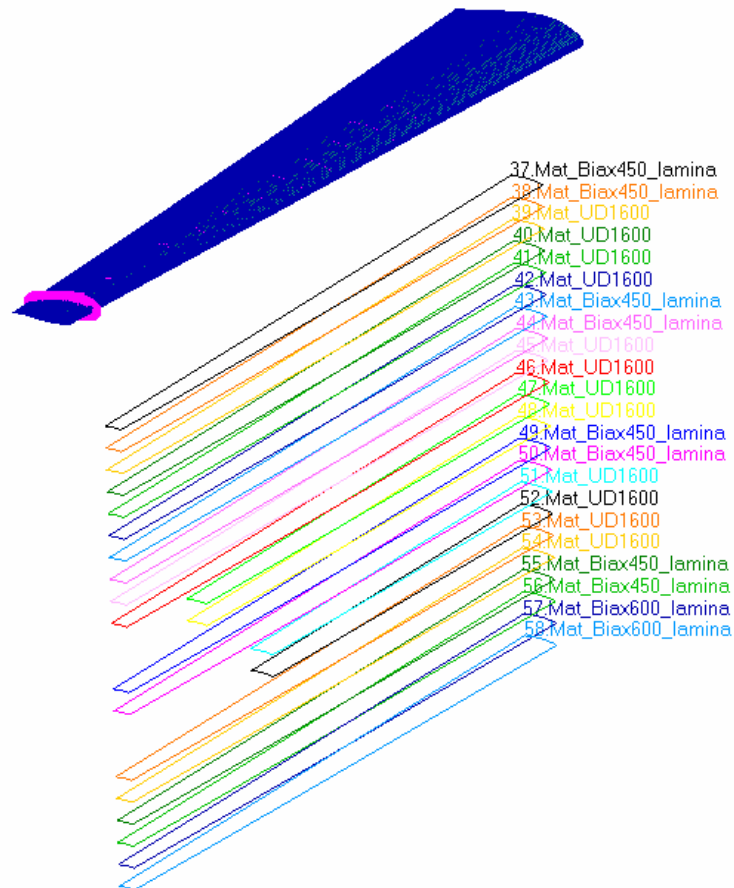


Figure 6.2.32 - Laminate modeler, exploded view of the spar cap layup

The shell/solid FE-model used the mid-thickness shell formulation for the sandwich skins, the leading and trailing edge and the spar caps.

The outer surface of the blade section was available from the CAD model so this surface was used as the location for the mid-thickness shells. This means that the outer sandwich skins and leading/trailing edge laminates do not align with the physical outer surface, but that they have an incorrect offset of half the thickness, see for example the leading edge in *Figure 6.2.36*.

A numerical study showed that the flapwise bending stiffness only decreased 0.4% when going from mid-thickness (incorrect) to shell offset formulation (correct).

Furthermore, a numerical study showed that the edgewise bending stiffness only decreased 0.2% when going from mid-thickness (incorrect) to shell offset formulation (correct).

The results from the two numerical studies are reliable since Laird and Malcolm concluded that one can obtain accurate bending results with shell element offset, as long as the radius/thickness ratio is not very low.

A similar numerical study regarding the torsional stiffness was not performed since the results from the shell offset model cannot be trusted.

The details of the shell/solid model are shown below:

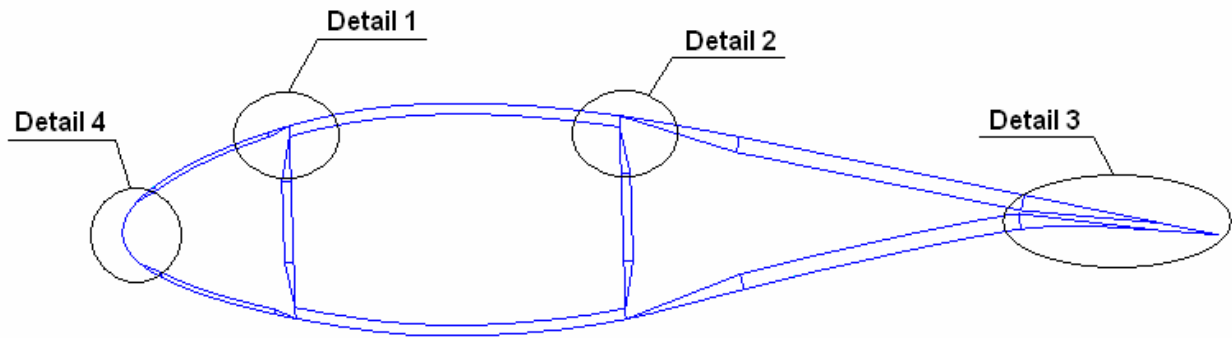


Figure 6.2.33 - Details

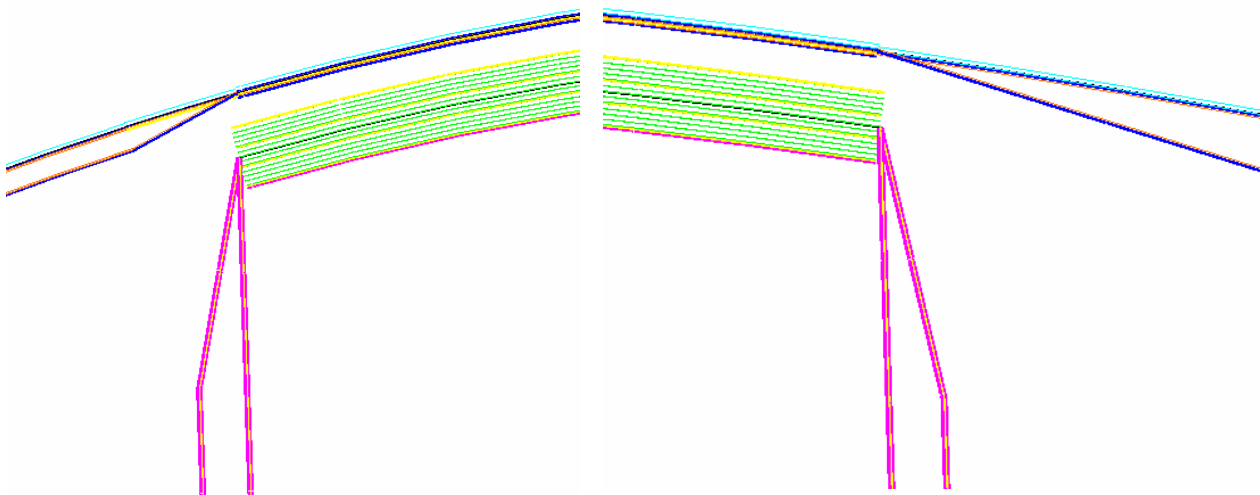


Figure 6.2.34 – Detail 1

Figure 6.2.35 – Detail 2

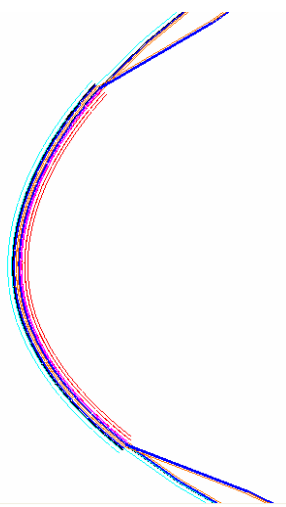


Figure 6.2.36 – Detail 4

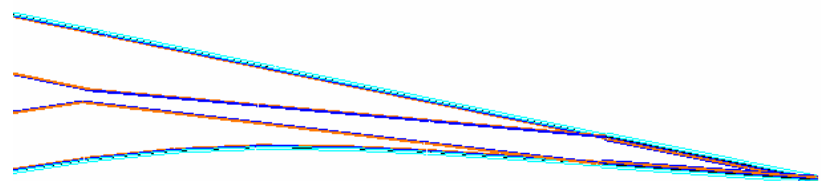


Figure 6.2.37 – Detail 3

The green lines are UD layers, yellow lines are Biax450 layers, pink lines are Biax600 layers, blue lines are Triax layers and the cyan line is the Gelcoat.

The black line in the middle of the spar cap is the middle surface or mid-thickness where the shell elements are located.

One cannot model the blade section 100% correct with the mid-thickness shell configuration. But in this case are the errors that are introduced so small that the shell/solid mid-thickness configuration is the most optimal way to model the blade section.

The only alternatives to the shell/solid model are a layered solid model or a full solid model where all plies are modeled with layers of solid elements.

Adhesive bond modification

As described earlier, the spar caps were modeled with mid-thickness shell elements. The correct location of these shell elements is critical in order to have an accurate model. The shell elements in the spar caps are connected to the aerodynamic shell via the adhesive bonds.

The spar caps are about 12mm thick and it was therefore necessary to model the adhesive bonds about three times thicker than the real bonds, in order to have the correct location of the shell elements.

The real adhesive bond is 5mm thick but in the shell/solid FE-model is the thickness 16.2mm and the affect from this on the stiffnesses was therefore investigated.

The study began by reducing the E- and G-modulus by a factor of 3 since the adhesive bond in the FE-model is about 3 times thicker and in this way, one keeps the extensional stiffness (AE) constant. The study showed that the flapwise bending stiffness was reduced by 3% and the edgewise bending stiffness by 1% when the E-modulus was reduced by a factor of 3.

The study also showed that the torsional stiffness was reduced by 3.5% when the G-modulus was reduced by a factor of 3.

The changes in the stiffnesses varied along the blade, so the percentages mentioned above are all average values.

Overall, the study showed that a general modification of the properties for the adhesive bond was too simple and a more accurate modification was needed.

Instead of the simple modification mentioned above, where one keeps the extensional stiffness of the adhesive bond constant, then a more accurate modification was introduced that is based on the bending and torsional stiffnesses of the adhesive bond itself:

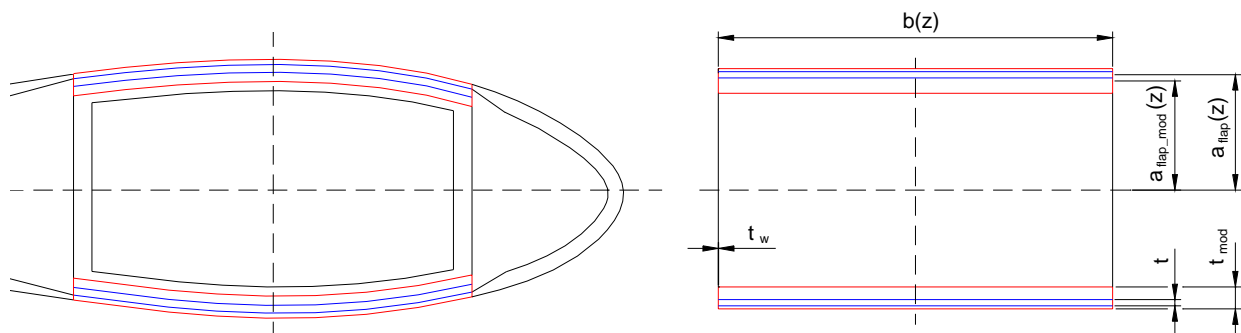


Figure 6.2.38 – Right figure, real blade cross section with the adhesive bond. The blue lines show the original bond and the red shows the modified bond that is used in the shell/solid FE-model. Left figure, simplified adhesive bond used for calculating the modified E- and G-modulus that are used in the FE-model

Since the adhesive bond has a significant influence on the stiffnesses, then a set of modified E- and G-modulus was determined. The new modulus together with the modified bond must give the same stiffnesses as for the original blade:

$$E_{\text{flap}} \cdot I_{\text{flap}} = E_{\text{flap_mod}} \cdot I_{\text{flap_mod}} \quad \Leftrightarrow \quad E_{\text{flap_mod}}(z) = \frac{E_{\text{flap}} \cdot I_{\text{flap}}(z)}{I_{\text{flap_mod}}(z)}$$

$$E_{\text{edge_mod}}(z) = \frac{E_{\text{edge}} \cdot I_{\text{edge}}(z)}{I_{\text{edge_mod}}(z)} \quad \text{and} \quad G_{\text{mod}}(z) = \frac{G \cdot J(z)}{J_{\text{mod}}(z)}$$

One must know the location and orientation of the principal axes in order to determine the area moment of inertia (AMI) for the adhesive bonds. In this case, it was assumed that the elastic center is placed in the center of the spar and it was assumed that the flapwise principal axis is perpendicular to the shear webs, see *Figure 6.2.38*.

Both the original and the modified adhesive bond has the same breadth ($b(z)$) and the same curvature around the z -axis. This mean that the distances $a_{\text{flap}}(z)$ and $a_{\text{flap_mod}}(z)$ are the same and a simplified rectangular shape can therefore be used for calculating the area moment of inertia. By analyzing the adhesive bond as a rectangular tube, one can determine the area moment of inertia and the cross sectional torsion factor:

$$I_{\text{flap}}(z) = 2 \cdot \left(\frac{1}{12} \cdot b(z) \cdot t^3 + b(z) \cdot t \cdot a_{\text{flap}}(z)^2 \right) \quad I_{\text{edge}}(z) = 2 \cdot \left(\frac{1}{12} \cdot b(z)^3 \cdot t + b(z) \cdot t \cdot a_{\text{edge}}(z)^2 \right)$$

$$I_{\text{flap_mod}}(z) = 2 \cdot \left(\frac{1}{12} \cdot b(z) \cdot t_{\text{mod}}^3 + b(z) \cdot t_{\text{mod}} \cdot a_{\text{flap_mod}}(z)^2 \right)$$

$$I_{\text{edge_mod}}(z) = 2 \cdot \left(\frac{1}{12} \cdot b(z)^3 \cdot t_{\text{mod}} + b(z) \cdot t_{\text{mod}} \cdot a_{\text{edge_mod}}(z)^2 \right)$$

$$J(z) = \frac{2 \cdot t \cdot t_w \cdot b(z)^2 \cdot h(z)^2}{b(z) \cdot t_w + h_0(z) \cdot t_{\text{mod}}} \quad J_{\text{mod}}(z) = \frac{2 \cdot t_{\text{mod}} \cdot t_w \cdot b(z)^2 \cdot h_{\text{mod}}(z)^2}{b(z) \cdot t_w + h_1(z) \cdot t_{\text{mod}}}$$

$$h(z) = 2 \cdot a_{\text{flap}}(z) \quad h_{\text{mod}}(z) = 2 \cdot a_{\text{flap_mod}}(z)$$

The expression for the torsional factor J/J_{mod} is taken from [6].

As mentioned earlier, the adhesive bond was analyzed as a rectangular tube with the flange thicknesses t/t_{mod} and the web thickness t_w . It is necessary to define a web thickness and in this case, it is set to 10^{-8} m. If a web thickness is not defined then the expression will be zero, but by setting the web thickness to a small value then this problem will be eliminated and the webs will not contribute to the overall torsional factor.

The two modified E-modulus are not the same for the flapwise and edgewise direction, so an average value was used for the FE-model (E_{mod}):

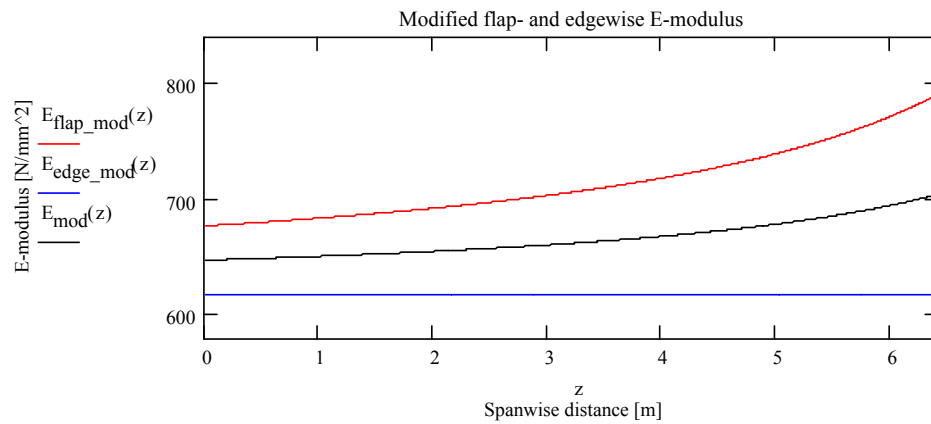


Figure 6.2.39 – E-modulus plot

The FE-model is divided into thirteen 0.5m sections along the z-axis. The sections have been assigned the following E-modulus [N/mm^2]:

$E_{\text{mod}}^T =$	1	2	3	4	5	6	7	8	9	10	11	12	13
1	647.9	649.5	651.4	653.5	655.9	658.6	661.7	665.4	669.7	674.8	681.1	688.7	698.3

The thirteen sections have been assigned the following average G-modulus [N/mm^2]:

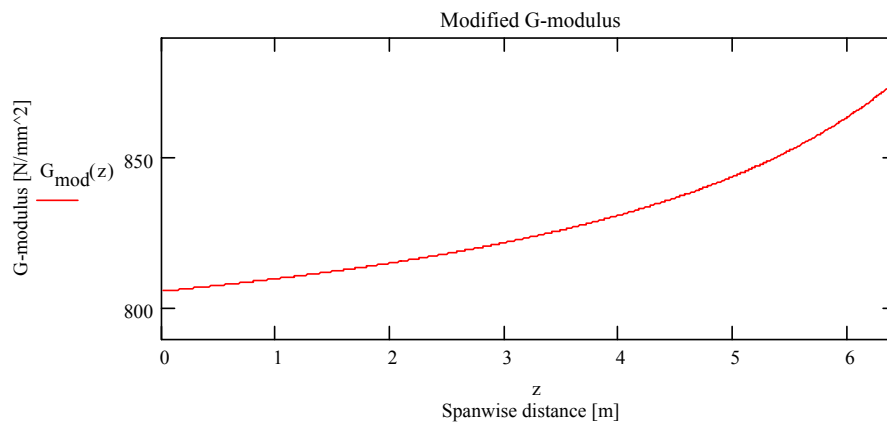


Figure 6.2.40 – G-modulus plot

$G_{\text{mod}}^T =$	1	2	3	4	5	6	7	8	9	10	11	12	13
1	806.6	808.6	810.9	813.5	816.4	819.7	823.6	828	833.3	839.6	847.3	856.6	868.4

FE-modeling of the extra UD-layers

As described earlier, one of the aims with this project is to create a FE-model that is capable of modeling correct bend-twist coupling behavior.

The original blade section was modified and four layers of UD1200 were laminated on the pressure and suction side to create a measurable flapwise bend-twist coupling.

The extra UD layers were modeled with solid elements on top of the existing outer surface shell elements. Four UD layers were added, each UD has a thickness of 1.1mm, so the solid elements were created with a thickness of 4.4mm.

The extra UD layers were meshed with 20-noded solid elements (Hex20) and 1 solid element was used through the thickness. The total number of DOF's for the FE-model increased from 600.000 to 700.000 with the additional solid elements.

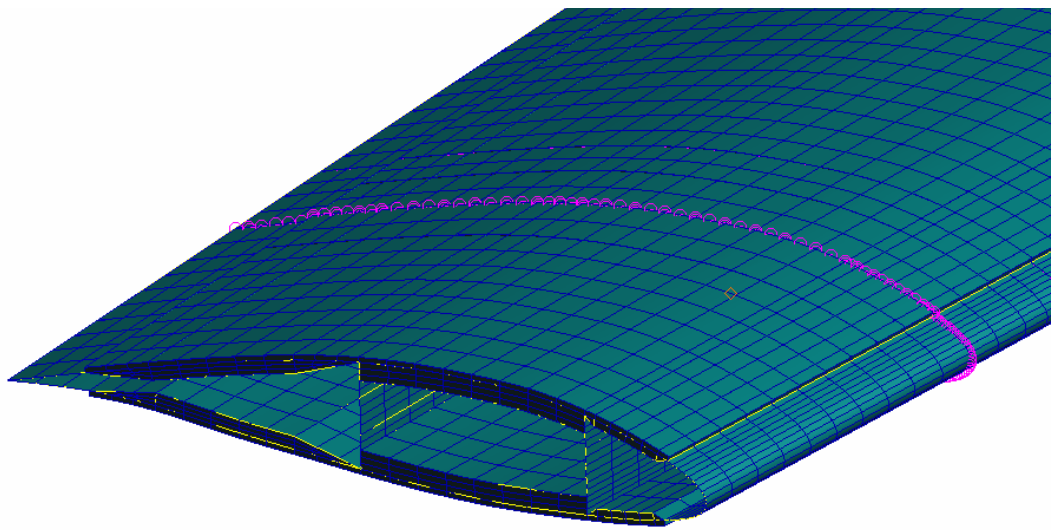


Figure 6.2.41 – Shell/solid model with extra UD layers

7. Validation of FEM

The three FE-models of the original blade are compared with the experimental results in this chapter. The most accurate FE-model is then chosen and modified by including the additional UD layers on the suction and pressure side of aerodynamic profile. This modified FE-model is then compared with the experimental results obtained from the static load cases that were performed on the modified blade section.

7.1. Global comparison of exp. and num. results for the original blade section

The numerical and experimental deflections and rotations are compared globally for the following three static load cases:

- Flapwise bending
- Edgewise bending
- Torsion (Locked Torsion)

The three deflections and rotations for each of the FE-models cross sections are calculated by using the same method as used for the experimental tests (least squares method). The results from the least squares method is plotted below. The results are illustrated for a FE-analysis of a flapwise bending test:

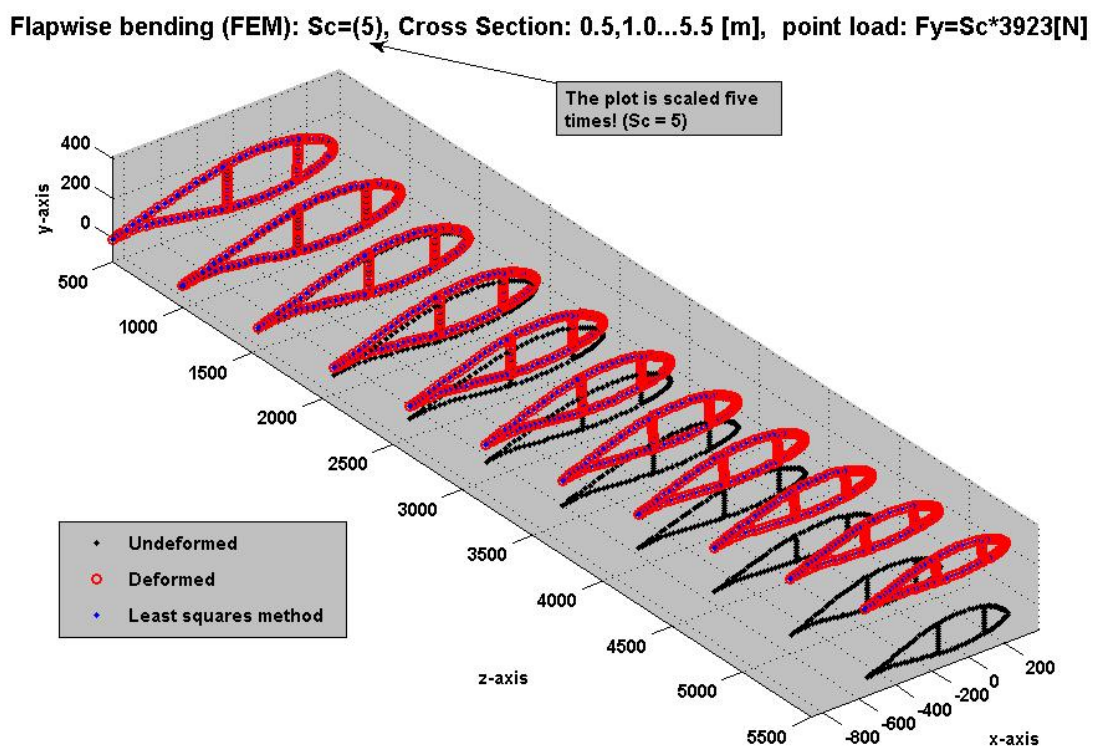


Figure 7.1.1 – Least squares method on FEM

As mentioned earlier, the FE-model is fully fixed in cross section 0.0m and the load is applied in cross section 6.057m by using a MPC element. The “fixed end” is then moved to cross section 0.5m by subtracting the deflections and rotations at this cross section from all the other cross

sections. The last half meter of the FE-model is not considered. The reason for doing this is to minimize the affect of the two rigid regions, which will increase the stiffness near the two ends due to the increasing warping resistance.

7.1.1. Flapwise bending of the original blade section (experimental vs. FEM)

The experimental result of the flapwise bending test is compared with the numerical results of the different FE-models. The three FE-models are:

- A simple shell model created with shell offset.
- A shell model created by using mid-thickness, which are linked with rigid elements.
- A more complex model using solid elements to describe the core-material and using “mid-surface” shell elements to describe the solid laminates.

A more detailed description of the three FE-models can be found in chapter 6. The flapwise bending test was performed by applying a point load in the y-direction at cross section 6.057m.

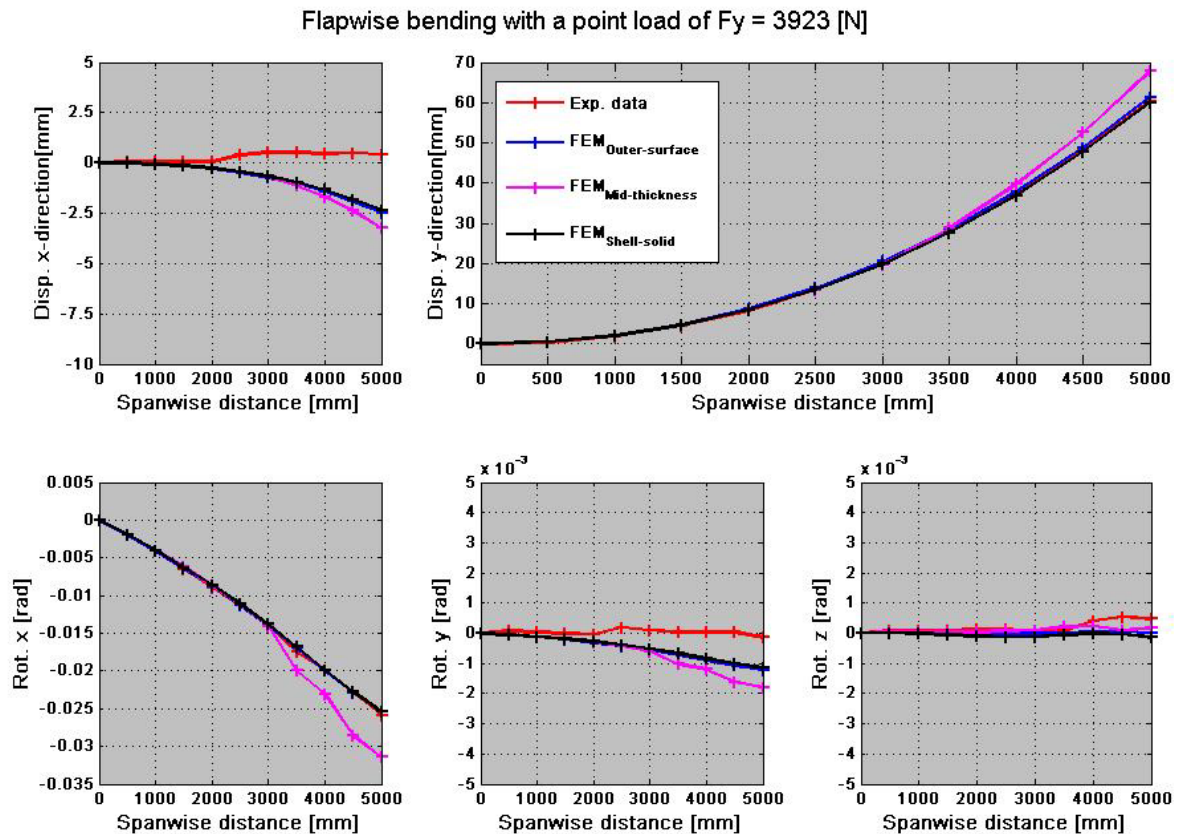


Figure 7.1.2 - Comparison of numerical and experimental results from flapwise bending test

Experimental vs. FEM_{outer-surface}

It can be concluded that the numerical flapwise displacement (disp. y-direction) is in excellent agreement with the experimental results; the deviation is only about 1.5%. Furthermore, it can also be concluded that the rotation about the x-axis is in excellent agreement with the numerical results; the deviation is only about 1.6%.

The agreements between the numerical and experimental results for the displacement in the x-direction and the rotation about the y-axis are not good.

The deviations in the x-direction displacements and y-axis rotation could be due to;

- a) The hydraulic press was not perfectly aligned with the vertical plane which could result in a small force component in the x-direction.
- b) The experimental values are very small and therefore subjected to some measuring uncertainties.
- c) The experimental setup could deviate from the FE-model in terms of the orientation of the blade section. The chord at clamp 1 should be aligned with the horizontal plane but this was practically difficult to achieve which mean that the orientation of the blade section could deviate slightly from the FE-model.

The agreement between the numerical and experimental results for the rotation about the z-axis is relatively good. If it is assumed that the shear center is located at the center of the spar, then it can be concluded that both the numerical and experimental bend-twist coupling (flapwise) is of limited size. The deviation in the rotation about the z-axis is due to uncertainties regarding the hydraulic press, experimental measuring accuracy and experimental setup as described earlier.

Experimental vs. FEM_{mid-thickness}

In general, it can be concluded that the FE-model is in good agreement with the experimental results at the first 3m but then the FE-model starts to deviate drastically.

This is the case for all the displacements and rotations which indicates that there is a serious general problem with the numerical model. One can see that the rotation about the x-axis drops when going from 3 – 3.5m and again when going from 4 – 4.5m.

The blade section has a ply drop-off in the spar caps at these two locations at this was modeled in mid-thickness FE-model by dividing each spar cap into three areas with different lay-up's.

The three spar cap areas represent the three different mid-thicknesses and are connected via rigid (fixed) elements across the caps.

The FE-model was checked several times for possible modeling errors without finding anything. The FE-model was then modified by deleting the rigid elements and then connecting the adjacent nodes where the rigid elements used to be. The nodes were connected by bending the adjacent shell elements about the mid nodes, this is poor FE-modeling but was done in order to see if the problems was due to the rigid elements in the spar caps.

The modified mid-thickness was in relative good agreement with the experimental results over the whole length and it can therefore be concluded that one cannot model correct flapwise bending with the mid-thickness FE-model if details like ply drop-off etc. are included.

Experimental vs. FEM_{shell-solid}

The flapwise bending behavior of the shell/solid FE-model is almost identical to the flapwise bending behavior of the outer surface FE-model. The conclusions for the shell/solid model when compared to the experimental results are therefore identical to the conclusions for the outer surface model.

The deviation between the num. and exp. results for the displacement in the y-direction is about 1% and about 2% for the rotation about the x-axis.

7.1.2. Edgewise bending of original blade section (experimental vs. FEM)

The edgewise bending test was performed by applying a point load in the x-direction at cross section 6.057m.

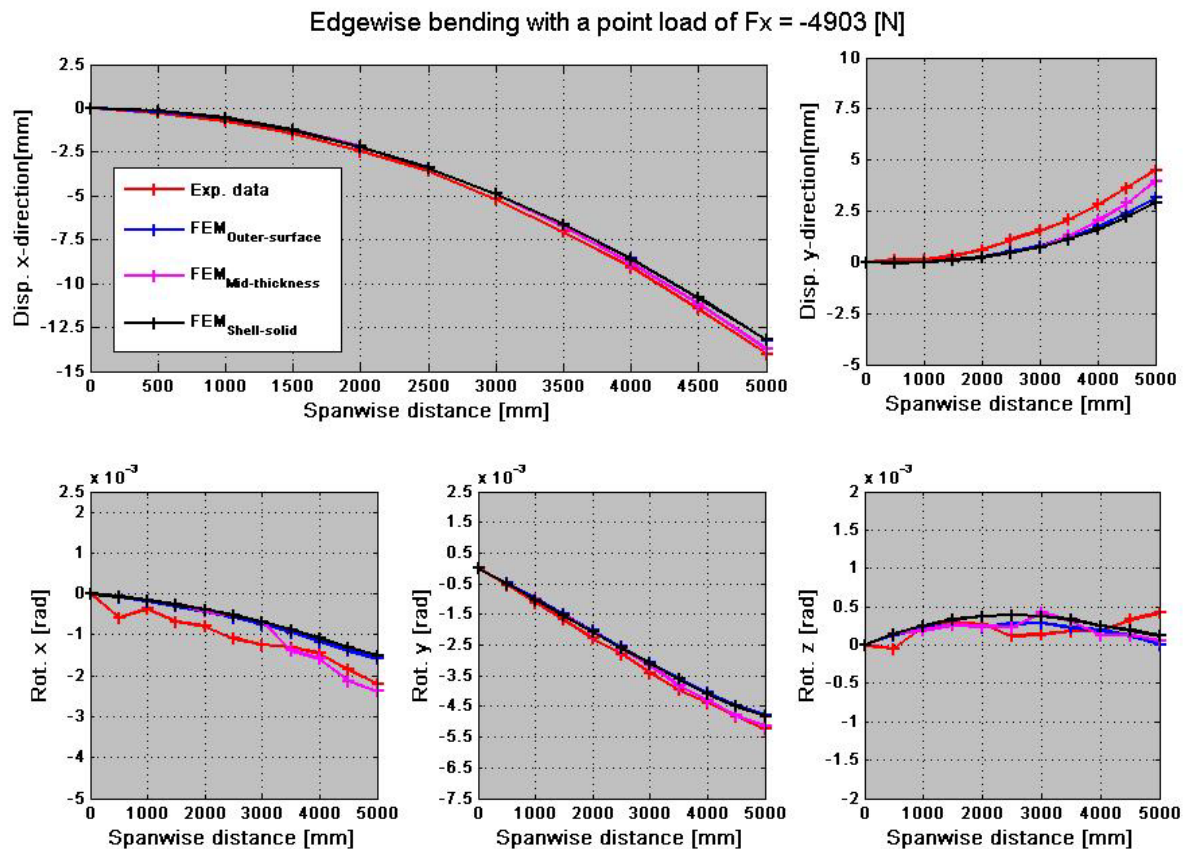


Figure 7.1.3 - Comparison of numerical and experimental results from edgewise bending test

Experimental vs. FEM_{outer-surface}

It can be concluded that the numerical edgewise displacement (disp. x-direction) is in relative good agreement with the experimental results; the deviation is about 6%. Furthermore, it can also be concluded that the rotation about the y-axis is in relative good agreement with the numerical results; the deviation is about 8%.

The agreements between the numerical and experimental results for the displacement in the y-direction and the rotation about the x-axis are not perfect, there exist some disagreement and the deviation is about 30 - 40%.

The agreement between the numerical and experimental results for the rotation about the z-axis is relative good at the first 2m but at the last 3m is there some deviation. The experimental results are very small and not well defined so the rotation about the z-axis is a bit unstable along the blade. The deviation between num. and exp. results could therefore be due to uncertainties regarding the measuring accuracy.

The edgewise deviations could in general be due to;

a) Experimental measuring accuracy, the displacement that were measured during the edgewise experiment are relative small, the blade was only deformed about 40mm at the tip. The reason for this small tip displacement was primarily because of problems with the trailing part of the

blade section under clamp 2. The sandwich panels in the trailing part of the blade are relative soft and the reaction forces in clamp 2 are primarily on these panels during edgewise bending. So to avoid crushing of the panels then the magnitude of the edgewise point load was relative small which meant that the edgewise displacement also was limited.

b) The hydraulic press started out with being horizontal aligned but this changed as the load increased, because the edgewise principal axis is not vertical.

The principal axes rotate along the blade and the blade was therefore also bended in the flapwise direction when the horizontal force was applied. The flapwise displacement during the edgewise test affects the orientation of the hydraulic press so that the edgewise point load is no longer applied horizontally as in the beginning. The flapwise bending of the blade contributes to the displacement in the x-direction because the flapwise principal axis is not perpendicular to the y-axis.

c) The experimental setup could deviate from the FE-model in terms of the orientation of the blade section as described earlier.

d) The hydraulic press was not aligned perfectly with the horizontal plane.

e) The FE-model is based on a shell element offset configuration which can give poor bending results if the radius/thickness ratio is low (see chapter 6 for a more detailed description).

Experimental vs. FEM_{mid-thickness}

The edgewise bending behavior (x- and y-disp. and x-, y- and z-rot.) of the mid-thickness FE-model is almost identical to the outer surface and shell/solid FE-models at the first 3m.

But again, the mid-thickness FE-model starts to behave strangely at 3m span which especially can be seen on the plots of the y-displacement and the x-axis rotation (flapwise).

This strange behavior is due to the problems with the rigid elements that were described earlier. The same strange behavior can also be seen in the plots of the displacement in the x-direction and the rotation about the y-axis.

Experimental vs. FEM_{shell-solid}

Again, the edgewise bending behavior of the shell/solid FE-model is almost identical to the edgewise bending behavior of the outer surface FE-model. The conclusions for the shell/solid model when compared to the experimental results are therefore identical to the conclusions for the outer surface model. The shell/solid was not created with a shell element offset configuration so the problem with poor bending results when the radius/thickness ratio is low was eliminated with this FE-model.

The deviation between the num. and exp. results for the displacement in the x-direction is about 6% and about 8% for the rotation about the y-axis.

The deviation between the num. and exp. results for the displacement in the y-direction is about 40 - 50% and about 45% for the rotation about the x-axis.

7.1.3. Locked Torsion of original blade section (experimental vs. FEM)

The numerical locked torsion test was performed by locking the tip cross section in a point directly over the center of the spar. This point cannot move in the vertical plane, but is able to move in the horizontal plane in a circular arc movement. The cross section is of course able to rotate about this point. For the experimental locked torsion test is the point located on the top of the loading clamp (for a more detailed description of this test, see chapter 5).

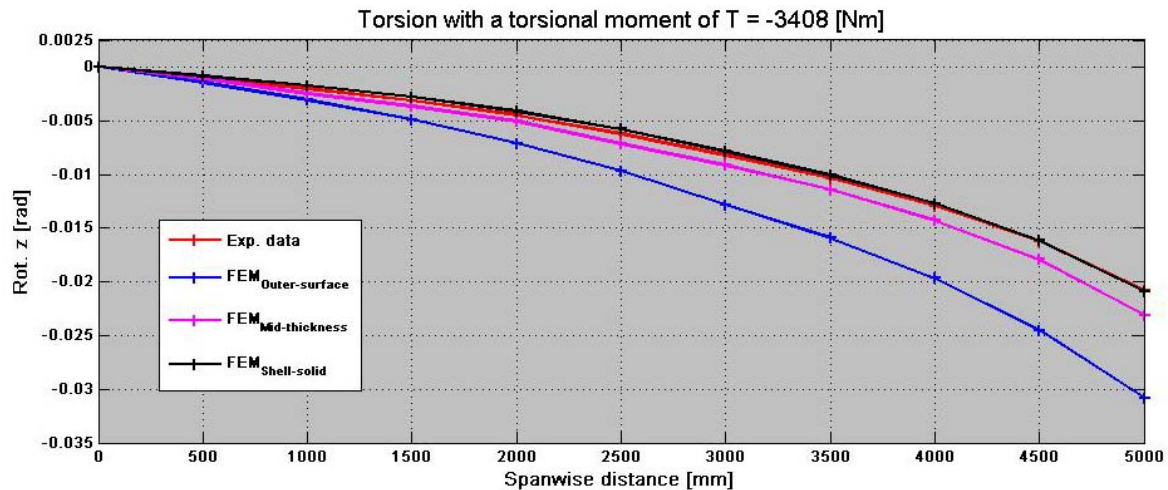


Figure 7.1.4 – Results from the locked torsion test

Experimental vs. FEM_{outer-surface}

The agreement between the num. and exp. results is very poor and the deviation is about 32%. The major part of the disagreement is due to the FE-model which is based on a shell element offset configuration. This configuration has serious problems with modeling correct torsional behaviour as it can be seen in Figure 7.1.4.

Experimental vs. FEM_{mid-thickness}

The agreement between the num. and exp. results for the rotation about the z-axis is not perfect; the deviation is about 10 - 12%. The major part of the disagreement is probably due to the rigid elements that run along the blade which connects the shell elements in the areas with different material thicknesses.

Experimental vs. FEM_{shell-solid}

The agreement between the num. and exp. results for the rotation about the z-axis is generally very good. The deviation is only about 1 – 4% on the last 3.5m of the blade section.

The FE-model is not twisting nearly as much as the experiment and the deviation at the first 1.5m is about 5 – 9%. The deviations could be due to;

- Affects from the boundary conditions in the FE-model. The fixed end of the blade section cannot warp when the blade is subjected to torsion and the torsional stiffness could therefore increase considerably when this out-of-plane distortion is restrained.
- The experimental measuring accuracy.
- The hydraulic press was not perfectly aligned with the vertical plane.

7.2. Comparison of stiffnesses for the original blade section

As stated before, the blade section is divided into ten beam elements of equal length. The stiffnesses are calculated by the moment distribution and the relative rotation over each element. The procedure for calculating the stiffness parameters are shown below:

$$L_z^T = (0 \ 0.5 \ 1 \ 1.5 \ 2 \ 2.5 \ 3 \ 3.5 \ 4 \ 4.5 \ 5) \quad i = 1..rows(L_z)$$

$$EI_{flap_i} = \frac{-\int_{L_{z_i}}^{L_{z_{i+1}}} M_x(z) dz}{r_{x_{i+1}} - r_{x_i}} \quad EI_{edge_i} = \frac{\int_{L_{z_i}}^{L_{z_{i+1}}} M_y(z) dz}{r_{y_{i+1}} - r_{y_i}} \quad GJ_i = \frac{-T \cdot (L_{z_{i+1}} - L_{z_i})}{r_{z_{i+1}} - r_{z_i}}$$

Equation 7.1

In the plot below are the three stiffness parameters (flapwise bending stiffness, edgewise bending stiffness and torsional stiffness) plotted. Since the location of the shear center and the orientation of the principle axes are not known, then shall these values only be looked at as an estimate of the three stiffness parameters. Note that it is assumed that the bend-twist coupling is equal to zero. The circles in the plot are the elements stiffnesses and the solid lines are second order polynomial-fit based on the elements stiffnesses:

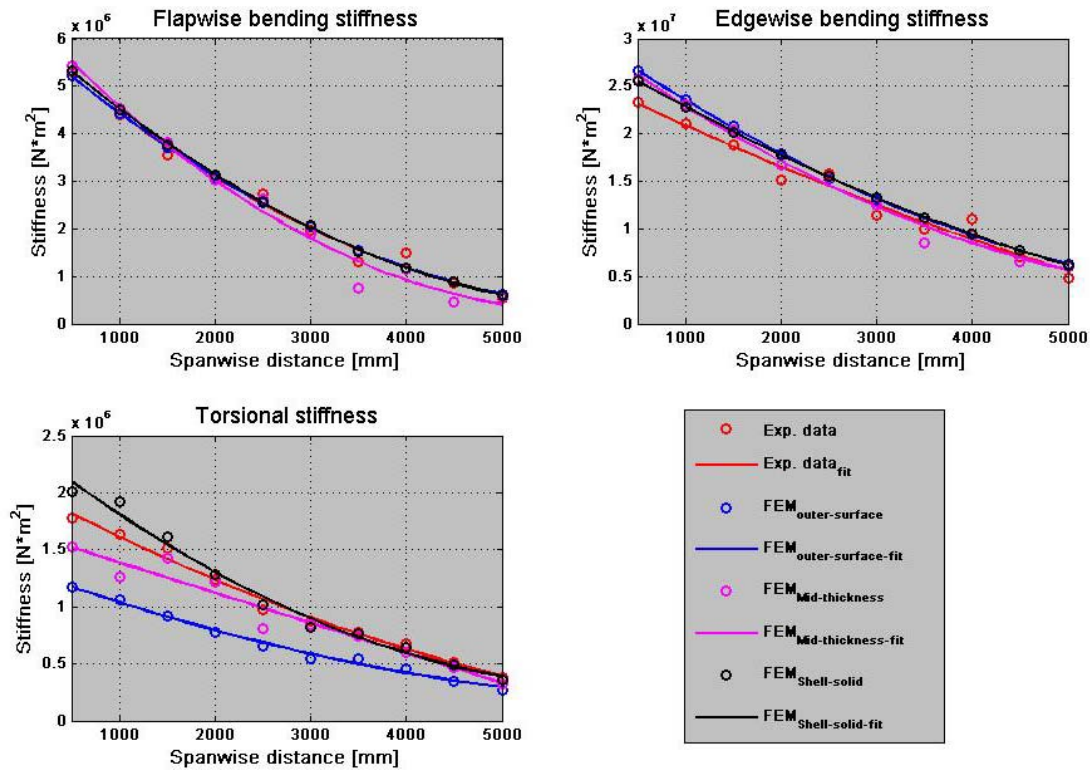


Figure 7.2.1 - Comparison of stiffness parameters for the original blade section

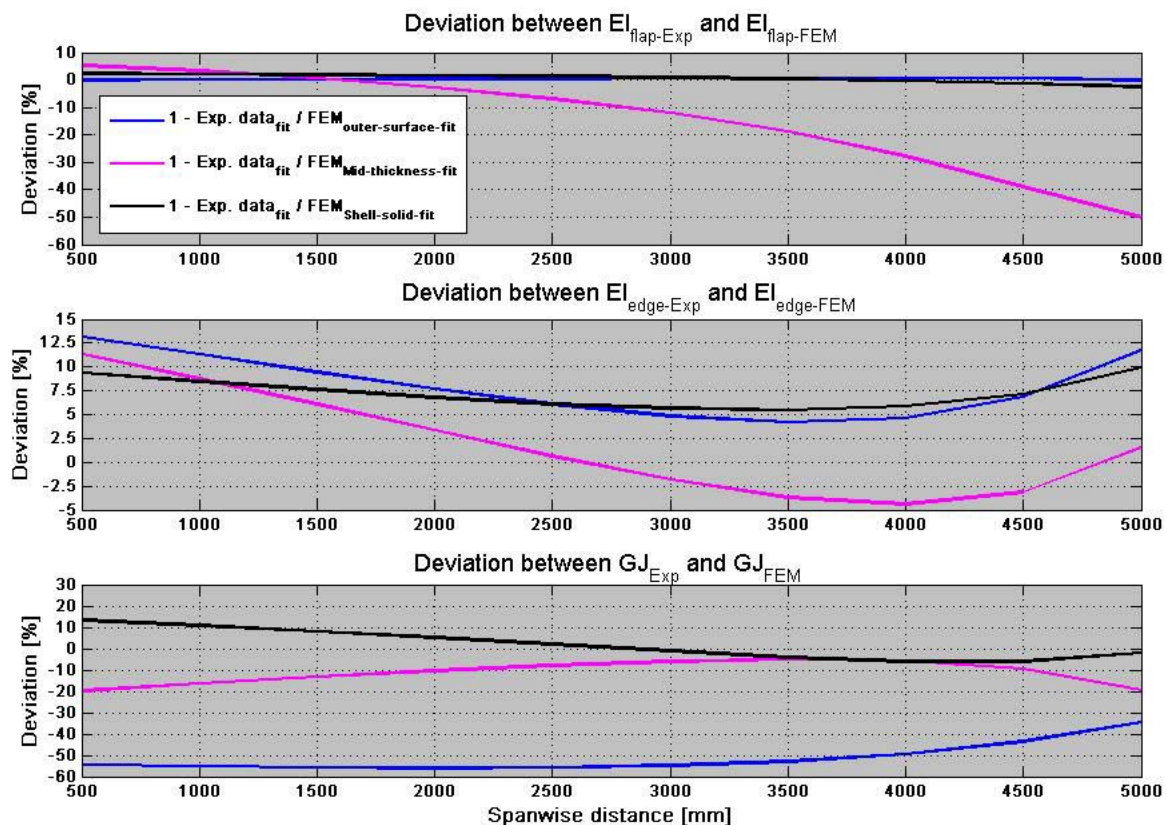


Figure 7.2.2 – Deviation between experimental and numerical estimated stiffnesses

General comment

Note that a second order polynomial fit has been used in order to create the stiffness curves. This is primarily because the experimental determined stiffnesses are not completely smooth along the blade due to measuring uncertainties. The reason for this is that the stiffness of each element is determined by the moment distribution and the relative rotation over the element. These relative element rotations are in general very small and therefore require very accurate experimental measurements.

So in short, in order to perform a direct stiffness comparison between experimental and numerical results, one must have experimental data with very high precision. The same high precision is not required for a global response comparison.

Outer surface FE-model

It can be concluded that the numerical determined flapwise bending stiffness is in excellent agreement with the experimental determined flapwise bending stiffness; the maximum deviation is only about 1% at the tip of the blade section.

It can also be concluded that the num. determined edgewise bending stiffness is in relative good agreement with the exp. determined edgewise bending stiffness, although the maximum deviation is about 13% at the fixed end of the blade section. Note, as stated before, that the experimental data used to determine the edgewise bending stiffness is subjected to some uncertainties.

Finally, it can be concluded that the num. determined torsional stiffness is in poor agreement with the exp. determined torsional stiffness; the maximum deviation is as high as 55% at the 2m span.

Mid-thickness FE-model

As stated before, the mid-thickness model has some general problems with the rigid element configuration. These problems affect the element stiffnesses.

Shell/solid FE-model

It can be concluded that the numerical determined flapwise bending stiffness is in excellent agreement with the experimental determined flapwise bending stiffness; the maximum deviation is only about 2% at the tip of the blade section.

It can also be concluded that the num. determined edgewise bending stiffness is in relative good agreement with the exp. determined edgewise bending stiffness, although the maximum deviation is about 10% at the tip end of the blade section.

Finally, it can be concluded that the num. determined torsional stiffness is in good agreement with the exp. determined torsional stiffness, although the maximum deviation is about 11% at the fixed end of the blade section.

The numerical model is a bit too stiff near the fixed end compared to the experimental results.

This deviation could be due to the increasing warping resistance from the fixed end of the FE-model and due to uncertainties regarding the experimental measurements.

The displacements that were measured during the locked torsion experiment are very small near the clamps and are therefore subjected to some uncertainties.

The reason why the numerical model is a bit too flexible at the last 2m is because the torsional stiffness is determined by a second order polynomial that is based on the element stiffnesses.

The numerical torsional stiffnesses of the last 8 elements are all in very good agreement with the experimental element stiffnesses but the first 2 elements have some deviation and this influences the overall torsional stiffness curve.

Other general uncertainties

Besides the uncertainties described above then the following factors could also influence the experimental results:

- Geometry.
The FE-model was created from the geometry of the Pro/E CAD model. This geometry could differ from the geometry of actual blade section.
- Ply-thickness.
The FE-model was created with the material thickness given by Vestas Wind Systems A/S. These thicknesses could vary and influence the area moment of inertia, bending stiffnesses etc.
- Layup and fiber orientation.
The blade section was manufactured with production tolerances which mean that the actual blade could differ from the technical drawings in terms of fiber angles etc.
- Mechanical properties in general.
The mechanical properties of the laminas are subjected to some uncertainties because of the varying resin volume fraction.

7.2.1. Sensitivity study for the original blade section

This section describes the parameter sensitivity studies that were carried out in order to reduce the deviation between the experimental and numerical results.

The ply properties are subjected to some uncertainties because the volume fraction of the resin can vary. This variation will influence all the laminae properties (E_1 , E_2 , G_{12} and ν_{12}).

The following studies were carried out:

- a) Reduction of E_1 by a factor of 1.1 for the UD-layers in the spar.
- b) Increase of E_1 by a factor of 1.1 for the UD-layers in the spar.
- c) Reduction of G_{12} by a factor of 1.1 for the UD-layers in the spar.
- d) Increase of G_{12} by a factor of 1.1 for the UD-layers in the spar.
- e) Reduction of G_{12} by a factor of 1.1 for the biax- and triax-layers.
- f) Increase of G_{12} by a factor of 1.1 for the biax- and triax-layers.

Case (a) and (b) were carried out in order to see if the changes in the bending stiffnesses are linear when the E-modulus is varied. The study showed that the bending stiffnesses vary linearly when one is operating inside the range from $E_1/1.1$ to $1.1E_1$.

Only the UD-layers were modified because they form the load carrying part of the blade section. The study showed that the bending stiffnesses are reduced by 6.8% and increased by 6.8% when E_1 goes from $E_1/1.1$ to $1.1E_1$.

As one can see, the bending stiffnesses are very sensitive to any variation in the fiber/resin fraction for the UD-layers, which means that the flapwise and edgewise bending stiffnesses could be subjected to some uncertainties.

Case (c), (d), (e) and (f) were carried out in order to see if the change in torsional stiffness is linear when the G-modulus is varied. The study showed that the torsional stiffness vary linearly when one is operating inside the range from $G_{12}/1.1$ to $1.1G_{12}$.

First, only the G-modulus for the UD layers was modified in order to see the UD layers influence on the torsional stiffness. The study showed that the torsional stiffness was reduced by 1.9% and increased by 1.9% when G_{12} goes from $G_{12}/1.1$ to $1.1G_{12}$.

Second, only the G-modulus for the biax- and triax-layers was modified in order to see the biax- and triax-layers influence on the torsional stiffness. The study showed that the torsional stiffness was reduced by 0.6% and increased by 0.6% when G_{12} goes from $G_{12}/1.1$ to $1.1G_{12}$.

As one can see, the torsional stiffness is not very sensitive to any variation in the fiber/resin fraction for the biax- and triax-layers. Although the biax- and triax-layers have a higher G-modulus than the UD layers, they only form a small part of the torsional stiffness since there are so few of them compared to the UD-layers.

7.2.2. Conclusion on the comparison of the original blade section

It can be concluded that one can obtain accurate flapwise bending results and relatively accurate edgewise bending results with the outer-surface FE-model which is based on a shell element configuration with offset. One should be careful with using shell element offset if the radius/thickness ratio is low.

It can also be concluded that the outer surface FE-model is not capable of modeling accurate torsional behavior and bend-twist couplings. The deviation between the num. and exp. results for the rotation about the z-axis was as high as 32%.

It can be concluded that the mid-thickness FE-model is not capable of modeling accurate flapwise and edgewise bending if one models details like ply drop-offs in the spar caps and etc. Using rigid elements to connect regions with different material thickness cannot in general be recommended.

Finally, by comparison of the global displacements and rotations for the shell/solid FE-model and for the experiments, it can be concluded that the shell/solid model is capable of modeling accurate flapwise-, edgewise- and torsional behavior.

The shell/solid model is more detailed and accurate than the two shell models, but the size of the shell/solid model is also considerable larger and therefore more time consuming to analyze. Furthermore, the high detail level of the shell/solid model is also ideal for analyzing stresses and strains.

The overall conclusion is that the shell/solid FE-model is by far the best numerical model of the three that were analyzed during this work.

7.3. Global comparison of exp. and num. results for the modified blade section

The numerical and experimental deflections and rotations for the modified blade are compared globally for the following static load cases:

- Flapwise bending
- Flapwise bending and torsion

7.3.1. Flapwise bending of the modified blade section (exp. vs. FEM)

The experimental results from the flapwise bending test is compared with the numerical results.

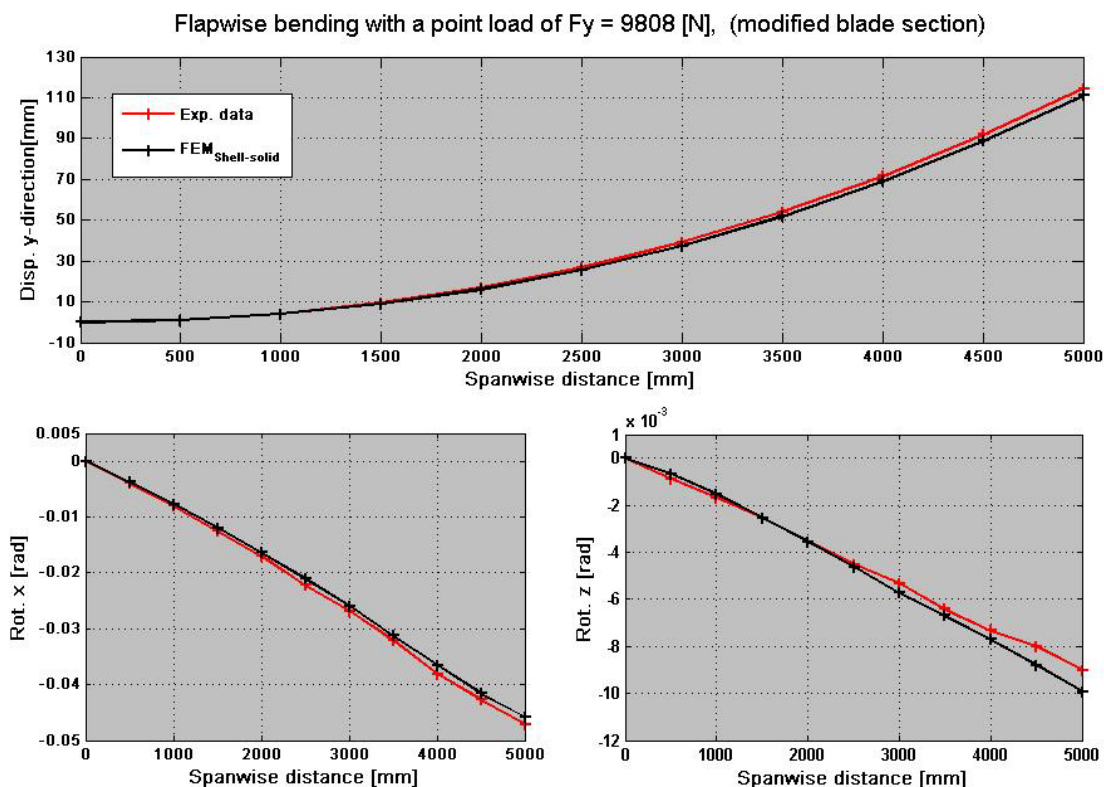


Figure 7.3.1 – Comparison of numerical and experimental results from the flapwise bending test (modified blade section)

Comment:

It can be concluded that the numerical flapwise displacement (disp. y-direction) is in good agreement with the experimental results; the maximum deviation is about 3.5%.

It can also be concluded that the rotation about the x-axis is in good agreement with the numerical results; the maximum deviation is about 5%.

The agreement between the numerical and experimental results for the rotation about the z-axis is very good at the first 2.5m but the FE-model deviates from the experimental results on the last 2.5m; the maximum deviation is about 9% at the tip.

The FE-model is twisting more than the experiment which could be due to an experimental problem. The flapwise tip load is applied by a hydraulic press and the press is of course in contact with the blade section. This contact could restrain the free tip twist of blade section during the experiment.

The FE-model is not twisting nearly as much as the experiment on the first 1.5m and this could be due to the effects from the boundary conditions. Again, torsion related warping is restrained in the numerical model in the fixed end which is not the case during the experiment.

A series of sensitivity studies were carried out in order to reduce the deviation between the experimental and numerical results.

7.3.2. Sensitivity study for the modified blade section

As described earlier, there are two key parameters that affect the magnitude of the coupling coefficient ψ (see description “Simple composite beam model with bend-twist coupling”). The two key parameters are the fiber orientation angle and the materials of the laminate. The UD material properties are the major uncertainty data input because the exact volume fractions are unknown.

The following sensitivity studies were carried out:

- a) 5% reduction of the E_1 -modulus.
- b) 5% reduction of the UD thickness (from 4.4mm to 4.2mm).
- c) Changing the fiber orientation from 25° to 24° and from 25° to 26° .

One would expect that the global displacement deviations (numerical vs. experimental) from the flapwise bending of the original blade would be approximately the same as the deviations from the flapwise bending of the modified blade. This was expected because the blade has only undergone a simple modification. Solid elements were created on the original FE-model, this is a simple procedure and since the added geometry is not complex, then it seems like there is a problem with the material properties or the fiber angle.

The modified blade deviates more from the experimental flapwise results than the original blade. This indicates that the value of E_1 might be too optimistic and sensitivity case (a) was therefore carried out. The results from case (a) are shown in *Figure 7.3.2* and *Figure 7.3.3*.

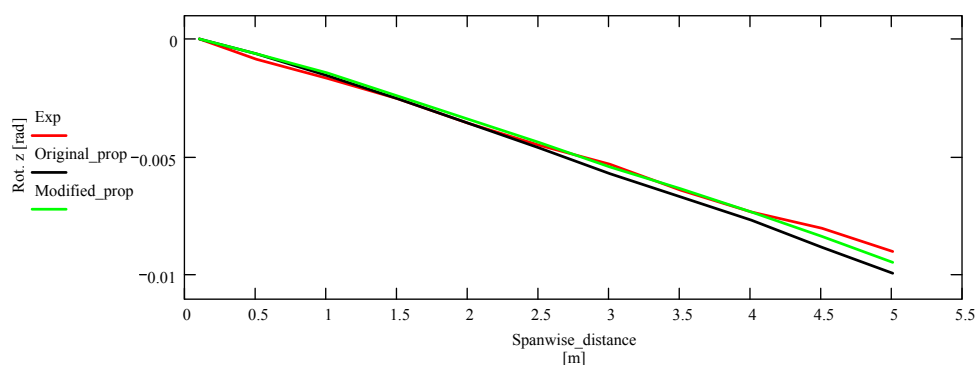


Figure 7.3.2 – Comparison of rotation about z for experimental, modified blade with original material properties and modified blade with modified material properties

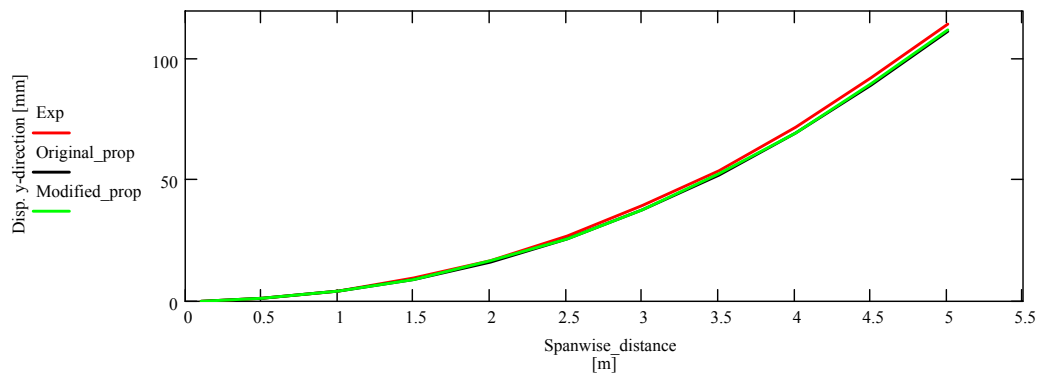


Figure 7.3.3 - Comparison of flapwise displacement for experimental, modified blade with original material properties and modified blade with modified material properties

Case (a) showed that the agreement between the numerical and experimental results for the rotation about the z-axis was improved; the maximum deviation was about 4.5% when the E_1 -modulus was reduced by 5%, from 34 GPa to 32.3 GPa.

Case (a) also showed that the agreement between the num. and exp. results for the displacement in the y-direction was improved; the maximum deviation was about 2 - 3%

As expected, it can be concluded from case (a) that the coupling coefficient is very sensitive to the longitudinal properties (E_1 -modulus) of the extra UD layers; therefore, it seems likely that a major part of the disagreement between the numerical and experimental results are due to uncertainties regarding the material properties since both the flapwise and twisting behavior of FE-model are in closer agreement with the experimental results if the E_1 -modulus is modified.

The results from case (b) are shown in *Figure 7.3.4* and *Figure 7.3.5*.

Case (b) showed that the agreement between the numerical and experimental results for the rotation about the z-axis was improved; the maximum deviation was about 6% when the thickness of the extra UD layers was reduced by 5%, from 4.4mm to 4.2mm.

Case (b) also showed that the agreement between the num. and exp. results for the displacement in the y-direction was improved; the maximum deviation was about 2 - 3%

It can be concluded from case (b) that the coupling coefficient is relatively sensitive to the thickness of the extra UD layers because this affects the bending and torsional stiffness of the blade.

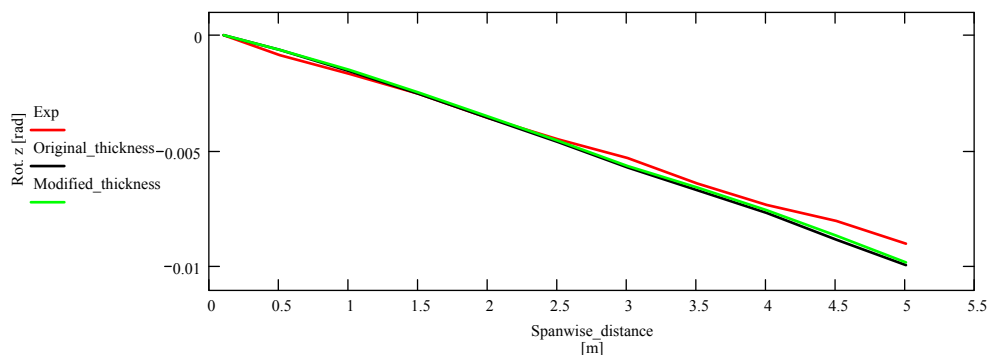


Figure 7.3.4 – Comparison of rotation about z for experimental, modified blade with original thickness and modified blade with modified thickness

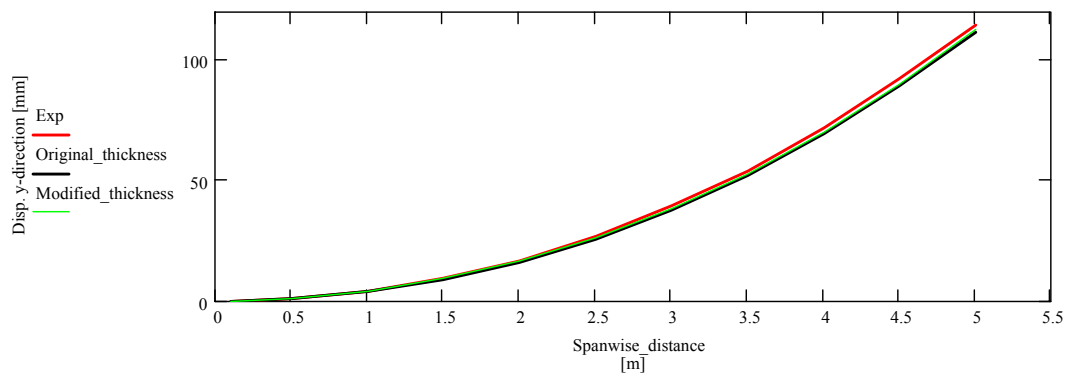


Figure 7.3.5 - Comparison of flapwise displacement for experimental, modified blade with original thickness and modified blade with modified thickness

The results from case (c) are shown in *Figure 7.3.6* and *Figure 7.3.7*. It is only the results from the 26° study that are shown because the 24° study is almost identical.

Case (c) showed that the twist rotation was increased a bit (less than 0.2%) over the whole length when the fiber orientation was changed from 25° to 26° .

This result was a bit surprising but can be explained by how the optimal fiber angle was determined. The optimal fiber angle was determined from the outer surface FE-model with layers of UD1600 material. First, the outer surface model is not capable of modeling correct torsional behavior, but only the outer surface model was created at the time when it was decided that extra UD layers were going to be laminated on the blade.

Second, the UD properties that were used for determining the optimal fiber angle, were the mechanical properties taken from the UD1600 layers used in the spar caps.

It is not possible to achieve the same “high” mechanical properties for the extra UD layers as for the spar cap UD layers when using a vacuum infusion process.

This combination of incorrect torsional behavior and slightly wrong mechanical properties could mean that 25° is not the exact optimal fiber angle.

There is only a small change in twist rotation when changing the fiber angle from 25° to 26° which means that 25° is very close to being optimal.

Case (c) also showed that the agreement between the numerical and experimental results for the displacement in the y-direction was improved when the fiber angle was changed from 25° to 26° . The flapwise displacement increased over the whole length (about 0.7%) but this was also expected because the fibers are rotated away from the longitudinal direction which makes the blade more flapwise flexible.

The flapwise displacement decreased over the whole length (about 0.6%) when the fiber angle was changed from 25° to 24° and the z-rotation was more or less unchanged.

It can be concluded from case (c) that the coupling coefficient is not sensitive to small changes in the fiber orientation. A fiber misalignment of $\pm 1^\circ$ would not change the twisting behaviour of the blade significantly; therefore, it seems unlikely that the twist deviation between numerical and experimental results is because of a fiber misalignment.

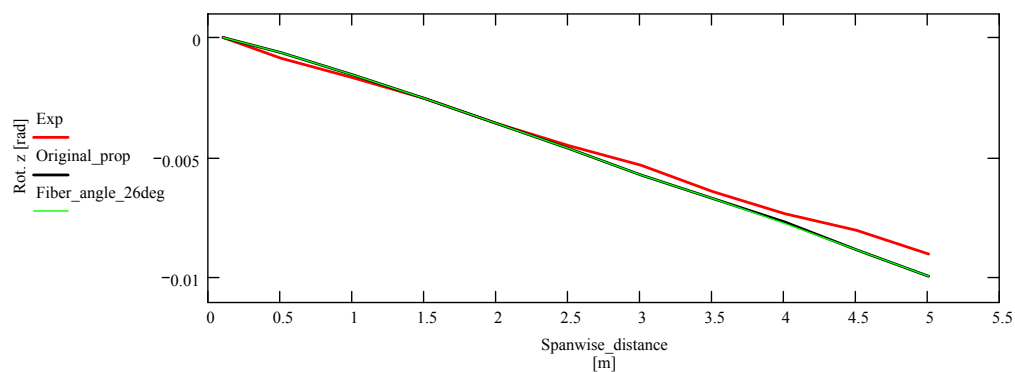


Figure 7.3.6 - Comparison of rotation about z for experimental, modified blade with original fiber angle and modified blade with 26° fiber angle

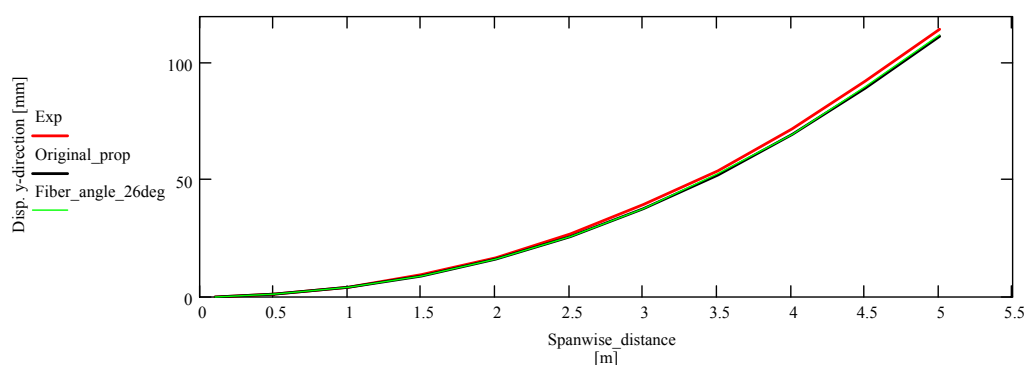


Figure 7.3.7 - Comparison of flapwise displacement for experimental, modified blade with original fiber angle and modified blade with 26° fiber angle

7.3.3. Flapwise bending and torsion of the modified blade section (experimental vs. FEM)

The experimental results from the flapwise bending and torsion test are compared with the numerical results. For a detailed description of this test method, see chapter 5.

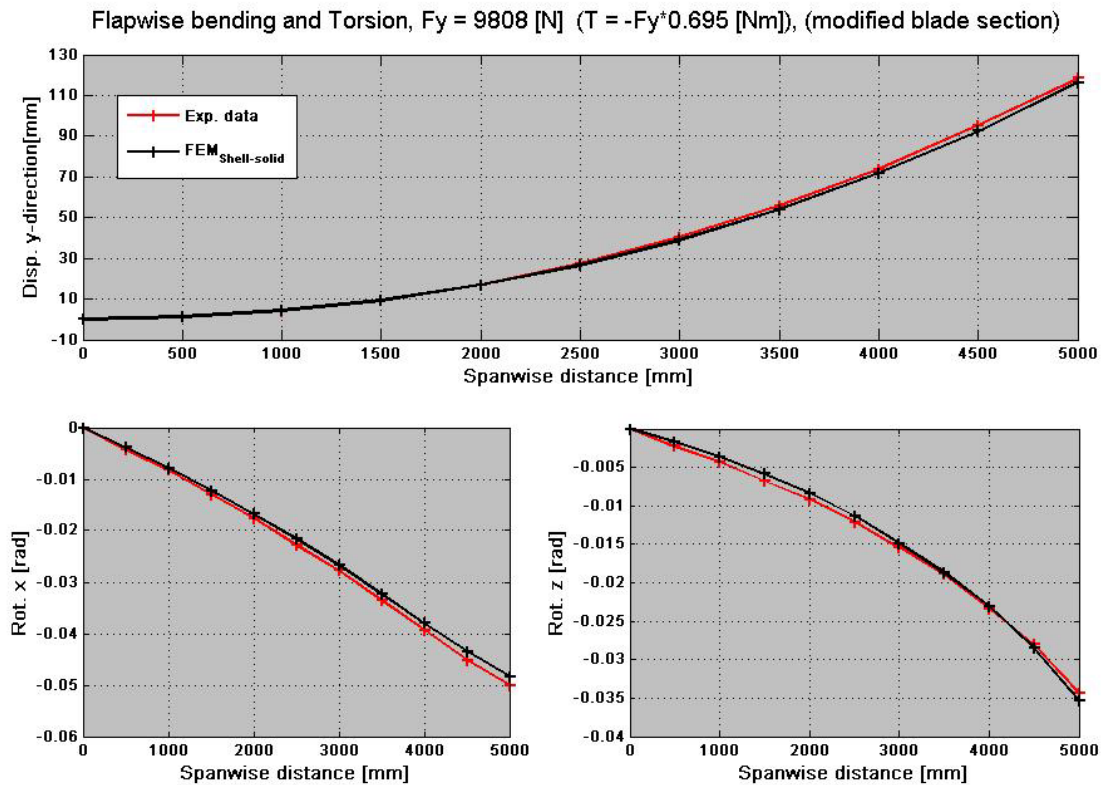


Figure 7.3.8 - Comparison of numerical and experimental results from the flapwise bending and torsion test (modified blade section).

Comment

It can be concluded that the numerical flapwise displacement (disp. y-direction) is in good agreement with the experimental results; the maximum deviation is about 2%.

It can also be concluded that the rotation about the x-axis is in good agreement with the numerical results; the maximum deviation is about 3.4%.

The agreement between the numerical and experimental results for the rotation about the z-axis is in general good agreement. The experimental twisting is a bit larger than the numerical twisting at the first 3m but the global twist is in good agreement; the deviation is about 3%. The deviation at the first 3m could be due to the restraint torsional warping, which increases the torsional stiffness of the FE-model.

Overall, it can be concluded that there is a good agreement between the numerical and experimental results for the flapwise bending and torsion load case.

7.3.4. Conclusion on the comparison of the modified blade section

The overall conclusion for the comparison between the numerical and experimental results for the modified blade section is that the results are in good agreement. The reasons for the relative small deviations are stated above.

It can be concluded that the FE-model is capable of modeling the flapwise, torsion and bend-twist coupling response with reasonable accuracy.

8. Conclusion and future work

One of the primary aims of this work was to set up guidelines for reliable determination of torsional stiffness and bend-twist couplings using FEM. The responses of the three different FE-models were compared with experimental results from static testing on a full-scale blade section. The blade section was modified by adding some additional angled UD layers on the suction and pressure side of the aerodynamic profile during the project. These extra UD layers were applied so that one could investigate if the FE-model was capable of model the bend-twist coupling that was introduced by these angled UD layers.

It can be concluded that a simple shell model with an offset configuration can model flapwise and edgewise bending behavior, but not torsional behavior. The poor torsional behavior is due to the offset configuration. By placing the shell elements in the material mid-thickness, it is possible to obtain a reasonable torsional behavior. The problem with a mid-thickness FE-model is that ply drop-offs and other details become impossible to model correctly. It can therefore be concluded that neither an offset shell model nor a mid-thickness shell-model can describe the complete stiffness behavior.

A third FE-model was also analyzed in this work. This FE-model was designed with solid hex 20 elements as core-material and 8-noded quad shell elements placed in the mid-thickness of the laminates. The results of the FE-analyses showed that this model was in general good agreement with the experimental results (flapwise bending, edgewise bending and torsion) of the original blade section and the modified blade section. It can therefore be concluded that this third model is recommendable if the complete stiffness behavior is needed. This model is of course more time consuming to analyze because the total number of degrees-of-freedom is reasonable high compared with the shell models.

One of the time consuming parts of this project was the experimental work. It was a big task to get the experimental setup up and running but an even bigger task to analyze the data. The measuring was performed with a 3D optical equipment (Aramis system), which was able to measure 3D displacements. A least squares algorithm was used in this work to determine the rotations and displacements of a number of deformed cross sections along the blade section. It can be concluded that this least squares algorithm was a strong tool when experimental and numerical results were compared.

Another aim of this work was to determine the full Timoshenko constitutive matrix, which can be used as an input to the HAWC2 code. A number of FE-models were analyzed during the project and the constitutive matrices for these models were determined by using a Beam-Property-Extracting-method. The method worked by placing MPC-RBE3 elements in a number of cross sections along the numerical beam models. The rotations and displacements at these cross sections could then be determined by analyzing the master-nodes in the MPC elements. The results of the BPE-method for simple FE-models with double symmetric isotropic cross sections, gave results which were in excellent agreement with theoretical values. The results from the BPE-method were subjected to some uncertainties as the cross sections became asymmetric and anisotropic. The constitutive matrices from the BPE-method should in theory be symmetric, but as these cross sections became asymmetric and anisotropic then were these matrices not completely symmetric. This indicates that the BPE-method is not computing the completely correct constitutive matrix. It is not clear what causes this asymmetric in the constitutive matrices, but it seems that it is primarily related to the shear deformation because the

asymmetric terms are primarily located in the first two columns and rows in the constitutive matrices. The reason could also be that it is too simple to assume that a cross section with hundreds of degrees-of-freedom can be described by single set of rotations and displacements (three rotations and displacements).

The original blade section was analyzed with the BPE-method and the results were compared with the stiffness determined by simple beam theory and showed to be in general good agreement. It was assumed that this comparison was valid as the original blade section has limited coupling.

Future work

The future work should include the following milestones:

- The future work should include future investigations of the BPE-method. A number of cross sections where the cross sectional properties are known, should be analyzed to indicate what this asymmetric of the constitutive matrix is caused by.
- Alternative FE-model should also be considered. A FE-model designed with layered structural solid elements could be one model, which could have potential.
- Since the experimental edgewise bending test is subjected to uncertainties then it would be preferable to perform a new edgewise bending test. Since the additional UD layers on the blade has stiffened the cross section at the location of the clamp 2 (fixed end) then it is possible to tighten the bolt connections more and by that creating a more “fixed” boundary. It would also be possible to bend the blade section more without damaging the core material in the trailing edge, because the additional UD layers protects the core material. In short, with the knowledge gained in this project, a new edgewise bending test would probably be subjected to fewer uncertainties.

9. Bibliography

- [1] Berring, P. and Knudsen, H., Torsional Performance of Large Wind Turbine Blades- Experimental Test Design, 2006.
- [2] Malcolm, D.J. and Laird, D.L., Identification and Use of Blade Physical Properties, 2005.
- [3] Jones, R.M., Mechanics of composite materials, 2nd edition, 1998.
- [4] Weisshaar, T.A., Vibration tailoring of advanced composite lifting surfaces, 1985
- [5] Pedersen, P., Elasticity – Anisotropy – Laminates, 1998.
- [6] Seaburg, P.A., Carter, C.J., AISC – Torsional Analysis of Structural Steel Members, 2003.
- [7] Pedersen, T.P. and Jensen. J.J, Styrkeberegning Af Maritime Konstruktioner, 1983.
- [8] Hodges, D.H., Nonlinear Composite Beam Theory, 2006.
- [9] Laird, D.L., Montoya, F.C. and Malcolm, D.J., Finite Element Modeling of Wind Turbine Blades, 2005.

10. Appendix

The most important programs/codes are shown on the DVD. These programs/codes are the following:

1. The analytical BPE-model of the rectangular steel tube.
2. The results of the numerical BPE-method performed on the rectangular steel tube.
3. Matlab's built-in Lyapunov solver (determination of the constitutive matrices).
4. Matlab program for determining experimental displacements and rotations.

The CD also contains the complete folders with experimental measuring data and the programs for analyzing this data.

The CD also contains the result files from the FE-analyses of the original and modified blades section and the BPE-programs for analyzing these files.